UNIVERSITY OF SOUTHAMPTON

GROUND VIBRATIONS GENERATED FROM TRAINS

By

Xiaozhen Sheng

Submitted for the degree of

Doctor of Philosophy

Institute of Sound and Vibration Research

Faculty of Engineering and Applied Science

DECEMBER 2001

UNIVERSITY OF SOUTHAMPTON

ABSTRACT

FACULTY OF ENGINEERING AND APPLIED SCIENCE
INSTITUTE OF SOUND AND VIBRATION RESEARCH

Doctor of Philosophy

GROUND VIBRATIONS GENERATED FROM TRAINS

A semi-analytical mathematical model has been developed for the prediction of ground vibrations generated by surface trains. This model incorporates the necessary components of the railway system. The vehicles, track and ground are described in a sufficiently detailed manner. The vehicles are described as multiple rigid body systems and only vertical dynamics is considered. The track is modelled as multiple beams supported by vertical springs with consistent mass. The ground is represented by horizontal layers on a homogeneous half-space or a rigid foundation. The governing equations of the vehicles are solved in the frequency domain and those of the track-ground system in the frequency-wavenumber domain. The Fast Fourier Transform technique is used to convert the responses of the track and the ground from the frequency-wavenumber domain into the frequency-space and time-space domains. This model uses the moving axle loads and/or the wheel/rail combined irregularities as its inputs. Outputs include the dynamic wheel-rail forces, the displacements and displacement spectra of the track and the ground. The model has been validated using measured data from three sites. These sites present different ground conditions (very soft, fairly soft and hard) and different train-traffic operations (high-speed passenger trains and low-speed freight trains of two-axle wagons). The effects of various parameters on the ground vibration have been investigated using this model, especially the layered structure of the ground, the mass of the ballast, the train speed and the frequency of excitation. A number of findings have been obtained and the roles are demonstrated of the two mechanisms, quasi-static and dynamic, at different frequencies and for train speeds below and above the lowest ground wave speed. The validation of the model suggests that it can be used as a tool for predicting ground vibration levels of new lines and for investigating the nature of vibration observed at particular sites and studying vibration reduction measures.

ACKNOWLEDGMENTS

I thank deeply my supervisors, Dr C J C Jones and Dr D J Thompson, for their regular help and guidance during this work. My thanks also go to Dr Mike Brennan for his valuable suggestions at each review meeting.

I am grateful to A. Smekal and Dr M. Li of the Swedish National Rail Administration (BANVERKET), Dr C. G. Lai (Studio Geotecnico Italiano S.r.l., Milano, Italy) and J. Block (AEA Technology, UK) and their organisations for their provision of parameters and measured data.

Finally, I would like to thank my wife, my son and my parents for their understanding and support of my pursuit of the PhD degree.

CONTENTS

LIST OF TABLES

LIST OF SYMBOLS

A. ROMAN SYMBOLS

a_l : Longitudinal coordinate of the lth wheelset or lth wheel-rail force at time $t = 0$.

b: Half width of the track/ground contact plane.

$\{b\}$ or $\{B\}$: A vector.

$[B]$: A matrix.

c: Train speed.

c_1, c_2, c_R: P-wave, S-wave and Rayleigh wave speeds.

c_{S1}: Viscous damping coefficient of the primary suspension per axle.

c_{S2}: Viscous damping coefficient of the secondary suspension per bogie.

$[D]$: See Section 3.2, Chapter 3.

E: Young's modulus.

EI: Bending stiffness of a beam.

f: Frequency.

F: Force.

G: Wheel-rail contact constant; Shear modulus.

[G]: See equation (2.24).

h_j: Thickness of the jth layer of a layered ground.

[H]: See equation (2.27).

i: Unit imaginary number, $i = \sqrt{-1}$.

$[I]$: Unit matrix.

j, k, l, m, n: Subscripts.

J_B: Pitch inertia of a bogie.

J_C: Pitch inertia of a car body.

k_B : Vertical stiffness of ballast per unit length of track.

k_G: Vertical stiffness of a Winkler foundation.

k_{Hl}: Stiffness of the Hertz contact spring between the lth wheelset and the rail

k_P : Stiffness of railpad per unit length of track.

k_{S1}: Stiffness of the primary suspension per axle.

$k_{S1}^{'}$: Stiffness per axle of the damper in the primary suspension.

k_{S2}: Stiffness of the secondary suspension per bogie.

$k_{S2}^{'}$: Stiffness per bogie of the damper in the secondary suspension.

$[K_V]$: Complex stiffness matrix of a vehicle.

l_B: Half distance between two adjacent bogies in a vehicle.

l_P: Number of the soil layer containing the source.

l_R: Number of the soil layer containing the observer.

l_W: Half distance between two wheelsets in a bogie.

m_B : Mass of ballast per unit length of track

m_R : Mass of (two) rails per unit length of track

m_S : Mass of sleepers per unit length of track

M: Number of wheel-rail forces.

M_B: Mass of a bogie.

M_C: Mass of a car body.

M_W: Mass of a wheelset.

n: Number of layers of a layered ground.

N: Number of vehicles in a train.

$p_x(x, y)$, $p_y(x, y)$, $p_z(x, y)$: Loads per unit area on the ground surface in x-, y- and z-directions.

$P_l(t)$: The lth wheel-rail force.

$\tilde{P}_l(\Omega)$: Defined as $P_l(t) = \tilde{P}_l(\Omega)e^{i\Omega t}$.

$P_u(x, y, f)$, $P_v(x, y, f)$ and $P_w(x, y, f)$: Longitudinal, lateral and vertical displacement power spectra of the ground surface at point (x, y) at frequency f.

$[Q]$: Dynamic flexibility matrix of the ground.

$[\tilde{Q}(\beta, \gamma, \omega)]$: Fourier transformed dynamic flexibility matrix of the ground.

R: Rolling radius of a wheel.

$S_u(x, y, f)$, $S_v(x, y, f)$ and $S_w(x, y, f)$: Longitudinal, lateral and vertical displacement spectra of the ground surface at point (x, y) at frequency f.

$S_u^0(x, y, f; \Omega)$, $S_v^0(x, y, f; \Omega)$ and $S_w^0(x, y, f; \Omega)$: Longitudinal, lateral and vertical displacement spectra of the ground surface at point (x, y) at frequency f due to a unit rail irregularity of wavelength $\lambda = 2\pi c / \Omega$.

$u(x, y, z, t)$, $v(x, y, z, t)$, $w(x, y, z, t)$: Longitudinal, lateral and vertical displacements of the ground at point (x, y, z) and time t.

$[\tilde{U}(\beta, \gamma, \omega)]$, $[\tilde{V}(\beta, \gamma, \omega)]$: Fourier transformed stress matrices.

$w_R(x, t)$: Displacement of the rails at position x and time t.

$w_S(x, t)$: Displacement of the sleeper at position x and time t.

$w_C(x, t)$: Displacement of the centre-line in the track-ground contact plane at position x and time t.

$\overline{w}(\beta,\gamma,t)$: Fourier transform of $w(x, y, z, t)$.

$\tilde{w}(\beta,\gamma)$: defined by $\overline{w}(\beta,\gamma,t) = \tilde{w}(\beta,\gamma)e^{i(\Omega-\beta c)t}$.

$z(x)$: Vertical profile of the rail.

$z_{Wl}(t)$: Displacement of the lth wheelset.

$\tilde{z}_{Wl}(\Omega)$: Defined as $z_{Wl}(t) = \tilde{z}_{Wl}(\Omega)e^{i\Omega t}$.

$z_{Rl}(t)$: Displacement of the rail at the lth wheel-rail contact point.

$\tilde{z}_{Rl}(\Omega)$: Defined as $z_{Rl}(t) = \tilde{z}_{Rl}(\Omega)e^{i\Omega t}$.

B. GREEK SYMBOLS

α, β, γ: Wavenumbers in z-, x- and y-directions in radians per metre.

$\delta(x)$: Dirac-δ function.

$[\tilde{\delta}]$: See equation (2.41).

ζ : Viscous damping ratio.

ζ_{j1}, ζ_{j2} : P- and S-wavenumbers in the jth layer defined as $\zeta_{j1} = \omega / c_{j1}, \zeta_{j2} = \omega / c_{j2}$.

η: Loss factor.

λ: Wavelength.

λ, μ: Lamé constants.

ν: Possion ratio.

ρ: Density.

τ: Stress.

ω: Defined as $\omega = \Omega - \beta c$.

Ω: Angular frequency observed in the frame of reference that moves with the train.

$[\Sigma_R]$: Receptance matrix of the track-ground system at wheel-rail contact points.

$[\Sigma_V]$: Receptance matrix of a vehicle.

$[\Sigma_W]$: Receptance matrix of a vehicle at the wheelsets.

$[\Sigma_T]$: Receptance matrix of the train at the wheelsets.

Chapter 1

INTRODUCTION

This chapter, having emphasized the impact of train-induced ground vibration on the environment and hi-tech production, reviews previous work on the study of train-induced ground vibration. Relevant data are collected and the tasks of the current project are defined based on the literature review.

1.1 IMPACT OF GROUND VIBRATION AND ITS SOURCES

In recent years rail transport systems have increasingly received complaints of disturbance and annoyance from people living and working alongside lines and people living above underground lines. The disturbance is caused not only by the direct emission of noise from the railway, but also by the low-frequency whole-body vibration of the buildings and the noise radiated by the vibrating walls and floors, due to the ground motion induced by the rail traffic.

For the perception of whole-body vibration, the important frequency range is 2 to 80 Hz [ISO 2631-1:1997], and usually relates to the operation of heavy axle-load trains running at low speeds on lines on the ground surface. Vibration in the frequency range from 30 Hz to 200 Hz [Grootenhuis 1977] excites the bending resonances of walls and floors in buildings which then radiate sound directly into rooms. This structure-borne noise (often termed 'groundborne noise') is predominantly associated with trains running in tunnels and therefore is a major concern for metropolitan railways (metros) running largely in tunnels in heavily built-up areas. Surface-running 'light-rail' vehicles which pass very close to buildings can also cause unacceptable levels of this 'rumbling' noise.

The operation of high-speed trains highlights the problem of ground vibration. When a high-speed railway goes through a region with a soft ground, the train speed may be close to, or exceed, the lowest wave speed in the ground. In that case a very high level of ground vibration may appear and propagate [Krylov 1995]. Such a high level of vibration has been observed in Sweden in the operation of the X2000 train [Madshus & Kaynia 1998(a)]. Several hi-tech enterprises in the Tainan Science Park in Taiwan are planning to move out of the park because of the concerns about the impact of the strong vibration from the Taiwan High-Speed Railway on the production of hi-tech products

[news on 12/05/2001 on www.zaobao.com.sg]. Using typical data from measurements, Dowding [2000] presented an investigation on the effects of ground motions from high-speed trains on structures, instruments and humans.

In some countries, guidelines have been derived for acceptable vibration levels in buildings near existing and new railway tracks. For example, in Sweden [Banverket BVPO 724.001], for existing tracks, a velocity of 1 mm/s (maximum rms) has been chosen as the highest level to which a dwelling should be exposed. In the vicinity of new tracks, an even stricter level of 0.4 mm/s has been chosen as the trigger for consideration of countermeasures.

The sources from which the ground vibration is produced are the wheel-rail interaction forces. When a wheelset runs along rails, it applies a force on the head of each rail. This force is termed the wheel-rail contact force or simply the wheel-rail force. A wheel-rail force can be decomposed into longitudinal, lateral and vertical components. The longitudinal component is small compared with the other two components if the train runs on a level straight track at a uniform speed. As shown in Figure 1.1(a), P_l and P_r refer to the vertical forces on the heads of the left rail and the right rail, respectively, and Q_l , Q_r refer to the lateral forces. Usually P_l is not equal to P_r, and neither is Q_l to Q_r. Responses to the force configuration in Figure 1.1(a) can be viewed as a resultant of those to the force configurations in Figures 1.1 (b), (c), (d) and (e). The first three force configurations excite the track to vibrate vertically, torsionally and laterally, and consequently produce ground vibration and propagation. It is clear that the forces in Figure 1.1(e) have little effect in generating ground vibration due to the bending stiffness of the sleepers.

A vertical force exerted on the rails by the wheels may have three types [Sheng, Jones and Petyt 1999 (b)]. The first is a moving axle load (termed *quasi-static load*). When the train speed is much lower than the wave speeds in the ground, a quasi-static load will only produce a nearly static deformation of the track and the ground and no propagation is expected. However, if the train speed is close to or exceeds the wave speeds in the ground, a very high level of ground vibration may appear and propagate. The second type is a *fixed-point dynamic load* at the track, which is produced when wheels pass and impact a fixed irregularity on the rail such as a rail joint. The vibration and propagation properties associated with this component depend on its frequency

contents and on the dynamic properties of the track and the ground. The third type is a *moving dynamic load* generated from the acceleration of an unsprung mass on the vehicle. This acceleration is produced from the irregularities of the wheels and rails, and is a function of vehicles, track, ground and train speed. When the train speed is well below the wave speeds in the ground, this component can be treated as a fixed-point dynamic load.

There are a number of factors affecting the vibration level perceived by people in buildings. These factors can be grouped into four subsystems: vehicles (train), track, ground and buildings. It is well known that the unsprung mass of a vehicle has a great effect on the dynamic wheel-rail forces [Zai 1997] and thus on the ground. To attenuate vibration and noise produced by railways, a number of types of track, for example ballasted tracks with ballast mats and floating slab tracks, have been designed and used in practice. The ground vibration level is greatly affected by the ratio of the train speed to the lowest wave speed of the ground determined by the soil properties. Buildings may amplify or attenuate the ground vibration depending on the dynamic properties of the building structures. The interactions between these four subsystems make the problem very complicated. The complexity is also addressed by the fact that, for the study of ground vibration, various approaches have been devised and used to account for different aspects of the problem. A literature review now is carried out in the next section.

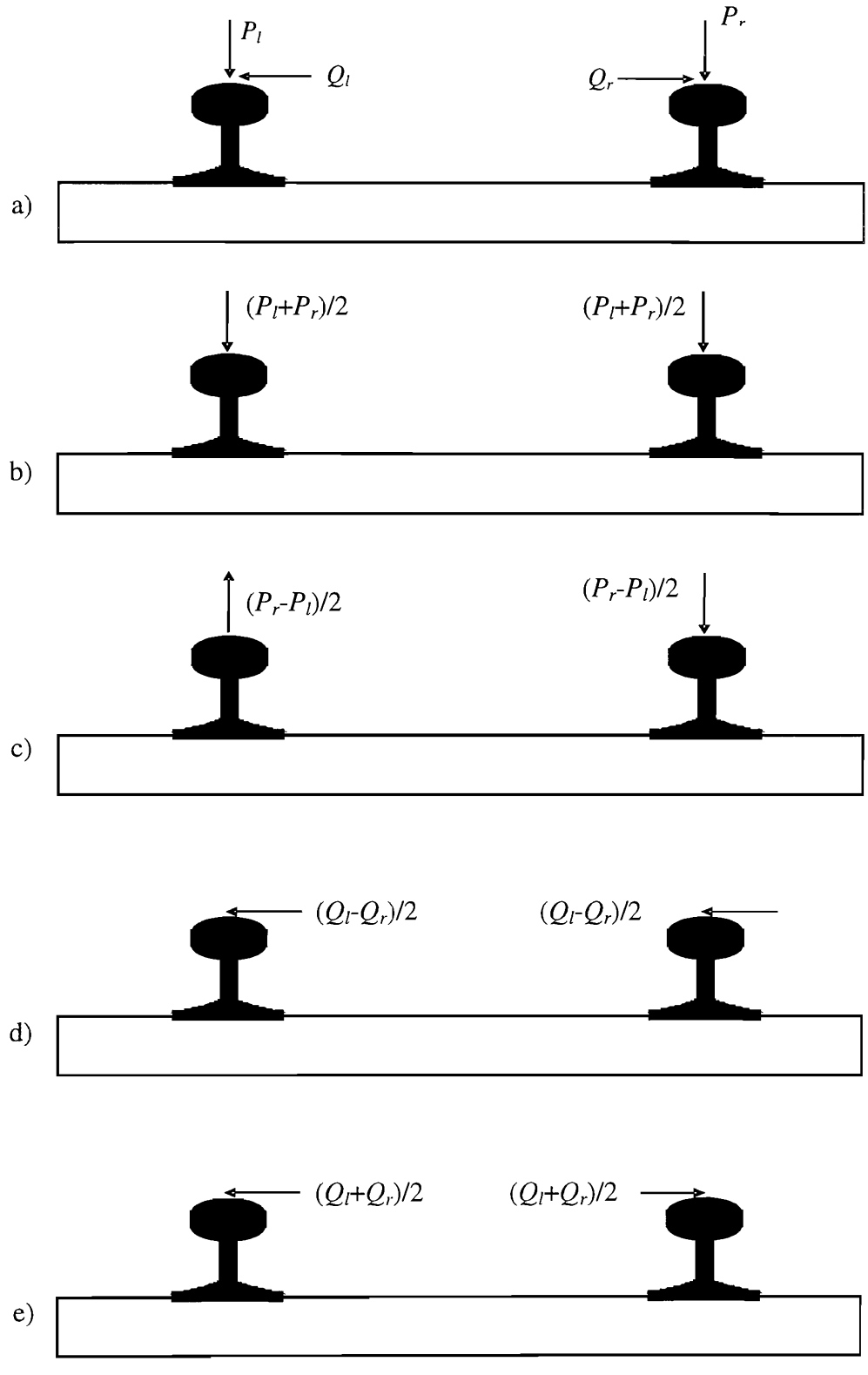

Figure 1.1. Wheel-rail forces. (a) Forces acting on each rail. (b) and (c) Symmetric and antisymmetric components of vertical force. (d) and (e) Symmetric and antisymmetric components of lateral force.

1.2 LITERATURE REVIEW

There are many researchers who have worked or are working on ground vibration from railways. They are interested in different aspects of the problem. A seminar was held focussing on ground vibrations induced by high-speed trains in March, 2000 at Gothenburg, Sweden. At this seminar, about 50 researchers from different countries exchanged their experiences on the topic. At the workshop WAVE 2000 held in December, 2000 at Bochum, Germany, a large proportion of the papers were devoted to ground vibrations from railway trains [Chouw and Schmid 2000]. One of the important issues is to develop a mathematical model and produce the relevant software for predicting train-induced ground vibration. A mathematical model can be used for [Petyt and Jones 1999]: a) developing the understanding of the physical process involved; b) enabling the development of track or ground engineering solutions for reducing vibration transmission; c) providing data to be used with empirical predictions of vibration for environmental assessment of new lines. Since there are a number of effects of vibration covering surface propagation and tunnel vibration in different frequency ranges, it is not surprising that a number of different modelling approaches have been devised. The modelling approaches can be divided into three categories, i.e. analytical wavenumber-frequency domain approach, numerical approach, and empirical approach. The wavenumber-frequency domain approach is also referred to as the integral transform method (ITM), and the numerical approach usually includes the finite element method (FEM) and/or the boundary element method (BEM). Grundmann [1997] has presented a general discussion and comparison between ITM, FEM and BEM. A review of the state of the art of the mathematical modelling of railway vibration up to 1997 can be found in reference [Villot, Jean and Chanut 1997].

1.2.1 WAVENUMBER-FREQUENCY DOMAIN APPROACH

This approach uses a single and a double spatial Fourier transform to transform the governing equations of the track and the ground from the physical domain (xyz domain, where the x-axis is directed in the railway direction (longitudinal direction), the y-axis is directed in the horizontal plane and normal to the railway (lateral direction), and the z-axis is directed vertically) into the wavenumber domain (β, γ, z), where β, γ are wave numbers in the x- and y-directions, respectively. Having solved the Fourier

transformed equations of motion, an inverse Fourier transform is performed to give the solution in the physical domain.

If a harmonic vibration is assumed, and if the ground consists of horizontally parallel layers of homogeneous materials (layered ground), then the Fourier transformed equations of motion for the ground can be solved analytically in terms of the vertical co-ordinate z. This results in relations between the Fourier transformed displacements and stresses at both sides of a layer. Several forms of these relationships are available. One relates the displacements and stresses at one side of the layer to the corresponding variables at the other side of the layer. This formulation is generally known as Haskell-Thomson technique [Thomson 1950, Haskell 1953] in the fields of soil dynamics, earthquake engineering and geophysics. An alternative is to relate the displacements at both sides of the layer to the stresses at both sides of the layer, resulting in a direct or exact dynamic stiffness matrix [Kausel and Roesset 1981, Wolf 1985]. The two aforementioned methods use the analytical solution of the wave equation in a displacement formulation. When, alternatively, the exact solution of the wave equation is maintained in the horizontal direction, while a polynomial expansion is used in the vertical direction, a so-called thin layer formulation is obtained [Lysmer and Waas 1972, Waas 1972, Kausel and Peek 1982, Tassoulas and Kausel 1983, Kausel 1986]. This thin layer formulation (also called *thin layer element method*) can avoid computational difficulties arising when the thickness of a layer is too big. However as a sacrifice, the scale of calculation is increased.

Rather than use either the exact or discretized dynamic stiffness matrix techniques, it has been found [Sheng, Jones and Petyt 1999 (a)] that improved computational efficiency can be achieved by using the *dynamic flexibility matrix approach* since all the matrices being manipulated are of order less than or equal to six. The details of this method and its extension to account for calculating stresses due to both stationary harmonic loads and moving harmonic loads will be presented in Chapter 2 of this thesis.

Since 1991, Jones and Petyt [1991, 1993(a), 1993(b), 1997, and 1998] have published a series of papers on vibration propagation from railways. In their work, the ground is modelled, first as a homogeneous half-space, and then as a layer on an elastic homogeneous half-space or on a rigid foundation, and the thin layer formulation is used.

Without including any track structure, the load applied by the track is assumed as a harmonic pressure of constant amplitude over a rectangular area on the ground surface.

The transient response of the ground due to a transient load can be constructed from that due to harmonic loads. In addition to this conventional method, some special methods have been suggested [Lee and Ma 2000(a), (b)].

The method of coupling the railway track with the ground was proposed by Jones [Jones 1994, 1996] and was first published in 1999 [Sheng, Jones and Petyt 1999 (a)]. In references [Jones 1994, 1996], use is made of the cubic-polynomial shape functions rather than the linear approximation across each three-dimensional layer element. In reference [Sheng, Jones and Petyt 1999 (a)], the dynamic flexibility matrix approach is used to increase calculation efficiency and accuracy. Though only one harmonic load, which acts at a fixed point on the rails, is considered, the importance of the layered structure of the ground and the structure of the railway track has been revealed. It is shown that the layered structure of the ground may produce a number of propagation modes, and the presence of a railway track may modify these modes. Example calculations show that the overall effect of the presence of the track is to increase the amplitude of vibration by a factor of two [Sheng, Jones and Petyt 1999 (a)].

The work mentioned above only considered stationary loads. When the train speed is close to, or exceeds, the lowest wave speed in the ground, the stationary load models are not applicable. Therefore a model to account for moving loads is required. Making use of an exact factorisation of the displacement and stress fields in terms of generalised transmission and reflection coefficients, Barros and Luco [1994] proposed a procedure to calculate the steady state displacements and stresses (termed *moving Green's functions*) within a layered ground generated by a buried or surface harmonic load moving with constant speed parallel to the ground surface. In this work, the displacements and stresses are formulated in terms of a double integral with respect to frequency and wavenumber in the lateral direction. Jones, Le Houedec and Petyt [1998] investigated the ground vibration generated by a moving harmonic load acting directly in a rectangular area on the ground surface. In this work, the ground is modelled as a homogenous half-space and the dynamic stiffness matrix of the half-space has been used. Groundmann, Lieb and Trommer [1999] also calculated the response of a layered ground to pre-assumed moving traffic loads using the thin layer formulation. In this work, the

inhomogeneous property in a layer in the vertical direction is introduced and the inverse FFT implemented by the wavelet transform is used to get the response in the spatial domain.

When the train speed is very low, and when the axle spacing is long enough, it may be sufficient to consider only a single load on the rails because of the rapid decay of the ground vibration of low frequency. However, for high-speed trains, the moving loads may excite a propagating mode in the ground, which propagates over a much longer distance along the track. In this case, the interference between adjacent axles may have an important effect on the ground response. Even for low-speed freight trains, since the axle spacing is short, the coupling between adjacent loads may still have a significant effect. In both of these cases, multiple moving loads need to be considered.

Alabi [1992], without implementing any model of railway track, modelled the loads applied by the railway track on the ground surface as a uniform moving load of infinite length in the moving direction and of finite width in the lateral direction.

Krylov [1994, 1995] studied ground vibration from the whole set of moving static loads of a train on a track structure. In his study, a static deformation pattern of the rails under the axle loads is assumed to move at the train speed and thus to produce a dynamic force for each sleeper all of which together excite the ground. In this model, the track is modelled as a single beam resting on a Winkler foundation and only a single Rayleigh wave type has been taken into account in the ground part of the model. However, in his later papers, Krylov [1996, 1997, 1998, 1999 and 2000] included some of the effects of a layered ground into the same modelling approach by using a frequency-dependent Rayleigh wave speed. Since Krylov's model is relatively simple in calculation, it has been employed by many researchers [e.g. Lai, Callerio, Faccioli and Martino 2000, Degrande and Lombaert 2000].

It has been demonstrated by Lai et al [Lai, Callerio, Faccioli and Martino 2000] that, at least in some measurement conditions, a model only incorporating quasi-static loads would underestimate the ground vibration level, especially for higher excitation frequencies.

Jones and Block [1996] divided the vibration observed at the track during the passage of a train into two parts. The first consisted of the time history of the quasi-static

deformation pattern due to successive axles as the train passes a fixed point, and the second, the response to dynamic loads caused by the acceleration of the masses of the train over the combined irregular profile of the wheels and track. For the propagation of vibration in the ground, they used a model of wave propagation from a fixed-point harmonic load on the track. The effect of the movement of the train was introduced as phase delay in the summation of vibration contributions from different sleeper positions along the track. The phase delay consisted of two parts: one corresponding to the time needed for a wave in the ground to travel from the excitation point to the observation point, and for this part the assumptions of a single wave speed in the ground was used; the other part corresponding to the time needed for an axle load to move over the corresponding distance.

All the models mentioned so far account for the ground vibration induced by surface trains. In these models only the vertical dynamics of the track has been considered. In fact, a wheelset may also apply a lateral force to the rails, which will excite the track to vibrate laterally (see Figure 1.1(d)). It is also the case that, due to the track twist irregularity, a wheelset may apply a torsion moment on the track that will excite the track to twist (see Figure 1.1(c)). The ground vibrations induced by the lateral movement and torsion of the track have received almost no attention. It is also remarked that the interactions between vehicles and a track/ground system have received little attention. In the related field of vehicle dynamics, the track is usually considered as a stiffness at each wheel.

The wavenumber-frequency approach, in addition to being applied to study the vibration of a layered ground without any inclusion (tunnel, cutting etc.), has also been applied for a layered ground with an inclusion [Luco and Barros 1993] of infinite length. This application makes use of the homogeneity of the inclusion in the longitudinal direction and has some advantages over other methods [Aubry, Clouteau and Bonnet 1994].

An important issue in which people are interested is the so-called critical speed of a moving load. A *critical load speed* is defined as that at which a load moves when the steady state amplitude of an undamped ground becomes infinite. In the presence of damping, this load speed will produce the strongest vibration. The phenomenon of critical load speed has been observed in Sweden [Madshus and Kaynia 1998]. Dieterman

and Metrikine [1997(b)] used a model of a point harmonic load moving along an elastic layer (extending to infinite in the lateral direction) resting on a rigid foundation to study the existence of critical load speeds in the ballast layer, showing that resonance occurs when the load speed is equal to the group speeds of the wave generated in the layer by the load. Usually there are several critical speeds for a layered ground. The presence of a beam may increase or decrease the critical load speeds [Dieterman and Metrikine 1997(a)].

1.2.2 NUMERICAL APPROACH

The wavenumber-frequency approach is analytical or semi-analytical and is well adapted to infinite boundaries without frequency limitations. However it can only be used in case of ground layers with parallel interfaces. If the ground has arbitrary geometry or if it has some inclusion, which is not homogeneous in the longitudinal direction, then numerical approaches must be employed. Two numerical approaches are used most commonly, one is the finite element method (FEM), and the other is the boundary element method (BEM). In FEM, structures and part of the ground (an artificial boundary must be introduced) are discretised and vibration levels (displacement, velocity or acceleration) are calculated at nodes. The artificial boundaries of the ground must incorporate the travelling wave propagation of an infinite medium. In other words, one must deduce proper boundary conditions, often termed 'transmitting boundary conditions', for the artificial boundary in order to ensure that no wave of significant amplitude is reflected by this artificial boundary. One type of such conditions was developed by Waas [1972] for two-dimensional problems and by Kausel [1974] for axially symmetric problems. The difficulty in using FEM is that, for a three-dimensional problem (when the movement of trains is considered then a three-dimensional problem results) there is a large number of elements involved in the analysis. Whereas infinite elements have been developed for two-dimensional problems in elasto-dynamics, they have not been developed for three-dimensional problems.

The BEM is very well suited for dynamics of infinite media. Boundless regions are naturally represented. The radiation of waves towards infinity is automatically included in a BEM model which is based on an integral representation valid for internal and external regions. However, BEM is not optimal for thin structures such as tunnels since both faces of a structure have to be discretized, and BEM has numerical problems

for thin domains. Therefore for the dynamics of soil-structure interaction, a combination of FEM and BEM appears logically in which the finite structure is modelled using FEM and the ground is modelled using BEM [Jones, Thompson and Petyt 1999, 2000].

In the application of BEM to the study of ground vibration, the Green's functions play a key role. The *Green's functions* are defined as displacements (or other quantities) of the ground due to a single unit concentrated load. The Green's functions are available for a homogenous full-space [Eason, Fulton and Sneddon 1956] and for a layered half-space [Sheng, Jones and Petyt 1999(c)]. Green's functions for a so-called two-and-half-dimensional homogeneous whole-space have also been derived [Tadeu and Kausel 2000]. If the Green's functions of a homogenous full-space are employed, then not only the interface of the ground and the built structure, but also the ground surface and the interfaces of the layers need to be discretised. In other words, only part of the ground surface and interfaces is taken into account, thus introducing artificial boundaries. However since the Green's functions for a full-space are formulated in a closed form, they are therefore easy to use. On the other hand, if the layered half-space Green's functions are employed, then for a ground consisting of parallel layers, only the interface of the ground and the built structure need to be discretised. However, the Green's functions for a layered half-space are expressed in terms of boundless integrals, the evaluation of which is time consuming.

Though the numerical approach can deal with arbitrary geometry such as trenches and buried walls, and ground with sloping layers, cuttings and embankments, it has a high frequency limitation depending on the order of elements and the computing resources used. In addition to that, a fully three-dimensional model is not used in practice because of the complexity and excessive computation time.

Wei & Petyt [1987] used the FEM to analyse the two-dimensional problem of a single layer on a rigid foundation. Both cuttings and embankments were introduced on the ground surface. The part of the layer containing the load and the geometric irregularities was modelled using linear, four noded, plane strain quadrilateral elements. Comparison with a dynamic stiffness solution indicated that ten elements per wavelength should be used.

Jones, Wang and Dawn [1995] used the FEM to predict vibration propagation from a bored tunnel (modelled as a two-dimensional problem). Finite elements (12 noded

quadrilaterals and 10 noded triangles) were used to model the tunnel and the adjacent ground, and semi-infinite elements were used to model the wave propagation away from this region.

For the two-dimensional ground vibration problem, Peplow, Jones and Petyt [1999] used single-noded boundary elements on each of which the displacement was modelled as having a constant value. This approach demands that elements should be very much smaller than a wavelength of the wave in the solid and is adequate for low frequencies. To account for the high frequencies associated with ground-borne noise, Jones, Thompson and Petyt [1999, 2000] used boundary elements with three nodes and quadratic shape functions. In this work, the FEM was also used to analyse built structures such as bored tunnel linings or cut-and-cover tunnels.

The numerical approach has been used to investigate the effectiveness of barriers, such as trenches, piles, and line-side masses, for ground vibration reduction. Ahmad and Al-Hussaini [1991], using a two-dimensional BEM model, and Yang and Hung [1997], using a two-dimensional Finite-Infinite-Element model, studied the effectiveness of open trenches and in-filled trenches. It was shown that trenches are primarily effective at high frequencies, and are most effective in screening against surface waves. Open trenches are more effective as barriers than solid barriers (such as in-filled trenches), but the latter are more practical because of the difficult stability and ground water problems associated with the open trenches. Piles appear to be the least effective type of barrier.

Takemiya and Fujiwara [1994] and Takemiya, Shiotsu and Yuasa [2000] also used a combined FEM and BEM model to investigate the line-side ground vibration induced by high-speed trains and the mitigation measure of a wave impedance block (WIB). A wave impedance block is a block that is made of different material from the soil and is inserted into the ground to modify its propagating wave modes. The combined FEM/BEM method and its application to traffic-induced ground vibration have attracted increasing attention (see [Chouw and Schmid 2000]).

1.2.3 EMPIRICAL APPROACH

Empirical methods, i.e. those that predict on the basis of trend analysis from a database of measurement data, are used successfully for the prediction of environmental vibration. Because of the large number of factors affecting ground vibration, they cannot

be used to demonstrate the physical process of vibration excitation and propagation or used to study the design of reduction measures. In general, empirical prediction formulae can only be used for situations similar to those upon which the empirical formulae are extracted. For these reasons, empirical methods are not compatible with the purposes of the present work and are not considered further in this thesis. A detail and comprehensive summary of empirical prediction methods can be found in reference [Sharif 1997].

1.2.4 MODELS OF RAILWAY TRACKS

Various railway track dynamics models have been developed to study the vertical and lateral track dynamics in different frequency ranges [Grassie et al 1982, Thompson 1993, Knothe et al 1994, Mead 1996, Zai 1997 and Wu and Thompson 1999]. The purpose of these models has been to study the vehicle-rail interaction and/or the wheel-rail noise and therefore none of them have taken into account the effect of the ground supporting the railway track. Recently, Knothe and Wu [1999] presented a track model incorporating the ground. In this model the rail is modelled as an infinite Timoshenko beam, the ballast below each sleeper is modelled as a mass block. Under the mass block a uniformly distributed pressure is assumed to act over a rectangular surface area of the subgrade. The subgrade is modelled as a homogeneous elastic half-space or as a layered half-space. The calculations of the receptance of the rails show that, in the low and medium frequency range up to 250 Hz great differences are observed between this model and the previous models in which the energy propagation into the ground has not been considered.

Van den Broeck and De Roeck [1999] investigated the vertical receptance of a track including soil-structure interaction. Their calculations show that for frequencies lower than 200 Hz, the loading point position (above a sleeper or at the middle of a span) makes negligible difference in the vertical receptance; the rail and the sleeper move together with a large deformation of the ballast and the subgrade as a result. These results indicate that, for that frequency range, a continuously supported rail model is suitable. Man and Kok [2000] also studied the effect of change in ballast stiffness on the response, showing that low frequency response is highly dependant on the ballast properties. From those observations, an important conclusion can be drawn that, in the low frequency range (less than 250 Hz), the dynamic behaviour of the ballast and the subgrade have to be modelled correctly.

In modelling the railway track, the rails are usually modelled as an Euler beam or a Timoshenko beam. The latter includes the effects of the shear deformation and rotational inertia of the beam. For frequencies below about 500 Hz for a normal steel rail section, the difference between these two beam models is negligible [Qu 1992].

1.3 PARAMETERS OF VEHICLES, RAILWAY TRACKS AND GROUNDS

To model the ground vibration from trains, a number of parameters describing vehicles, tracks and grounds are needed. These parameters, as well as some typical rail irregularity data, have been provided by several organisations and are listed in Tables 1.1 to 1.5.

1.3.1 PARAMETERS OF VEHICLES

Table 1.1 lists parameters of four types of vehicle, from passenger coaches to freight wagons.

In addition to these the parameters for an X2000 train have been used in this work and these parameters have been provided in confidence.

TABLE 1.1

Parameters for vehicles

Parameters \ Types of Vehicle	Mk 3 Passenger Coach[1] (UK) (4 axles)	HAA Coal Wagon (Loaded)[2] (UK) (2 axles)	LTF Freight Wagon[3] (UK) (4 axles)	C_{62A} Freight Wagon[4] (China) (4 axles)
Body mass (kg)	21400	42330	93640	77000
Body pitch inertia (kg-m^2)	8.3×10^5	1.7×10^5	4.41×10^6	1.2×10^6
Bogie sprung mass (kg)	2707	—	1880	1100
Bogie pitch inertia (kg-m^2)	1970	—	1710	760
Secondary vertical stiffness per bogie (N/m)	0.81×10^6	—	6.2×10^6	5.32×10^6
Secondary vertical damping per bogie (Ns/m)	74000	—	1×10^5	7×10^4
Secondary damper stiffness per bogie (N/m)†		—		
Primary vertical stiffness per axle (N/m)	0.359×10^6	3.3×10^6	1.3×10^7	—
Primary vertical damping per axle (Ns/m)	8400	$2.0\times10^{5*}$	9×10^4	—
Primary damper stiffness per axle (N/m)†	14×10^6	$100\times10^{6*}$		—
Bogie centres (m)	2×8	—	2×4.039	2×4.25
Bogie wheelbase (m)	2×1.3	2×2.781	2×0.875	2×0.875
Wheelset mass (kg)	1375	1925	1150	1200
Wheel diameter (m)	0.914	0.92	0.84	0.84
Vehicle length (m)	23	9.04		13

Notes:

1. Provided by Manchester Metropolitan University.
2. Provided by AEA Technology Rail.
3. From reference [Zai, 1997].
4. From reference [Zai, 1997].

*. The suspension is a leaf spring with friction damping. These parameters have been assumed as approximate equivalent values to fit a viscously damped suspension model.

†. This stiffness is in series with the damper.

1.3.2 PARAMETERS OF TRACKS

Tables 1.2 to 1.4 list parameters for track elements from different sources.

TABLE 1.2

Parameters for railway tracks

Reference	[Thompson 1997]	[Van den Broeck et al 1999]
Rail type	UIC 60	UIC 60
Rail mass (kg/m)	60	60
Vertical bending stiffness of rail (EI) (Nm^2)		6.46×10^6
Pads thickness (mm)	6	
Pad vertical stiffness (N/m)	3.5×10^8	2.8×10^8
Pad lateral stiffness (N/m)	5.0×10^7	
Sleeper spacing (m)	0.6	0.6
Sleeper type	Monobloc concrete	Monobloc concrete
Sleeper mass (kg)	324	355
Ballast vertical stiffness (N/m)	7×10^7	1.77×10^8
Ballast lateral stiffness (N/m)	1.1×10^8	

TABLE 1.3

Static and dynamic stiffness of Pandrol studded 10 mm railpad
[Thompson, Van Vliet and Verheij 1998]

Preload (kN)	20	30	40	60	80
Static stiffness (MN/m)	19	25	37	95	200
Dynamic stiffness at 50 Hz (MN/m)	61	82	130	300	650
Dynamic stiffness at 200 Hz (MN/m)	69	92	140	330	690
Dynamic stiffness at 500 Hz (MN/m)	81	110	170	390	780

TABLE 1.4

Vertical ballast stiffness for a sleeper block with an area of 0.23 m^2
[Frémion, Goudard and Vincent 1996]

Static load (kN)	50 Hz (MN/m)	200 Hz (MN/m)	500 Hz (MN/m)
1.2	50	130	—
11	120	210	420
21	125	240	480

Wu and Thompson [1999] have investigated the effects of local preload on the foundation stiffness and the vertical dynamics of a railway track. Calculation shows that the point receptances of a railway track at low frequency (below the pinned-pinned resonance) are governed by the local supports near the wheel load, i.e., the analysis can be carried out with a model having uniform foundation stiffness, as long as it is the same as the real stiffness under the wheel load. Calculation also shows that the local stiffness variation in the rail foundation near the wheel load has no obvious effects on the pinned-pinned resonance. The effect of the local stiffness variation in the track foundation near the wheel load on the average wave propagation decay rate is very limited.

Fenander [1997] presents measurements of the vertical stiffness and loss factor of studded rubber railpads, both in a complete track and in a test rig, as functions of frequency under different static preloads. For more compact polymer-based railpads, track measurements were also performed. The stiffness of the studded railpads was found to increase strongly with preload, but weakly with frequency. Table 1.3 also shows this feature. The loss factor of the studded railpads was found to be nearly independent of preload and to increase only slightly with frequency (0.1-0.2 for a frequency range of 0-500 Hz).

1.3.3 DATA FOR THE VERTICAL PROFILE OF RAILS

The dynamic excitations at wheel-rail contact points come from rail and wheel irregularities. The rail irregularities include dipped joints and corrugation as well as the general undulation in the 'track top'. The wheel irregularities can be wheel flats, surface irregularities and wheel eccentricity. The variations in the vertical profiles of either surface (wheel and rail) introduce a relative displacement input to the vehicle and track systems. The process is usually assumed to be linear, so that for a given wavelength λ, a displacement input is generated at the passing frequency $f = c / \lambda$, where c denotes the train speed. For the frequency range of 5 to 80 Hz of interest for perception of ground vibration and a train speed range of 36 to 250 km/h (10 to 70 m/s), the wavelengths of important vertical irregularities lie within the range 0.125 to 14 m (or in the wavenumber range of 0.07 to 8 cycle/m). Most conventional wheelsets used in main line vehicles have rolling radii varying from 0.4 to 0.5 m. For operational train speeds between 10 and 70 m/s, the wheel irregularities produce an excitation with a fundamental frequency ($f = c / (2\pi R)$) ranging from 4 to 22 Hz. This frequency range is within the range of interest, 5 to 80 Hz, for ground vibration.

Measurements of wheel and rail irregularities were carried out by, for example ORE C116 [1971] and more recently for short wavelengths by, for example Dings and Dittrich [1996]. In a wavelength range of 1 to 100 m, ORE C116 gave the power spectral density of rail irregularities, showing that with increasing wavelength, the power density increases rapidly. Esveld [Esveld 1989] also gives the power spectral density of rail irregularities in different European countries. Dings and Dittrich only gave the roughness for wavelengths of 0.08 to 0.2 m. For rail corrugation, Grassie and Kalousek [1993] presented a detailed discussion on its characteristics, causes and treatments. It has been observed in practice that the wavelength of rail corrugation varies only slightly with the running speeds of trains. Therefore, the frequency of excitation at wheel-rail contact points increases proportionally with the train speed for a train running on corrugated rails. Recent developments on research into rail corrugations and out-of-round wheels can be found in the Workshop on Rail Corrugations and Out-of-round Wheels [Knothe and Grassie 1999].

Figure 1.2 shows examples of the vertical roughness levels expressed in terms of one-third octave band wavelength in the wavelength range of 1 to 20 m. These curves are

calculated from data measured on several main lines in Britain. For the wavelength range of 0.08 to 2 m, a measured roughness spectrum for a continuously welded rail is shown in Figure 1.3 [Jones 1996]. Figure 1.4 shows roughness spectra for the wavelength range of 0.01 to 0.63 m. These spectra are from an average of the roughness spectra of rails used in several European countries.

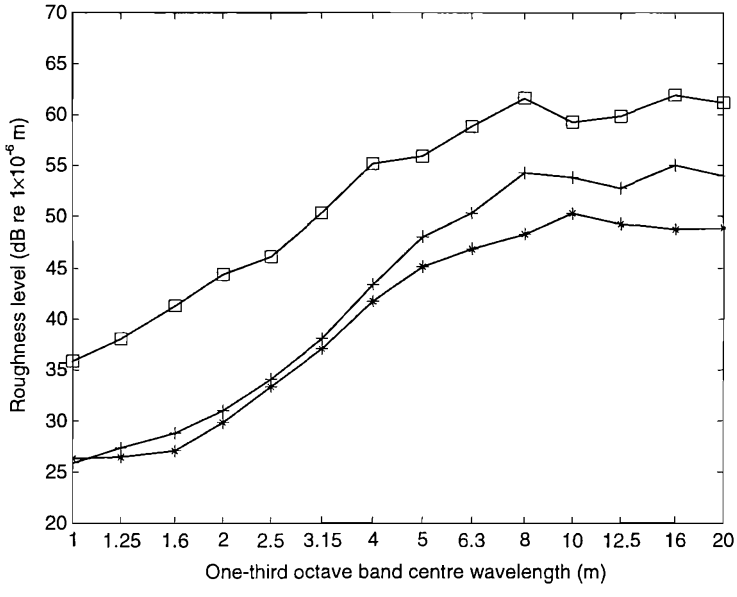

Figure 1.2. Vertical roughness levels (an average over several sites) measured on several lines in Britain. *: Good quality ballasted track; +: good quality freight ballasted track; □: poor quality freight ballasted track. Roughness data purchased from Serco Railtest Limited.

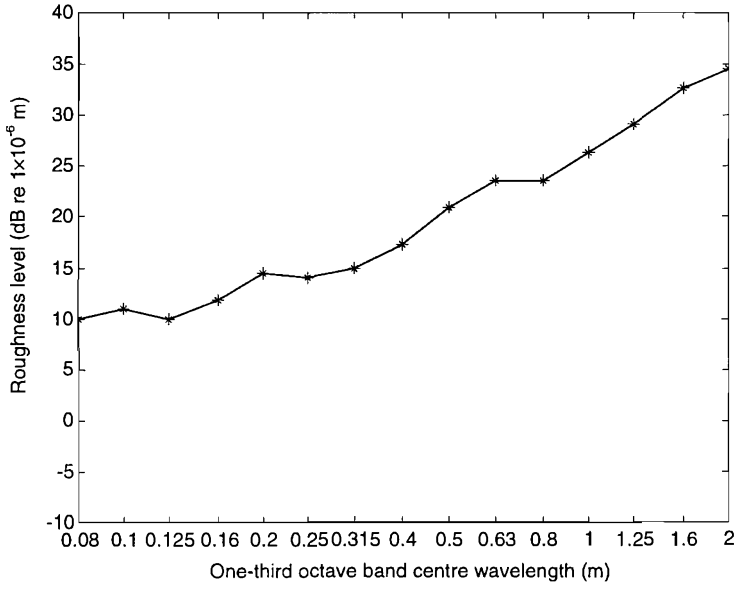

Figure 1.3. Vertical roughness levels in the wavelength range of 0.08 to 2 m for a continuously welded rail [Jones 1996].

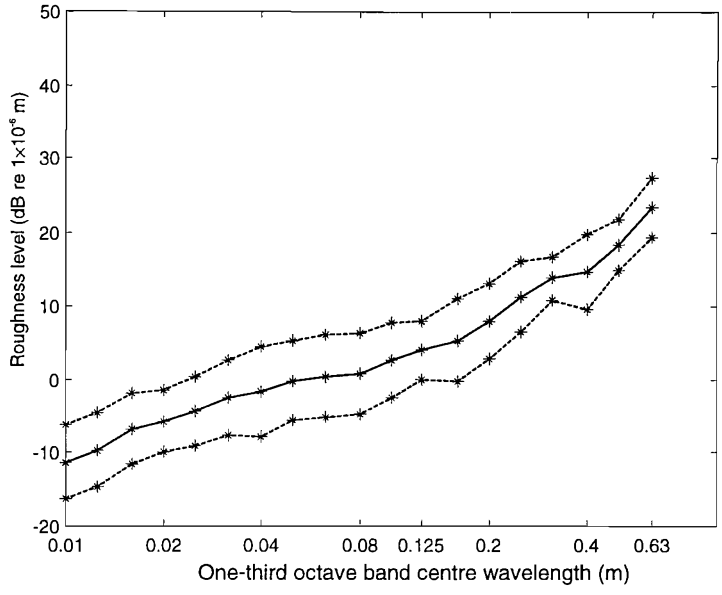

Figure 1.4. Vertical roughness levels in the wavelength range of 0.01 to 0.63 m (from "Draft Proposal for Noise Measurement Standard for ERRI Committee C163''). ——, mean values; – – –, mean ± standard deviation.

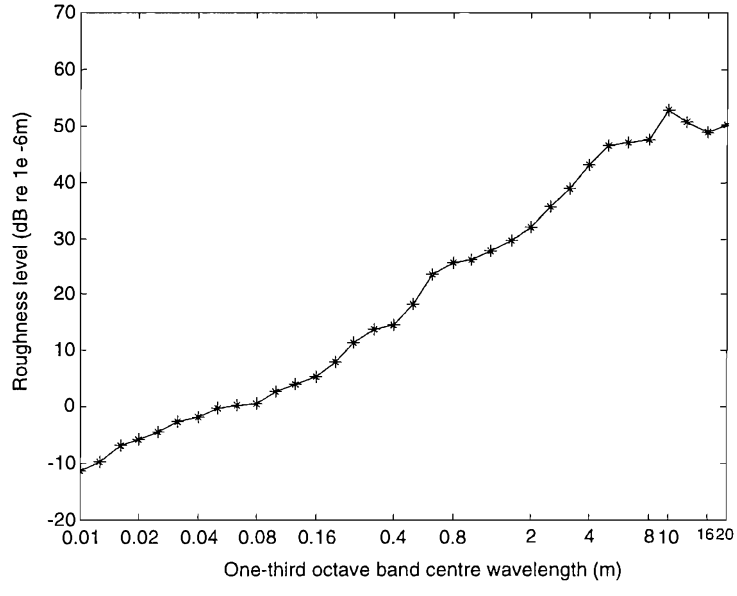

Figure 1.5. Vertical roughness levels in the wavelength range of 0.01 to 20 m, synthesized from a 'good quality track' data shown in Figure 1.2 and those shown in Figures 1.3 and 1.4.

It can be seen from Figures 1.2 to 1.4 that some variation is to be expected in the irregular profile and that no one measurement method encompasses the whole possible range of wavelength relevant to ground vibration excitation (0.125 m to 14 m). Figure 1.5 shows a spectrum that has been synthesized by combining a 'good quality track' spectrum shown in Figure 1.2 and the spectra shown in Figures 1.3 and 1.4. This has

been used in the present work as a typical representative roughness spectrum for the purpose of example calculations.

1.3.4 PARAMETERS OF GROUNDS

For a layered ground, the thickness, Young's modulus, Possion's ratio, mass density and damping of each layer are needed. These parameters vary greatly from site to site. The most often cited values of mass density are from 1500 kg/m^3 to 2000 kg/m^3. Representative values of Possion's ratio can be found from Shamsher Prakash's book [Prakash 1981] and are listed as follows:

TABLE 1.5

Representative values of Possion's ratio of soils [Prakash 1981]

Type of soil	Possion's ratio
Clay	0.4-0.5
Sand	0.3-0.35
Rock	0.15-0.25

Rather than elastic modulus, the shear wave speed defined by $c_2 = \sqrt{G/\rho}$ is more often used, where G is the shear modulus and ρ the mass density. The shear wave speed may be as low as 50 m/s [Adolfsson, Andreasson, Bengtsson and Zackrisson 1999] which is lower than the operational speeds of high-speed trains (e.g. 300 km/h or 83 m/s) at some site locations and, as high as 200 m/s or more at others. The thickness of the upper layer is important if the wavelength in this layer is greater than the thickness.

Damping in soils is the most difficult parameter to determine. It is generally accepted that the soil damping exhibits a hysteretic nature [Prange 1978] so that a loss factor is often used to describe the damping mechanism. For simplicity, for vibrations of low amplitude and low frequency, most researchers choose a "constant hysteresis" damping model, in which the loss factor is set to be independent of frequency. However, this damping model would produce non-causality for impulse excitation [Crandall 1970], i.e., the impulse response appears prior to the action of the impulse. The higher the damping is, the stronger the non-causal effects would be. More detailed discussion on this is given in Appendix 1. For low frequencies, a viscous damping nature has also been observed to be consistent with site measurements at some locations [Jones 1994]. Thus it may be more reasonable to model the damping for low frequencies as viscous, and for other frequencies as hysteretic. The problem still remains open that on one hand, there is

not enough knowledge of the dividing point below which the viscous damping model is applicable; on the other hand, this combined model does not definitely avoid the non-causality. Fortunately, for a layered ground, ground vibration produced by a moving train has a dominating component in a particular frequency range, which is determined by the properties of the soil, the train speed and the excitation frequency. If the loss factor in the "constant hysteresis" damping model is selected as the same as the actual loss factor at this frequency, the response of the model will be sufficiently close to that of the actual system. At most frequencies the model will have an inaccurate representation of damping but the effect on the dynamic response will not be significant if the damping is light. Bearing this in mind, the "constant hysteresis" damping model is used in this thesis, although the model allows for an alternative viscous damping characteristic and frequency-dependant loss factor.

1.3.5 PARAMETERS OF GROUNDS AND TRACKS USED IN THIS THESIS

The parameters listed in Tables 1.6 to 1.9 will be, unless otherwise stated, used in this work. The grounds specified by parameters in Tables 1.6 and 1.7 consist of a single layer of 2 m thickness overlying a much stiffer homogeneous half-space. The Rayleigh wave speed of the upper layer of the 'stiffer ground' is 112 m/s while that of the 'softer ground' is 77 m/s. The ballasted tracks specified by parameters in Tables 1.8 and 1.9 differ only in the ballast: the former, termed the lighter track, has a lower ballast height thus more vertical stiffness and less mass; the latter, called the heavier track, has a higher ballast height thus less vertical stiffness and more mass. The 'rail' in these tracks represents two rails by a single equivalent beam.

TABLE 1.6

Parameters for a stiffer ground

Layer	Depth (m)	Young's modulus (10^6 Nm^{-2})	Poisson's ratio	Density (kg/m^3)	Loss factor	P-wave speed (m/s)	S-wave speed (m/s)	Rayleigh wave speed (m/s)
1	2.0	60	0.44	1500	0.1	360	117.9	112
Half space		360	0.49	2000	0.1	1755	245	233

TABLE 1.7

Parameters for a softer ground

Layer	Depth (m)	Young's modulus (10^6 Nm^{-2})	Poisson's ratio	Density (kg/m^3)	Loss factor	P-wave speed (m/s)	S-wave speed (m/s)	Rayleigh wave speed (m/s)
1	2.0	30	0.47	1550	0.1	340	81.1	77
Half space		360	0.49	2000	0.1	1755	245	233

TABLE 1.8

Parameters for a lighter ballasted track

Mass of rail beam per unit length of track	120 kg/m
Bending stiffness of rail beam	1.26×10^{7} Nm^2
Loss factor of the rail	0.01
Rail pad stiffness	3.5×10^{8} N/m^2
Rail pad loss factor	0.15
Mass of sleepers per unit length of track	490 kg/m
Mass of ballast per unit length of track	1200 kg/m
Ballast stiffness per unit length of track	3.15×10^{8} N/m^2
Loss factor of ballast	1.0
Contact width of railway and ground	2.7m

TABLE 1.9

Parameters for a heavier ballasted track

Mass of rail beam per unit length of track	120 kg/m
Bending stiffness of rail beam	1.26×10^{7} Nm^2
Loss factor of the rail	0.01
Rail pad stiffness	3.5×10^{8} N/m^2
Rail pad loss factor	0.15
Mass of sleepers per unit length of track	490 kg/m
Mass of ballast per unit length of track	3300 kg/m
Ballast stiffness per unit length of track	1.775×10^{8} N/m^2
Loss factor of ballast	1.0
Contact width of railway and ground	2.7m

Railpad stiffnesses vary considerably (by more than an order of magnitude). The value used here is a 'medium' stiffness, typical of modern track, corresponding to 105 MN/m per pad.

1.4 WORK TO BE CARRIED OUT IN THIS PROJECT

From the literature review, some points may be summarised as follows:

(1) Free vibrations have been investigated for a layered ground without any built structure by many researchers (resulting in modes and dispersion curves), but there is little knowledge of the modification caused by the presence of a railway track to the free ground vibrations. This sort of knowledge may be helpful for other aspects of the study of ground vibration such as determining the critical train speeds.

(2) The vibration of a layered ground generated from surface trains has been studied mainly for the case of the track vibrating vertically. The wheelsets may apply lateral forces and/or torsion moments on the track. Though these lateral forces and torsional moments may have relatively small magnitudes compared to the vertical wheel-

rail forces, due to their different frequency contents from those of the vertical wheel-rail forces, they may also have significant contributions to the total response.

(3) Most of the existing models have only taken into account the quasi-static loads. Such models cannot predict the ground vibration level due to the dynamic wheel-rail forces. A relationship is needed between the track quality (wheel-rail combined irregularities) and the ground vibration level.

(4) Tracks should be modelled in such a manner that the dynamic behaviour of the ballast and the embankment is implemented in the model.

(5) The methods of assessing the efficiency of vibration reduction measures are based on velocity measurement at one point before and after treatment. This approach seems too simple and might give erroneous results [Villot, Jean and Chanut 1997]. A more correct efficiency should be estimated from the energy transmitted to the ground or from the energy stored somewhere (in a tunnel wall or in a reception structure for instance) estimated from spatially averaged velocity.

The aim of this project is not to solve all of the problems but develop a comprehensive model for predicting ground vibrations generated from surface trains. By this means the physical mechanisms of ground vibration excitation and transmission through the ground are studied in a number of stages and a better understanding of the phenomenon is derived. At the end of the project, it is intended that this model can be used as a prediction tool for ground vibration, and for studying vibration reduction measures and to investigate the nature of vibration observed at particular sites. Thus this model should incorporate the necessary components for an accurate prediction of vibration from actual railway traffic. To this end, the vehicles, the track and the subsoil (a layered ground) are modelled in a sufficiently detailed manner. To enable the investigation into the understanding of the physics involved in the problem and provide a reference base for numerical models, the wavenumber-frequency domain approach is used. The governing equations are solved analytically in the frequency-wavenumber domain, and then the inverse Fourier transform technique is used to obtain the actual solutions. Thus this model is a semi-analytical model. This model uses the quasi-static loads and the wheel-rail combined irregularities as its inputs. Outputs include the dynamic wheel-rail forces, the displacements and displacement (velocity and acceleration) spectra of the track and the ground surface. The frequency range of interest

is up to about 80 Hz. It is not intended to predict ground borne noise which has a higher frequency range, nor is it intended in this thesis to study trains in tunnels. The tasks for each stage of the development of the model are stated as below.

In Chapter 2, the solution for steady state displacements and stresses (Green's functions) of a layered ground due to stationary or moving unit harmonic loads is derived. This work is similar to that of Barros and Luco [1994], but more properties of the resulting Green's functions, such as reciprocity relations, are revealed. This makes the Green's functions derived here more computationally efficient to use.

In Chapter 3, a study is carried out for vibration propagation in a layered ground. Dispersion curves, cut-on (natural) frequencies, receptances and critical load speeds are topics to be discussed. It is expected that the presence of a track will modify these features to some extent, thus this study will be helpful in the understanding of dynamics of a track-ground system.

To get an understanding of the track dynamics, in Chapter 4, an investigation is carried out for the steady-state responses of a railway track on a Winkler foundation to a moving harmonic load.

In Chapter 5, a model to predict ground vibrations generated by vertical wheel-rail forces is developed by adding the track to the ground model of Chapter 2. This model is intended to serve two purposes: one is to study ground vibration generated by the quasi-static loads (multiple axle loads) and the other is to provide a step in the development of a ground vibration model which comprises vehicles, track and ground. A number of results from this model are presented in Chapter 6 in order to investigate the effects of various factors on the ground vibration.

Based on the formulation in Chapter 5, in Chapter 7, the vertical dynamics of vehicles are coupled with the track-ground system to produce a whole model incorporating vehicles, track and ground. In this chapter, the relationship is derived between the combined wheel-rail roughness power spectral density and the ground vibration power spectra.

To validate the model developed in Chapter 7, in Chapter 8, ground vibration spectra at three sites are predicted and compared with measured data. These sites represent different ground conditions (very soft, fairly soft and hard) and different train-

traffic operations (high-speed passenger trains and low speed freight trains comprising two-axle wagons). From the predictions for the three sites, the roles are demonstrated of the quasi-static and dynamic components of vibration at different frequencies and for train speeds below and above the lowest ground wave speed.

Finally, the conclusions drawn from each chapter are summarized in Chapter 9 and some possible future work is suggested.

1.5 MAIN CONTRIBUTION OF THIS THESIS

The main contribution of this PhD thesis is the development of a comprehensive mathematical model for the prediction of ground vibrations generated by surface trains. This differs from the existing ones in that it couples a moving train of vehicles, a railway track and a layered ground and it uses both the moving axle loads (quasi-static loads) and the rail/wheel irregularities as its inputs. A relationship is derived between the combined wheel-rail roughness power spectral density and the ground vibration power spectra, which makes the outputs of the model comparable to measured data. Using this model, the roles are demonstrated of the two excitation mechanisms, quasi-static and dynamic, at different frequencies and for train speeds below and above the lowest ground wave speed. The model has been validated by using the measured data at three sites. Thus this model can be used as a prediction tool for ground vibration, for studying vibration reduction measures and to investigate the nature of vibration observed at particular sites.

Chapter 2

STEADY STATE DISPLACEMENTS AND STRESSES OF A LAYERED GROUND DUE TO STATIONARY OR MOVING HARMONIC LOADS[1]

2.1 INTRODUCTION

For many applications, the steady state displacements and stresses of a ground subject to stationary (loads acting at a fixed point) or moving (loads moving in a fixed direction) harmonic loads are necessary. If the ground consists of a number of horizontal parallel layers, these displacements and stresses can be solved in the wavenumber domain analytically. In the stationary case, several forms of relationship between Fourier transformed loads (or stresses) and Fourier transformed displacements are available [Thomson 1950, Haskell 1953, Kausel and Roesset 1981, Wolf 1985, Lysmer and Waas 1972, Waas 1972, Kausel and Peek 1982, Tassoulas and Kausel 1983, Kausel 1986].

In the moving load case, making use of an exact factorisation of the displacement and stress fields in terms of generalised transmission and reflection coefficients, Barros and Luco [1994] proposed a procedure to obtain the steady state displacements and stresses within a layered ground generated by a buried or surface load moving with constant speed parallel to the ground surface. The displacements and stresses are formulated in terms of a double integral with respect to frequency and wavenumber in the lateral direction orthogonal to the direction of motion of the load.

Rather than use either the exact or discretized dynamic stiffness matrix techniques, it has been shown by Sheng, Jones and Petyt [1999 (a)] that improved computational efficiency can be achieved by using the dynamic flexibility matrix approach (similar to the Haskell-Thomson technique) since all the matrices being manipulated are of order less than or equal to 6. The definition of the dynamic flexibility matrix in the stationary case is given in Section 2.2. The derivation of the flexibility

[1]The displacement part of this Chapter is due to the work (recorded in the ISVR Technical Memorandum No. 837, March 1999) carried out when the author was an academic visitor. Improvements and an extension to account for the calculation of stresses were made after registration as an MPhil/PhD student.

matrix for a three-dimensional ground layer is described for a Cartesian co-ordinate system in Section 2.3. With some mathematical treatment, and making use of some properties of the matrix described in Section 2.4, numerical difficulties that occur in a number of previous works are avoided and explicit analytical expressions of the formulae are obtained. In Section 2.5, the formulae developed for the stationary case are extended to include the case when harmonic loads move uniformly along a direction parallel to the ground surface. For both the stationary and moving cases, the steady state displacements and stresses are formulated in terms of a double integral with respect to the wavenumbers in the longitudinal and lateral directions. This double integral can be transformed into a double integral with respect to frequency and wavenumber in the lateral direction as given by Barros and Luco [1994]. Some reciprocity relations, which have been observed by Barros and Luco [1994] through numerical tests, are then proved. The formulae obtained so far are summarised in Section 2.6.

It is assumed that the ground consists of a number, n, of parallel layers of different materials. The nth layer overlies a half-space or a rigid foundation, which is identified as 'layer' number $(n+1)$. For the jth layer the material constants are: elastic modulus, E_j, Poisson ratio, ν_j, density, ρ_j, loss factor, η_j and layer thickness, h_j.

2.2 DEFINITION OF THE DYNAMIC FLEXIBILITY MATRIX

Referring to Figure 2.1, let point P(0, 0) be the origin point on the top side of the l_Pth $(1 \le l_P \le n+1)$ layer and point B(x, y) on the top side of the l_Rth $(1 \le l_R \le n+1)$ layer. Suppose a unit harmonic load $e^{i\omega t}$, where $i = \sqrt{-1}$, ω is angular frequency, acts at point P(0, 0) in the x direction. Then the steady state displacement amplitudes of point B(x, y) in x, y, z directions, are denoted by $Q_{11}(x, y)$, $Q_{21}(x, y)$ and $Q_{31}(x, y)$, respectively. When the unit harmonic load acts at P in the y direction, the amplitudes are denoted by $Q_{12}(x, y)$, $Q_{22}(x, y)$, $Q_{32}(x, y)$, and similarly, by $Q_{13}(x, y)$, $Q_{23}(x, y)$ and $Q_{33}(x, y)$ for the load acting in the z direction. A matrix, $[Q(x, y)]$, is defined as

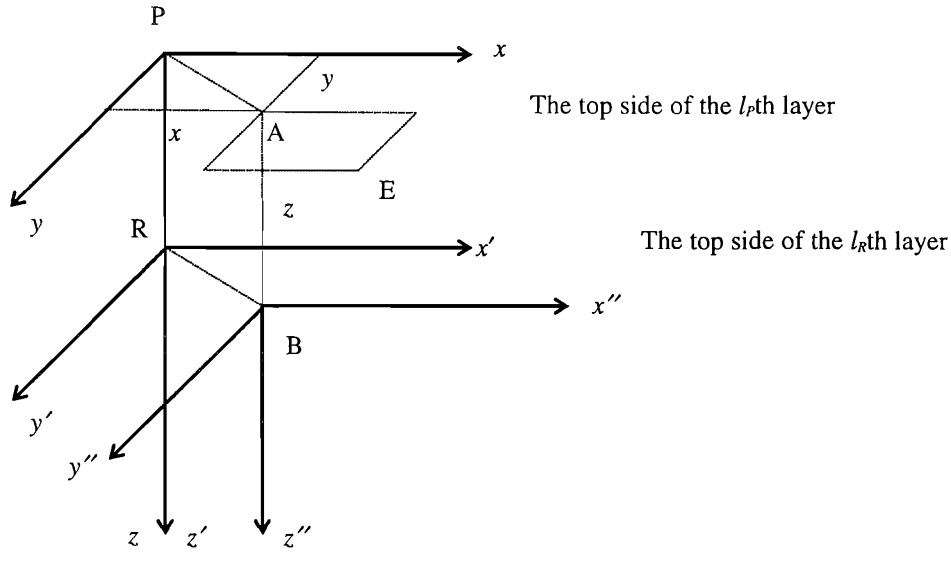

Figure 2.1. The co-ordinate system

$$[Q(x,y)]=\begin{bmatrix} Q_{11}(x,y) & Q_{12}(x,y) & Q_{13}(x,y) \\ Q_{21}(x,y) & Q_{22}(x,y) & Q_{23}(x,y) \\ Q_{31}(x,y) & Q_{32}(x,y) & Q_{33}(x,y) \end{bmatrix} \tag{2.1}$$

This is called *the stationary dynamic flexibility matrix of l_R to l_P* (meaning that, the unit harmonic loads act at the origin point of the top interface of l_P th layer and the displacements are for the points in the top interface of the l_R th layer), or simply, *stationary dynamic flexibility matrix*. In general the Q's are complex, and alternatively are called *displacement Green's functions*.

Now suppose that, at the topside of the l_P th layer, the harmonic load distributions, $p_x(x,y)e^{i\omega t}, p_y(x,y)e^{i\omega t}, p_z(x,y)e^{i\omega t}$, act in the x, y, z directions respectively. The total steady state displacement amplitudes in x, y, z directions, of point B(x, y) at the top side of the l_R th layer, denoted by $u_{l_R0}(x,y), v_{l_R0}(x,y), w_{l_R0}(x,y)$, are given by

$$\begin{Bmatrix} u_{l_R0}(x,y) \\ v_{l_R0}(x,y) \\ w_{l_R0}(x,y) \end{Bmatrix} = \begin{Bmatrix} u_{l_R0} \\ v_{l_R0} \\ w_{l_R0} \end{Bmatrix} = \int_{-\infty}^{\infty}\int_{-\infty}^{\infty} [Q(x-r,y-s)] \begin{Bmatrix} p_x(r,s) \\ p_y(r,s) \\ p_z(r,s) \end{Bmatrix} drds \tag{2.2}$$

Equation (2.2) is a convolution integration. Using the Fourier transform pairs

$$\left.\begin{aligned} \tilde{f}(\beta) &= \int_{-\infty}^{\infty} f(x)e^{-i\beta x}dx, \qquad f(x) = \frac{1}{2\pi}\int_{-\infty}^{\infty} \tilde{f}(\beta)e^{i\beta x}d\beta \\ \tilde{f}(\beta,\gamma) &= \int_{-\infty}^{\infty}\int_{-\infty}^{\infty} f(x,y)e^{-i(\beta x+\gamma y)}dxdy, f(x,y) = \frac{1}{4\pi^2}\int_{-\infty}^{\infty}\int_{-\infty}^{\infty} \tilde{f}(\beta,\gamma)e^{i(\beta x+\gamma y)}d\beta d\gamma \end{aligned}\right\} \quad (2.3)$$

to transform equation (2.2) into the domain of the wavenumbers β in the x direction and γ in the y direction, yields

$$\begin{Bmatrix} \tilde{u}_{l_R 0}(\beta,\gamma) \\ \tilde{v}_{l_R 0}(\beta,\gamma) \\ \tilde{w}_{l_R 0}(\beta,\gamma) \end{Bmatrix} = [\tilde{Q}(\beta,\gamma)] \begin{Bmatrix} \tilde{p}_x(\beta,\gamma) \\ \tilde{p}_y(\beta,\gamma) \\ \tilde{p}_z(\beta,\gamma) \end{Bmatrix} = [\tilde{Q}(\beta,\gamma)]\{\tilde{p}(\beta,\gamma)\} \quad (2.4)$$

where, $\tilde{u}_{l_R 0}(\beta,\gamma)$ denotes the Fourier transform of $u_{l_R 0}(x,y)$, etc. The matrix $[\tilde{Q}(\beta,\gamma)]$ is called *the Fourier transformed stationary dynamic flexibility matrix of l_R to l_P*, or more simply, *the Fourier transformed stationary dynamic flexibility matrix.* The derivation of an exact expression for this matrix is dealt with below in Section 2.3.

2.3 DERIVATION OF THE FOURIER TRANSFORMED DYNAMIC FLEXIBILITY MATRIX

2.3.1 ANALYSIS FOR A SINGLE LAYER

The steady state displacements at the point (x, y, z) (where $z \in (0, h_j)$ is local to the layer) in the jth layer are denoted by $u_j(x,y,z)e^{i\omega t}, v_j(x,y,z)e^{i\omega t}, w_j(x,y,z)e^{i\omega t}$, where $u_j(x,y,z)$ etc. are generally complex numbers and their Fourier transforms are denoted by $\tilde{u}_j(\beta,\gamma,z)$, $\tilde{v}_j(\beta,\gamma,z)$ and $\tilde{w}_j(\beta,\gamma,z)$. The stress tensor contains nine components, however only three are required to study the interaction of parallel layers. The three relevant components of stress in the x, y, z directions in the horizontal plane containing the point are denoted by $\tau_{xzj}(x,y,z)e^{i\omega t}, \tau_{yzj}(x,y,z)e^{i\omega t}, \tau_{zzj}(x,y,z)e^{i\omega t}$, and the Fourier transformed stress amplitudes by $\tilde{\tau}_{xzj}(\beta,\gamma,z), \tilde{\tau}_{yzj}(\beta,\gamma,z), \tilde{\tau}_{zzj}(\beta,\gamma,z)$.

Put

$$\left.\begin{aligned}
\{\tilde{u}\}_{j0} &= (\tilde{u}_j(\beta,\gamma,0),\tilde{v}_j(\beta,\gamma,0),\tilde{w}_j(\beta,\gamma,0))^T \\
\{\tilde{\tau}\}_{j0} &= (\tilde{\tau}_{xzj}(\beta,\gamma,0),\tilde{\tau}_{yzj}(\beta,\gamma,0),\tilde{\tau}_{zzj}(\beta,\gamma,0))^T \\
\{\tilde{S}\}_{j0} &= \begin{Bmatrix}\{\tilde{u}\}_{j0}\\ \{\tilde{\tau}\}_{j0}\end{Bmatrix}
\end{aligned}\right\} \tag{2.5a}$$

$$\left.\begin{aligned}
\{\tilde{u}\}_{j1} &= (\tilde{u}_j(\beta,\gamma,h_j),\tilde{v}_j(\beta,\gamma,h_j),\tilde{w}_j(\beta,\gamma,h_j))^T \\
\{\tilde{\tau}\}_{j1} &= (\tilde{\tau}_{xzj}(\beta,\gamma,h_j),\tilde{\tau}_{yzj}(\beta,\gamma,h_j),\tilde{\tau}_{zzj}(\beta,\gamma,h_j))^T \\
\{\tilde{S}\}_{j1} &= \begin{Bmatrix}\{\tilde{u}\}_{j1}\\ \{\tilde{\tau}\}_{j1}\end{Bmatrix}
\end{aligned}\right\} \tag{2.5b}$$

where $\{\tilde{S}\}_{j0}$ is the (Fourier transformed) state vector containing displacements and stresses of the top interface of the *j*th layer, and $\{\tilde{S}\}_{j1}$ is the corresponding vector for the bottom. It should be noticed that at the top interface of the l_P th layer, the stresses are not continuous because of the applied loads. In this case the definition in equations (2.5) is modified as

$$\left.\begin{aligned}
\{\tilde{\tau}\}_{l_P 0} &= (\tilde{\tau}_{xzl_P}(\beta,\gamma,0^+),\tilde{\tau}_{yzl_P}(\beta,\gamma,0^+),\tilde{\tau}_{zzl_P}(\beta,\gamma,0^+))^T \\
\{\tilde{\tau}\}_{l_P-1,1} &= (\tilde{\tau}_{xz,l_P-1}(\beta,\gamma,h_{l_P-1}^-),\tilde{\tau}_{yz,l_P-1}(\beta,\gamma,h_{l_P-1}^-),\tilde{\tau}_{zz,l_P-1}(\beta,\gamma,h_{l_P-1}^-))^T
\end{aligned}\right\} \tag{2.6}$$

The relation between $\{\tilde{S}\}_{j0}$ and $\{\tilde{S}\}_{j1}$ will be derived below.

Because all displacements are harmonic, Navier's equation for the *j*th layer can be written as

$$\left.\begin{aligned}
&(\lambda_j+\mu_j)\frac{\partial \Delta_j}{\partial x}+\mu_j\nabla^2 u_j=-\rho_j\omega^2 u_j\\
&(\lambda_j+\mu_j)\frac{\partial \Delta_j}{\partial y}+\mu_j\nabla^2 v_j=-\rho_j\omega^2 v_j\\
&(\lambda_j+\mu_j)\frac{\partial \Delta_j}{\partial z}+\mu_j\nabla^2 w_j=-\rho_j\omega^2 w_j\\
&\Delta_j=\frac{\partial u_j}{\partial x}+\frac{\partial v_j}{\partial y}+\frac{\partial w_j}{\partial z}\\
&\lambda_j=\frac{\nu_j E_j(1+i\eta_j \mathrm{sgn}(\omega))}{(1+\nu_j)(1-2\nu_j)}\\
&\mu_j=\frac{E_j(1+i\eta_j \mathrm{sgn}(\omega))}{2(1+\nu_j)}
\end{aligned}\right\}\quad (j=1,2,\cdots,n+1) \tag{2.7}$$

where damping has been defined in terms of a loss factor η_j by making E_j complex.

Fourier transforming equation (2.7) gives

$$\tilde{\Delta}_j=i\beta\tilde{u}_j+i\gamma\tilde{v}_j+\frac{d\tilde{w}_j}{dz} \tag{2.8}$$

$$\left.\begin{aligned}
&(\lambda_j+\mu_j)i\beta\tilde{\Delta}_j+\mu_j[\frac{d^2\tilde{u}_j}{dz^2}-(\beta^2+\gamma^2-\frac{\omega^2\rho_j}{\mu_j})\tilde{u}_j]=0\\
&(\lambda_j+\mu_j)i\gamma\tilde{\Delta}_j+\mu_j[\frac{d^2\tilde{v}_j}{dz^2}-(\beta^2+\gamma^2-\frac{\omega^2\rho_j}{\mu_j})\tilde{v}_j]=0\\
&(\lambda_j+\mu_j)\frac{d\tilde{\Delta}_j}{dz}+\mu_j[\frac{d^2\tilde{w}_j}{dz^2}-(\beta^2+\gamma^2-\frac{\omega^2\rho_j}{\mu_j})\tilde{w}_j]=0
\end{aligned}\right\}\quad (j=1,2,\cdots,n+1) \tag{2.9}$$

From equations (2.8) and (2.9) this results in

$$\frac{d^2\tilde{\Delta}_j}{dz^2}-(\beta^2+\gamma^2-\zeta_{j1}^2)\tilde{\Delta}_j=0 \tag{2.10}$$

where, if the compression and shear wave speeds of the *j*th layer are denoted by

$$c_{j1}=\sqrt{\frac{\lambda_j+2\mu_j}{\rho_j}},\quad c_{j2}=\sqrt{\mu_j/\rho_j} \tag{2.11}$$

respectively, then

$$\zeta_{j1}=\omega/c_{j1},\ \zeta_{j2}=\omega/c_{j2} \tag{2.12}$$

are the compression and shear wavenumbers.

The general solution to equation (2.10) for $\tilde{\Delta}_j$, and then to equation (2.9) for $\tilde{u}_j, \tilde{v}_j$ and $\tilde{w}_j$, can be obtained by the characteristic root method of solving ordinary differential equations, i.e. $\tilde{\Delta}_j = e^{\pm\alpha_{j1}z}$ are permissible solutions, where $\pm\alpha_{j1}$ are the characteristic roots. Substituting the solutions to equations (2.9) and (2.10) into the Fourier transformed stress-strain relation of the material, i.e.

$$\left.\begin{aligned} \tilde{\tau}_{xzj} &= \mu_j (i\beta\tilde{w}_j + d\tilde{u}_j / dz) \\ \tilde{\tau}_{yzj} &= \mu_j (i\gamma\tilde{w}_j + d\tilde{v}_j / dz) \\ \tilde{\tau}_{zzj} &= (\lambda_j \tilde{\Delta}_j + 2\mu_j d\tilde{w}_j / dz) \end{aligned}\right\} \tag{2.13}$$

gives $\tilde{\tau}_{xzj}$ etc. All the results may be expressed in matrix forms as

$$\left\{\tilde{S}\right\}_{j0} = [A]_{j0}\{b\}_j \tag{2.14}$$

$$\left\{\tilde{S}\right\}_{j1} = e^{\alpha_{j1}h_j}[A]_{j1}\{b\}_j \tag{2.15}$$

where, $\{b\}_j \in C^6$ are integration constants, and $[A]_{j0}, [A]_{j1}$ are 6×6 matrices dependent on wavenumbers β and γ, frequency ω and material parameters. When $\beta = 0$, the detailed expressions for $[A]_{j0}, [A]_{j1}$ and other formulae are given in Section 2.6, with

$$\alpha_{j1}^2 = \beta^2 + \gamma^2 - \zeta_{j1}^2,\ \alpha_{j2}^2 = \beta^2 + \gamma^2 - \zeta_{j2}^2 \tag{2.16}$$

It will be shown in Section 2.4 that it is sufficient to know $[A]_{j0}, [A]_{j1}$ for the special case $\beta = 0$.

The combination of equations (2.14) and (2.15) to eliminate $\{b\}_j$ links the Fourier transformed displacements and the stresses at the bottom of the layer with those at the top:

$$\left\{\tilde{S}\right\}_{j1} = e^{\alpha_{j1}h_j}[A]_{j1}[A]_{j0}^{-1}\left\{\tilde{S}\right\}_{j0} \tag{2.17}$$

2.3.2 ANALYSIS FOR THE HALF-SPACE

Putting

$$\left.\begin{aligned}\{\tilde{u}\}_{n+1,0} &= (\tilde{u}_{n+1}(\beta,\gamma,0),\tilde{v}_{n+1}(\beta,\gamma,0),\tilde{w}_{n+1}(\beta,\gamma,0))^T \\ \{\tilde{\tau}\}_{n+1,0} &= (\tilde{\tau}_{xz,n+1}(\beta,\gamma,0),\tilde{\tau}_{yz,n+1}(\beta,\gamma,0),\tilde{\tau}_{zz,n+1}(\beta,\gamma,0))^T\end{aligned}\right\}$$

similar to equation (2.17), it can be shown that

$$\{\tilde{u}\}_{n+1,0} = [R][S]^{-1}\{\tilde{\tau}\}_{n+1,0} \tag{2.18}$$

where $[R]$ and $[S]$ are 3×3 matrices, the elements of which are shown in Section 2.6.

2.3.3 ANALYSIS FOR THE LAYERED GROUND

The continuity of displacements and the balance of stresses at each interface of the layers imply that $\{\tilde{S}\}_{j1} = \{\tilde{S}\}_{j+1,0}(j = 1,2,\cdots,n, j \neq l_P - 1), \{\tilde{S}\}_{l_P-1,1} = \{\tilde{S}\}_{l_P 0} + \{\tilde{S}\}^P$, where $\{\tilde{S}\}^P = (0,0,0,\tilde{p}_x,\tilde{p}_y,\tilde{p}_z)^T$ is the applied load. From equation (2.17) yields

$$\begin{aligned}\{\tilde{S}\}_{n1} &= e^{\sum_{j=l_P}^{n}\alpha_{j1}h_j}[A]_{n1}[A]_{n0}^{-1}[A]_{n-1,1}[A]_{n-1,0}^{-1}\cdots[A]_{l_P1}[A]_{l_P0}^{-1}\{\tilde{S}\}_{l_P0} \\ &= e^{\sum_{j=l_P}^{n}\alpha_{j1}h_j}[A]_{n1}[A]_{n0}^{-1}[A]_{n-1,1}[A]_{n-1,0}^{-1}\cdots[A]_{l_P1}[A]_{l_P0}^{-1}(\{\tilde{S}\}_{l_P-1,1} - \{\tilde{S}\}^P) \\ &= e^{\sum_{j=1}^{n}\alpha_{j1}h_j}[A]_{n1}[A]_{n0}^{-1}[A]_{n-1,1}[A]_{n-1,0}^{-1}\cdots[A]_{11}[A]_{10}^{-1}\{\tilde{S}\}_{10} - \\ &\quad - e^{\sum_{j=l_P}^{n}\alpha_{j1}h_j}[A]_{n1}[A]_{n0}^{-1}[A]_{n-1,1}[A]_{n-1,0}^{-1}\cdots[A]_{l_P1}[A]_{l_P0}^{-1}\{\tilde{S}\}^P\end{aligned}$$

Putting

$$[T] = \begin{bmatrix}[T]_{11} & [T]_{12}\\ [T]_{21} & [T]_{22}\end{bmatrix} = [A]_{n1}[A]_{n0}^{-1}[A]_{n-1,1}[A]_{n-1,0}^{-1}\cdots[A]_{11}[A]_{10}^{-1} \tag{2.19}$$

$$[F] = \begin{bmatrix}[F]_{11} & [F]_{12}\\ [F]_{21} & [F]_{22}\end{bmatrix} = [A]_{n1}[A]_{n0}^{-1}[A]_{n-1,1}[A]_{n-1,0}^{-1}\cdots[A]_{l_P1}[A]_{l_P0}^{-1} \tag{2.20}$$

where $[T]_{11}$, $[F]_{11}$ etc. are 3×3 matrices, results in

$$\begin{Bmatrix} \{\tilde{u}\}_{n1} \\ \{\tilde{\tau}\}_{n1} \end{Bmatrix} = e^{\sum_{j=1}^{n}\alpha_{j1}h_j} \begin{bmatrix} [T]_{11} & [T]_{12} \\ [T]_{21} & [T]_{22} \end{bmatrix} \begin{Bmatrix} \{\tilde{u}\}_{10} \\ \{\tilde{\tau}\}_{10} \end{Bmatrix} - e^{\sum_{j=l_P}^{n}\alpha_{j1}h_j} \begin{bmatrix} [F]_{11} & [F]_{12} \\ [F]_{21} & [F]_{22} \end{bmatrix} \begin{Bmatrix} 0 \\ \{\tilde{p}\} \end{Bmatrix} \tag{2.21}$$

If the $(n + 1)$th layer is a half-space, then $\{\tilde{u}\}_{n+1,0} = \{\tilde{u}\}_{n1}, \{\tilde{\tau}\}_{n+1,0} = \{\tilde{\tau}\}_{n1}$. From equations (2.18) and (2.21) and noticing that $\{\tilde{\tau}\}_{10} = 0$, yields

$$\{\tilde{u}\}_{10} = e^{-\sum_{j=1}^{l_P-1}\alpha_{j1}h_j} ([R][S]^{-1}[T]_{21} - [T]_{11})^{-1}([R][S]^{-1}[F]_{22} - [F]_{12})\{\tilde{p}\} \tag{2.22}$$

If the n+1th layer is a rigid foundation, then $\{\tilde{u}\}_{n+1,0} = \{\tilde{u}\}_{n1} = 0$, and equation (2.21) yields

$$\{\tilde{u}\}_{10} = e^{-\sum_{j=1}^{l_P-1}\alpha_{j1}h_j} [T]_{11}^{-1}[F]_{12}\{\tilde{p}\} \tag{2.23}$$

Equations (2.22) and (2.23) give the relationships between the Fourier transformed displacement vector on the ground surface and the Fourier transformed load vector on the top side of the l_Pth layer. Notice that if $l_P = 1$, the exponential term in equations (2.22) and (2.23) disappear and $[F] = [T]$. If $l_P = 1$ and the ground is just a half-space (in this case, $n = 0$), equation (2.18) yields $\{\tilde{u}\}_{10} = -[R][S]^{-1}\{\tilde{p}\}$, since $\{\tilde{p}\} = -\{\tilde{\tau}\}_{10}$.

2.3.4 THE FOURIER TRANSFORMED DYNAMIC FLEXIBILITY MATRIX AND THE FOURIER TRANSFORMED STRESS MATRIX

For the responses (displacements and stresses) of the top surface of the l_R th layer, three cases should be accounted for:

(1) When $l_R < l_P$ (i.e., the observer is above the source)

Equation (2.17) yields

$$\left\{\tilde{S}\right\}_{l_R 0} = e^{\sum_{j=1}^{l_R-1}\alpha_{j1}h_j}[A]_{l_R-1,1}[A]^{-1}_{l_R-1,0}\cdots[A]_{11}[A]^{-1}_{10}\left\{\tilde{S}\right\}_{10}$$

Putting

$$[G]=\begin{bmatrix}[G]_{11} & [G]_{12}\\ [G]_{21} & [G]_{22}\end{bmatrix}=[A]_{l_R-1,1}[A]^{-1}_{l_R-1,0}\cdots[A]_{11}[A]^{-1}_{10} \tag{2.24}$$

where $[G]_{11}$ etc. are 3×3 matrices. Equation (2.22) then yields

$$\left\{\tilde{u}\right\}_{l_R 0} = e^{-\sum_{j=l_R}^{l_P-1}\alpha_{j1}h_j}[G]_{11}([R][S]^{-1}[T]_{21}-[T]_{11})^{-1}([R][S]^{-1}[F]_{22}-[F]_{12})\left\{\tilde{p}\right\} \tag{2.25}$$

$$\left\{\tilde{\tau}\right\}_{l_R 0} = e^{-\sum_{j=l_R}^{l_P-1}\alpha_{j1}h_j}[G]_{21}([R][S]^{-1}[T]_{21}-[T]_{11})^{-1}([R][S]^{-1}[F]_{22}-[F]_{12})\left\{\tilde{p}\right\} \tag{2.26}$$

(2) When $l_R > l_P$ (i.e. the observer is below the source)

$$\left\{\tilde{S}\right\}_{l_R 0} = e^{\sum_{j=1}^{l_R-1}\alpha_{j1}h_j}[A]_{l_R-1,1}[A]^{-1}_{l_R-1,0}\cdots[A]_{11}[A]^{-1}_{10}\left\{\tilde{S}\right\}_{10} -$$
$$- e^{\sum_{j=l_P}^{l_R-1}\alpha_{j1}h_j}[A]_{l_R-1,1}[A]^{-1}_{l_R-1,0}\cdots[A]_{l_P1}[A]^{-1}_{l_P0}\left\{\tilde{S}\right\}^{P}$$

Putting

$$[H]=\begin{bmatrix}[H]_{11} & [H]_{12}\\ [H]_{21} & [H]_{22}\end{bmatrix}=[A]_{l_R-1,1}[A]^{-1}_{l_R-1,0}\cdots[A]_{l_P1}[A]^{-1}_{l_P0} \tag{2.27}$$

equation (2.22) yields

$$\left\{\tilde{u}\right\}_{l_R 0} = e^{\sum_{j=l_P}^{l_R-1}\alpha_{j1}h_j}\{[G]_{11}([R][S]^{-1}[T]_{21}-[T]_{11})^{-1}([R][S]^{-1}[F]_{22}-[F]_{12})-[H]_{12}\}\left\{\tilde{p}\right\} \tag{2.28}$$

$$\left\{\tilde{\tau}\right\}_{l_R 0} = e^{\sum_{j=l_P}^{l_R-1}\alpha_{j1}h_j}\{[G]_{21}([R][S]^{-1}[T]_{21}-[T]_{11})^{-1}([R][S]^{-1}[F]_{22}-[F]_{12})-[H]_{22}\}\left\{\tilde{p}\right\}$$

(2.29)

(3) When $l_R = l_P$

$$\{\tilde{u}\}_{l_R 0} = [G]_{11}([R][S]^{-1}[T]_{21} - [T]_{11})^{-1}([R][S]^{-1}[F]_{22} - [F]_{12})\{\tilde{p}\} \tag{2.30}$$

$$\{\tilde{\tau}\}_{l_R 0} = \{[G]_{21}([R][S]^{-1}[T]_{21} - [T]_{11})^{-1}([R][S]^{-1}[F]_{22} - [F]_{12}) - [I]\}\{\tilde{p}\} \tag{2.31}$$

where $[I]$ denotes the unit matrix.

Comparing equations (2.25), (2.28) and (2.30) with (2.4), it is seen that

$$\left[\tilde{Q}(\beta,\gamma)\right] = e^{-\sum_{j=l_R}^{l_P-1}\alpha_{j1}h_j}[G]_{11}([R][S]^{-1}[T]_{21} - [T]_{11})^{-1}([R][S]^{-1}[F]_{22} - [F]_{12}),\ (l_R < l_P) \tag{2.32}$$

$$\left[\tilde{Q}(\beta,\gamma)\right] = e^{\sum_{j=l_P}^{l_R-1}\alpha_{j1}h_j}\{[G]_{11}([R][S]^{-1}[T]_{21} - [T]_{11})^{-1}([R][S]^{-1}[F]_{22} - [F]_{12}) - [H]_{12}\}$$

$$(l_R > l_P) \tag{2.33}$$

$$\left[\tilde{Q}(\beta,\gamma)\right] = [G]_{11}([R][S]^{-1}[T]_{21} - [T]_{11})^{-1}([R][S]^{-1}[F]_{22} - [F]_{12}),\ (l_R = l_P) \tag{2.34}$$

By writing

$$\{\tilde{\tau}\}_{l_R 0} = [\tilde{U}(\beta,\gamma)]\{\tilde{p}\} \tag{2.35}$$

where $[\tilde{U}(\beta,\gamma)] = \begin{bmatrix} \tilde{U}_{11}(\beta,\gamma) & \tilde{U}_{12}(\beta,\gamma) & \tilde{U}_{13}(\beta,\gamma) \\ \tilde{U}_{21}(\beta,\gamma) & \tilde{U}_{22}(\beta,\gamma) & \tilde{U}_{23}(\beta,\gamma) \\ \tilde{U}_{31}(\beta,\gamma) & \tilde{U}_{32}(\beta,\gamma) & \tilde{U}_{33}(\beta,\gamma) \end{bmatrix}$ is called the Fourier transformed stress matrix of l_R to l_P, it follows from equations (2.26) (2.29) and (2.31) that

$$\left[\tilde{U}(\beta,\gamma)\right] = e^{-\sum_{j=l_R}^{l_P-1}\alpha_{j1}h_j}[G]_{21}([R][S]^{-1}[T]_{21} - [T]_{11})^{-1}([R][S]^{-1}[F]_{22} - [F]_{12}),(l_R < l_P) \tag{2.36}$$

$$\left[\tilde{U}(\beta,\gamma)\right] = e^{\sum_{j=l_P}^{l_R-1}\alpha_{j1}h_j}\{[G]_{21}([R][S]^{-1}[T]_{21} - [T]_{11})^{-1}([R][S]^{-1}[F]_{22} - [F]_{12}) - [H]_{22}\}$$

$$(l_R > l_P) \tag{2.37}$$

$$\left[\tilde{U}(\beta,\gamma)\right]=[G]_{21}([R][S]^{-1}[T]_{21}-[T]_{11})^{-1}([R][S]^{-1}[F]_{22}-[F]_{12})-[I],\ (l_R=l_P) \quad (2.38)$$

Similarly, another Fourier transformed stress matrix of l_R to l_P, denoted by $[\tilde{V}(\beta,\gamma)]=(\tilde{V}_{kj})$, can be defined, where $\tilde{V}_{kj}$ stands for the Fourier transforms of stresses $\tau_{xy}(k=1),\tau_{xx}(k=2),\tau_{yy}(k=3)$ at the top interface of the l_Rth layer due to a unit harmonic force acting at the original point of the top side of the l_Pth layer in x ($j=1$), y ($j=2$) and z ($j=3$) directions respectively. The calculation of $[\tilde{V}(\beta,\gamma)]$ will be discussed in Section 2.4.

It should be noticed that when $l_P=n+1$, $[F]$ should be set as a unit matrix; when $l_R=1$, $[G]$ should also be set as a unit matrix. Equations (2.36) and (2.37) show that the Fourier transformed stresses on the interface where the loads are applied are not continuous.

2.4 SOME PROPERTIES OF $[\tilde{Q}(\beta,\gamma)]$, $[\tilde{U}(\beta,\gamma)]$ AND $[\tilde{V}(\beta,\gamma)]$

2.4.1 PROPERTIES OF $[\tilde{Q}(\beta,\gamma)]$

It is worth noting some properties of $[\tilde{Q}(\beta,\gamma)]$ that lead to efficiencies in the calculation. From the symmetries (or the anti-symmetries) of the displacements about the z-axis, it can be shown that, if putting $\beta=\rho\cos\phi,\gamma=\rho\sin\phi$, then

$$\left[\tilde{Q}(\beta,\gamma)\right]=\begin{bmatrix}\sin\phi & \cos\phi & 0\\ -\cos\phi & \sin\phi & 0\\ 0 & 0 & 1\end{bmatrix}\left[\tilde{Q}(0,\rho)\right]\begin{bmatrix}\sin\phi & -\cos\phi & 0\\ \cos\phi & \sin\phi & 0\\ 0 & 0 & 1\end{bmatrix} \quad (2.39)$$

It follows from equation (2.39) that

(1) $\tilde{Q}_{13}(\beta,\gamma)$, $\tilde{Q}_{31}(\beta,\gamma)$ are odd functions of β, and even functions of γ.

(2) $\tilde{Q}_{23}(\beta,\gamma),\tilde{Q}_{32}(\beta,\gamma)$ are even functions of β, and odd functions of γ.

(3) $\tilde{Q}_{11}(\beta,\gamma),\tilde{Q}_{22}(\beta,\gamma),\tilde{Q}_{33}(\beta,\gamma)$ are even functions of β and γ.

(4) $\tilde{Q}_{12}(\beta,\gamma),\tilde{Q}_{21}(\beta,\gamma)$ are odd functions of β and γ.

(5) Thus $\tilde{Q}_{13}(0,\rho) = \tilde{Q}_{31}(0,\rho) = \tilde{Q}_{12}(0,\rho) = \tilde{Q}_{21}(0,\rho) \equiv 0$, and equation (2.39) becomes

$$\left.\begin{aligned}
&\tilde{Q}_{13}(\beta,\gamma) = \tilde{Q}_{23}(0,\rho)\cos\phi \\
&\tilde{Q}_{23}(\beta,\gamma) = \tilde{Q}_{23}(0,\rho)\sin\phi \\
&\tilde{Q}_{33}(\beta,\gamma) = \tilde{Q}_{33}(0,\rho) \\
&\tilde{Q}_{31}(\beta,\gamma) = \tilde{Q}_{32}(0,\rho)\cos\phi \\
&\tilde{Q}_{32}(\beta,\gamma) = \tilde{Q}_{32}(0,\rho)\sin\phi \\
&\tilde{Q}_{11}(\beta,\gamma) = \tilde{Q}_{11}(0,\rho)\sin^2\phi + \tilde{Q}_{22}(0,\rho)\cos^2\phi \\
&\tilde{Q}_{22}(\beta,\gamma) = \tilde{Q}_{11}(0,\rho)\cos^2\phi + \tilde{Q}_{22}(0,\rho)\sin^2\phi \\
&\tilde{Q}_{12}(\beta,\gamma) = \tilde{Q}_{21}(\beta,\gamma) = (\tilde{Q}_{22}(0,\rho) - \tilde{Q}_{11}(0,\rho))\sin\phi\cos\phi
\end{aligned}\right\} \qquad (2.40)$$

Formula (2.40) is very useful, because it reduces the calculation of matrix $[\tilde{Q}]$ from a plane to an axis. On the other hand, from equations (2.32) to (2.34) in order to calculate $[\tilde{Q}]$ it is first necessary to calculate the matrices $[T]$, $[G]$ and $[H]$, which requires calculating the inverse of the matrices $[A]_{j0}$ $(j = 1,2,\cdots,n)$. When $\beta = 0$, it can be seen from Section 2.6 that there are many zero elements in the matrices $[A]_{j0}$, resulting in the fact that the inverse of $[A]_{j0}$ can easily be expressed analytically. As for the calculation of the inverse matrix in equations (2.32) to (2.34), it also can be easily expressed analytically because the matrix to be inverted is of order 3.

(6) If the Fourier transformed dynamic flexibility matrix of l_R to l_P is denoted by $[\tilde{Q}(\beta,\gamma)]$, and that of l_P to l_R by $[\tilde{\delta}(\beta,\gamma)]$, from the Betti reciprocity theorem [Dominguez 1993] and the axisymmetry of the problem, it can be shown that

$$\begin{bmatrix} \tilde{Q}_{11} & \tilde{Q}_{12} & \tilde{Q}_{13} \\ \tilde{Q}_{21} & \tilde{Q}_{22} & \tilde{Q}_{23} \\ \tilde{Q}_{31} & \tilde{Q}_{32} & \tilde{Q}_{33} \end{bmatrix} = \begin{bmatrix} \tilde{\delta}_{11} & \tilde{\delta}_{21} & -\tilde{\delta}_{31} \\ \tilde{\delta}_{12} & \tilde{\delta}_{22} & -\tilde{\delta}_{32} \\ -\tilde{\delta}_{13} & -\tilde{\delta}_{23} & \tilde{\delta}_{33} \end{bmatrix} \qquad (2.41)$$

Equation (2.41) is proved as follows. Consider the situation shown in Figure 2.1. When the harmonic forces are applied at point P, the dynamic flexibility matrix at point B is denoted by $[Q(x,y,z)]$. When the harmonic forces are applied at point R, the dynamic flexibility matrix at point A is denoted by $[\delta(x,y,-z)]$. When the forces are applied at

point B, the dynamic flexibility matrix at point P is denoted by $[P(-x,-y,-z)]$. It follows from the displacement reciprocity relation that

$$[Q(x,y,z\ )]=[P(-x,-y,-z\ )]^T$$

It can be seen from Figure 2.1 that

$$[P(-x,-y,-z\ )]=\begin{bmatrix} \delta_{11}(x,y,-z) & \delta_{12}(x,y,-z) & -\delta_{13}(x,y,-z) \\ \delta_{21}(x,y,-z) & \delta_{22}(x,y,-z) & -\delta_{23}(x,y,-z) \\ -\delta_{31}(x,y,-z) & -\delta_{32}(x,y,-z) & \delta_{33}(x,y,-z) \end{bmatrix} \tag{2.42}$$

Thus

$$[Q(x,y,z)]=\begin{bmatrix} \delta_{11}(x,y,-z) & \delta_{12}(x,y,-z) & -\delta_{13}(x,y,-z) \\ \delta_{21}(x,y,-z) & \delta_{22}(x,y,-z) & -\delta_{23}(x,y,-z) \\ -\delta_{31}(x,y,-z) & -\delta_{32}(x,y,-z) & \delta_{33}(x,y,-z) \end{bmatrix}^T \tag{2.43}$$

which, after being Fourier transformed over x and y, gives equation (2.41).

This property can be used to avoid numerical difficulties in the calculation of the Fourier transformed dynamic flexibility matrix of l_R to l_P, i.e. $[\tilde{Q}(\beta,\gamma)]$, when $l_R > l_P$. Examination of equations (2.32), (2.34) and those in Section 2.6 shows that, when $l_R \le l_P$, no terms involve exponents of which the real parts are larger than zero, as a result of which no numerical difficulties are encountered for large layer thickness. However, when $l_R > l_P$, due to the term $e^{\sum_{j=l_P}^{l_R-1}\alpha_{j1}h_j}$ in equations (2.33), this formula is inappropriate for numerical calculation. In this case, one may calculate the Fourier transformed dynamic flexibility matrix of l_P to l_R instead, and get the flexibility matrix of l_R to l_P through equation (2.41).

If $l_R = l_P$, equation (2.41) shows that

$$\left.\begin{aligned} \tilde{Q}_{12}(\beta,\gamma)&=\tilde{Q}_{21}(\beta,\gamma) \\ \tilde{Q}_{13}(\beta,\gamma)&=-\tilde{Q}_{31}(\beta,\gamma) \\ \tilde{Q}_{23}(\beta,\gamma)&=-\tilde{Q}_{32}(\beta,\gamma) \end{aligned}\right\} \tag{2.44}$$

2.4.2 PROPERTIES OF $[\tilde{U}(\beta,\gamma)]$

The properties (1) to (5) of $[\tilde{Q}(\beta,\gamma)]$ as well as equation (2.39) still hold when $[\tilde{Q}(\beta,\gamma)]$ is replaced with $[\tilde{U}(\beta,\gamma)]$. Hence

(1) $\tilde{U}_{13}(\beta,\gamma),\tilde{U}_{31}(\beta,\gamma)$ are odd functions of β, and even functions of γ.

(2) $\tilde{U}_{23}(\beta,\gamma),\tilde{U}_{32}(\beta,\gamma)$ are even functions of β, and odd functions of γ.

(3) $\tilde{U}_{11}(\beta,\gamma),\tilde{U}_{22}(\beta,\gamma),\tilde{U}_{33}(\beta,\gamma)$ are even functions of β and γ.

(4) $\tilde{U}_{12}(\beta,\gamma),\tilde{U}_{21}(\beta,\gamma)$ are odd functions of β and γ.

(5) Therefore

$$\left.\begin{aligned}
&\tilde{U}_{13}(\beta,\gamma)=\tilde{U}_{23}(0,\rho)\cos\phi\\
&\tilde{U}_{23}(\beta,\gamma)=\tilde{U}_{23}(0,\rho)\sin\phi\\
&\tilde{U}_{33}(\beta,\gamma)=\tilde{U}_{33}(0,\rho)\\
&\tilde{U}_{31}(\beta,\gamma)=\tilde{U}_{32}(0,\rho)\cos\phi\\
&\tilde{U}_{32}(\beta,\gamma)=\tilde{U}_{32}(0,\rho)\sin\phi\\
&\tilde{U}_{11}(\beta,\gamma)=\tilde{U}_{11}(0,\rho)\sin^2\phi+\tilde{U}_{22}(0,\rho)\cos^2\phi\\
&\tilde{U}_{22}(\beta,\gamma)=\tilde{U}_{11}(0,\rho)\cos^2\phi+\tilde{U}_{22}(0,\rho)\sin^2\phi\\
&\tilde{U}_{12}(\beta,\gamma)=\tilde{U}_{21}(\beta,\gamma)=(\tilde{U}_{22}(0,\rho)-\tilde{U}_{11}(0,\rho))\sin\phi\cos\phi
\end{aligned}\right\} \qquad (2.45)$$

When $l_R > l_P$, due to the term $e^{\sum_{j=l_P}^{l_R-1}\alpha_{j1}h_j}$ in equations (2.37), this formula is also inappropriate for numerical calculation. To overcome this, one may calculate the derivative over z of the Fourier transformed dynamic flexibility matrix of l_R to l_P, and then use the Fourier transformed Hooke's law (see equations (2.49) and (2.50)).

2.4.3 PROPERTIES OF $[\tilde{V}(\beta,\gamma)]$

(1) $\tilde{V}_{11}(\beta,\gamma),\tilde{V}_{22}(\beta,\gamma),\tilde{V}_{32}(\beta,\gamma)$ are even with β, and odd with γ.

(2) $\tilde{V}_{23}(\beta,\gamma),\tilde{V}_{33}(\beta,\gamma)$ are even with β and γ.

(3) $\tilde{V}_{12}(\beta,\gamma)$, $\tilde{V}_{21}(\beta,\gamma)$, $\tilde{V}_{31}(\beta,\gamma)$ are odd with β , and even with γ .

(4) $\tilde{V}_{13}(\beta,\gamma)$ is odd with β and γ .

(5) By putting $\beta = \rho\cos\phi, \gamma = \rho\sin\phi, (\therefore \rho = \sqrt{\beta^2+\gamma^2}, \phi = \tan^{-1}\frac{\gamma}{\beta})$, then

$$\left.\begin{aligned}
\tilde{V}_{11}(\beta,\gamma) &= -\tilde{V}_{11}(0,\rho)\sin\phi\cos 2\phi - \tilde{V}_{22}(0,\rho)\sin\phi\cos^2\phi + \tilde{V}_{32}(0,\rho)\sin\phi\cos^2\phi \\
\tilde{V}_{12}(\beta,\gamma) &= \tilde{V}_{11}(0,\rho)\cos\phi\cos 2\phi - \tilde{V}_{22}(0,\rho)\cos\phi\sin^2\phi + \tilde{V}_{32}(0,\rho)\cos\phi\sin^2\phi \\
\tilde{V}_{13}(\beta,\gamma) &= -\tfrac{1}{2}\tilde{V}_{23}(0,\rho)\sin 2\phi + \tfrac{1}{2}\tilde{V}_{33}(0,\rho)\sin 2\phi \\
\tilde{V}_{21}(\beta,\gamma) &= \tilde{V}_{11}(0,\rho)\sin\phi\sin 2\phi + \tilde{V}_{22}(0,\rho)\cos\phi\sin^2\phi + \tilde{V}_{32}(0,\rho)\cos\phi\cos^2\phi \\
\tilde{V}_{22}(\beta,\gamma) &= -\tilde{V}_{11}(0,\rho)\cos\phi\sin 2\phi + \tilde{V}_{22}(0,\rho)\sin\phi\sin^2\phi + \tilde{V}_{32}(0,\rho)\sin\phi\cos^2\phi \\
\tilde{V}_{23}(\beta,\gamma) &= \tilde{V}_{23}(0,\rho)\sin^2\phi + \tilde{V}_{33}(0,\rho)\cos^2\phi \\
\tilde{V}_{31}(\beta,\gamma) &= -\tilde{V}_{11}(0,\rho)\sin\phi\sin 2\phi + \tilde{V}_{22}(0,\rho)\cos\phi\cos^2\phi + \tilde{V}_{32}(0,\rho)\cos\phi\sin^2\phi \\
\tilde{V}_{32}(\beta,\gamma) &= \tilde{V}_{11}(0,\rho)\cos\phi\sin 2\phi + \tilde{V}_{22}(0,\rho)\sin\phi\cos^2\phi + \tilde{V}_{32}(0,\rho)\sin\phi\sin^2\phi \\
\tilde{V}_{33}(\beta,\gamma) &= \tilde{V}_{23}(0,\rho)\cos^2\phi + \tilde{V}_{33}(0,\rho)\sin^2\phi
\end{aligned}\right\} \quad (2.46)$$

(6) The Fourier transformed stress reciprocity relations

From Hooke's law

$$\left.\begin{aligned}
\tau_{xz} &= \mu(\frac{\partial w}{\partial x} + \frac{\partial u}{\partial z}) \\
\tau_{yz} &= \mu(\frac{\partial w}{\partial y} + \frac{\partial v}{\partial z}) \\
\tau_{zz} &= \lambda(\frac{\partial u}{\partial x} + \frac{\partial v}{\partial y}) + (\lambda+2\mu)\frac{\partial w}{\partial z}
\end{aligned}\right\} \quad (2.47)$$

$$\left.\begin{aligned}
\tau_{xy} &= \mu(\frac{\partial v}{\partial x} + \frac{\partial u}{\partial y}) \\
\tau_{xx} &= \lambda(\frac{\partial v}{\partial y} + \frac{\partial w}{\partial z}) + (\lambda+2\mu)\frac{\partial u}{\partial x} \\
\tau_{yy} &= \lambda(\frac{\partial u}{\partial x} + \frac{\partial w}{\partial z}) + (\lambda+2\mu)\frac{\partial v}{\partial y}
\end{aligned}\right\} \quad (2.48)$$

it follows that

$$\left.\begin{aligned}
\tilde{U}_{1j} &= \mu_{l_R}(i\beta\tilde{Q}_{3j} + \frac{\partial\tilde{Q}_{1j}}{\partial z}) \\
\tilde{U}_{2j} &= \mu_{l_R}(i\gamma\tilde{Q}_{3j} + \frac{\partial\tilde{Q}_{2j}}{\partial z}) \\
\tilde{U}_{3j} &= \lambda_{l_R}(i\beta\tilde{Q}_{1j} + i\gamma\tilde{Q}_{2j}) + (\lambda_{l_R} + 2\mu_{l_R})\frac{\partial\tilde{Q}_{3j}}{\partial z}
\end{aligned}\right\} \tag{2.49}$$

$$\left.\begin{aligned}
\tilde{V}_{1j} &= \mu_{l_R}(i\beta\tilde{Q}_{2j} + i\gamma\tilde{Q}_{1j}) \\
\tilde{V}_{2j} &= \lambda_{l_R}(i\gamma\tilde{Q}_{2j} + \frac{\partial\tilde{Q}_{3j}}{\partial z}) + (\lambda_{l_R} + 2\mu_{l_R})i\beta\tilde{Q}_{1j} \\
\tilde{V}_{3j} &= \lambda_{l_R}(i\beta\tilde{Q}_{1j} + \frac{\partial\tilde{Q}_{3j}}{\partial z}) + (\lambda_{l_R} + 2\mu_{l_R})i\gamma\tilde{Q}_{2j}
\end{aligned}\right\} \tag{2.50}$$

where, as has been defined in Section 2.3.4, $\tilde{V}_{kj}$ stands for the Fourier transforms of stresses $\tau_{xy}(k=1), \tau_{xx}(k=2), \tau_{yy}(k=3)$ at point B, due to a unit harmonic force acting at point P (see Figure 2.1) in $x(j=1), y(j=2), z(j=3)$ directions respectively, and λ_{l_R}, μ_{l_R} are Lamé constants of the l_R th layer.

From equations (2.50), (2.41) and (2.40)

$$\begin{aligned}
\tilde{V}_{11} &= \mu_{l_R}(i\beta\tilde{Q}_{21} + i\gamma\tilde{Q}_{11}) = \mu_{l_R}(i\beta\tilde{Q}_{12} + i\gamma\tilde{Q}_{11}) \\
&= \mu_{l_R}(i\beta\tilde{\delta}_{21} + i\gamma\tilde{\delta}_{11}) = \mu_{l_R} / \mu_{l_P}\tilde{W}_{11}
\end{aligned} \tag{2.51}$$

$$\begin{aligned}
\tilde{V}_{12} &= \mu_{l_R}(i\beta\tilde{Q}_{22} + i\gamma\tilde{Q}_{12}) = \mu_{l_R}(i\beta\tilde{Q}_{22} + i\gamma\tilde{Q}_{21}) \\
&= \mu_{l_R}(i\beta\tilde{\delta}_{22} + i\gamma\tilde{\delta}_{12}) = \mu_{l_R} / \mu_{l_P}\tilde{W}_{12}
\end{aligned} \tag{2.52}$$

where

$$\tilde{W}_{11} = \mu_{l_P}(i\beta\tilde{\delta}_{22} + i\gamma\tilde{\delta}_{12}), \tilde{W}_{12} = \mu_{l_P}(i\beta\tilde{\delta}_{22} + i\gamma\tilde{\delta}_{12}) \tag{2.53}$$

are Fourier transforms of stress τ_{xy} at point A of the top of the l_P th layer due to a unit harmonic force acting at point R in directions x and y, respectively. Equations (2.51) and (2.52) show a generalised reciprocity relationship for the stress component τ_{xy}. For other stress components, there is no such reciprocity relationship.

2.5 THE FOURIER TRANSFORMED MOVING DYNAMIC FLEXIBILITY MATRIX

2.5.1 THE FOURIER TRANSFORMED MOVING DYNAMIC FLEXIBILITY MATRIX OF l_R TO l_P

Now suppose that, at the top side of the l_Pth layer, harmonic load distributions, $p_x(x,y)e^{i\Omega t}, p_y(x,y)e^{i\Omega t}, p_z(x,y)e^{i\Omega t}$, acting in *x, y, z* directions respectively, move in the *x* direction at speed *c*. Then Navier's equation for the ground is

$$\left.\begin{aligned}
(\lambda+\mu)\frac{\partial\Delta}{\partial x}+\mu\nabla^2 u &= \rho\frac{\partial^2 u}{\partial t^2}-\delta(z-z_P)p_x(x-ct,y)e^{i\Omega t}\\
(\lambda+\mu)\frac{\partial\Delta}{\partial y}+\mu\nabla^2 \upsilon &= \rho\frac{\partial^2 \upsilon}{\partial t^2}-\delta(z-z_P)p_y(x-ct,y)e^{i\Omega t}\\
(\lambda+\mu)\frac{\partial\Delta}{\partial z}+\mu\nabla^2 w &= \rho\frac{\partial^2 w}{\partial t^2}-\delta(z-z_P)p_z(x-ct,y)e^{i\Omega t}
\end{aligned}\right\} \tag{2.54}$$

where z_P is the depth of the top side of the l_Pth layer, and $\delta(\cdot)$ is the Dirac-δ function. As shown in equation (2.54), Navier's equation is written for any layer and a global vertical coordinate, *z*, is used. The Fourier transform of equation (2.54) is

$$\left.\begin{aligned}
(\lambda+\mu)i\beta\overline{\Delta}+\mu[\frac{d^2\overline{u}}{dz^2}-(\beta^2+\gamma^2)\overline{u}] &= \rho\frac{\partial^2\overline{u}}{\partial t^2}-\delta(z-z_P)\tilde{p}_x(\beta,\gamma)e^{i(\Omega-\beta c)t}\\
(\lambda+\mu)i\gamma\overline{\Delta}+\mu[\frac{d^2\overline{\upsilon}}{dz^2}-(\beta^2+\gamma^2)\overline{\upsilon}] &= \rho\frac{\partial^2\overline{\upsilon}}{\partial t^2}-\delta(z-z_P)\tilde{p}_y(\beta,\gamma)e^{i(\Omega-\beta c)t}\\
(\lambda+\mu)\frac{d\overline{\Delta}}{dz}+\mu[\frac{d^2\overline{w}}{dz^2}-(\beta^2+\gamma^2)\overline{w}] &= \rho\frac{\partial^2\overline{w}}{\partial t^2}-\delta(z-z_P)\tilde{p}_z(\beta,\gamma)e^{i(\Omega-\beta c)t}
\end{aligned}\right\} \tag{2.55}$$

where $\tilde{p}_x(\beta,\gamma), \tilde{p}_y(\beta,\gamma), \tilde{p}_z(\beta,\gamma)$ are the Fourier transforms of $p_x(x,y), p_y(x,y), p_z(x,y)$, and $\overline{u}=\overline{u}(\beta,\gamma,z,t)$ is the Fourier transform of $u(x,y,z,t)$. Now the steady state solution to equation (2.55) may be written as

$$\left.\begin{aligned}
\overline{\Delta} &= \tilde{\Delta}e^{i(\Omega-\beta c)t}\\
\overline{u} &= \tilde{u}e^{i(\Omega-\beta c)t}\\
\overline{\upsilon} &= \tilde{\upsilon}e^{i(\Omega-\beta c)t}\\
\overline{w} &= \tilde{w}e^{i(\Omega-\beta c)t}
\end{aligned}\right\} \tag{2.56}$$

Equation (2.56) means that, if $u^*(x,y,z)$ is the inverse Fourier transform of $\tilde{u}(\beta,\gamma,z)$, the actual longitudinal displacement of point (x, y, z) in the ground is given by

$$u(x,y,z,t) = u^*(x-ct,y,z)e^{i\Omega t} \tag{2.57}$$

Equation (2.56) may also be given another physical interpretation as $\bar{u}(\beta,\gamma,z,t)$ is time harmonic with the amplitude $\tilde{u}(\beta,\gamma,z)$ and the frequency $\omega = \Omega - \beta c$. This frequency may take negative values, indicating that each loss factor, say η, appearing in the differential equations of motion of the layered ground, should take the form of $\eta\,\mathrm{sgn}(\omega)$ as already shown in equation (2.7). Therefore the steady state displacements (and other quantities) consist of an infinite number of spatially harmonic components. Furthermore, each spatially harmonic component is time harmonic the frequency and amplitude of which are dependent on the wavenumber of this spatially harmonic component.

Substitution of equation (2.56) into equation (2.55), yields,

$$\left.\begin{aligned}
(\lambda+\mu)i\beta\tilde{\Delta} + \mu[\frac{d^2\tilde{u}}{dz^2} - (\beta^2+\gamma^2)\tilde{u}] &= -\rho(\Omega-\beta c)^2\tilde{u} - \delta(z-z_P)\tilde{p}_x(\beta,\gamma)\\
(\lambda+\mu)i\gamma\tilde{\Delta} + \mu[\frac{d^2\tilde{\upsilon}}{dz^2} - (\beta^2+\gamma^2)\tilde{\upsilon}] &= -\rho(\Omega-\beta c)^2\tilde{\upsilon} - \delta(z-z_P)\tilde{p}_y(\beta,\gamma)\\
(\lambda+\mu)\frac{d\tilde{\Delta}}{dz} + \mu[\frac{d^2\tilde{w}}{dz^2} - (\beta^2+\gamma^2)\tilde{w}] &= -\rho(\Omega-\beta c)^2\tilde{w} - \delta(z-z_P)\tilde{p}_z(\beta,\gamma)
\end{aligned}\right\} \tag{2.58}$$

This equation reduces to equation (2.9) if one substitutes

$$\omega = \Omega - \beta c \tag{2.59}$$

Therefore, for the top side of the l_R th layer, the following relations may be used from Section 2.3

$$\begin{Bmatrix} \tilde{u}_{l_R 0}(\beta,\gamma) \\ \tilde{\upsilon}_{l_R 0}(\beta,\gamma) \\ \tilde{w}_{l_R 0}(\beta,\gamma) \end{Bmatrix} = [\tilde{Q}(\beta,\gamma)] \begin{Bmatrix} \tilde{p}_x(\beta,\gamma) \\ \tilde{p}_y(\beta,\gamma) \\ \tilde{p}_z(\beta,\gamma) \end{Bmatrix} \tag{2.60}$$

$$\begin{Bmatrix} \tilde{\tau}_{xzl_R 0} \\ \tilde{\tau}_{yzl_R 0} \\ \tilde{\tau}_{zzl_R 0} \end{Bmatrix} = [\tilde{U}(\beta,\gamma)] \begin{Bmatrix} \tilde{p}_x(\beta,\gamma) \\ \tilde{p}_y(\beta,\gamma) \\ \tilde{p}_z(\beta,\gamma) \end{Bmatrix} \tag{2.61}$$

$$\begin{Bmatrix} \tilde{\tau}_{xyl_R 0} \\ \tilde{\tau}_{xxl_R 0} \\ \tilde{\tau}_{yyl_R 0} \end{Bmatrix} = [\tilde{V}(\beta,\gamma)] \begin{Bmatrix} \tilde{p}_x(\beta,\gamma) \\ \tilde{p}_y(\beta,\gamma) \\ \tilde{p}_z(\beta,\gamma) \end{Bmatrix} \tag{2.62}$$

and from equation (2.56) the time varying Fourier transformed displacements on the top side of the l_R th layer are obtained by multiplying by the factor $e^{i(\Omega-\beta c)t}$.

The matrix $[\tilde{Q}(\beta,\gamma)]$ is called *the Fourier transformed moving dynamic flexibility matrix of l_R to l_P for motion in the x direction* (meaning that, the loading point is moving along the x-axis on the top side of the l_P th layer and the displacements are for the top side of the l_R th layer), or simply, *the Fourier transformed moving dynamic flexibility matrix.* $[\tilde{U}(\beta,\gamma)]$ and $[\tilde{V}(\beta,\gamma)]$ are called *the Fourier transformed moving stress matrices.* The calculation of these matrices is exactly the same as that described in Section 2.3 with the substitution $\omega = \Omega - \beta c$. These matrices may be denoted, for example, by $[\tilde{Q}(\beta,\gamma,\Omega-\beta c)]$, to emphasise their dependence on $\omega = \Omega - \beta c$.

2.5.2 SOME PROPERTIES OF $[\tilde{Q}(\beta,\gamma,\Omega-\beta c)]$, $[\tilde{U}(\beta,\gamma,\Omega-\beta c)]$ AND $[\tilde{V}(\beta,\gamma,\Omega-\beta c)]$

If $\omega = \Omega - \beta c$ is kept fixed, then all the properties explored in Section 2.4 will still hold. Especially, if the Fourier transformed moving dynamic flexibility matrix of l_R to l_P is denoted by $[\tilde{Q}(\beta,\gamma,\Omega-\beta c)]$, and that of l_P to l_R by $[\tilde{\delta}(\beta,\gamma,\Omega-\beta c)]$, then equation (2.41) yields

$$\begin{bmatrix} \tilde{Q}_{11} & \tilde{Q}_{12} & \tilde{Q}_{13} \\ \tilde{Q}_{21} & \tilde{Q}_{22} & \tilde{Q}_{23} \\ \tilde{Q}_{31} & \tilde{Q}_{32} & \tilde{Q}_{33} \end{bmatrix}_{(\beta,\gamma,\Omega-\beta c)} = \begin{bmatrix} \tilde{\delta}_{11} & \tilde{\delta}_{21} & -\tilde{\delta}_{31} \\ \tilde{\delta}_{12} & \tilde{\delta}_{22} & -\tilde{\delta}_{32} \\ -\tilde{\delta}_{13} & -\tilde{\delta}_{23} & \tilde{\delta}_{33} \end{bmatrix}_{(\beta,\gamma,\Omega-\beta c)} \tag{2.63}$$

where the subscripts in the round brackets indicate that each element of the matrices is a function of β,γ and $\Omega-\beta c$. Similarly from equations (2.51) and (2.52) it is found that

$$\tilde{V}_{11}(\beta,\gamma,\Omega-\beta c) = \mu_{l_R} / \mu_{l_P} \tilde{W}_{11}(\beta,\gamma,\Omega-\beta c) \tag{2.64}$$

$$\tilde{V}_{12}(\beta,\gamma,\Omega-\beta c)=\mu_{l_R}/\mu_{l_P}\tilde{W}_{12}(\beta,\gamma,\Omega-\beta c) \tag{2.65}$$

where $\tilde{V}_{12}(\beta,\gamma,\Omega-\beta c)$ is the Fourier transform of τ_{xy} (dropping the factor $e^{i(\Omega-\beta c)}$) at the top side of the l_Rth layer due to a unit harmonic load at the top side of the l_Pth layer which points in the y' direction and whose point of application moves uniformly at speed c along the x'axis (see Figure 2.1). $\tilde{W}_{12}(\beta,\gamma,\Omega-\beta c)$ is the Fourier transform of τ_{xy} at the top side of the l_Pth layer due to a unit harmonic load at the top side of the l_Rth layer which acts in the y direction and moves uniformly at speed c along the x axis.

If $\omega=\Omega-\beta c$ is not kept fixed, some properties with respect to β disappear due to the load motion. However, some observations can be made in the case of $\Omega=0$. In this case, any unit point moving load component, for instance, $p_z=e^{i\Omega t}=1$, is a real number, thus, taken as an example, the longitudinal steady state displacement due to this load, given by (see equation (2.57))

$$u^*(x,y,z)=\frac{1}{4\pi^2}\int_{-\infty}^{\infty}\int_{-\infty}^{\infty}\tilde{Q}_{13}(\beta,\gamma,-\beta c)e^{i\beta x}e^{i\gamma y}d\beta d\gamma$$

must also be a real number. Since $\tilde{Q}_{13}(\beta,\gamma,-\beta c)$ is an even function of γ, $u^*(x,y,z)$ can be written as

$$\begin{aligned}u^*(x,y,z)&=\frac{2}{4\pi^2}\int_0^{\infty}[\int_{-\infty}^{\infty}(\mathrm{Re}(\tilde{Q}_{13})+i\,\mathrm{Im}(\tilde{Q}_{13}))(\cos\beta x+i\sin\beta x)d\beta]\cos\gamma y d\gamma\\&=\frac{2}{4\pi^2}\int_0^{\infty}\{\int_{-\infty}^{\infty}[\mathrm{Re}(\tilde{Q}_{13})\cos(\beta x)-\mathrm{Im}(\tilde{Q}_{13})\sin\beta x+i(\mathrm{Re}(\tilde{Q}_{13})\sin\beta x+\\&\quad+\mathrm{Im}(\tilde{Q}_{13})\cos\beta x)]d\beta\}\cos\gamma y d\gamma\end{aligned}$$

Since $u^*(x,y,z)$ is real, it is required that, for any x, $\mathrm{Re}(\tilde{Q}_{13})\sin\beta x+\mathrm{Im}(\tilde{Q}_{13})\cos(\beta x)$ must be an odd function of β. Therefore, the real part of $\tilde{Q}_{13}(\beta,\gamma,-\beta c)$ must be an even function of β, and the imaginary part of $\tilde{Q}_{13}(\beta,\gamma,-\beta c)$ must be an odd function of β. Similar arguments can be made concerning other displacement components. A conclusion drawn from these discussions is that:

When $\Omega = 0$, the real parts of $\tilde{Q}_{11}(\beta,\gamma,-\beta c)$, $\tilde{Q}_{22}(\beta,\gamma,-\beta c)$, $\tilde{Q}_{33}(\beta,\gamma,-\beta c)$, $\tilde{Q}_{13}(\beta,\gamma,-\beta c)$, and $\tilde{Q}_{31}(\beta,\gamma,-\beta c)$ are even functions of β, and their imaginary parts are odd functions of β; the real parts of $\tilde{Q}_{12}(\beta,\gamma,-\beta c)$, $\tilde{Q}_{21}(\beta,\gamma,-\beta c)$, $\tilde{Q}_{23}(\beta,\gamma,-\beta c)$ and $\tilde{Q}_{32}(\beta,\gamma,-\beta c)$ are odd functions of β, and their imaginary parts are even functions of β.

2.5.3 RECIPROCITY RELATIONS

2.5.3.1 *DISPLACEMENTS RECIPROCITY RELATIONS*

Suppose at time $t = 0$, that a lateral (in the y direction) unit harmonic load moving in the positive x-direction acts at the point (r, s) on the top side of the l_P th layer, i.e. $p_x = 0, p_y = \delta(x - r, y - s), p_z = 0$, and $\tilde{p}_x = 0, \tilde{p}_y = e^{-i(\beta r+\gamma s)}, \tilde{p}_z = 0$, then the longitudinal (in x-direction) displacement of point (p, q) on the top side of the l_R th layer comes from equations (2.56) and (2.60) as follows

$$u_{l_R 0}(p,q,t) = \frac{1}{4\pi^2}\int_{-\infty}^{\infty}\int_{-\infty}^{\infty}\tilde{Q}_{12}(\beta,\gamma,\Omega-\beta c)e^{i(\Omega-\beta c)t}e^{i\beta(p-r)}e^{i\gamma(q-s)}d\beta d\gamma \tag{2.66}$$

Now let the source-observer configuration be interchanged, i.e. at time $t = 0$ a longitudinal unit harmonic load moving in the negative x-direction acts at the point (p, q) on the top side of the l_R th layer, i.e. $p_x = \delta(x - p, y - q), p_y = 0, p_z = 0$, and $\tilde{p}_x = e^{-i(\beta p+\gamma q)}, \tilde{p}_y = 0, \tilde{p}_z = 0$, then the lateral displacement of point (r, s) on the top side of the l_P th layer comes from equations (2.56) and (2.60)

$$v_{l_P 0}(r,s,t) = \frac{1}{4\pi^2}\int_{-\infty}^{\infty}\int_{-\infty}^{\infty}\tilde{\delta}_{21}(\beta,\gamma,\Omega+\beta c)e^{i(\Omega+\beta c)t}e^{i\beta(r-p)}e^{i\gamma(s-q)}d\beta d\gamma$$

which from equation (2.63), becomes

$$v_{l_P 0}(r,s,t) = \frac{1}{4\pi^2}\int_{-\infty}^{\infty}\int_{-\infty}^{\infty}\tilde{Q}_{12}(\beta,\gamma,\Omega+\beta c)e^{i(\Omega+\beta c)t}e^{i\beta(r-p)}e^{i\gamma(s-q)}d\beta d\gamma$$

which, due to the fact that $\tilde{Q}_{12}(-\beta,-\gamma,\Omega+\beta c) = \tilde{Q}_{12}(\beta,\gamma,\Omega+\beta c)$ (see Section 2.4.1 property (4)), can be written as

$$\upsilon_{l_\mu 0}(r,s,t) = \frac{1}{4\pi^2}\int_{-\infty}^{\infty}\int_{-\infty}^{\infty}\tilde{Q}_{12}(-\beta,-\gamma,\Omega+\beta c)e^{i(\Omega+\beta c)t}e^{i\beta(r-p)}e^{i\gamma(s-q)}d\beta d\gamma$$
$$= \frac{1}{4\pi^2}\int_{-\infty}^{\infty}\int_{-\infty}^{\infty}\tilde{Q}_{12}(\beta,\gamma,\Omega-\beta c)e^{i(\Omega-\beta c)t}e^{i\beta(p-r)}e^{i\gamma(q-s)}d\beta d\gamma \qquad (2.67)$$

It is shown that $u_{l_R 0}(p,q,t) = \upsilon_{l_\mu 0}(r,s,t)$ by equations (2.66) and (2.67). Obviously, for other source-observer configurations, the same result holds.

It can be further proved that, the displacement of point A in direction 1 due to a unit harmonic load acting in direction 2 and moving at speed c along a line parallel to the ground surface and passing through point B (called line B, at $t = 0$ the load acts at point B), is equal to the displacement of point B in direction 2 due to a unit harmonic load of the same frequency acting in direction 1 and moving in the opposite direction at speed c along line A which passes through point A and is parallel to line B (at $t = 0$, the load acts at point A).

For the proof of this, without loss of generality, let line A and line B be parallel to the x-axis. If direction 1 is specified by a unit vector (m_1, m_2, m_3), and direction 2 by (n_1, n_2, n_3), then the displacement of point A in direction 1 is given by

$$d_A = u_A m_1 + \upsilon_A m_2 + w_A m_3 = [m_1 \quad m_2 \quad m_3][Q]\begin{Bmatrix} n_1 \\ n_2 \\ n_3 \end{Bmatrix} \qquad (2.68)$$

where, u_A, υ_A, w_A are the displacement components of point A in the x-, y- and z-directions, $[Q] = (Q_{ij})_{i,j=1,2,3}$, and Q_{ij} is the displacement of point A in direction i ($i = x$, y, z) due to a unit harmonic load acting in direction j ($j = x$, y, z) and moving at speed c along line B. Similarly, the displacement of point B in direction 2 is given by

$$d_B = u_B n_1 + \upsilon_B n_2 + w_B n_3 = [n_1 \quad n_2 \quad n_3][\delta]\begin{Bmatrix} m_1 \\ m_2 \\ m_3 \end{Bmatrix} \qquad (2.69)$$

where $[\delta] = (\delta_{ij})_{i,j=1,2,3}$, and δ_{ij} is the displacement of point B in direction $i(i = x, y, z)$ due to a unit harmonic load acting in direction $j(j = x, y, z)$ and moving at speed $-c$

along line A. As has been proved above that $Q_{ij} = \delta_{ji}$, thus $[Q]^T = [\delta]$, and equations (2.68) and (2.69) yield $d_A = d_B$.

2.5.3.2 *STRESS RECIPROCITY RELATIONS*

Suppose at time $t = 0$ that a lateral (in y direction) unit harmonic load moving in the positive x-direction acts at the point (r, s) on the top side of the l_Pth layer, i.e. $p_x = 0, p_y = \delta(x - r, y - s), p_z = 0$, and $\tilde{p}_x = 0, \tilde{p}_y = e^{-i(\beta r + \gamma s)}, \tilde{p}_z = 0$, then the stress τ_{xy} of point (p, q) on the top side of the l_Rth layer is given by

$$\tau_{xyl_R0}(p,q,t) = \frac{1}{4\pi^2}\int_{-\infty}^{\infty}\int_{-\infty}^{\infty}\tilde{V}_{12}(\beta,\gamma,\Omega-\beta c)e^{i(\Omega-\beta c)t}e^{i\beta(p-r)}e^{i\gamma(q-s)}d\beta d\gamma \tag{2.70}$$

Again let the source-observer points be interchanged, i.e. at time $t = 0$ a longitudinal unit harmonic load moving in the negative x-direction acts at the point (p, q) on the top side of the l_Rth layer, i.e. $p_x = 0, p_y = \delta(x - p, y - q), p_z = 0$, and $\tilde{p}_x = 0, \tilde{p}_y = e^{-i(\beta p + \gamma q)}, \tilde{p}_z = 0$, then the stress τ_{xy} of point (r, s) on the top side of l_Pth layer is given by

$$\tau_{xyl_P0}(r,s,t) = \frac{1}{4\pi^2}\int_{-\infty}^{\infty}\int_{-\infty}^{\infty}\tilde{W}_{12}(\beta,\gamma,\Omega+\beta c)e^{i(\Omega+\beta c)t}e^{i\beta(r-p)}e^{i\gamma(s-p)}d\beta d\gamma$$

According to equations (2.65), this becomes

$$\tau_{xyl_P0}(r,s,t) = \frac{\mu_{l_P}}{\mu_{l_R}}\frac{1}{4\pi^2}\int_{-\infty}^{\infty}\int_{-\infty}^{\infty}\tilde{V}_{12}(\beta,\gamma,\Omega+\beta c)e^{i(\Omega+\beta c)t}e^{i\beta(r-p)}e^{i\gamma(s-q)}d\beta d\gamma$$

Noticing that $\tilde{V}_{12}(-\beta,-\gamma,\Omega+\beta c) = -\tilde{V}_{12}(\beta,\gamma,\Omega+\beta c)$, it follows that

$$\begin{aligned}\tau_{xyl_P0}(r,s,t) &= -\frac{\mu_{l_P}}{\mu_{l_R}}\frac{1}{4\pi^2}\int_{-\infty}^{\infty}\int_{-\infty}^{\infty}\tilde{V}_{12}(-\beta,-\gamma,\Omega+\beta c)e^{i(\Omega+\beta c)t}e^{i\beta(r-p)}e^{i\gamma(s-q)}d\beta d\gamma \\ &= -\frac{\mu_{l_P}}{\mu_{l_R}}\frac{1}{4\pi^2}\int_{-\infty}^{\infty}\int_{-\infty}^{\infty}\tilde{V}_{12}(\beta,\gamma,\Omega-\beta c)e^{i(\Omega-\beta c)t}e^{i\beta(p-r)}e^{i\gamma(q-s)}d\beta d\gamma\end{aligned}$$

Thus

$$\tau_{xyl_P0}(r,s,t) = -\frac{\mu_{l_P}}{\mu_{l_R}}\tau_{xyl_R0}(p,q,t) \tag{2.71}$$

Barros and Luco [1994, Section 4.3] have observed the above reciprocity relations for a special case, i.e. $r = p$, $s = q$, through a numerical test but did not give a proof.

2.6 FORMULAE FOR $[A]_{j0}, [A]_{j0}^{-1}, [A]_{j1}, [R], [S], [R][S]^{-1}$

In this section the various matrices used in the model are given explicitly for the special case of $\beta = 0$. Putting

$$\zeta_{j1} = \omega / c_{j1}, \zeta_{j2} = \omega / c_{j2}$$
$$\alpha_{j1} = \sqrt{\beta^2 + \gamma^2 - \zeta_{j1}^2}, \alpha_{j2} = \sqrt{\beta^2 + \gamma^2 - \zeta_{j2}^2}$$

then

2.6.1 WHEN $\beta = 0$, AND $\omega \neq 0$

(1) Matrix $[A]_{j0} = (a_{kl})$, $(k, l = 1,2,\cdots,6; j = 1,2,\cdots,n)$

$$a_{12} = 1, a_{15} = 1, a_{23} = 1, a_{26} = 1, \quad a_{21} = -i\gamma / \zeta_{j1}^2, a_{24} = a_{21}$$

$$a_{31} = -\alpha_{j1} / \zeta_{j1}^2, a_{33} = -i\gamma / \alpha_{j2}, a_{34} = -a_{31}, a_{36} = -a_{33}$$

$$a_{42} = \alpha_{j2}\mu_j, a_{45} = -a_{42}$$

$$a_{51} = -2i\mu_j \alpha_{j1}\gamma / \zeta_{j1}^2, a_{53} = \mu_j(\gamma^2 / \alpha_{j2} + \alpha_{j2}), a_{54} = -a_{51}, a_{56} = -a_{53}$$
$$a_{61} = -\mu_j(\zeta_{j2}^2 + 2\alpha_{j2}^2) / \zeta_{j1}^2, a_{63} = -2i\mu_j\gamma, a_{64} = a_{61}, a_{66} = a_{63}$$

other a's are zero.

(2) Matrix $[A]_{j1}$ $(j = 1,2,\cdots,n)$

$$[A]_{j1} = [A]_{j0}[D]_j$$

where $[D]_j$ is a diagonal matrix with the elements

$$d_{11} = 1, d_{22} = e^{(\alpha_{j2} - \alpha_{j1})h_j}, d_{33} = d_{22}, d_{44} = e^{-2\alpha_{j1}h_j}, d_{55} = e^{-(\alpha_{j1} + \alpha_{j2})h_j}, d_{66} = d_{55}$$

(3) Matrices $[R]$ and $[S]$

$$[R]=\begin{bmatrix} 0 & 1 & 0 \\ -\dfrac{i\gamma}{\zeta_{n+1,1}^2} & 0 & 1 \\ \dfrac{\alpha_{n+1,1}}{\zeta_{n+1,1}^2} & 0 & \dfrac{i\gamma}{\alpha_{n+1,2}} \end{bmatrix}$$

$$[S]=\begin{bmatrix} 0 & -\mu_{n+1}\alpha_{n+1,2} & 0 \\ \dfrac{2i\mu_{n+1}\alpha_{n+1,1}\gamma}{\zeta_{n+1,1}^2} & 0 & -\dfrac{\mu_{n+1}(\gamma^2+\alpha_{n+1,2}^2)}{\alpha_{n+1,2}} \\ \lambda_{n+1}-2\mu_{n+1}\dfrac{\alpha_{n+1,1}^2}{\zeta_{n+1,1}^2} & 0 & -2i\mu_{n+1}\gamma \end{bmatrix}$$

(4) Matrix $[R][S]^{-1}$

Putting

$$\Delta=[\frac{4\mu_{n+1}^2\alpha_{n+1,1}\gamma^2}{\zeta_{n+1,1}^2}+\frac{\mu_{n+1}(\gamma^2+\alpha_{n+1,2}^2)}{\alpha_{n+1,2}}(\lambda_{n+1}-2\mu_{n+1}\frac{\alpha_{n+1,1}^2}{\zeta_{n+1,1}^2})]\alpha_{n+1,2}$$

$$=\frac{\mu_{n+1}^3}{\zeta_{n+1,1}^2}[4\alpha_{n+1,1}\alpha_{n+1,2}\gamma^2-(2\gamma^2-\zeta_{n+1,2}^2)^2]$$

then

$$[R][S]^{-1}=$$

$$=\frac{1}{\Delta}\begin{bmatrix} -\dfrac{\Delta}{\alpha_{n+1,2}} & 0 & 0 \\ 0 & \alpha_{n+1,2}(\lambda_{n+1}-2\mu_{n+1}\dfrac{\alpha_{n+1,1}^2+\gamma^2}{\zeta_{n+1,1}^2}) & \dfrac{i\mu_{n+1}\gamma}{\zeta_{n+1,1}^2}(2\alpha_{n+1,1}\alpha_{n+1,2}-\gamma^2-\alpha_{n+1,2}^2) \\ 0 & \dfrac{-2i\mu_{n+1}\gamma}{\zeta_{n+1,1}^2}(\alpha_{n+1,1}\alpha_{n+1,2}+\alpha_{n+1,1}^2)+i\lambda_{n+1}\gamma & -\dfrac{\alpha_{n+1,1}\mu_{n+1}\zeta_{n+1,2}^2}{\zeta_{n+1,1}^2} \end{bmatrix}$$

2.6.2 WHEN $\beta=0$, AND $\omega=0$

(1) Matrix $[A]_{j0}=(a_{kl})$, $(k,l=1,2,\cdots,6;\ j=1,2,\cdots,n)$

$a_{12}=1, a_{15}=1, a_{23}=1, a_{26}=1$

$$a_{31} = (\lambda_j + 3\mu_j)/2\alpha_{j1}\mu_j, a_{33} = -i\gamma/\alpha_{j2}, a_{34} = -a_{31}, a_{36} = -a_{33}$$
$$a_{42} = \alpha_{j2}\mu_j, a_{45} = -a_{42}$$
$$a_{51} = i\mu_j\gamma/\alpha_{j1}, a_{53} = \mu_j(\gamma^2/\alpha_{j2} + \alpha_{j2}), a_{54} = -a_{51}, a_{56} = -a_{53}$$
$$a_{61} = \lambda_j + 2\mu_j, a_{63} = -2i\mu_j\gamma, a_{64} = a_{61}, a_{66} = a_{63}$$

other a's are zero.

(2) Matrix $[A]_{j1}$ (j = 1, 2, .., n)

$$[A]_{j1} = [A']_{j0}[D]_j$$

where $[D]_j$ is a diagonal matrix with the elements

$$d_{11} = 1, d_{22} = e^{(\alpha_{j2}-\alpha_{j1})h_j}, d_{33} = d_{22}, d_{44} = e^{-2\alpha_{j1}h_j}, d_{55} = e^{-(\alpha_{j1}+\alpha_{j2})h_j}, d_{66} = d_{55}$$

and $[A']_{j0} = (a'_{kl})(k,l = 1,2,\cdots,6; j = 1,2,\cdots,n)$ are 6×6 matrices the elements of which are the same as those of $[A]_{j0}$ except for the elements in the first and fourth columns:

$$a'_{11} = 0, \quad a'_{21} = -\frac{i(\lambda_j+\mu_j)\gamma h_j}{2\alpha_{j1}\mu_j}, \quad a'_{31} = \frac{\lambda_j+3\mu_j}{2\alpha_{j1}\mu_j} - \frac{\lambda_j+\mu_j}{2\mu_j}h_j$$
$$a'_{41} = 0, \quad a'_{51} = i\gamma[\frac{\mu_j}{\alpha_{j1}} - (\lambda_j+\mu_j)h_j], \quad a'_{61} = (\lambda_j+\mu_j)(\mu_j - a_{j1}h_j)$$

$$a'_{14} = 0, \quad a'_{24} = -a'_{21}, \quad a'_{34} = -(\frac{\lambda_j+3\mu_j}{2\alpha_{j1}\mu_j} + \frac{\lambda_j+\mu_j}{2\mu_j}h_j)$$
$$a'_{44} = 0, \quad a'_{54} = -i\gamma[\frac{\mu_j}{\alpha_{j1}} + (\lambda_j+\mu_j)h_j], \quad a'_{64} = (\lambda_j+\mu_j)(\mu_j + a_{j1}h_j)$$

(3) Matrices $[R]$ and $[S]$

$$[R] = \begin{bmatrix} 0 & 1 & 0 \\ 0 & 0 & 1 \\ -\frac{\lambda_{n+1}+3\mu_{n+1}}{2\alpha_{n+1,1}\mu_{n+1}} & 0 & \frac{i\gamma}{\alpha_{n+1,2}} \end{bmatrix}$$

$$[S]=\begin{bmatrix} 0 & -\mu_{n+1}\alpha_{n+1,2} & 0 \\ -\frac{i\gamma\mu_{n+1}}{\alpha_{n+1,1}} & 0 & -\frac{\mu_{n+1}(\gamma^2+\alpha_{n+1,2}^2)}{\alpha_{n+1,2}} \\ \lambda_{n+1}+2\mu_{n+1} & 0 & -2i\mu_{n+1}\gamma \end{bmatrix}$$

2.6.3 THE INVERSES OF MATRICES $[A]_{j0}$ AND $[A']_{j0}$

All these matrices have the form of

$$\begin{bmatrix} 0 & 1 & 0 & 0 & 1 & 0 \\ a_{21} & 0 & 1 & a_{21} & 0 & 1 \\ a_{31} & 0 & a_{33} & -a_{31} & 0 & -a_{33} \\ 0 & a_{42} & 0 & 0 & -a_{42} & 0 \\ a_{51} & 0 & a_{53} & -a_{51} & 0 & -a_{53} \\ a_{61} & 0 & a_{63} & a_{61} & 0 & a_{63} \end{bmatrix}$$

the inverse of which is given by

$$\begin{bmatrix} 0 & \frac{a_{63}}{2(a_{21}a_{63}-a_{61})} & \frac{a_{53}}{2(a_{53}a_{31}-a_{51}a_{33})} & 0 & -\frac{a_{33}}{2(a_{53}a_{31}-a_{51}a_{33})} & -\frac{1}{2(a_{21}a_{63}-a_{61})} \\ \frac{1}{2} & 0 & 0 & \frac{1}{2a_{42}} & 0 & 0 \\ 0 & -\frac{a_{61}}{2(a_{21}a_{63}-a_{61})} & -\frac{a_{51}}{2(a_{53}a_{31}-a_{51}a_{33})} & 0 & \frac{a_{31}}{2(a_{53}a_{31}-a_{51}a_{33})} & \frac{a_{21}}{2(a_{21}a_{63}-a_{61})} \\ 0 & \frac{a_{63}}{2(a_{21}a_{63}-a_{61})} & -\frac{a_{53}}{2(a_{53}a_{31}-a_{51}a_{33})} & 0 & \frac{a_{33}}{2(a_{53}a_{31}-a_{51}a_{33})} & -\frac{1}{2(a_{21}a_{63}-a_{61})} \\ \frac{1}{2} & 0 & 0 & -\frac{1}{2a_{42}} & 0 & 0 \\ 0 & -\frac{a_{61}}{2(a_{21}a_{63}-a_{61})} & \frac{a_{51}}{2(a_{53}a_{31}-a_{51}a_{33})} & 0 & -\frac{a_{31}}{2(a_{53}a_{31}-a_{51}a_{33})} & \frac{a_{21}}{2(a_{21}a_{63}-a_{61})} \end{bmatrix}$$

2.7 SUMMARY

In this chapter, an efficient and analytical method is proposed to calculate the Fourier transformed displacements and stresses due to stationary harmonic loads, and the Fourier transformed steady state displacements and stresses due to harmonic loads moving uniformly along a line parallel to the ground surface. This is more efficient than previously used calculations of similar type because of the use of symmetry and reciprocity relationships. The source and observer may be located on the ground surface or at any depth in the ground. These formulae will lead to significant advances in the investigation of a variety of radiation, scattering and interaction problems associated with

stationary and moving disturbances in a layered ground, such as surface trains and underground trains. The reciprocity relations which are well known in the stationary case are extended to the moving case.

Chapter 3

A STUDY OF VIBRATION PROPAGATION IN THE GROUND MODEL

3.1 INTRODUCTION

It is well known that responses of a finite structure to an external load depend greatly on the free dynamics of the structure, i.e. its natural frequencies and mode shapes. Similarly, vibrations of a ground can also be interpreted by its free vibration characteristics, i.e., its dispersion curves and mode shapes of propagating wave modes of the ground. Several papers have been found dealing with the calculation of dispersion curves and mode shapes for a ground. Fu and Newlands [Fu 1946, Newlands 1952], by substituting for the displacements in Navier's elastodynamic equations with potential functions, and assuming harmonic waves with no transverse motion, sought a solution for the relevant boundary conditions, zero surface stresses, and continuity of stresses and displacements at the layer/half-space interface. This gave the dispersion equation as a determinant equated to zero. For a given frequency, this equation gives the corresponding propagating wave numbers. An alternative method of calculating the dispersion curves is due to the work of Wittrick and Williams [1971]. Their method allows the eigenvalue solution of the non-linear dynamic stiffness matrix for a layered ground, though, in order to achieve a given precision the layers should be divided into many sub-layers. Jones [1987] also used this method in his PhD thesis.

In this chapter, the equation for the dispersion curves is derived using the formulae developed in Chapter 2. The approach is straightforward. Attention is paid to the cut-on frequencies at which a new propagating mode appears. It is well known that for a structure of finite dimensions, there exist discrete natural frequencies. When a harmonic force excites the structure at one of these frequencies, the response of the structure will be infinite in the absence of damping. For a layered ground, the same phenomenon can be expected at the cut-on frequencies. For this reason, these cut-on frequencies may be also termed the natural frequencies of the ground. The displacement spectrum due to a moving harmonic load and the critical load speed are also discussed in this chapter.

3.2 DISPERSION CURVES OF A LAYERED GROUND

An undamped ground can sustain free propagating waves in which each particle of the ground vibrates harmonically at a single frequency. The wavenumbers of the free propagating waves depend on the frequency of vibration. These free propagating waves are termed *the propagating modes* (or simply *the modes*) *of the ground*. The propagating modes may be divided into two types: the P-SV modes (waves) and the SH modes (waves). For a P-SV mode, particles in the ground have displacement components not only in the vertical direction but also in the horizontal propagation direction while for a SH mode, the particles vibrate only in a direction parallel to the ground surface but perpendicular to the horizontal propagation direction. The P-SV modes and the SH modes in the ground can be uncoupled.

The dispersion curves, which are defined as wavenumbers of propagating modes (P-SV and SH modes) in the ground plotted against frequency, are helpful in the investigation of the mechanism of ground vibration. There are different methods to calculate the dispersion curves [Jones 1987]. The formulae developed in Chapter 2 may also be applied to produce the dispersion curves without any numerical difficulties. For a ground consisting of a number, n, of layers which overly a half-space (n+1th layer), the Fourier transformed displacement vector $\{\tilde{u}\}_{n+1,0}$ and the Fourier transformed stress vector $\{\tilde{\tau}\}_{n+1,0}$ on the top interface of the n+1th layer (i.e. the half-space) have the relationship (see equation (2.18))

$$\{\tilde{\tau}\}_{n+1,0} = [S][R]^{-1}\{\tilde{u}\}_{n+1,0} \tag{3.1}$$

When stationary harmonic loads are applied on the ground surface, i.e. $l_P = 1$, then from equations (2.19) and (2.20) yields $[T] = [F]$, and equation (2.21) becomes

$$\begin{Bmatrix} \{\tilde{u}\}_{n1} \\ \{\tilde{\tau}\}_{n1} \end{Bmatrix} = e^{\sum_{j=1}^{n}\alpha_{j1}h_j} \begin{bmatrix} [T]_{11} & [T]_{12} \\ [T]_{21} & [T]_{22} \end{bmatrix} \begin{Bmatrix} \{\tilde{u}\}_{10} \\ \{\tilde{\tau}\}_{10} \end{Bmatrix} \tag{3.2}$$

Since $\{\tilde{\tau}\}_{n1} = \{\tilde{\tau}\}_{n+1,0}, \{\tilde{u}\}_{n1} = \{\tilde{u}\}_{n+1,0}$, equations (3.1) and (3.2) give

$$([T]_{21} - [S][R]^{-1}[T]_{11})\{\tilde{u}\}_{10} = ([S][R]^{-1}[T]_{12} - [T]_{22})\{\tilde{\tau}\}_{10} \tag{3.3}$$

or,

$$([S][R]^{-1}[T]_{11}-[T]_{21})\{\tilde{u}\}_{10}=([S][R]^{-1}[T]_{12}-[T]_{22})\{\tilde{p}\} \tag{3.4}$$

where $\{\tilde{u}\}_{10}$ and $\{\tilde{\tau}\}_{10}$ are the Fourier transformed displacement vector and the Fourier transformed stress vector on the ground surface, and $\{\tilde{p}\}=-\{\tilde{\tau}\}_{10}$ is the Fourier transformed load vector applied on the ground surface. Putting $\{\tilde{p}\}=0$ in equation (3.4) results in the so-called free vibration equation of the ground

$$([S][R]^{-1}[T]_{11}-[T]_{21})\{\tilde{u}\}_{10}=0 \tag{3.5}$$

For non-zero solutions to exist, the determinant of the coefficient matrix of equation (3.5) must be equal to zero, i.e.

$$\det([S][R]^{-1}[T]_{11}-[T]_{21})=0 \tag{3.6}$$

For a given frequency f, the real values of β,γ satisfying equation (3.6), give the wave numbers of propagating wave modes at that frequency (the waves propagating in the x- and y-directions). Equation (3.6) is termed the dispersion equation of the ground.

Denoting the matrix $[S][R]^{-1}[T]_{11}-[T]_{21}$ by $[D(\beta,\gamma,\omega)]$ and $[S][R]^{-1}[T]_{12}-[T]_{22}$ by $[D'(\beta,\gamma,\omega)]$, it can be shown that (see equation (2.39))

$$[D(\beta,\gamma,\omega]=\begin{bmatrix}\sin\phi & \cos\phi & 0\\ -\cos\phi & \sin\phi & 0\\ 0 & 0 & 1\end{bmatrix}[D(0,\rho,\omega)]\begin{bmatrix}\sin\phi & -\cos\phi & 0\\ \cos\phi & \sin\phi & 0\\ 0 & 0 & 1\end{bmatrix} \tag{3.7}$$

$$[D'(\beta,\gamma,\omega]=\begin{bmatrix}\sin\phi & \cos\phi & 0\\ -\cos\phi & \sin\phi & 0\\ 0 & 0 & 1\end{bmatrix}[D'(0,\rho,\omega)]\begin{bmatrix}\sin\phi & -\cos\phi & 0\\ \cos\phi & \sin\phi & 0\\ 0 & 0 & 1\end{bmatrix} \tag{3.8}$$

where $\rho=\sqrt{\beta^2+\gamma^2}$, $\cos\phi=\beta/\rho, \sin\phi=\gamma/\rho$, and

$$[D(0,\rho,\omega)]=\begin{bmatrix}d_{11} & 0 & 0\\ 0 & d_{22} & d_{23}\\ 0 & d_{32} & d_{33}\end{bmatrix} \tag{3.9}$$

$$[D'(0,\rho,\omega)]=\begin{bmatrix} d'_{11} & 0 & 0 \\ 0 & d'_{22} & d'_{23} \\ 0 & d'_{32} & d'_{33} \end{bmatrix} \tag{3.10}$$

with d_{11}, d_{22} etc. being complex functions of ρ and ω.

From equations (3.7) and (3.9), the dispersion equation (3.6) gives,

$$d_{11} = 0 \tag{3.11}$$

or

$$d_{22}d_{33} - d_{23}d_{32} = 0 \tag{3.12}$$

For a given frequency *f*, equation (3.11) gives the wave numbers for SH modes and (3.12) gives those for P-SV modes.

3.2.1 THE SH MODES OF A GROUND CONSISTING OF A SINGLE LAYER ON A HOMOGENEOUS HALF-SPACE

For the study of ground vibration induced by traffic, the ground normally is modelled as consisting of only one layer of depth h_1 which rests on a homogeneous half-space. In this case, equation (3.11) can be written explicitly as

$$d_{11} = \mu_1\alpha_{12}(1-e^{-2\alpha_{12}h_1}) + \mu_2\alpha_{22}(1+e^{-2\alpha_{12}h_1}) = 0 \tag{3.13}$$

where, as defined in Chapter 2, μ_1, μ_2 are the shear moduli of the materials in the layer and in the half-space, respectively, and

$$\alpha_{j2} = \sqrt{\gamma^2 - \frac{\omega^2}{c_{j2}^2}} \qquad (j = 1,2) \tag{3.14}$$

where, c_{12}, c_{22} are the shear wave speeds in the layer and in the half-space. Without loss of generality, the symbol γ has been used instead of ρ. Equation (3.13) is the well-known equation for Love waves in a ground consisting of a single layer on a homogeneous half-space [Zhang 2000]. Love waves are special SH waves which propagate along the interface of two solids and decay quickly away from the interface.

Equation (3.13) can be rewritten as

$$\frac{\mu_2}{\mu_1}\frac{\alpha_{22}}{\alpha_{12}} = -(1-e^{-2\alpha_{12}h_1})/(1+e^{-2\alpha_{12}h_1}) \tag{3.15}$$

Assume $c_{22} > c_{12}$, i.e., the shear wave speed in the half-space is greater than that in the layer. Then when $\gamma^2 < \frac{\omega^2}{c_{22}^2} < \frac{\omega^2}{c_{12}^2}$, both α_{12} and α_{22} are purely imaginary numbers, as indicated by equation (3.14), and the left-hand side term of equation (3.15) is a real number, but the right-hand side term of equation (3.15) is a purely imaginary one (equal to $i\frac{\sin\theta}{1+\cos\theta}$, where $\theta = 2\sqrt{\frac{\omega^2}{c_{12}^2}-\gamma^2}h_1$). Thus, when $c_{22} > c_{12}$, all the real roots of equation (3.13) must satisfy $\gamma^2 \geq \frac{\omega^2}{c_{22}^2}$. On the other hand, if $\gamma^2 \geq \frac{\omega^2}{c_{12}^2} > \frac{\omega^2}{c_{22}^2}$, then both α_{12} and α_{22} are positive numbers, and equation (3.13) does not hold. Thus when $c_{22} > c_{12}$, all the real roots of equation (3.13) must satisfy $\frac{\omega^2}{c_{22}^2} \leq \gamma^2 < \frac{\omega^2}{c_{12}^2}$. In other words, when the shear wave speed in the layer is lower than that in the half-space, then for any given frequency, the phase speeds of the SH modes are greater than the shear wave speed in the layer but lower than or equal to that in the half-space.

Similarly it can be shown that when the shear wave speed in the layer is greater than that in the half-space, then there exist no SH propagating modes in the ground, i.e. $d_{11} \neq 0$.

Now for $c_{22} > c_{12}$, i.e., the shear wave speed in the half-space is greater than that in the layer, put $\gamma^2 = \frac{\omega^2}{c_{22}^2}$ in equation (3.13) to solve this equation for ω. Since $\alpha_{22} = 0$, equation (3.13) becomes

$$\mu_1\alpha_{12}(1-e^{-2\alpha_{12}h_1}) = 0$$

which, since $c_{22} > c_{12}$, $\alpha_{12} \neq 0$, will be satisfied if and only if

$$-2\alpha_{12}h_1 = -2\sqrt{\frac{\omega^2}{c_{22}^2}-\frac{\omega^2}{c_{12}^2}}h_1 = i2k\pi$$

where k is an integer. This equation gives

$$\omega_0 = \frac{c_{22}c_{12}}{\sqrt{c_{22}^2-c_{12}^2}}\frac{k\pi}{h_1} \quad (k = 1,2,\cdots) \tag{3.16}$$

which are termed *the SH cut-on frequencies* since, at these frequencies, the number of roots of equation (3.13) changes (see the examples below). The point $(\frac{\omega_0}{2\pi}, \frac{\omega_0}{c_{22}})$ on the frequency-wavenumber plane is termed the *SH bifurcation point.*

It can be shown that, for $c_{22} > c_{12}$, at the bifurcation points, the SH dispersion curves have the same slope as that of the pure shear wave in the half-space.

For later use, the partial derivative of d_{11} with respect to γ is calculated as follows

$$\frac{\partial d_{11}}{\partial \gamma} = [\mu_1 + (-\mu_1 + 2\mu_1 h_1 \alpha_{12} - 2\mu_2 h_1 \alpha_{22}) e^{-2\alpha_{12} h_1}] \frac{\partial \alpha_{12}}{\partial \gamma} + \mu_2 (1 + e^{-2\alpha_{12} h_1}) \frac{\partial \alpha_{22}}{\partial \gamma}$$

At the bifurcation points, $\alpha_{22} = 0, -2\alpha_{12} h_1 = i2k\pi$, where $k = 1,2,\cdots$, thus

$$\left.\frac{\partial d_{11}}{\partial \gamma}\right|_{(\omega_0, \frac{\omega_0}{c_{22}})} = -i2k\pi\mu_1 \left.\frac{\gamma}{\sqrt{\gamma^2 - \frac{\omega^2}{c_{12}^2}}}\right|_{\substack{\omega=\omega_0 \\ \gamma=\omega_0/c_{22}}} + 2\mu_2 \left.\frac{\gamma}{\sqrt{\gamma^2 - \frac{\omega^2}{c_{22}^2}}}\right|_{\substack{\omega=\omega_0 \\ \gamma=\omega_0/c_{22}}}$$

i.e.

$$\left.\frac{\partial \operatorname{Re}(d_{11})}{\partial \gamma}\right|_{(\omega_0, \frac{\omega_0}{c_{22}})} = \begin{cases} +\infty, & \gamma \to (\omega_0 / c_{22})^+ \\ -2k\pi\mu_1 \dfrac{c_{12}}{\sqrt{c_{22}^2 - c_{12}^2}}, & \gamma \to (\omega_0 / c_{22})^- \end{cases} \tag{3.17}$$

$$\left.\frac{\partial \operatorname{Im}(d_{11})}{\partial \gamma}\right|_{(\omega_0, \frac{\omega_0}{c_{22}})} = \begin{cases} 0, & \gamma \to (\omega_0 / c_{22})^+ \\ -\infty, & \gamma \to (\omega_0 / c_{22})^- \end{cases} \tag{3.18}$$

Equations (3.17) and (3.18) show that, at the bifurcation points, although d_{11} is continuous but it is not smooth.

3.2.2 THE P-SV MODES OF A GROUND CONSISTING OF A SINGLE LAYER ON A HOMOGENEOUS HALF-SPACE

When $c_{22} > c_{12}$, for the P-SV mode dispersion equation (3.12), there are also cut-on frequencies (also denoted by ω_0) and bifurcation points $(\frac{\omega_0}{2\pi}, \frac{\omega_0}{c_{22}})$, as seen in Figure 3.1 below. However, it is difficult to derive a formula like equation (3.16) to calculate these cut-on frequencies.

It is worthwhile pointing out that, if the layer rests on a rigid foundation, then the dispersion equation (3.6) becomes

$$\det([T]_{11}) = 0 \tag{3.19}$$

from which the dispersion equation for both SH modes and P-SV modes can be derived as

$$1 + e^{-2\alpha_{1j}h_1} = 0 \ (j = 1, 2) \tag{3.20}$$

By setting $\gamma = 0$ in equations (3.19) and (3.20), they can be solved for ω as

$$\omega_0 = \frac{(2k-1)\pi}{2h_1} c_{1j} \ (k = 1,2,3,\cdots) \tag{3.21}$$

where $j = 1$ gives the P-SV cut-on frequencies, $j = 2$ the SH cut-on frequencies and k is a positive integer. From equations (3.21) and (3.16), it can be seen that equation (3.21) cannot be derived from equation (3.16) by letting $c_{22} \to \infty$. In fact, putting $c_{22} \to \infty$ in equation (3.16) results in $\omega_0 \to c_{12}\frac{k\pi}{h_1}$, which are the shear vibration natural frequencies of a layer having free top and bottom surfaces.

3.2.3 EXAMPLES

Dispersion curves are calculated for two ground structures. These two grounds have the same substratum on which one has a stiffer layer and the other has a softer layer. In each case the layer has a thickness of 2 m. The parameters for these two ground structures are listed in Tables 1.6 and 1.7, respectively. The loss factor of the ground material will not be used here in the calculation of the dispersion curves.

3.2.3.1 *FOR THE STIFFER GROUND*

Figure 3.1 shows the P-SV dispersion curves for the stiffer ground. It can be seen that, at about 22 Hz, a second P-SV mode appears and a third and a fourth appear at 47 Hz and 83 Hz. These frequencies are, as defined above, cut-on frequencies of the ground. Also shown in the figure are the Rayleigh wave dispersion line of the upper layer material and the shear wave dispersion line of the half-space. It can be seen that at high frequencies, say higher than 47 Hz, the wave number of the first mode (which has the largest wavenumber) is very close to that of the Rayleigh wave of the upper layer.

However, at low frequencies, say below 20 Hz, the wavenumber of the first mode is much less than that of the Rayleigh wave of the layer but close to that of the shear wave of the half-space.

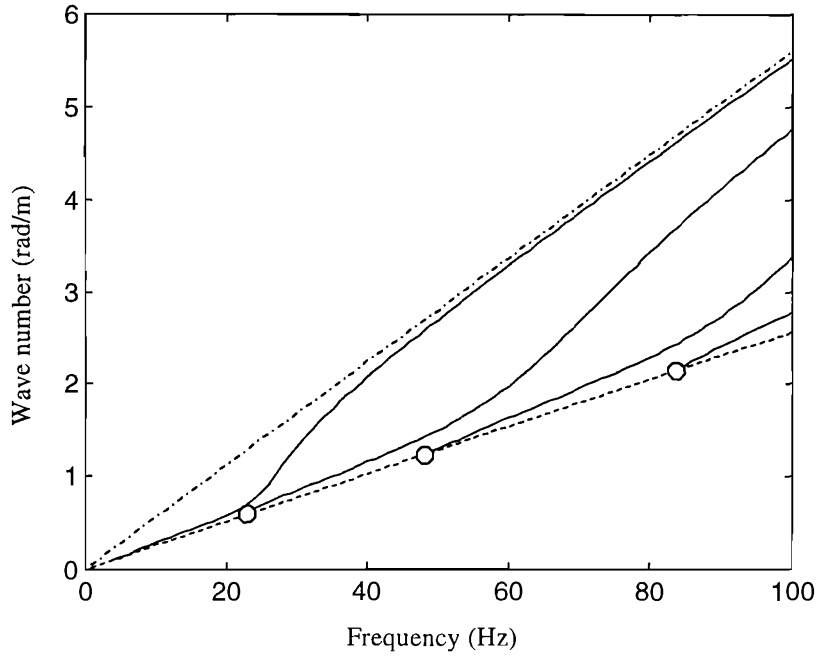

Figure 3.1. Dispersion curves for the stiffer ground. ——, P-SV dispersion curves; – – –, shear wave of the underlying half-space; – · –, Rayleigh wave of the upper layer; o, cut-on points.

Figures 3.2 to 3.4 show the function $\Delta(0,\gamma,\omega) = d_{22}d_{33} - d_{23}d_{32}$ plotted against γ (see equation (3.12)) for $\omega_0 = 2\pi f_0$, where $f_0 = 22$ Hz, 47 Hz and 83 Hz, respectively. It can be seen that at the bifurcation points $(\frac{\omega_0}{2\pi}, \frac{\omega_0}{c_{22}})$ (i.e. (22, 0.56) for Figure 3.2, (47, 1.21) for Figure 3.3, and (83, 2.13) for Figure 3.4), as a function of γ, $\Delta(0,\gamma,\omega)$ is continuous but its left derivative and right derivative are different, i.e.

$$\left.\frac{\partial\Delta(0,\gamma,\omega_0)}{\partial\gamma}\right|_{\gamma=\gamma_0^-} \neq \left.\frac{\partial\Delta(0,\gamma,\omega_0)}{\partial\gamma}\right|_{\gamma=\gamma_0^+} \tag{3.22}$$

where $\gamma_0 = \frac{\omega_0}{c_{22}}$. It can also be seen that when $\gamma \geq \gamma_0$, the imaginary part of $\Delta(0,\gamma,\omega)$ is zero. At other root points such that $\Delta = 0$, $\Delta(0,\gamma,\omega)$ is smooth and $\frac{\partial\Delta}{\partial\gamma} \neq 0$. Inequality (3.22) will be used to prove that the ground resonates at the cut-on frequencies.

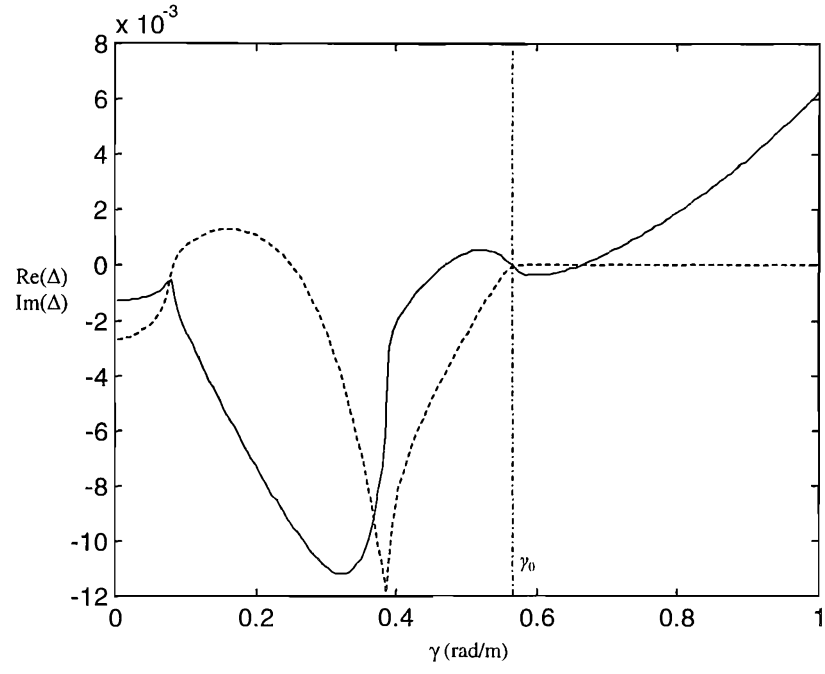

Figure 3.2. $\Delta(0,\gamma,\omega_0)$ plotted against γ for the stiffer ground with $f_0 = 22$ Hz. ——, real part; – – –, imaginary part.

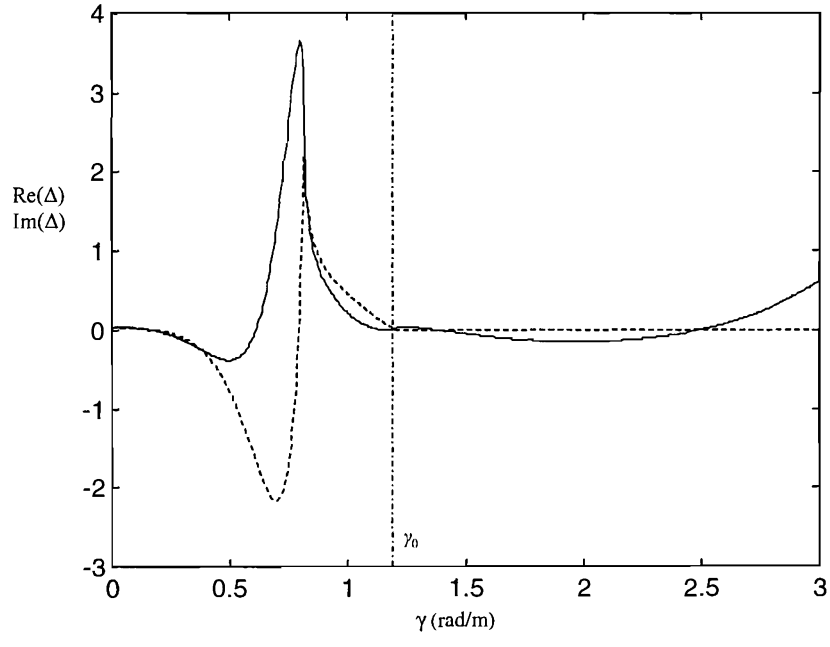

Figure 3.3. $\Delta(0,\gamma,\omega_0)$ plotted against γ for the stiffer ground with $f_0 = 47$ Hz. ——, real part; – – –, imaginary part.

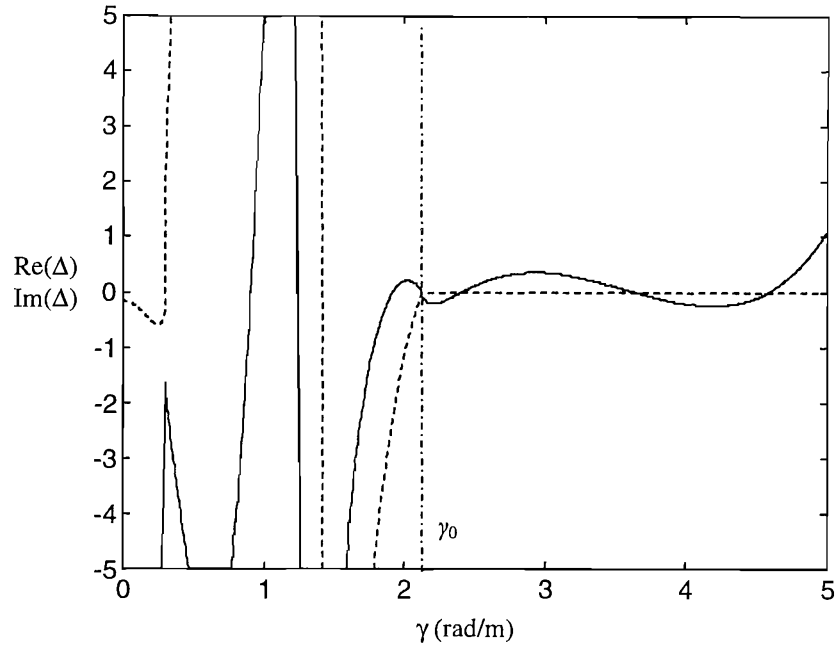

Figure 3.4. $\Delta(0,\gamma,\omega_0)$ plotted against γ for the stiffer ground with f_0 = 83 Hz. ——, real part; – – –, imaginary part.

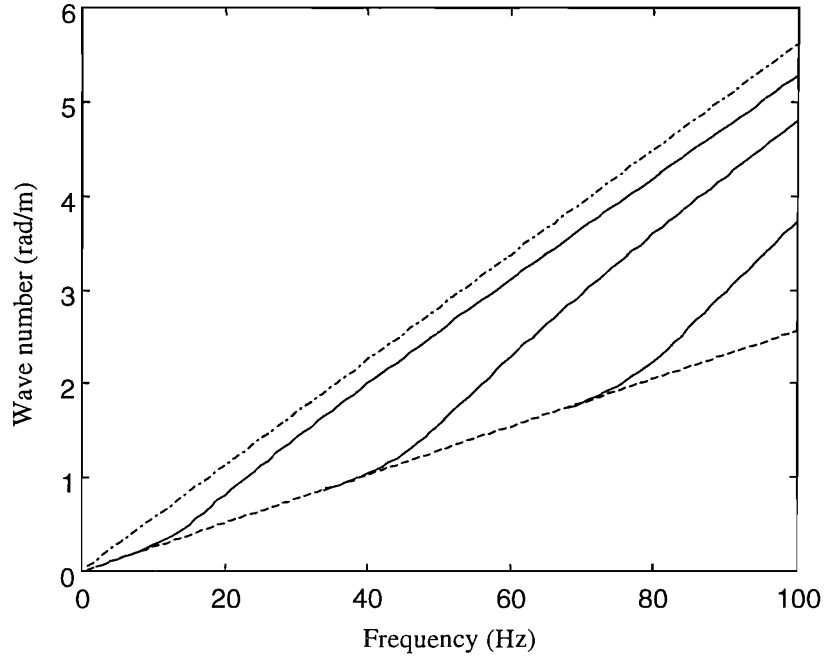

Figure 3.5. Dispersion curves for the stiffer ground. ——, SH dispersion curves; – – –, shear wave of the half-space; – · –, Rayleigh wave of the upper layer.

The dispersion curves for the SH modes of the stiffer ground are shown in Figure 3.5 which indicates two cut-on frequencies below 100 Hz, i.e., 34 Hz and 68 Hz. These two cut-on frequencies may be evaluated by equation (3.16). It is illustrated in this

figure that, at the bifurcation points, the dispersion curves have the same slope as the shear wave line in the half-space.

3.2.3.2 *FOR THE SOFTER GROUND*

Figure 3.6 shows the P-SV dispersion curves for the softer ground. It can be seen that there are five cut-on frequencies below 100 Hz, i.e. 13 Hz, 27 Hz, 51 Hz, 71 Hz and 93 Hz. It can be seen that below the first cut-on frequency, the wavenumber of the first mode is close to the shear wavenumber of the underlying half-space while above the second cut-on frequency, the wavenumber of the first mode approaches the Rayleigh wavenumber of the upper layer.

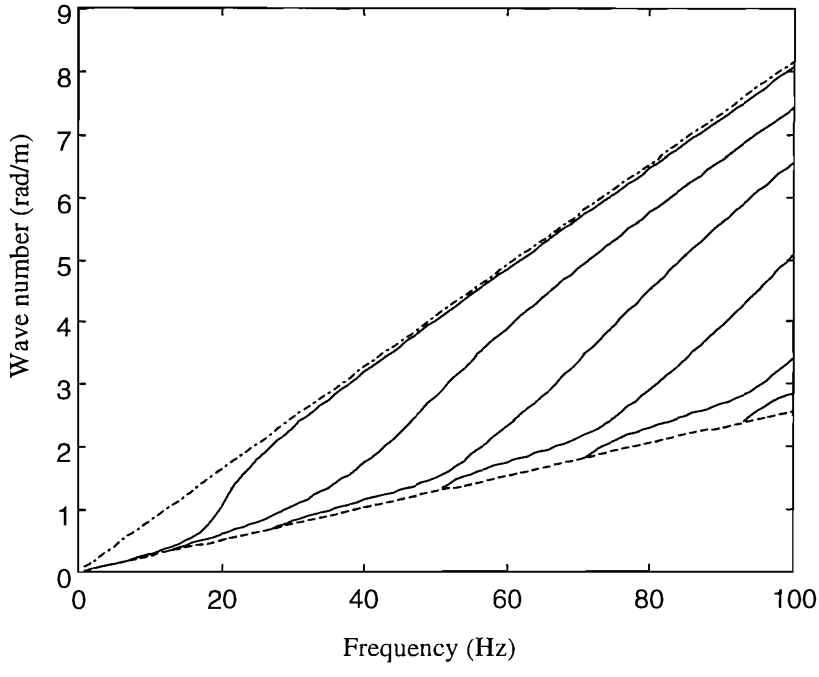

Figure 3.6. Dispersion curves for the softer ground. ——, P-SV dispersion curve; – – –, shear wave of the half-space; – · –, Rayleigh wave of the upper layer.

Figures 3.7 to 3.11 show the diagrams of function $\Delta(0,\gamma,\omega) = d_{22}d_{33} - d_{23}d_{32}$ plotted against γ for $\omega = 2\pi f_0$, where f_0=13 Hz, 27 Hz, 51 Hz, 71 Hz and 93 Hz. At the bifurcation points $(\frac{\omega_0}{2\pi}, \frac{\omega_0}{c_{22}})$, the inequality (3.22) also holds.

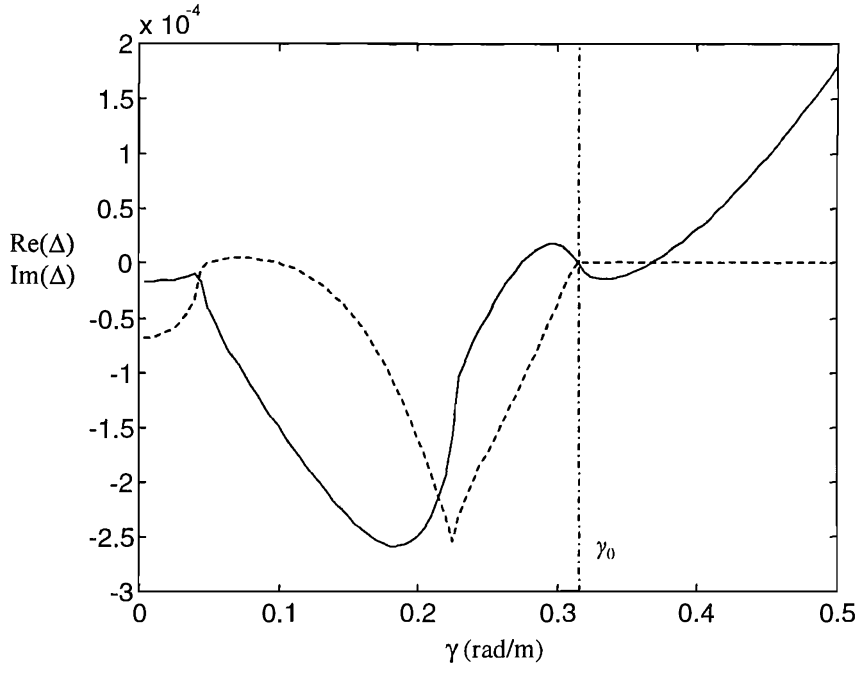

Figure 3.7. $\Delta(0,\gamma,\omega_0)$ plotted against γ for the softer ground with f_0 = 13 Hz. ——, real part; – – –, imaginary.

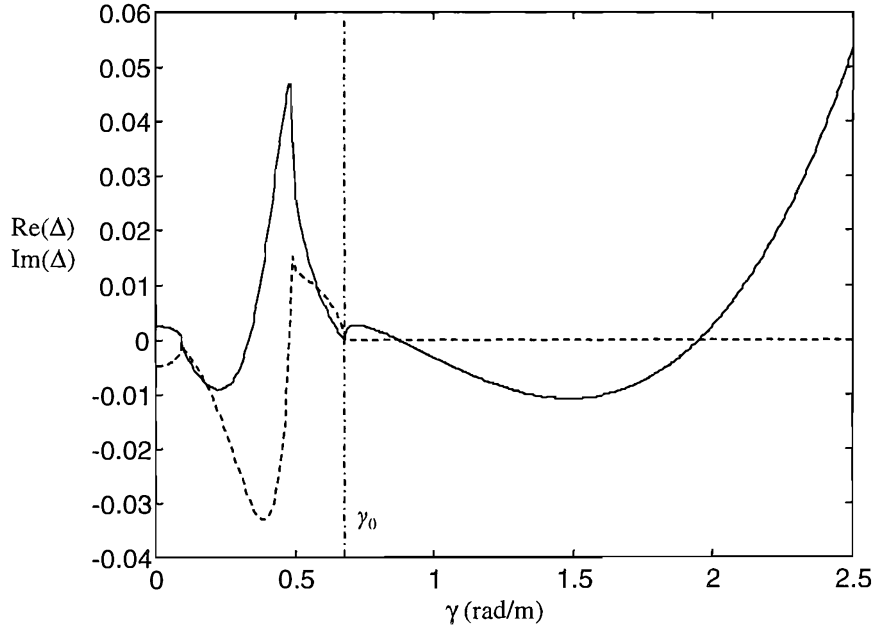

Figure 3.8. $\Delta(0,\gamma,\omega_0)$ plotted against γ for the softer ground with f_0 = 27 Hz. ——, real part; – – –, imaginary part.

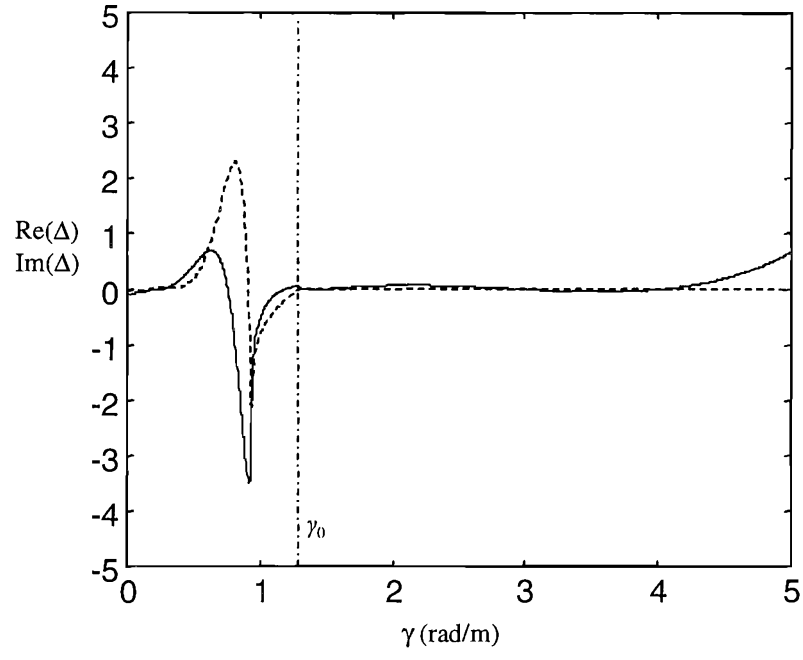

Figure 3.9. $\Delta(0,\gamma,\omega_0)$ plotted against γ for the softer ground with $f_0 = 51$ Hz. ——, real part; – – –, imaginary part.

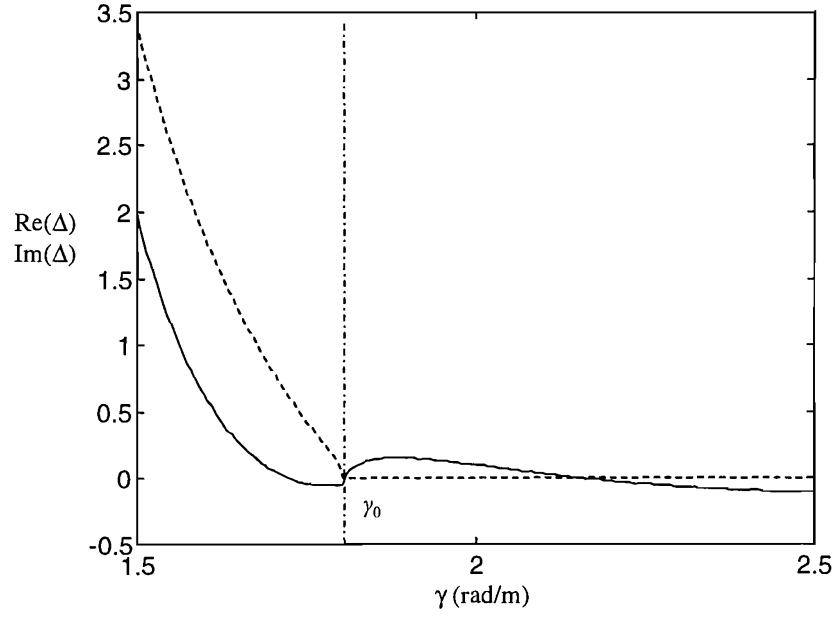

Figure 3.10 $\Delta(0,\gamma,\omega_0)$ plotted against γ for the softer ground with $f_0 = 71$ Hz. ——, real part; – – –, imaginary part.

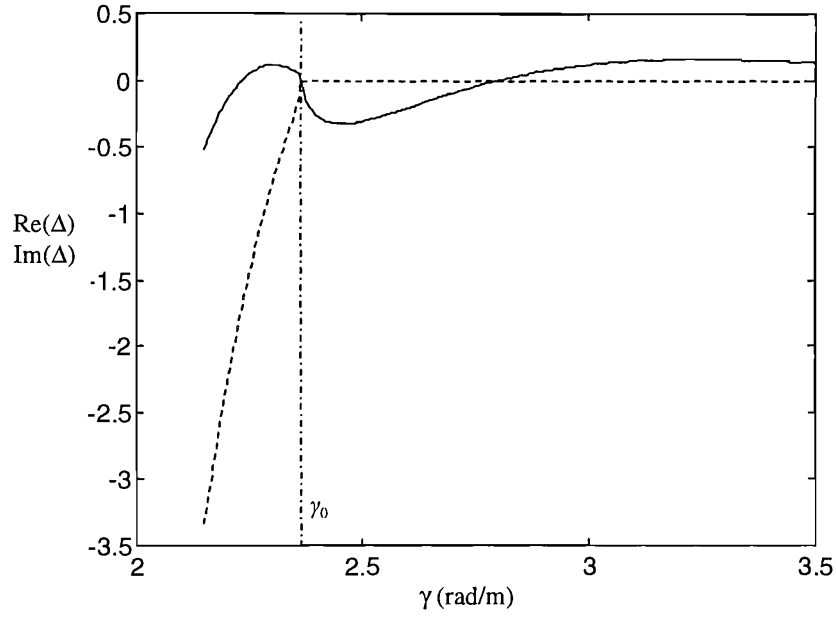

Figure 3.11. $\Delta(0,\gamma,\omega_0)$ plotted against γ for the softer ground with $f_0 = 93$ Hz. ——, real part; – – –, imaginary part.

The dispersion curves for the SH modes of the softer ground are shown in Figure 3.12 which indicates four cut-on frequencies below 100 Hz, i.e., 21.5 Hz, 43 Hz, 64.5 Hz and 86 Hz. These cut-on frequencies can also be evaluated using equation (3.16).

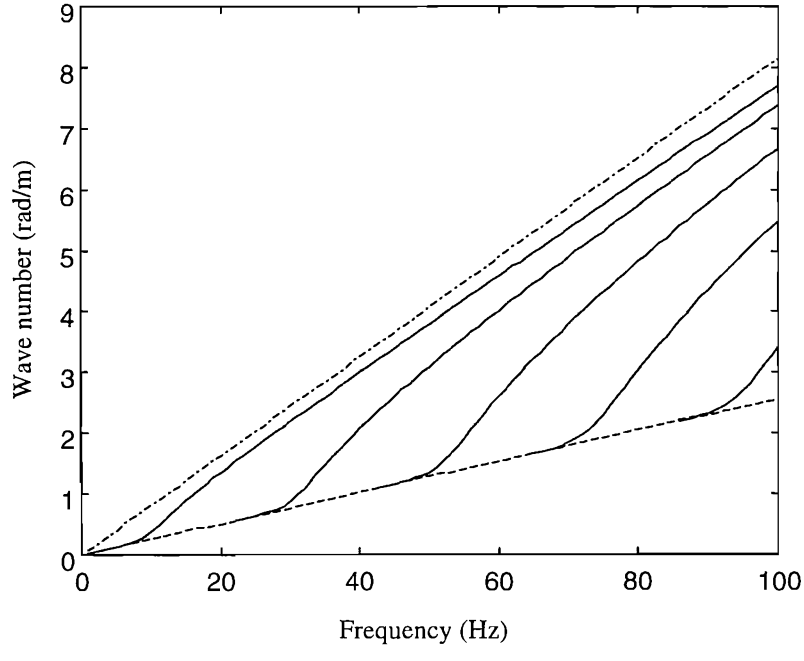

Figure 3.12. Dispersion curves for the softer ground. ——, SH dispersion curve; – – –, shear wave of the half-space; – · –, Rayleigh wave of the upper layer.

3.3 MODE SHAPES OF PROPAGATING WAVE MODES

The non-zero solutions to equation (3.5), i.e. the Fourier transformed ground surface displacements of propagating wave modes, can be categorised into two types, i.e., the SH modes and P-SV modes. From equation (3.9), for the SH modes, the solutions to equation (3.5) with $\beta = 0$ (i.e., waves with infinite wavelength in the x-direction and propagating only in the y-and z-directions) can be chosen as

$$\{\tilde{u}\}_{10} = \begin{Bmatrix} \tilde{u}_{10} \\ 0 \\ 0 \end{Bmatrix} = \begin{Bmatrix} 1 \\ 0 \\ 0 \end{Bmatrix} \tag{3.23}$$

and for the P-SV modes, as

$$\{\tilde{u}\}_{10} = \begin{Bmatrix} 0 \\ \tilde{v}_{10} \\ \tilde{w}_{10} \end{Bmatrix} = \begin{Bmatrix} 0 \\ -\dfrac{d_{23}}{d_{22}} \\ 1 \end{Bmatrix} \tag{3.24}$$

Equations (3.23) and (3.24) give the displacements of a propagating mode on the ground surface. The displacement vector of a mode within the ground can be readily calculated starting from $\{\tilde{u}\}_{10}$ by using equation (3.2). For a ground consisting of one layer which rests on a homogeneous half-space, the displacements of a mode in the layer and in the half-space can be evaluated using the following formulae:

In the layer

$$\begin{Bmatrix} \tilde{u}(z) \\ \tilde{v}(z) \\ \tilde{w}(z) \end{Bmatrix} = e^{\alpha_{11} z} [T]_{11}^{z} \{\tilde{u}\}_{10} \qquad (0 \le z \le h_1) \tag{3.25}$$

where $[T]_{11}^{z}$ is identical to $[T]_{11}$ if h_1 in $[T]_{11}$ is replaced by z.

In the half-space

$$\begin{Bmatrix} \tilde{u}(z) \\ \tilde{v}(z) \\ \tilde{w}(z) \end{Bmatrix} = e^{\alpha_{11} h_1} [R] \begin{bmatrix} e^{-\alpha_{21}(z-h_1)} & 0 & 0 \\ 0 & e^{-\alpha_{22}(z-h_1)} & 0 \\ 0 & 0 & e^{-\alpha_{22}(z-h_1)} \end{bmatrix} [R]^{-1} [T]_{11} \{\tilde{u}\}_{10} \quad (z \ge h_1)$$

where $\alpha_{2j} = \sqrt{\gamma^2 - \frac{\omega^2}{c_{2j}^2}}$ $(j = 1,2)$, c_{21} and c_{22} are compression and shear-wave speeds of the half-space. After expansion of the matrices in the equation above, it becomes

$$\begin{Bmatrix} \tilde{u}(z) \\ \tilde{v}(z) \\ \tilde{w}(z) \end{Bmatrix}$$

$$= \frac{1}{\det[R]} \frac{c_{21}^2}{\omega^2} \begin{bmatrix} (\alpha_{21}\alpha_{22} - \gamma^2) e^{-\alpha_{22}(z-h_1)} & 0 & 0 \\ 0 & (\alpha_{21}\alpha_{22} e^{-\alpha_{22}(z-h_1)} - \gamma^2 e^{-\alpha_{21}(z-h_1)}) & i\gamma\alpha_{22}(e^{-\alpha_{22}(z-h_1)} - e^{-\alpha_{21}(z-h_1)}) \\ 0 & i\gamma\alpha_{21}(e^{-\alpha_{22}(z-h_1)} - e^{-\alpha_{21}(z-h_1)}) & (\alpha_{21}\alpha_{22} e^{-\alpha_{21}(z-h_1)} - \gamma^2 e^{-\alpha_{22}(z-h_1)}) \end{bmatrix} \{\tilde{u}\}_{11}$$

$$(z \geq h_1) \qquad (3.26)$$

where $\{\tilde{u}\}_{11}$ is the displacement vector on the interface of the layer and the half-space.

3.3.1 FOR SH MODES

For the SH modes, $\tilde{v}(z) = \tilde{w}(z) = 0$, and

$$\tilde{u}(z) = \begin{cases} \frac{1}{2}(e^{\alpha_{12}z} + e^{-\alpha_{12}z})\tilde{u}_{10}, (0 \leq z \leq h_1) \\ \frac{1}{2}(e^{\alpha_{12}h_1} + e^{-\alpha_{12}h_1}) e^{-\alpha_{22}(z-h_1)} \tilde{u}_{10}, (z \geq h_1) \end{cases} \qquad (3.27)$$

Since the SH wavenumbers always make α_{12} purely imaginary and α_{22} positive or zero, $\tilde{u}(z)$ varies harmonically with z in the layer and decays exponentially (for $\alpha_{22} > 0$) with z in the half-space. At the bifurcation points, $\alpha_{22} = 0, \alpha_{12}h_1 = -ik\pi$, where k is a positive integer, thus

$$\tilde{u}(z) = (-1)^k \tilde{u}_{10}, (z \geq h_1) \qquad (3.28)$$

i.e., the displacement in the half-space does not vary with depth (a pure shear wave), and in the layer, the displacement is symmetric (for even k) or anti-symmetric (for odd k) about its middle plane.

3.3.2 FOR P-SV MODES

For the P-SV modes, $\tilde{u}(z) = 0$. At the bifurcation points, $\alpha_{22} = 0, \alpha_{21} > 0$, from equation (3.26) it follows that in the half-space, when $z \to \infty, \tilde{v} \to 0$ but $\tilde{w} \to$ a constant, i.e., the wave degenerates into a pure vertical shear wave.

3.3.3 EXAMPLE

The P-SV mode shapes are calculated for the stiffer ground. Figures 3.13 to 3.16 show the mode shapes of the first mode at 10 Hz ($\gamma = 0.28$ rad/m), 23 Hz ($\gamma = 0.70$ rad/m), 40 Hz ($\gamma = 2.08$ rad/m) and 60 Hz ($\gamma = 3.28$ rad/m) (vertical component is plotted in solid line while horizontal component in dashed line). The calculation shows that the vertical component is a real number while the horizontal component is a purely imaginary number. This means that there is a phase difference of 90 degrees between these two components. In other words, any particle moves along an elliptic trajectory. It can be seen from these figures that, at low frequencies, waves are developed over a large depth in the ground. However, at high frequencies, waves have the form of surface waves which propagate along the ground surface and the layer/half-space interface and decay quickly with distance away from the surface and the interface.

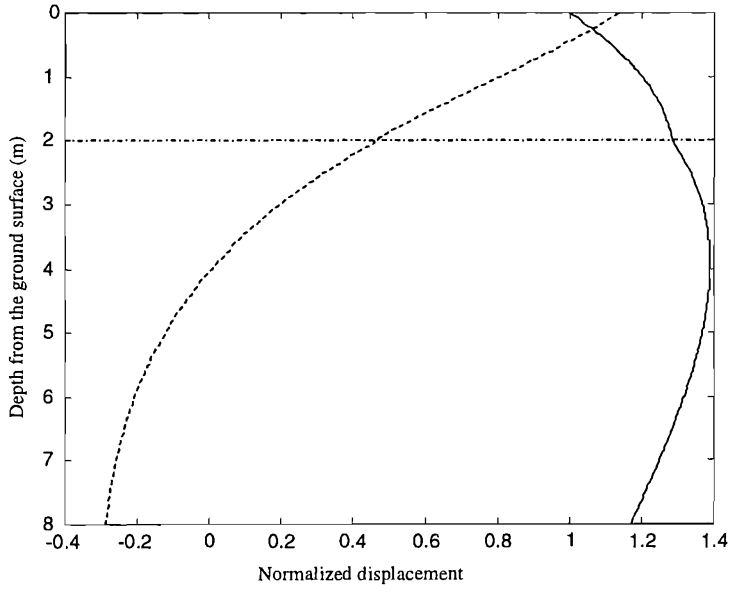

Figure 3.13. The P-SV mode shape of the first mode at 10 Hz (wavenumber = 0.28 rad/m) for the stiffer ground. ——, vertical component; – – –, horizontal component; – · –, layer interface.

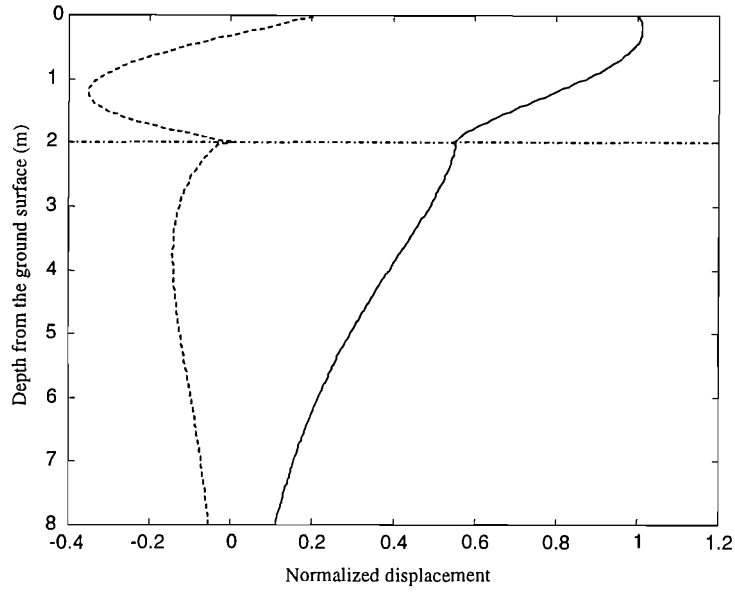

Figure 3.14. The P-SV mode shape of the first mode at 23 Hz (wavenumber = 0.70 rad/m) for the stiffer ground. ——, vertical component; – – –, horizontal component; – · –, layer interface.

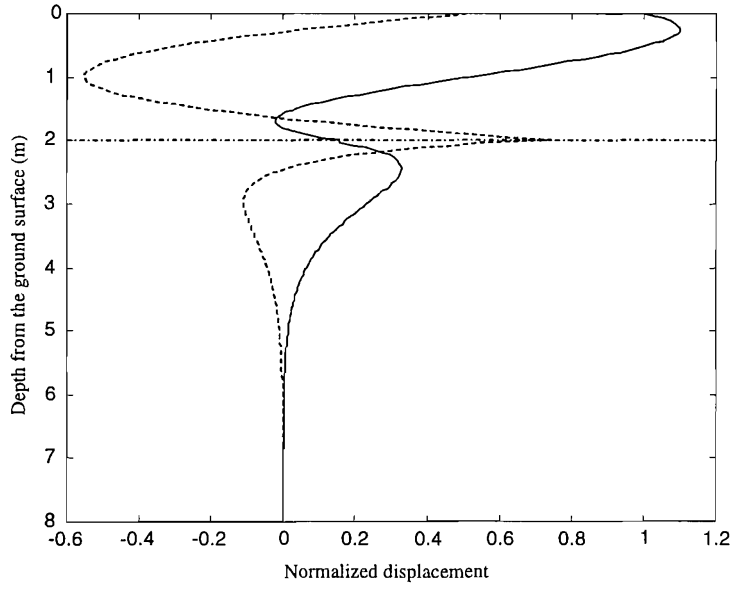

Figure 3.15. The P-SV mode shape of the first mode at 40 Hz (wavenumber = 2.08 rad/m) for the stiffer ground. ——, vertical component; – – –, horizontal component; – · –, layer interface.

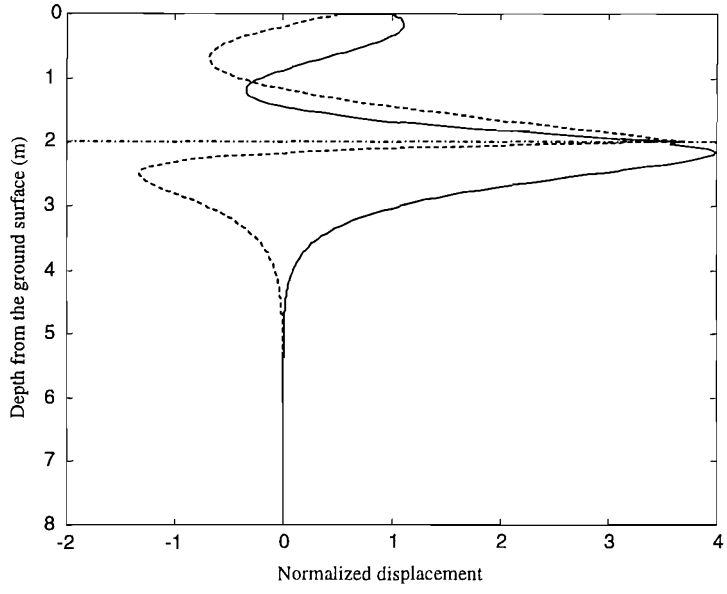

Figure 3.16. The P-SV mode shape of the first mode at 60 Hz (wavenumber = 3.28 rad/m) for the stiffer ground. ——, vertical component; – – –, horizontal component; – · –, layer interface.

3.4 RESONANCE OF A LAYERED GROUND AT ITS CUT-ON FREQUENCIES

3.4.1 MATHEMATICAL ILLUSTRATION

For a unit stationary load of frequency ω acting vertically on the ground surface, the vertical displacement at the loading point on the ground surface is determined by

$$w_{10}(0,0) = \frac{1}{4\pi^2} \int_{-\infty}^{\infty} \int_{-\infty}^{\infty} \tilde{w}_{10}(\beta,\gamma,\omega) d\beta d\gamma \tag{3.29}$$

where $\tilde{w}_{10}(\beta,\gamma,\omega) = \tilde{Q}_{33}(\beta,\gamma,\omega)$ (see Section 2.3) refers to the Fourier transformed vertical displacements of the ground surface at frequency ω. Using a polar co-ordinate system $\beta = \rho\cos\phi, \gamma = \rho\sin\phi$, and noticing the properties of $\tilde{Q}_{33}(\beta,\gamma,\omega) = \tilde{Q}_{33}(0,\rho,\omega)$ (see Section 2.4), equation (3.29) becomes

$$w_{10}(0,0) = \frac{1}{4\pi^2} \int_0^{2\pi} \int_0^{\infty} \tilde{Q}_{33}(0,\rho,\omega) \rho d\rho d\phi = \frac{1}{2\pi} \int_0^{\infty} \tilde{Q}_{33}(0,\gamma,\omega) \gamma d\gamma \tag{3.30}$$

If neglecting the damping in the ground, then there exists $\gamma = \gamma(\omega)$ such that $\tilde{Q}_{33}(0,\gamma(\omega),\omega) = \infty$. The function $\gamma = \gamma(\omega)$ defines the P-SV dispersion curves of the ground. $\tilde{Q}_{33}(0,\gamma,\omega)$ may be written, according to the Gramer's rule, as

$$\tilde{Q}_{33}(0,\gamma,\omega) = \frac{\Delta'(0,\gamma,\omega)}{\Delta(0,\gamma,\omega)} \tag{3.31}$$

where $\Delta(0,\gamma,\omega) = d_{22}d_{33} - d_{23}d_{32}$ (see equation (3.12)), and when $\gamma = \gamma(\omega)$,

$\Delta'(0,\gamma,\omega) \neq 0, \Delta(0,\gamma,\omega) = 0$. According to Theorem 2 in Appendix 2, if there exists a real isolated root γ_0 of the equation

$$\Delta(0,\gamma,\omega) = 0 \tag{3.32}$$

such that

$$\left.\frac{\partial\Delta}{\partial\gamma}\right|_{\gamma=\gamma_0^-} \neq \left.\frac{\partial\Delta}{\partial\gamma}\right|_{\gamma=\gamma_0^+} \tag{3.33}$$

then the integral of (3.30) diverges, meaning that the system is resonant at frequency ω. It has been shown in Section 3.2 that, at the bifurcation points, the inequality (3.33) holds. (The corresponding frequencies are the natural frequencies of the ground as defined above, and the wavenumbers are the shear wavenumbers of the underlying half-space at these frequencies). Thus, at these frequencies, the ground will be resonant. In the presence of damping, the response will have finite peaks at these frequencies.

Now suppose that a unit stationary harmonic load acts in the *y*-direction on the ground surface. Thus the lateral response of the loading point is determined by

$$v_{10}(0,0) = \frac{1}{4\pi^2}\int_{-\infty}^{\infty}\int_{-\infty}^{\infty}\tilde{v}_{10}(\beta,\gamma,\omega)d\beta d\gamma \tag{3.34}$$

where $\tilde{v}_{10}(\beta,\gamma,\omega) = \tilde{Q}_{22}(\beta,\gamma,\omega)$ refers to the Fourier transformed lateral displacement of the ground surface at frequency ω. By letting $\beta = \rho\cos\phi$ and $\gamma = \rho\sin\phi$, and noting the relation

$$\tilde{Q}_{22}(\beta,\gamma,\omega) = \tilde{Q}_{11}(0,\rho,\omega)\cos^2\phi + \tilde{Q}_{22}(0,\rho,\omega)\sin^2\phi$$

(see Section 2.4), equation (3.34) becomes

$$\begin{aligned} \upsilon_{10}(0,0) &= \frac{1}{4\pi^2}\int_0^{2\pi}\int_0^{\infty}[\tilde{Q}_{11}(0,\gamma,\omega)\cos^2\phi + \tilde{Q}_{22}(0,\gamma,\omega)\sin^2\phi]\gamma d\gamma d\phi \\ &= \frac{1}{4\pi}[\int_0^{\infty}\tilde{Q}_{11}(0,\gamma,\omega)\gamma d\gamma + \int_0^{\infty}\tilde{Q}_{22}(0,\gamma,\omega)\gamma d\gamma] \end{aligned} \tag{3.35}$$

where $\tilde{Q}_{11}(0,\gamma,\omega)$ is associated with the SH modes only while $\tilde{Q}_{22}(0,\gamma,\omega)$ with the P-SV modes. In other words, both the SH modes and the P-SV modes contribute to $\upsilon_{10}(0,0)$.

3.4.2 EXAMPLES

As an example, the lateral response of the ground surface to a lateral rectangular (2.7 m × 2.7 m) harmonic load at a range of frequencies is calculated. The total magnitude of the load is 1 N. The parameters for the softer ground, which are listed in Table 1.7, are used in the calculation. Figure 3.17 shows the lateral displacement magnitude at the centre of the loading area. It can be seen from this figure that there are five peaks corresponding to the P-SV natural frequencies of the ground (13 Hz, 27 Hz, 51 Hz, 71 Hz and 93 Hz). The SH natural frequencies (21.5 Hz, 43 Hz, 64.5 Hz and 86 Hz) seem to be less important than the P-SV natural frequencies for the lateral response. The lateral displacement at the centre of the loading area may be decomposed into two parts. The first part is contributed by the wave propagating along the *y*-axis (corresponding to the second integral in equation (3.35)). This wave is a P-SV wave, since displacements on the *y*-axis have two components, one in the *y*-direction and the other in the *z*-direction. The second part is provided by the wave propagating along the *x*-axis (related to the first integral in equation (3.35)). This wave is a SH wave, since displacements on the *x*-axis are in the *y*-direction.

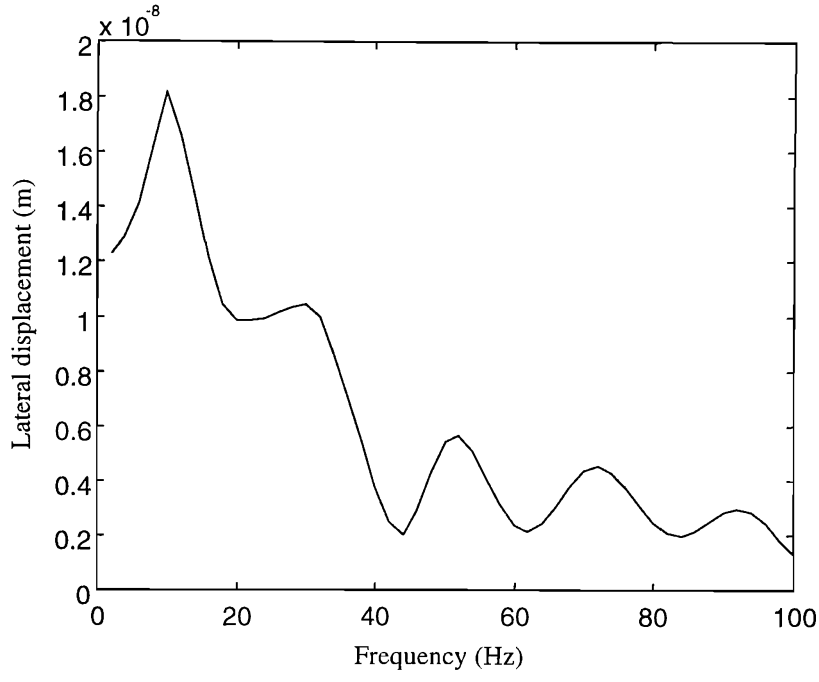

Figure 3.17. The lateral displacements at the centre of the loading area due to a rectangular (2.7 × 2.7 m) harmonic load acting laterally on the softer ground surface.

The resonance of a ground at some frequencies is due to the layered structure of the ground. The resonant behaviour of a layered ground has been verified by measurement, see [Auersch 1994, and Jones 1996]. In principle, since it is possible to measure the receptance of a ground, the natural frequencies of the ground can be determined from the peaks of the receptance curve. However, high damping and propagation of the energy away from the measurement point make the identification of many of the peaks not always possible.

3.4.3 COMPARISON BETWEEN A LAYERED GROUND AND A HOMOGENEOUS HALF-SPACE

For a homogeneous half-space, there exists no such resonance phenomenon as in a layered ground. Figure 3.18 shows the vertical displacement of the centre of the loading area of a vertical rectangular harmonic load (2.7 m × 2.7 m, the total magnitude of the load is 1 N), for a range of frequencies. Three grounds are considered in this figure: the stiffer layered ground, a homogeneous half-space made of the layer material and one of the underlying half-space material. For the stiffer layered ground, the parameters of which are tabulated in Table 1.6, a peak at around 25 Hz is clearly seen. A dip at about 77 Hz is due to the loading dimensions of the square loading patch. The dashed line is for the homogeneous half-space made of the layer material. It can be seen for high

frequencies (such that the wavelengths are less than the depth of the layer) that the responses of these two grounds are close to each other. The response of the half-space of the underlying material is quite different.

Comparison between the stiffer ground and the underlying half-space is also made for vertical displacements along the y-axis on the ground surfaces. As shown in Figure 3.19, for low frequencies and for points away from the load (such that both the distance of the observer and the wavelength are greater than the depth of the layer and the dimension of the load), the presence of the layer makes little difference.

Figure 3.20 shows a comparison between the stiffer ground and the homogeneous half-space made of the layer material at 60 Hz. To allow the wave propagation to be seen clearly, the real part of the complex displacement amplitude is shown in the figure. It can be seen that for high frequencies and for points near the load (such that both the distance of the observer and the wavelength are shorter than the depth of the layer and the dimension of the load), the layered ground behaves as a homogeneous half-space of the layer material. However, away from the loading point, the wave is modified by the layered structure of the ground. It can be seen in Figure 3.20 that the wave on the surface of the layered ground consists mainly of two components: the first has a wavelength of approximately 2 m and corresponds to the first P-SV mode of the stiffer layered ground, which is very close to the Rayleigh wave of the layer at the same frequency, as shown in Figure 3.1; the second has a wavelength of about 15 m which is much greater than the shear wavelength of the underlying half-space (according to Table 1.6, the shear wavelength of the underlying half-space at 60 Hz is about 4.1 m), and this component is not shown in the dispersion curve diagram in Figure 3.1 (see Section 6.3.1). Close to the loading area, the first component is dominant; but far away from the load, the second component becomes dominant.

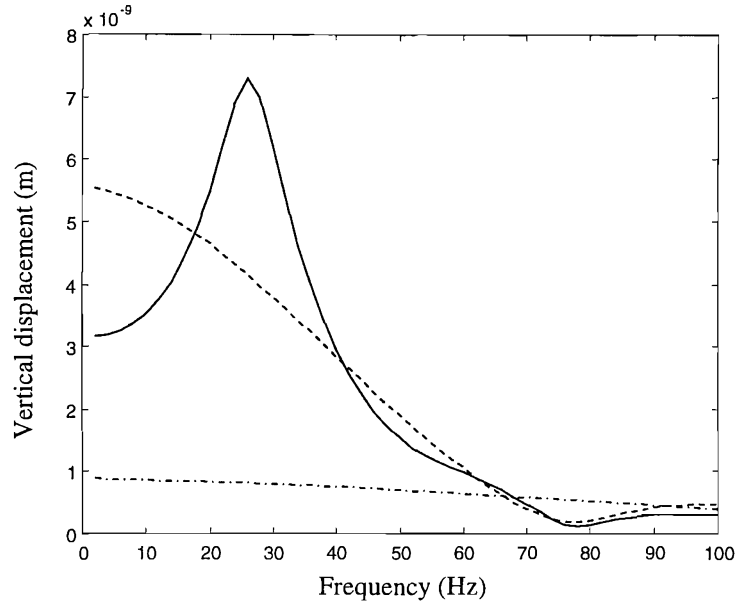

Figure 3.18. Vertical displacement at the centre of the loading area for different frequencies. — , for the stiffer layered ground; – – –, for a homogeneous half-space of the upper layer material; – · –, for the underlying homogeneous half-space of the layered ground.

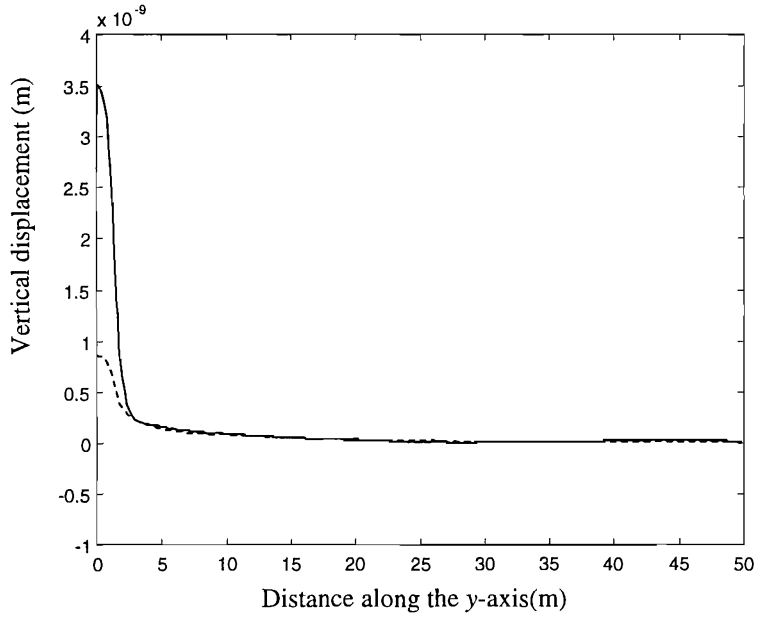

Figure 3.19. Vertical displacement along the y-axis on the ground surface at frequency 10 Hz. — —, for the stiffer layered ground; – – –, for the underlying homogeneous half-space of the layered ground.

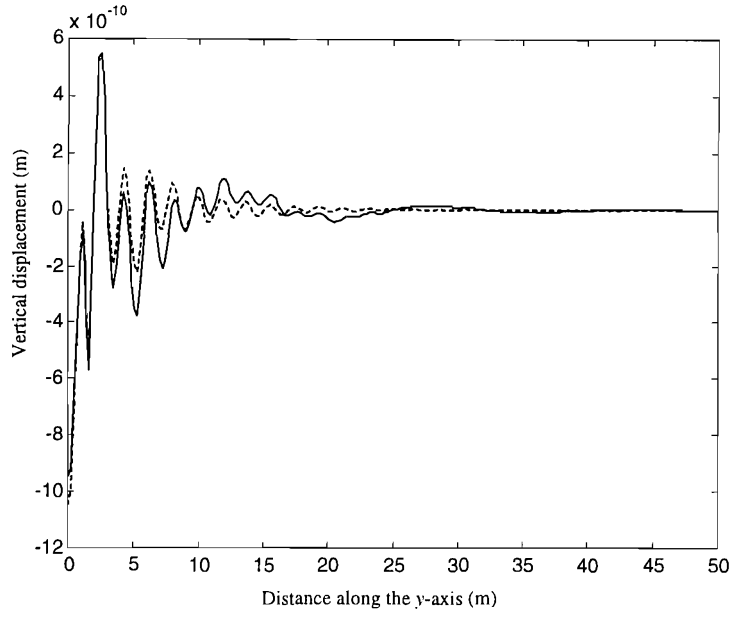

Figure 3.20. Vertical displacement along the y-axis on the ground surface at frequency 60 Hz. — —, for the stiffer layered ground; – – –, for the homogeneous half-space of the upper layer material.

3.5 DISPLACEMENT SPECTRA OF THE GROUND SURFACE DUE TO A MOVING HARMONIC LOAD

For a fixed-point load of finite frequency Ω, the propagating modes of the ground excited by the load are simply the modes existing at that frequency as indicated by the dispersion curves. For a moving load, modes are excited via the velocity of the load according to the Doppler effect. From [Sheng, Jones and Petyt 1999 (b), or see Chapter 5], the modes that are excited are determined by the intersections of lines

$$\beta = |(\Omega - 2\pi f)|/c \tag{3.36}$$

and the dispersion curves, where c is the load speed (here the modulus is used to make the line indicate the excitation of both the directions of the wave propagation in the ground with respect to the direction of movement of the load). The straight lines determined by equation (3.36) are termed *the load speed lines*. In the absence of damping, at the frequencies corresponding to these intersections, the displacement spectrum will be infinite. In fact, the spectrum of the vertical displacement of point (x, y) on the ground surface at frequency f due to a unit moving harmonic load of frequency Ω which acts vertically on the ground surface, is given by (see Chapter 5)

$$S_w(x, y, f) = \frac{1}{c} e^{i\beta x} \left(\frac{1}{2\pi} \int_{-\infty}^{\infty} \tilde{w}_1(\beta, \gamma, 0) e^{i\gamma y} d\gamma\right)$$

where $\beta = (\Omega - 2\pi f)/c$. By letting $x = 0, y = 0$, and noting

$$\tilde{w}_{10}(\beta,\gamma,2\pi f) = \tilde{Q}_{33}(\beta,\gamma,2\pi f) = \tilde{Q}_{33}(0,\rho,2\pi f) = \frac{\Delta'(0,\rho,2\pi f)}{\Delta(0,\rho,2\pi f)}$$

is an even function of γ, where $\rho = \sqrt{\beta^2 + \gamma^2}$, yields

$$S_w(0,0,f) = \frac{1}{\pi c}\int_0^\infty \frac{\Delta'(0,\rho,2\pi f)}{\Delta(0,\rho,2\pi f)} d\gamma \tag{3.37}$$

Perform the following operations,

$$\frac{\partial\Delta}{\partial\gamma} = \frac{\partial\Delta}{\partial\rho}\frac{\partial\rho}{\partial\gamma} = \frac{\partial\Delta}{\partial\rho}\frac{\gamma}{\rho} \tag{3.38}$$

$$\frac{\partial^2\Delta}{\partial\gamma^2} = \frac{\partial^2\Delta}{\partial\rho^2}\frac{\gamma^2}{\rho^2} + \frac{\partial\Delta}{\partial\rho}\frac{1}{\rho} - \frac{\partial\Delta}{\partial\rho}\frac{\gamma^2}{\rho^3} \tag{3.39}$$

At frequency f, such that $\beta = (\Omega - 2\pi f)/c$ does not equal any of the wavenumbers of the propagating modes at that frequency, then if $\Delta(0,\rho,2\pi f) = 0$ has a real root γ^*, γ^* must be different from zero (otherwise $\Delta(0,\beta,2\pi f) = 0$, i.e., β is the wavenumber of a propagating mode). In this case, if (f,ρ^*) does not coincide with any of the bifurcation points, where $\rho^* = \sqrt{\beta^2 + \gamma^{*2}}$, then $\left.\frac{\partial\Delta}{\partial\rho}\right|_{\rho=\rho^*}$ exists and $\neq 0$. According to equation (3.38), $\left.\frac{\partial\Delta}{\partial\gamma}\right|_{\gamma=\gamma^*} \neq 0$. Thus the integral (3.37) converges, implying that the amplitude is finite (see Appendix 2). However, if (f,ρ^*) coincides one of the bifurcation points, which implies $f = f_0$, where f_0 is a natural frequency of the ground, and

$$\beta = |\Omega - 2\pi f_0|/c < \frac{2\pi f_0}{c_{22}} \tag{3.40}$$

then $\left.\frac{\partial\Delta}{\partial\gamma}\right|_{\gamma=\gamma^{*-}} \neq \left.\frac{\partial\Delta}{\partial\gamma}\right|_{\gamma=\gamma^{*+}}$, thus the integral (3.37) diverges and the amplitude is infinite.

Additionally, when β equals one of the wavenumbers of the propagating modes, then the equation $\Delta(0,\rho,2\pi f) = 0$ at least has a root $\gamma = \gamma^* = 0$, and for this root,

equations (3.38) and (3.39) show that $\frac{\partial \Delta}{\partial \gamma}\Big|_{\gamma=0} = 0, \frac{\partial^2 \Delta}{\partial \gamma^2}\Big|_{\gamma=0} \neq 0$. Thus the integral in equation (3.37) diverges according to Theorem 2 in Appendix 2.

The discussion above shows that, in the absence of damping in the ground, the displacement spectrum $S_w(0,0,f)$ will be infinite at the frequencies corresponding to the intersections of the dispersion curves and the load speed lines. When damping is taken into account, the spectrum will have peaks at these frequencies, as indicated in Figures 3.21 and Figure 3.23. Figure 3.21 shows the amplitude of $S_w(0,0,f)$ due to a unit harmonic load of 40 Hz which moves along the x-axis over the stiffer ground surface, while Figure 3.23 shows the amplitude of $S_w(0,0,f)$ due to a unit harmonic load of 30 Hz moving along the x-axis over the softer ground surface. The intersections of the dispersion curves and the load speed lines given by equation (3.36) for these two grounds are shown in Figures 3.22 and 3.24, respectively. The correspondence between the spectrum peaks and the intersections can be clearly seen by comparing Figures 3.21 with 3.22 and Figures 3.23 with 3.24. Figures 3.21 and 3.23 show that the response to a moving harmonic load contains a wide range of frequency components, however, there is a dominating component frequency which is different from the load frequency due to the Doppler effect.

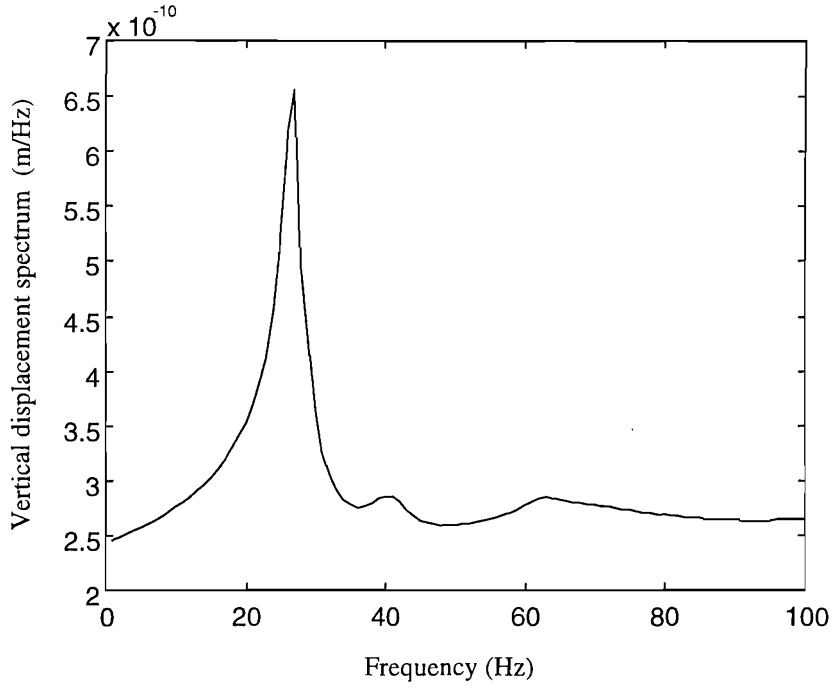

Figure 3.21. Vertical displacement spectrum at $y = 0$ m due to a unit vertical harmonic load of 40 Hz which moves along the x-axis at 83.3 m/s over the stiffer ground surface.

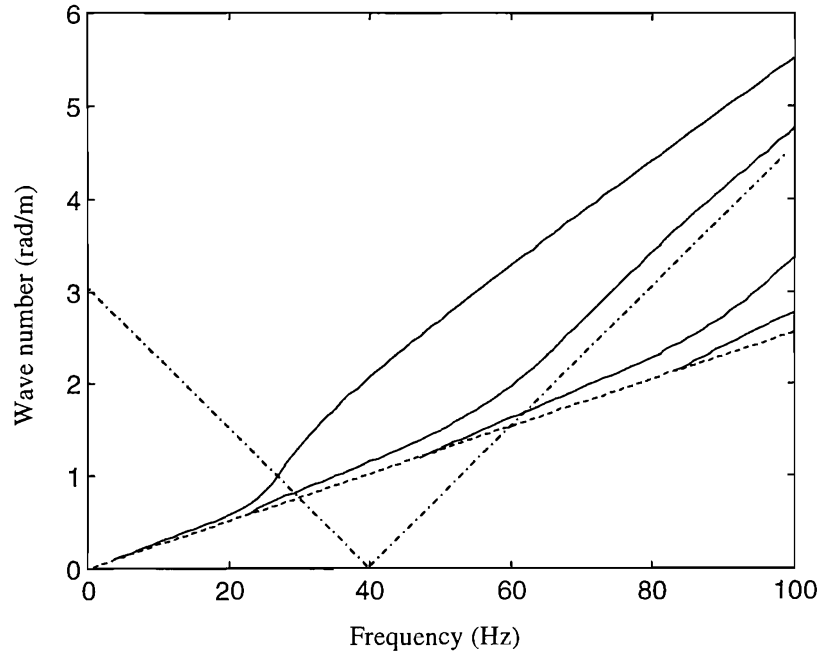

Figure 3.22. P-SV dispersion curves of the stiffer ground and load speed lines. ——, dispersion curves; – – –, load speed lines for a load of 40 Hz moving at 83.3 m/s.

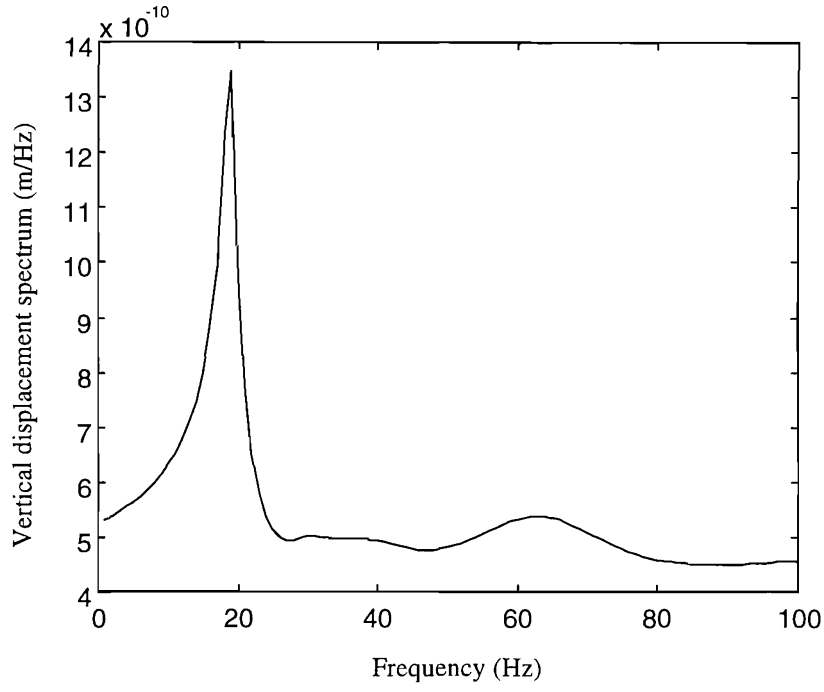

Figure 3.23. Vertical displacement spectrum at $y = 0$ m due to a unit vertical harmonic load of 30 Hz which moves along the x-axis at speed 83.3 m/s over the softer ground surface.

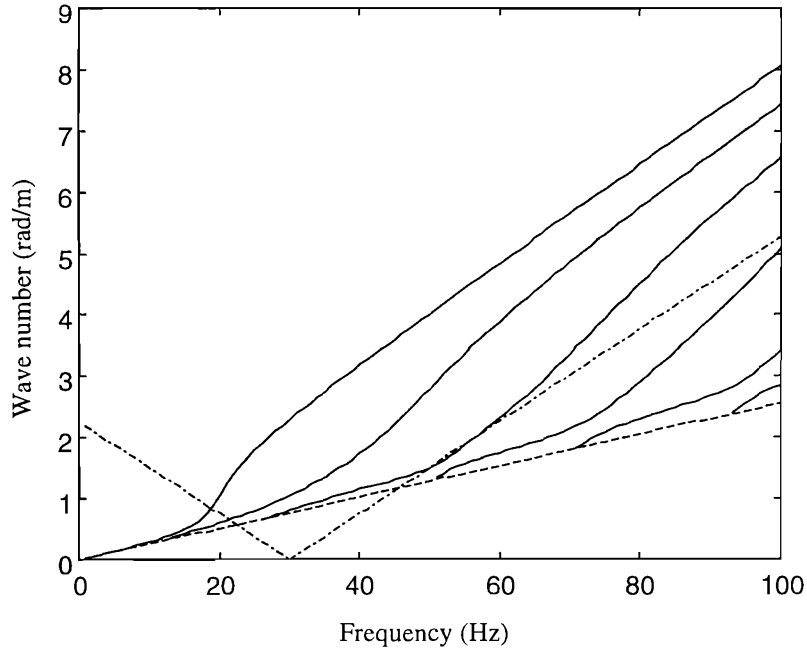

Figure 3.24. P-SV dispersion curves of the softer ground and load speed lines. ——, dispersion curves; – – –, load speed lines for a load of 30 Hz moving at 83.3 m/s.

3.6 CRITICAL LOAD SPEEDS OF THE GROUND

The response of a ground to a moving harmonic load depends on, amongst other things, the load speed. Dieterman and Metrikine [1997(b)] used a model of a point

harmonic load moving along an elastic layer resting on a rigid foundation to study the existence of critical speeds in the ballast layer. A critical speed is defined as that at which, in the absence of material damping, the steady-state amplitude of the layer vibration is infinite. It can be shown, by applying Theorem 1 in Appendix 2 that, the resonance occurs when the speed of the load is equal to the group velocity of the wave generated. Graphically, the resonance takes place when the load speed line is tangential to one of the dispersion curves. As has been indicated in Figures 3.1 and 3.6, the dispersion curve of the first mode approaches the Rayleigh wave dispersion line of the upper layer. Thus for a constant load, the critical load speed is identical to the Rayleigh wave speed in the upper layer. In the example results that follow, both the load and displacement act in the vertical direction.

Figure 3.25 shows the maximum amplitude of displacement along the x-axis on the softer ground surface and the amplitude of displacement of the loading point on the ground surface due to a unit vertical constant point load moving along the x-axis at different speeds. The peak in this figure occurs at 77 m/s, i.e., equal to the Rayleigh wave speed of the upper layer material.

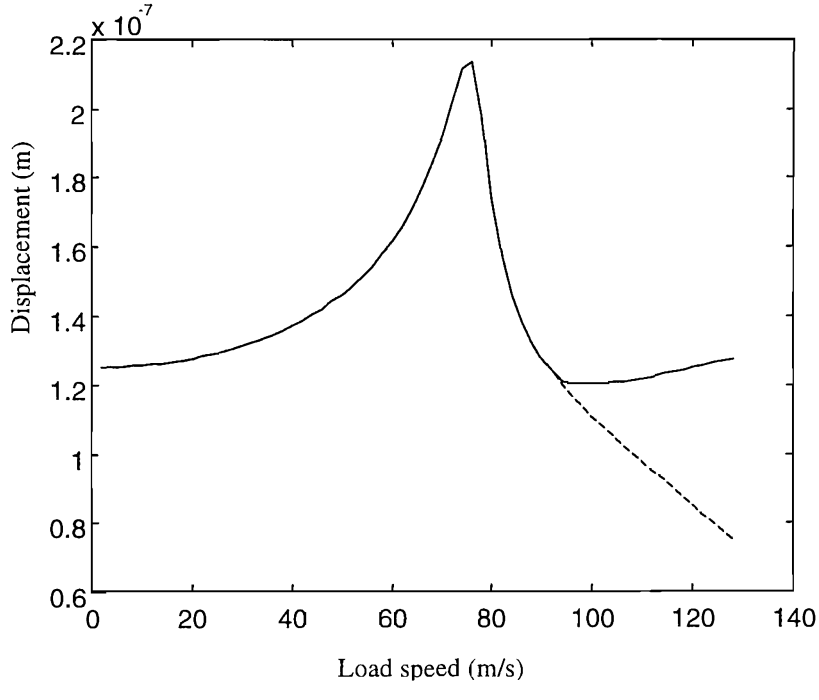

Figure 3.25. Maximum amplitude of displacement (——) along the x-axis on the softer ground surface and the amplitude of displacement (– – –) of the loading point on the ground surface due to a unit vertical constant point load moving along the x-axis at different speeds.

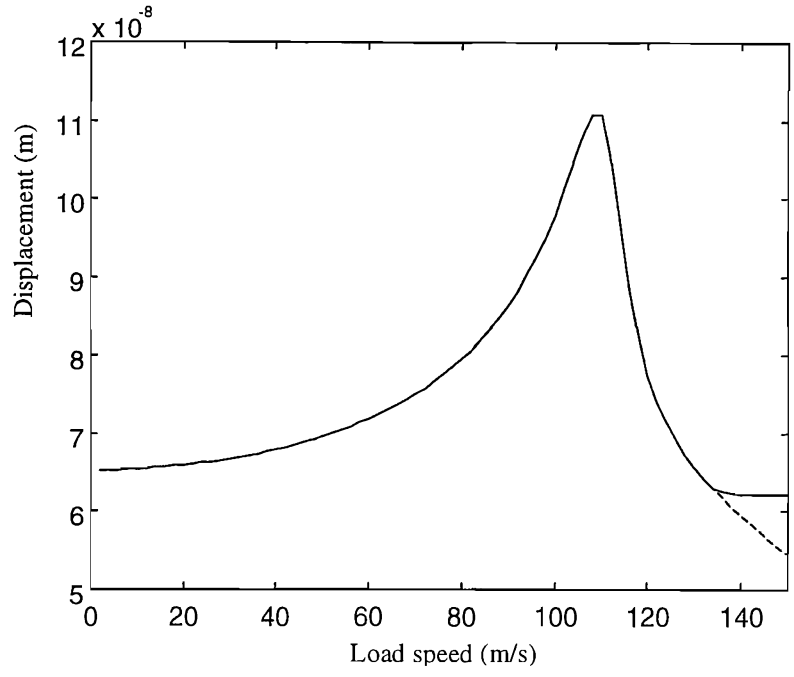

Figure 3.26. Maximum amplitude of displacement (——) along the x-axis on the stiffer ground surface and the amplitude of displacement (– – –) of the loading point on the ground surface due to a unit vertical constant point load moving along the x-axis at different speeds.

For the stiffer ground, results are presented in Figure 3.26. This figure also indicates the critical load speed is equal to the Rayleigh wave speed of the upper material, 112 m/s.

Figures 3.25 and 3.26 also show that, beyond a certain speed, the maximum displacement does not occur at the loading point but at some place behind the load.

3.7 SUMMARY

This chapter is devoted to the study of vibration propagation in a free ground. The ground considered consists of a single layer resting on a homogeneous half-space, and the shear wave speed in the layer is lower than that in the underlying half-space. By plotting the dispersion curves, it is found that there are cut-on (natural) frequencies at which a new propagating wave mode appears. For very low frequencies, the dispersion curve of the first model approaches the shear wave of the underlying half-space while for high frequencies it approaches the Rayleigh wave of the upper layer. The layered ground will be resonant at its cut-on frequencies. For some frequencies, there is a mode the wave speed of which is greater than that of the shear wave speed in the underlying half-space.

Under the action of a surface harmonic load, this type of wave may propagate for long distances over the ground surface and is dominant over other wave modes. This mode has a complex wavnumber with a small imaginary part and therefore is not shown in the dispersion diagram consisting of only real wavenumbers. For low frequencies and far away from a surface harmonic load (such that both the distance of the observer and the wavelength are greater than the depth of the layer and the dimensions of the load), the responses are mainly determined by the underlying half-space. For high frequencies and close to the load (such that both the distance of the observer and the wavelength are shorter than the depth of the layer), the layered ground behaves as a homogeneous half-space of the layer material. The displacement spectrum due to a moving harmonic load has peaks at the frequencies corresponding to the intersections of the dispersion curves and the load speed lines. For a constant load, the critical load speed is identical to the Rayleigh wave speed of the upper layer.

Chapter 4

STEADY STATE RESPONSES OF A RAILWAY TRACK ON A WINKLER FOUNDATION TO A MOVING HARMONIC LOAD

4.1 INTRODUCTION

The model of an infinite beam resting on a Winkler foundation, i.e. a continuous layer of springs, has been used to investigate the dynamics of a railway track. In 1959, Mathews [1958, 1959] presented a study on the steady-state vibrations of a beam on a Winkler foundation induced by a uniformly moving harmonic load. In his work, by employing the viscous damping model, Mathews sought the solution using an analytical approach. The example calculations revealed some dynamic features of the beam under the action of a moving load although those calculations were performed only for a constant load.

It was realised that a single beam on a Winkler foundation does not represent a railway track properly, due to the mass and elasticity of the sleepers and the ballast/embankment of the track. Thus a multiple beam track model has been suggested. It has further been recognized that, at middle and low frequencies, a Winkler foundation would not represent the ground properly [Knothe and Wu 1999]. However in this chapter, an analysis is made for the multiple beam track model on a Winkler foundation rather than on a ground in order to explore the dynamic features of a track. It will be shown that, under some assumptions, the analytical approach used by Mathews can also be used to find solutions for a track including sleepers and ballast/embankment. First in Section 4.2, the track is modelled as a multiple beam system, then the differential equation of motion of the system is derived and the steady state solutions are sought in the wavenumber domain. Then an inverse Fourier transform is performed to convert the steady state responses of the track from the wavenumber domain into the spatial domain. It is shown in Section 4.3, when the viscous damping model is used, that the inverse Fourier transform may be carried out analytically while for the hysteretic damping model a numerical approach (e.g. FFT) has to be used. Section 4.3 also presents several example calculations using the analytical approach.

With the help of the dispersion curves, some features of wave propagation in the track are explored. Recalculation is made in Section 4.4 using the FFT for the results presented in Section 4.3, showing that a good accuracy may be achieved by the FFT method. The comparison between the viscous damping model and the hysteretic damping model is given in Section 4.5, indicating that if the viscous damping is equivalent to the hysteretic damping at the frequency of the dominating component in the wave, then both damping models produce almost the same result. In Section 4.6, receptances are computed for both the multiple beam track model and an equivalent beam track model. Finally in Section 4.7, some conclusions are summarised.

4.2 DIFFERENTIAL EQUATION OF MOTION OF A TRACK AND ITS SOLUTION

A diagram is shown in Figure 4.1. The railway track is aligned in the x-direction. For the frequency range of interest, the rails and the sleepers are modelled as Euler beams. The mass per unit length of track of the rail beam and its bending stiffness are denoted by m_R and EI, respectively. The mass of the sleeper 'beam' per unit length of track is m_S, and no bending stiffness is introduced for the beam. The railpads are modelled as a continuously distributed complex spring stiffness, denoted by k_P, where

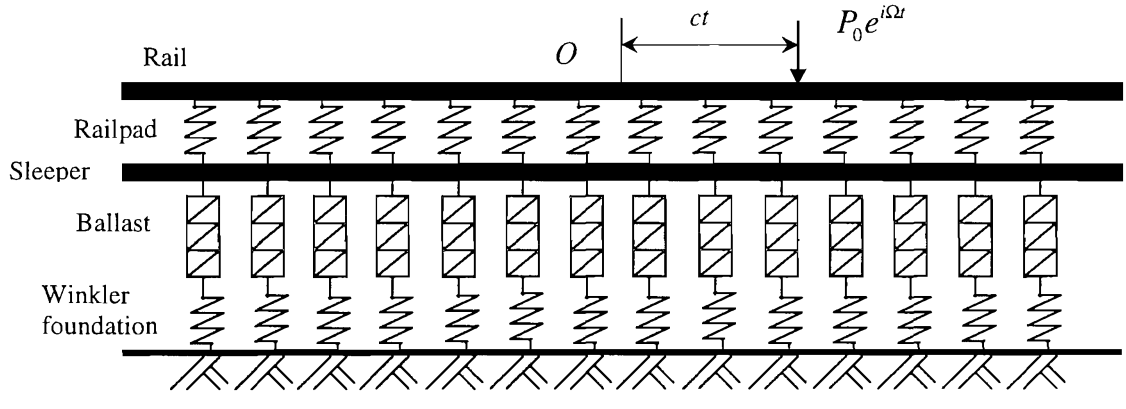

Figure 4.1. Model for a track on a Winkler foundation.

$k_P = k_P'(1+i\eta_P \operatorname{sgn}(\omega))$, where $i=\sqrt{-1}$, k_P' is the stiffness of the rail pad for a unit length of track, η_P is its loss factor and ω is the frequency. Since constraints in its cross-sections are weak, the ballast is modelled as elastic bars which have continuously distributed stiffness and mass along the track. The mass and vertical stiffness of the ballast per unit length of track are denoted by m_B and $k_B = k_B'(1+i\eta_B \operatorname{sgn}(\omega))$. An

embankment, if it is present, is modelled in the same way as the ballast. In other words, the bending stiffness of the embankment is ignored. A vertical harmonic load $P_0 e^{i\Omega t}$ moves along the rail uniformly at speed c. At instant t, the load is at a distance, ct, from the origin point. The ground supporting the track is modelled as a Winkler foundation with a stiffness $k_G = k_G'(1 + i\eta_G \operatorname{sgn}(\omega))$. Denoting the vertical displacements of the rail beam and the sleeper beam by $w_R(x,t)$ and $w_S(x,t)$, respectively, then the differential equations of motion of the track can be written as follows:

For the rail beam:

$$EI\frac{\partial^4 w_R(x,t)}{\partial x^4} + m_R\frac{\partial^2 w_R(x,t)}{\partial t^2} + k_P[w_R(x,t) - w_S(x,t)] = \delta(x - ct)P_0 e^{i\Omega t} \tag{4.1}$$

where $\delta(\cdot)$ is the Dirac-delta function.

For the sleeper 'beam':

$$m_S\frac{\partial^2 w_S(x,t)}{\partial t^2} + k_P[w_S(x,t) - w_R(x,t)] = -F_2(x,t) \tag{4.2}$$

where $F_2(x, t)$ denotes the vertical force between the sleeper beam and the ballast. Since the wavelengths of the waves propagating vertically in the ballast layer are much longer than its height (using typical values of parameters [Zai 1997], the wave speed in the vertical direction in the ballast is evaluated as about 200 m/s, and at 100 Hz, the wavelength is 2 m), the vertical displacement of the ballast is assumed to vary linearly over its height. Thus,

$$\frac{m_B}{6}\begin{bmatrix}2 & 1\\ 1 & 2\end{bmatrix}\begin{Bmatrix}\dfrac{\partial^2 w_S(x,t)}{\partial t^2}\\ \dfrac{\partial^2 w_C(x,t)}{\partial t^2}\end{Bmatrix} + k_B\begin{bmatrix}1 & -1\\ -1 & 1\end{bmatrix}\begin{Bmatrix}w_S(x,t)\\ w_C(x,t)\end{Bmatrix} = \begin{Bmatrix}F_2(x,t)\\ -k_G w_C(x,t)\end{Bmatrix} \tag{4.3}$$

where $w_C(x,t)$ denotes the displacement of the bottom of the ballast.

Equations (4.1), (4.2) and (4.3) give the differential equations of motion of the track. Now applying the Fourier transform pairs

$$\bar{f}(\beta) = \int_{-\infty}^{\infty} f(x)e^{-i\beta x}dx, \qquad f(x) = \frac{1}{2\pi}\int_{-\infty}^{\infty} \bar{f}(\beta)e^{i\beta x}d\beta \tag{4.4}$$

to transform equations (4.1) to (4.3) from the space-time domain into the wavenumber domain,

$$EI\beta^4\overline{w}_R(\beta,t)+m_R\frac{\partial^2\overline{w}_R(\beta,t)}{\partial t^2}+k_P[\overline{w}_R(\beta,t)-\overline{w}_S(\beta,t)]=P_0e^{i(\Omega-\beta c)t} \tag{4.5}$$

$$m_S\frac{\partial^2\overline{w}_S(\beta,t)}{\partial t^2}+k_P[\overline{w}_S(\beta,t)-\overline{w}_R(\beta,t)]=-\overline{F}_2(\beta,t) \tag{4.6}$$

$$\frac{m_B}{6}\begin{bmatrix}2&1\\1&2\end{bmatrix}\begin{Bmatrix}\frac{\partial^2\overline{w}_S(\beta,t)}{\partial t^2}\\\frac{\partial^2\overline{w}_C(\beta,t)}{\partial t^2}\end{Bmatrix}+k_B\begin{bmatrix}1&-1\\-1&1\end{bmatrix}\begin{Bmatrix}\overline{w}_S(\beta,t)\\\overline{w}_C(\beta,t)\end{Bmatrix}=\begin{Bmatrix}\overline{F}_2(\beta,t)\\-k_G\overline{w}_C(\beta,t)\end{Bmatrix} \tag{4.7}$$

where, $\overline{w}(\beta,t)$ denotes the Fourier transform of $w(x,t)$, and β is the wavenumber. For equations (4.5) to (4.7), the steady-state solution is sought, i.e., let

$$\overline{w}(\beta,t)=\tilde{w}(\beta)e^{i(\Omega-\beta c)t},\ \overline{F}_2(\beta,t)=\tilde{F}_2(\beta)e^{i(\Omega-\beta c)t} \tag{4.8}$$

Equation (4.8) shows that the Fourier transformed displacements (or displacements in the wavenumber domain) $\overline{w}(\beta,t)$ are harmonic, the frequency being

$$\omega=\Omega-\beta c \tag{4.9}$$

If the inverse Fourier transform of $\tilde{w}(\beta)$ is denoted by $w^*(x)$, then equation (4.8) implies that

$$w(x,t)=w^*(x-ct)e^{i\Omega t} \tag{4.10}$$

Now let $r=x-ct$, i.e., observation is made within a reference frame that moves together with the load. Equation (4.10) shows that, in the moving reference frame, the motion of the track is harmonic with the same frequency as that of the load.
Since $w^*(r)$ is a complex function of r, it can be rewritten as $w^*(r)=|w^*(r)|e^{i\phi(r)}$, where $\phi(r)$ denotes the phase angle. Then equation (4.10) becomes

$$w(x,t)=w(r+ct,t)=|w^*(r)|e^{i[\phi(r)+\Omega t]} \tag{4.11}$$

If $w(r+ct,t)$ is denoted by $W(r,t)$, then

$$W(r,t) = \mid w^*(r) \mid e^{i[\phi(r)+\Omega t]} \tag{4.12}$$

$W(r,t)$ describes a wave motion in the moving reference frame.

Now inserting equation (4.8) into equations (4.5) to (4.7), yields

$$EI\beta^4 \tilde{w}_R(\beta) - \omega^2 m_R \tilde{w}_R(\beta) + k_P[\tilde{w}_R(\beta) - \tilde{w}_S(\beta)] = P_0 \tag{4.13}$$

$$-\omega^2 m_S \tilde{w}_S(\beta) + k_P[\tilde{w}_S(\beta) - \tilde{w}_R(\beta)] = -\tilde{F}_2(\beta) \tag{4.14}$$

$$-\frac{m_B\omega^2}{6}\begin{bmatrix}2 & 1\\ 1 & 2\end{bmatrix}\begin{Bmatrix}\tilde{w}_S(\beta)\\ \tilde{w}_C(\beta)\end{Bmatrix} + k_B\begin{bmatrix}1 & -1\\ -1 & 1\end{bmatrix}\begin{Bmatrix}\tilde{w}_S(\beta)\\ \tilde{w}_C(\beta)\end{Bmatrix} = \begin{Bmatrix}\tilde{F}_2(\beta)\\ -k_G\tilde{w}_C(\beta)\end{Bmatrix} \tag{4.15}$$

From these equations $\tilde{w}_R(\beta)$ can be found as

$$\tilde{w}_R(\beta) = \frac{\Delta_1(\beta)}{\Delta(\beta)} \tag{4.16}$$

where

$$\Delta(\beta) = \begin{vmatrix} [k_P + k_B - (m_S + \frac{1}{3}m_B)\omega^2](EI\beta^4 + k_P - m_R\omega^2) - k_P^2 & k_B + \frac{1}{6}m_B\omega^2 \\ (k_B + \frac{1}{6}m_B\omega^2)(EI\beta^4 + k_P - m_R\omega^2) & k_B + k_G - \frac{1}{3}m_B\omega^2 \end{vmatrix} \tag{4.17}$$

$$\Delta_1(\beta) = \begin{vmatrix} [k_P + k_B - (m_S + \frac{1}{3}m_B)\omega^2]P_0 & k_B + \frac{1}{6}m_B\omega^2 \\ (k_B + \frac{1}{6}m_B\omega^2)P_0 & k_B + k_G - \frac{1}{3}m_B\omega^2 \end{vmatrix} \tag{4.18}$$

It is noticed that $\Delta(\beta)$ has a higher power of β than $\Delta_1(\beta)$. Equations (4.16) and (4.8) give the solution for waves in the track in the wavenumber domain

4.3 WAVES IN A TRACK WITH VISCOUS DAMPING: CALCULATED USING AN ANALYTICAL APPROACH

4.3.1 FORMULAE

To obtain the steady state response in the spatial domain, the inverse Fourier transform of $\tilde{w}_R(\beta)$ has to be performed. If the hysteretic damping model is used, then the inverse Fourier transform of $\tilde{w}_R(\beta)$ cannot be obtained analytically. In this case, the

FFT technique is often employed. However, if $\Delta(\beta), \Delta_1(\beta)$ are polynomials of β, then the inverse Fourier transform of $\tilde{w}_R(\beta)$ can be carried out analytically, as shown below. To do so, the viscous damping model is employed by making all the loss factors proportional to $\omega = \Omega - \beta c$, thus, $k_P = k_P^{'}(1+i\xi_P(\Omega-\beta c))$, $k_B = k_B^{'}(1+i\xi_B(\Omega-\beta c))$, and $k_G = k_G^{'}(1+i\xi_G(\Omega-\beta c))$, where ξ_P, ξ_B, ξ_G are termed 'viscous damping constants'. With the substitution of these expressions into $\Delta(\beta), \Delta_1(\beta)$, it can be found that $\Delta(\beta)$ is a polynomial of β of order 8, and $\Delta_1(\beta)$ is of order 4. Thus $\Delta(\beta)$ can be written as

$$\Delta(\beta) = \sum_{j=0}^{8} p_{9-j}\beta^j \tag{4.19}$$

where p_j, $j = 1,2,\cdots,9$, are coefficients of the polynomial $\Delta(\beta)$.

In general, the eight roots of equation (4.19) are denoted by

$$\beta_j = a_j + ib_j \quad (j = 1,2\cdots,8) \tag{4.20}$$

thus $\Delta(\beta) = p_1\prod_{k=1}^{8}(\beta - \beta_k)$ and equation (4.16) may be expressed as the sum of partial fractions

$$\tilde{w}_R(\beta) = \sum_{j=1}^{8} A_j \frac{1}{\beta - a_j - ib_j} \tag{4.21}$$

where

$$A_j = \Delta_1(\beta_j) / [p_1 \prod_{\substack{k=1 \\ k\neq j}}^{8}(\beta_j - \beta_k)] \tag{4.22}$$

By the definition of the Fourier transform, it can be shown that if $b_j \neq 0$, the inverse Fourier transform of $\frac{1}{\beta - a_j - ib_j}$ is given by

$$\mathrm{F}^{-1}[\frac{1}{\beta - a_j - ib_j}] = \frac{1}{2\pi}\int_{-\infty}^{\infty} \frac{1}{\beta - a_j - ib_j} e^{i\beta r} d\beta = \begin{cases} ie^{ia_j r}e^{-b_j r}H(r), b_j > 0 \\ -ie^{ia_j r}e^{-b_j r}H(-r), b_j < 0 \end{cases} \tag{4.23}$$

where

$$H(r)=\begin{cases}1, r\geq 0\\ 0, r<0\end{cases} \tag{4.24}$$

is the Heaviside unit function. Equations (4.21) and (4.23) show there are eight waves travelling along the rails. The wave corresponding to $\beta_j = a_j + ib_j$, is described in the moving reference frame by (see equation (4.10))

$$w_j^*(r,t)=\begin{cases}iA_j e^{ia_j r}e^{-b_j r}e^{i\Omega t}H(r), b_j>0\\ -iA_j e^{ia_j r}e^{-b_j r}e^{i\Omega t}H(-r), b_j<0\end{cases} \tag{4.25}$$

As indicated in equation (4.25), for $b_j > 0$, the wave exists in front of the load and propagates forwards (away from the load) if $a_j < 0$ or propagates backwards (towards the load) if $a_j > 0$. For $b_j < 0$, the relevant wave exists behind the load and propagates forwards if $a_j < 0$ or backward if $a_j > 0$. The wave speed (phase speed) observed in the moving reference frame is

$$c_{j\text{ph}} = \Omega / |a_j| \tag{4.26}$$

and the attenuation rate is $|b_j|$.

If observation is made from the ground, then the wave corresponding to $\beta_j = a_j + ib_j$ is described by

$$\begin{aligned} w_j(x,t) &= \begin{cases}iA_j e^{ia_j(x-ct)}e^{-b_j(x-ct)}e^{i\Omega t}H(r), b_j>0\\ -iA_j e^{ia_j(x-ct)}e^{-b_j(x-ct)}e^{i\Omega t}H(-r), b_j<0\end{cases}\\ &= \begin{cases}iA_j e^{ia_j x}e^{-b_j x}e^{b_j ct}e^{i(\Omega-a_j c)t}H(r), b_j>0\\ -iA_j e^{ia_j x}e^{-b_j x}e^{b_j ct}e^{i(\Omega-a_j c)t}H(-r), b_j<0\end{cases}\end{aligned} \tag{4.27}$$

from which it can be seen that:

(1) The wave has a frequency $|\Omega - a_j c|$ and propagates forwards if $a_j < 0$ or backwards if $a_j > 0$ and $\Omega > a_j c$. Thus the frequency of the forward-propagating wave is higher than that of the load while the frequency of the backward-propagating wave is lower. The wave speed observed from the ground is

$$c_j = \begin{cases} (\Omega - a_j c)/a_j = \Omega/a_j - c, \text{if } a_j > 0 \\ (\Omega - a_j c)/|a_j| = \Omega/|a_j| + c, \text{if } a_j < 0 \end{cases} \tag{4.28}$$

i.e., the wave speed observed from the ground is a resultant of the load speed and the wave speed relevant to the moving reference frame.

(2) For $b_j > 0$, a fixed point in front of the load experiences a harmonic vibration with exponentially increasing amplitude ($e^{b_j ct}$). On the other hand, for $b_j < 0$, a point behind the load experiences decaying harmonic vibration.

If the load is stationary, i.e., if $c = 0$, then equation (4.19) degenerates into a polynomial of β of order 4, and the roots of this degenerated polynomial take the form of

$$\beta_1 = a + ib, \beta_2 = -a - ib, \beta_3 = b - ia, \beta_4 = -b + ia \tag{4.29}$$

Equation (4.29) shows that waves ahead of and behind the load are symmetric.

If the load is constant, i.e., if $\Omega = 0$, then the roots of equation (4.19) take the form of

$$\beta_{1,2} = \pm a_1 + ib_1, \beta_{3,4} = \pm a_2 + ib_2, \beta_{5,6} = \pm a_3 + ib_3, \beta_{7,8} = \pm a_4 + ib_4 \tag{4.30}$$

In the case of zero damping, for a given angular frequency ω, the real roots of $\Delta(\beta) = 0$ give the propagating wavenumbers at that frequency. The plots of these wavenumbers against frequency $f = \frac{\omega}{2\pi}$ are the dispersion curves of the track. On the dispersion diagram, $\omega = \Omega - \beta c$ is a straight line and has been termed the load speed line. The intersections of the load speed line with the dispersion curves indicate the propagating wavenumbers excited by the moving load.

4.3.2 EXAMPLES

In this sub-section, the responses of a beam and a track on a Winkler foundation are computed by performing the inverse Fourier transforms analytically as described above. The track parameters are listed in Table 4.1.

TABLE 4.1
Parameters for a railway track on a Winkler foundation

Mass of rail beam per unit length of track	120 kg/m
Bending stiffness of rail beam	1.26×10^{7} Nm^2
Rail pad stiffness	3.5×10^{8}N/m^2
Rail pad viscous damping constant	0.001
Mass of sleepers per unit length of track	490 kg/m
Mass of ballast per unit length of track	1200 kg/m
Ballast stiffness per unit length of track	3.15×10^{8}N/m^2
Viscous damping constant of the ballast	0.001
Stiffness of the ground as a Winkler foundation	6×10^{6}N/m^2
Viscous damping constant of the Winkler foundation	0.001

4.3.2.1 *A BEAM ON A WINKLER FOUNDATION*

First, an Euler beam on a Winkler foundation is investigated. This Winkler foundation beam is equivalent to the track in the sense of that its mass is made up of all the masses of the track components and the stiffness of the Winkler foundation is equal to the total vertical stiffness of the track. Thus, the mass per unit length of the beam is $m_R = 1810$ kg/m, its bending stiffness $EI = 1.26\times10^{7}$ Nm^2, the vertical stiffness of the foundation $k_G^{'} = 5.79\times10^{6}$ N/m^2. The viscous damping constant of the foundation remains 0.001. For this simple case, equations (4.16) and (4.17) become

$$\tilde{w}_R(\beta) = \frac{P_0}{EI\beta^4 - m_R\omega^2 + k_G^{'}(1+i\xi_G\omega)} \tag{a}$$

$$\begin{aligned}\Delta(\beta) &= EI\beta^4 - m_R(\Omega-\beta c)^2 + k_G^{'}[1+i\xi_G(\Omega-\beta c)] \\ &= EI\beta^4 - m_R c^2\beta^2 + (2m_R\Omega c - i\xi_G k_G^{'} c)\beta + k_G^{'} - m_R\Omega^2 + ik_G^{'}\xi_G\Omega\end{aligned} \tag{b}$$

thus $\Delta(\beta)$ is a polynomial of order 4. The dispersion equation is

$$EI\beta^4 - m_R\omega^2 + k_G^{'} = 0 \tag{c}$$

Equation (b) has four roots, but none are purely real if $\xi_G \neq 0$, since the damping always makes waves attenuate. Figure 4.2 shows the dispersion curve of this beam. The frequency at which the wavenumber is zero is the natural frequency of the beam, which is evaluated as 9 Hz. The beam will be resonant at its natural frequency. Below the natural frequency, no propagating wave can be excited and all wave solutions are evanescent. The upper load speed line in Figure 4.2 for $f = 40$ Hz intersects the dispersion curve at wave numbers 1.3795 rad/m and -2.1176 rad/m, and the lower load

speed line for $f = 6\,\text{Hz}$, intersects the dispersion curve at wave numbers -0.3258 rad/m and -0.9577 rad/m. In both cases, the load speed $c = 60\,\text{m/s}$.

Figure 4.3 shows the waves in the beam produced by a unit load of 40 Hz moving at 60 m/s. The four roots of equation (b) are found to be, in radians per metre,

$\beta_1 = -2.1176 + 0.0055i$, $\beta_2 = 0.3749 + 1.6772i$,

$\beta_3 = 0.3632 - 1.6770i$, $\beta_4 = 1.3796 - 0.0058i$.

Waves corresponding to the roots having small (in magnitude) imaginary part will be dominating, since these waves are propagating and least attenuated. From Figure 4.2 it is identified that the propagating waves correspond to β_1 and β_4. Since the real part of β_1 is negative and its imaginary part is positive, the corresponding wave is located ahead of the load and propagates forwards (away from the load). Likewise, since the real part of β_4 is positive and its imaginary part is negative, the corresponding wave is located behind the load and propagates backwards (away from the load). The wave behind the load has a wavelength of $2\pi / 1.3795 = 4.55$ m, and the wave speed (in the moving reference frame, see equation (4.26)) is $40 \times 2\pi / 1.3795 = 182$ m/s. The wave ahead of the load has a wavelength of $2\pi / 2.1176 = 2.97$ m and its speed is 118.6 m/s. It is also shown that the amplitude of the wave behind the load is greater than that of the wave ahead of the load at this frequency.

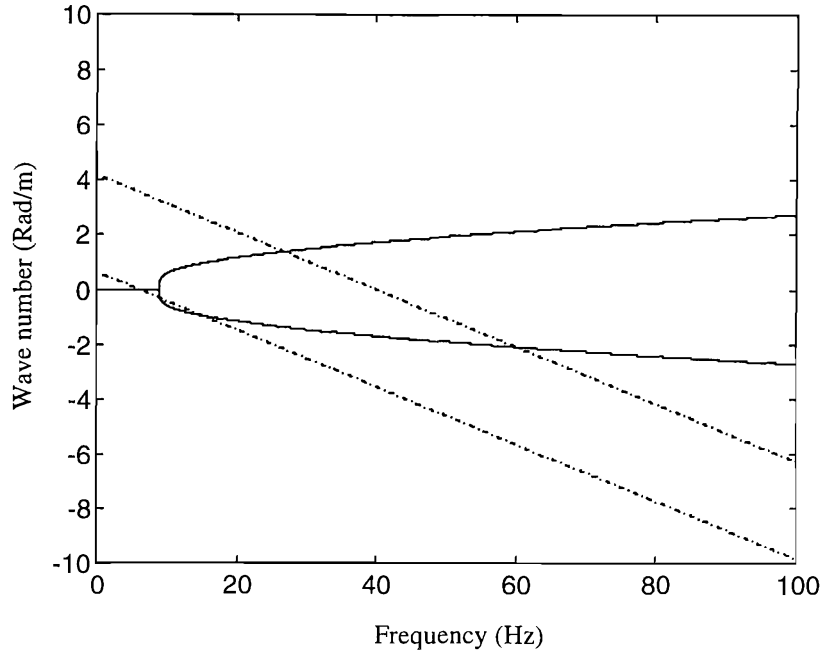

Figure 4.2. Dispersion curve for a beam on a Winkler foundation. The upper load speed line for $f = 40$ Hz, intersects the dispersion curve at wavenumbers 1.3795 rad/m and -2.1176 rad/m, and the lower load speed line for $f = 6$ Hz, has intersections at wavenumbers -0.3258 rad/m and -0.9577 rad/m. In both cases, the load speed $c = 60$ m/s.

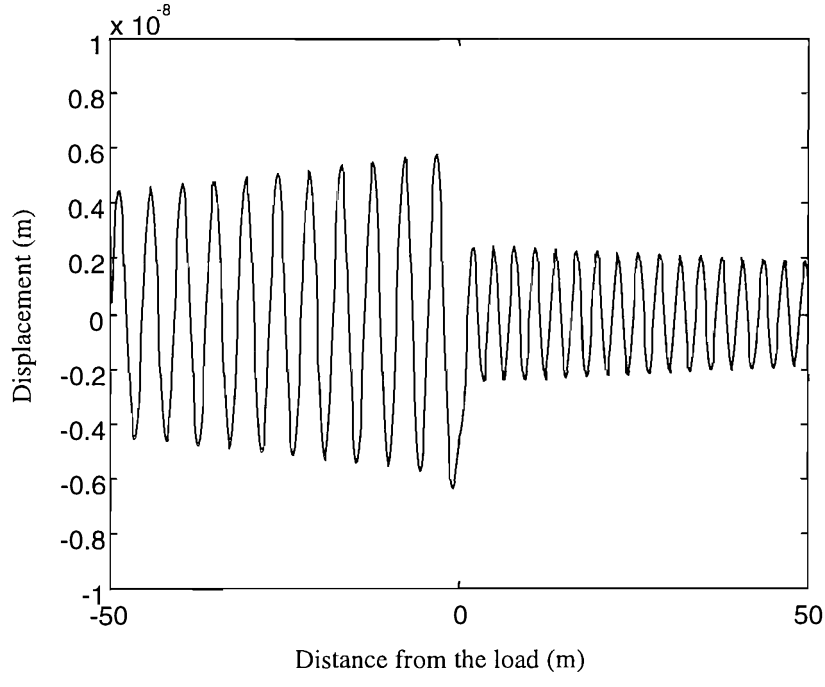

Figure 4.3. Waves in the beam produced by a unit load of 40 Hz moving at 60 m/s. Both the wave behind and ahead of the load propagate away from the load. The wave behind the load has a wavelength of 4.55 m. The wave ahead of the load has a wavelength of 2.97 m.

Figure 4.4 shows the waves in the beam induced by a unit load of 6 Hz moving at 60 m/s. The four roots of equation (b) are (in units rad/m)

$$\beta_1 = 0.6475 + 0.6413i,\ \beta_2 = 0.6360 - 0.6337i,$$

$$\beta_3 = -0.9588 + 0.0232i,\ \beta_4 = -0.3247 - 0.0309i.$$

Thus the propagating waves correspond to β_3 and β_4. Since the real part of β_3 is negative and its imaginary part is positive, the corresponding wave is located ahead of the load and propagates forwards (away from the load). Likewise, since both the real part and the imaginary part of β_4 are negative, the corresponding wave is located behind the load and, surprisingly, propagates forwards (*towards to the load*). The wave behind the load has a wavelength of $2\pi / 0.3247 = 19.34$ m and that ahead of the load has a wavelength of $2\pi / 0.9588 = 6.55$ m. Again the wave behind the load has greater amplitude than that ahead of the load.

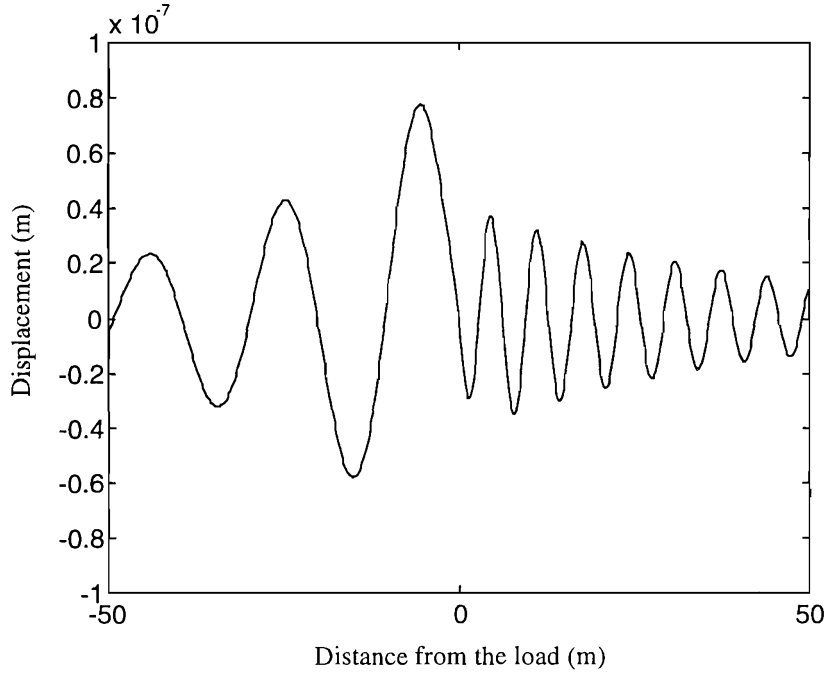

Figure 4.4. Waves in the beam produced by a unit load of 6 Hz moving at 60 m/s. Both the waves behind and ahead of the load propagate in the load motion direction. The wave behind the load has a wavelength of $2\pi / 0.3247 = 19.34$ m. The wave ahead of the load has a wave length of $2\pi / 0.9588 = 6.55$ m

From Figure 4.2 it can be seen that it is possible, only when the frequency of the load is less than the natural frequency of the beam, that both the waves behind and ahead the load propagate forward (both have negative wavenumbers on this graph). For higher

frequency, the two propagating wavenumbers are opposite in sign and thus the relevant waves propagate away from the load. If the ground supporting the beam is modelled as an elastic half-space rather than a Winkler foundation, the waves behind and ahead of the load always propagate away from the load.

4.3.2.2 *A TRACK ON A WINKLER FOUNDATION*

Figure 4.5 shows the dispersion curve of the track specified in Table 4.1. The wavenumber is zero at 9 Hz, the natural frequency of the track. The wavenumber goes to infinity at 68 Hz, which is the natural frequency of the sleeper-ballast mass on supports (rails and foundation). The load speed line corresponds to a load of frequency 40 Hz, moving at 100 m/s. Within the frequency range, the only propagating wavenumbers is 1.2056 rad/m.

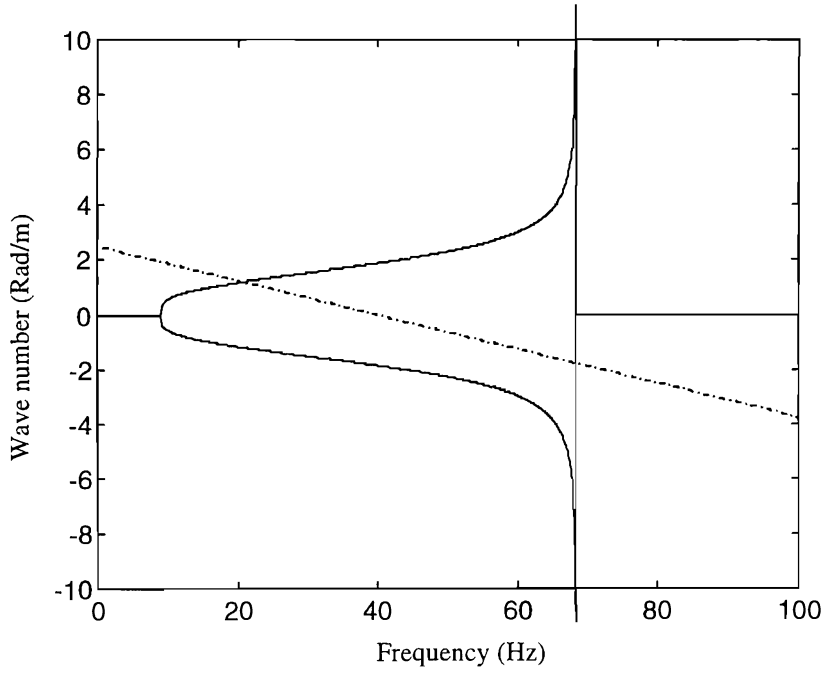

Figure 4.5. Dispersion curve for the track. The load speed line corresponds to a load of frequency 40 Hz, moving at 100 m/s. Within the frequency range, the propagating wavenumber is 1.2056 rad/m.

Figure 4.6 shows the waves in the rail beam produced by a unit harmonic load of 40 Hz moving at 100 m/s. The eight roots of equation $\Delta(\beta)$ are (in units rad/m)

$$\beta_1 = 12.5086 - 9.8005i,\ \beta_2 = -7.4833 - 9.8017i,\ \beta_3 = 6.6845 - 0.9145i,$$

$$\beta_4 = -1.9895 - 1.8869i,\ \beta_5 = -2.2837 + 0.9654i,\ \beta_6 = 0.7255 - 1.5189i \qquad \text{(d)}$$

$$\beta_7 = 0.6835 + 1.5193i,\ \beta_8 = 1.2054 - 0.0081i$$

The propagating wave corresponds to β_8 and is located behind the load and propagates backwards (away from the load). The wavelength is $2\pi / 1.2054 = 5.21\,\text{m}$.

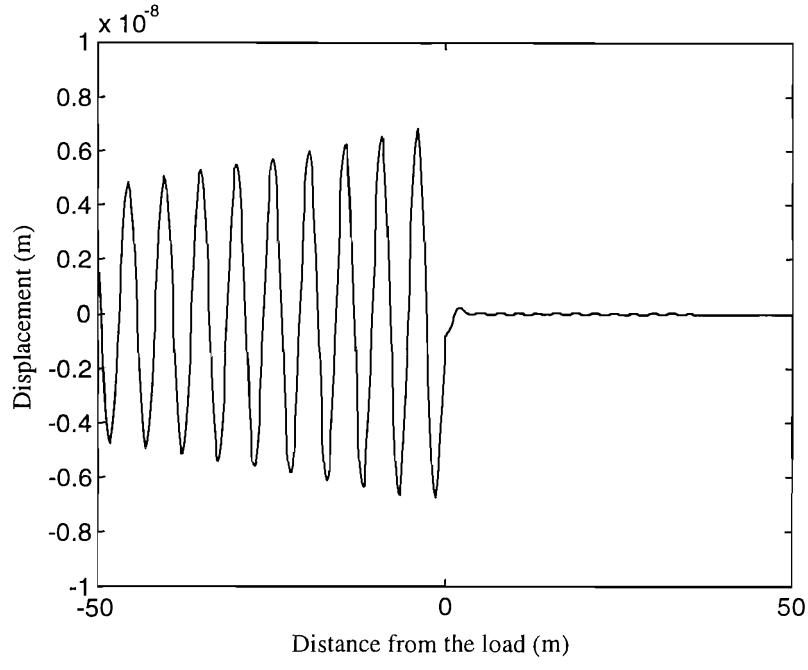

Figure 4.6. The waves in the rail beam produced by a unit load of 40 Hz moving at 100 m/s. The wave behind the load propagates away from the load and has a wavelength of 5.21 m.

Figure 4.7 shows the waves in the rail beam produced by a unit load of 6 Hz moving at 100 m/s. The eight roots of equation $\Delta(\beta)$ are (in units rad/m)

$$\beta_1 = 10.3740 - 9.8007i,\ \beta_2 = -9.6199 - 9.8009i,\ \beta_3 = 4.4571 - 0.9162i,$$

$$\beta_4 = -3.5715 - 0.9654i,\ \beta_5 = -1.5465 + 0.0503i,\ \beta_6 = 0.8169 + 0.5379i \qquad \text{(e)}$$

$$\beta_7 = 0.7947 - 0.5342i,\ \beta_8 = -0.1969 - 0.0167i$$

It can be seen that the propagating waves correspond to β_5 and β_8, and both of them propagate forwards. The wave behind the load has a wavelength of $2\pi / 0.1969 = 32$ m, and that ahead of the load has a wavelength of $2\pi / 1.5465 = 4$ m.

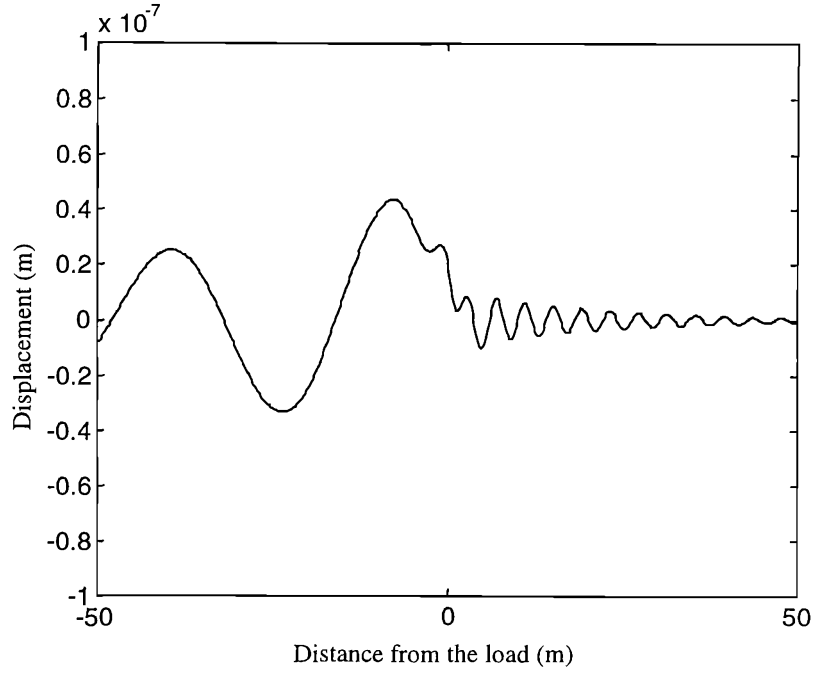

Figure 4.7. The waves in the rail beam produced by a unit load of 6 Hz moving at 100 m/s. The wave behind the load propagates towards the load and that ahead of the load propagates away from the load. The wave behind the load has a wavelength of 32 m, and that ahead the load has a wavelength of 4 m.

4.4 WAVES IN A TRACK WITH VISCOUS DAMPING: CALCULATED USING THE FAST FOURIER TRANSFORM

If the inverse Fourier transform of $\tilde{w}_R(\beta)$ cannot be performed analytically, either a quadrature or an FFT algorithm has to be employed. The advantage of using the FFT is that the displacements of many points can be obtained simultaneously. When using the FFT, $\tilde{w}_R(\beta)$ has to be discretised and truncated. It is important to ensure that the propagating wavenumbers are included. To check the accuracy of the FFT, in this section, recalculations are made using the FFT for the responses of the track shown in Section 4.3.2.2.

Figure 4.8 shows the FFT-calculated waves in the rail produced by the unit load of 40 Hz moving at 100 m/s. The spacing of the discrete values of β is $2\pi \times 0.0025$, and 2048 samples are used. The propagating wavenumber of the track, indicated in Figure 4.5 as 1.2056 rad/m, is within this range of β. According to the principle of the FFT, only waves in the range of -200 m $< r <$ 200 m ($1/0.0025/2 = 200$ m) are available. Compared with Figure 4.6, a good approximation is achieved, especially for the wave behind the load. However, animation of these waves shows that both the waves behind and ahead the load propagate backwards. The erroneously high amplitude of the wave

ahead of the load is due partly to the effect of 'frequency aliasing' or 'wrap-round'. If $\tilde{w}_R(\beta)$ is treated as a 'time history', then $w_R^*(r)$ is its 'frequency spectrum'. Referring to Figure 4.6, there actually is a propagating wave behind the load that is propagating backwards. When the FFT is used, the wave out of the 'Nyquist range', in the present case which is -200 m < r < 200 m, is brought into this range, as a result, yielding Figure 4.8 which shows an obvious wave ahead of the load. The part of the wave being aliased is shown in Figure 4.9 which is produced using the analytical calculation.

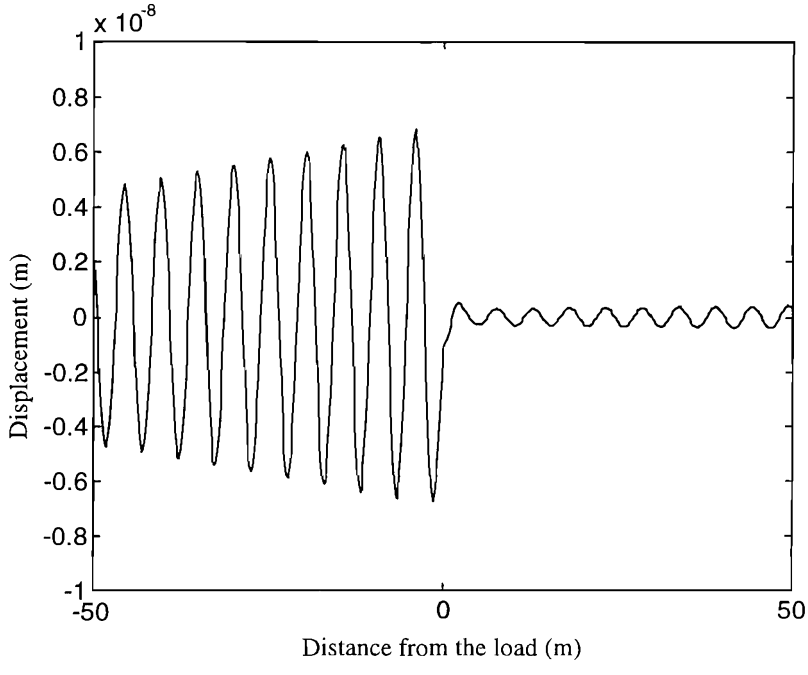

Figure 4.8. FFT-calculated waves in the rail produced by a unit load of 40 Hz moving at 100 m/s. The number of points in the FFT is 2048 and the spacing of β is $2\pi \times 0.0025$ rad/m.

A finer discretisation of $\tilde{w}_R(\beta)$ can mitigate the effect of 'frequency aliasing'. Figure 4.10 shows the results when the spacing of β is reduced to $2\pi \times 0.00125$. It is identical to Figure 4.6. The greater the attenuation rate of the wave is, the less is the effect of the 'frequency aliasing'. This is the case when the track rests on a ground due to the energy radiation into the ground.

Figure 4.11 shows the FFT-calculated waves in the rail produced by the 6 Hz load moving at 100 m/s. The spacing of β is $2\pi \times 0.0025$ rad/m, and 2048 samples are used. Animation of these waves shows that both the waves behind and ahead of the load propagate forwards. Comparison of Figures 4.7 and 4.11 indicates that a good accuracy is achieved. Because of the higher attenuation rate (as indicated by equations (d) and (e),

the attenuation rate for the 6 Hz load is 0.0167 neper/m while that for the 40 Hz load is 0.0081 neper/m), the effect of 'frequency aliasing' is unnoticeable.

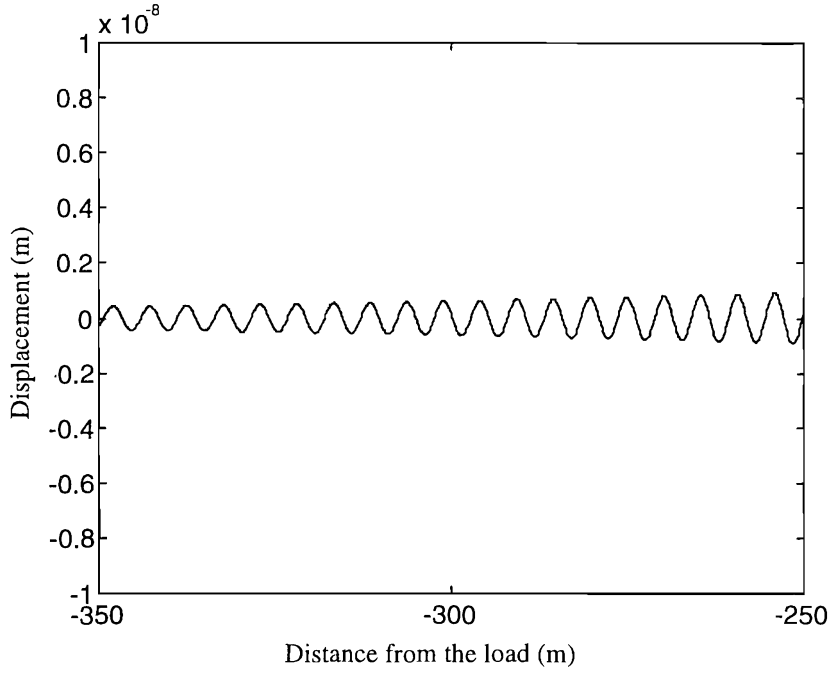

Figure 4.9. Analytically calculated waves in the rail produced by a unit load of 40 Hz moving at 100 m/s. The wave in this range will be brought into the range $-50 \text{ m} < r < 50 \text{ m}$ when using the FFT.

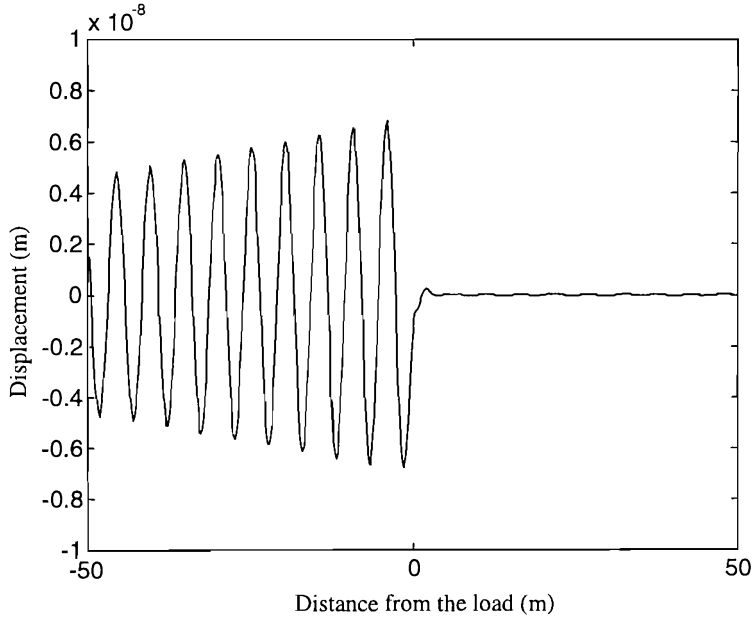

Figure 4.10. FFT-calculated waves in the rail produced by a unit load of 40 Hz load moving at 100 m/s. The number of points in the FFT is 2048 and the sample periodicity is $2\pi \times 0.00125$ rad/m.

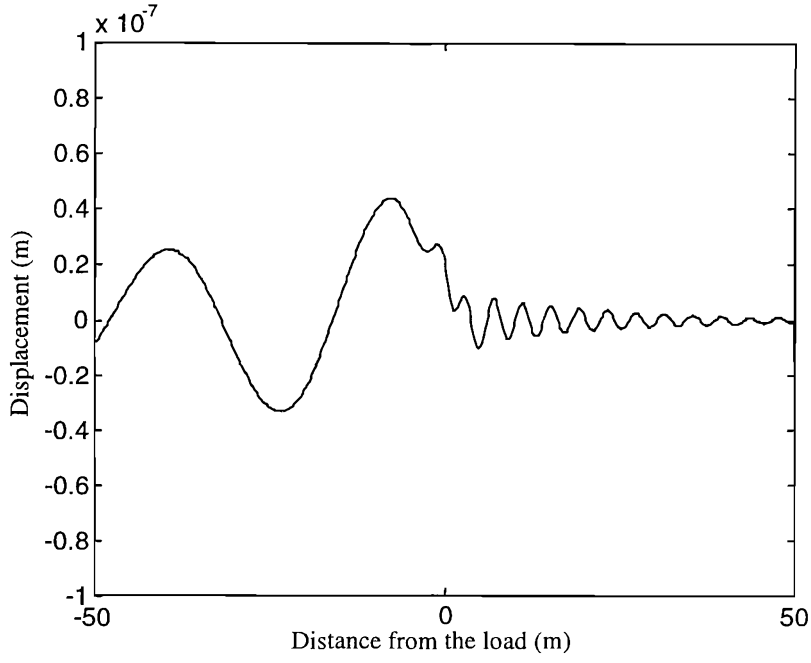

Figure 4.11. FFT-calculated waves in the rail produced by a unit load of 6 Hz load moving at 100m/s. The number of points in the FFT is 2048 and the sample periodicity is $2\pi \times 0.0025$ rad/m.

4.5 WAVES IN A TRACK WITH HYSTERETIC DAMPING: CALCULATED USING THE FAST FOURIER TRANSFORM

A loss factor is commonly used to describe the damping mechanism of a material experiencing harmonic deformation. Normally, loss factors of materials are dependent on the frequency of deformation, though for some materials this dependence is negligible. In equation (4.10) it is shown that the steady state displacements of the track are non-harmonic due to a moving harmonic load. Thus the materials in the track experience non-harmonic deformations. However, the steady state displacements can be regarded as a resultant of components of different wavenumbers shown in equation (4.8), and each component is harmonic. The frequency of each component depends on the wavenumber of this component and the speed and frequency of the load, i.e., upon $\omega = \Omega - \beta c$ (see equation (4.9)). This suggests that the hysteretic damping model may be applied by making use of frequency-dependant loss factors. However, as noticed in the previous sections, there is a component which is dominant over other components. If the loss factors are set to be constant and are given values equal to those at the frequency of the dominating component, the results are expected to be sufficiently accurate. To show this, calculations are made below using the hysteretic damping model. The results are compared with those obtained analytically using the viscous damping model. It is illustrated that the two damping models give almost the same results.

Figure 4.12 shows the FFT-calculated waves in the rail produced by a unit load of 40 Hz moving at 100 m/s. The number of points in the FFT is 2048 and the spacing of β is $2\pi \times 0.00125$ rad/m. The loss factors for the railpad, the ballast and the Winkler foundation are chosen as 0.13. This value is obtained by letting $\eta = \xi(\Omega - \beta c)$, where, $\xi = 0.001$, $\Omega = 2\pi \times 40$, $c = 100$ and β is the dominating propagating wavenumber which, as indicated in Figure 4.5, equals 1.2056 rad/m. It can be seen that the waves in Figure 4.12 are almost identical to the waves shown in Figure 4.6.

Figure 4.13 shows the FFT-calculated waves in the rail produced by a unit load of 6 Hz moving at 100 m/s. The number of pints in the FFT is 2048 and the spacing of β is $2\pi \times 0.0025$ rad/m. The loss factors for the railpad, the ballast and the Winkler foundation are evaluated by $\eta = \xi(\Omega - \beta c)$ as 0.057, where, $\xi = 0.001$, $\Omega = 2\pi \times 6$, $c = 100$ and β is the dominating propagating wavenumber, equal to -0.1969 rad/m. It can be seen that in Figure 4.13 the wave behind the load has a higher accuracy than that ahead of the load, compared with Figure 4.7.

Figure 4.14 shows waves in the rail produced by a unit constant load moving at 60 m/s. The dashed line is for the track with the viscous damping model, in which each damping constant is 0.001. The eight roots of equation (4.19) are evaluated as (in units rad/m)

-16.6631 -16.3346i, 16.6631 -16.3346i, -6.9579 - 1.5371i, 6.9579 - 1.5371i

-0.6930 + 0.4645i, 0.6930 + 0.4645i, -0.6712 - 0.4643i, 0.6712 - 0.4643i

from which it is known that the roots having least imaginary part are $\pm 0.6712 - 0.4643i$. The solid line, calculated by using FFT, is for the track with the hysteretic damping model. The number of points in the FFT is 2048 and the spacing of β is $2\pi \times 0.0025$ rad/m. The loss factors for the railpad, the ballast and the Winkler foundation are evaluated by $\eta = \xi(\Omega - \beta c)$ as 0.04, where, $\xi = 0.001$, $\Omega = 0$, $c = 60$ m/s and $\beta = -0.6712$ rad/m. It can be seen that two damping models give the closely similar results.

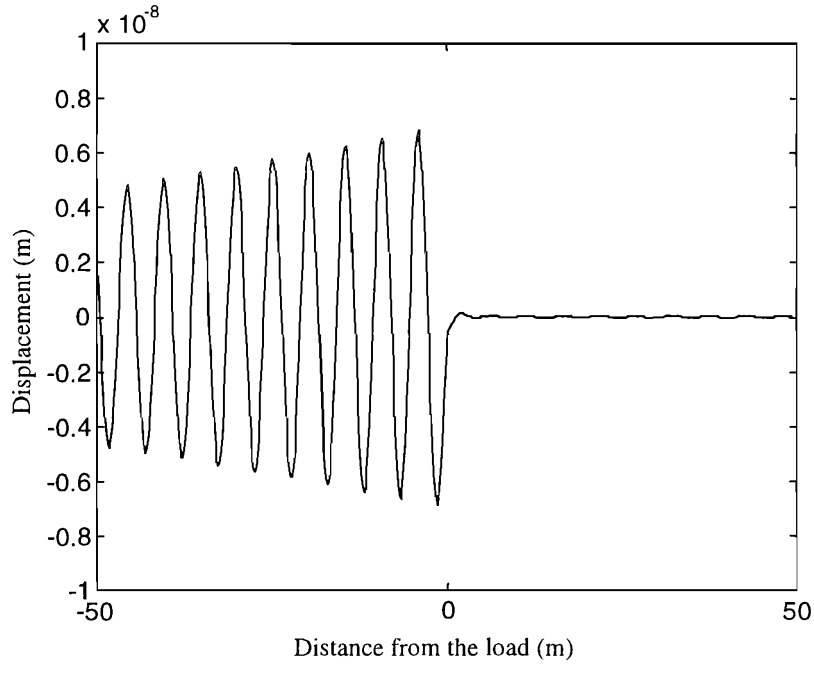

Figure 4.12. FFT-calculated waves in the rail with the hysteretic damping model for the 40 Hz load moving at 100 m/s.

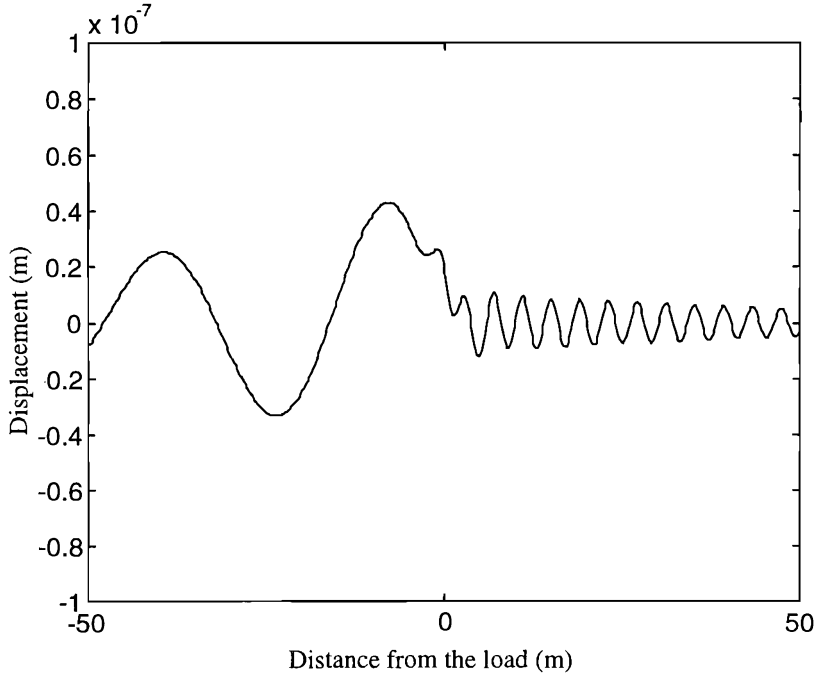

Figure 4.13. FFT-calculated waves in the rail with the hysteretic damping model for the 6 Hz load moving at 100 m/s.

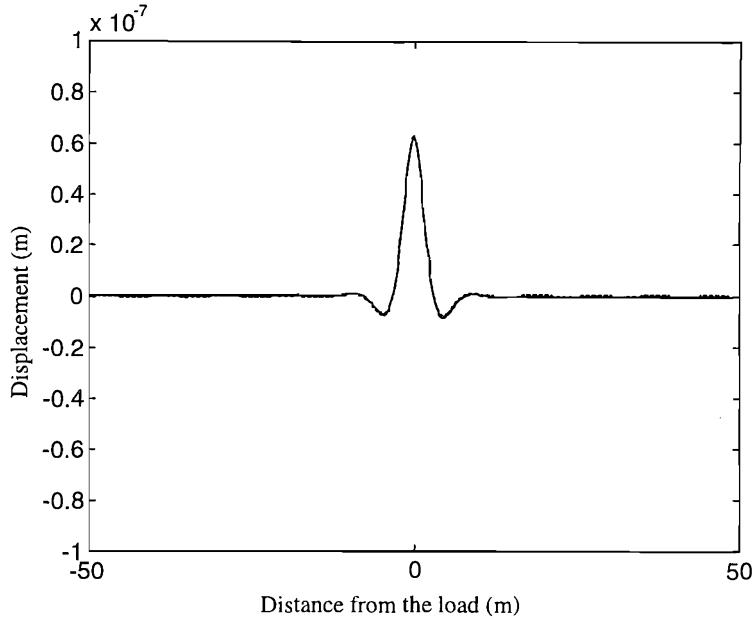

Figure 4.14 The waves in the rail produced by a unit constant load moving at 60 m/s. ——, viscous damping; – · –, hysteretic damping.

4.6 RECEPTANCES OF A TRACK ON A WINKLER FOUNDATION

For the multiple beam track model and the equivalent beam model used in Section 4.3, the displacements of the rails are calculated for a stationary unit harmonic load of different frequencies. The displacements are presented in Figure 4.15 for the loading point, Figure 4.16 at a distance of 10 m and Figure 4.17 at a distance of 20 m. In these figures, the solid line is calculated from the multiple beam track model while the dashed line is from the equivalent single beam model. It is illustrated that below the natural frequency, 9 Hz, two models give almost the same result. However, at frequencies much higher than the natural frequency, due to the different properties of wave propagation, these two models produce quite different responses. At the natural frequency of the sleeper plus ballast on their support (68 Hz), a minimum response is predicted from the multiple beam model.

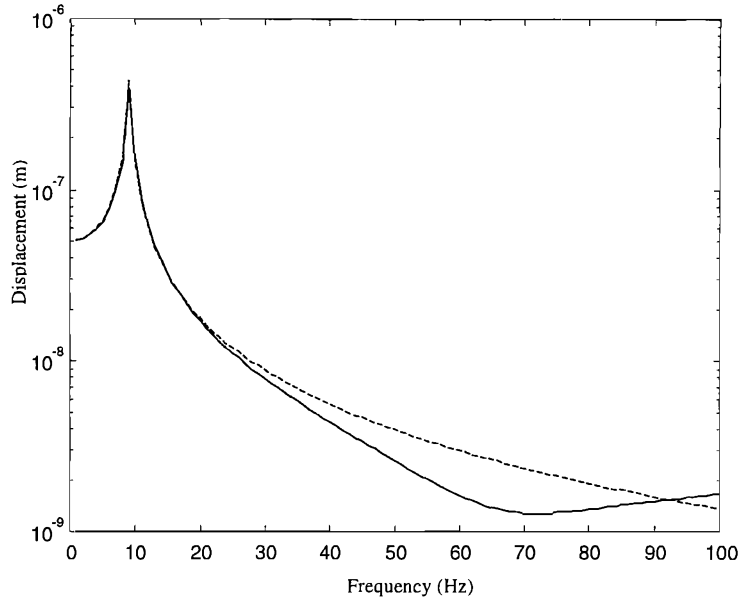

Figure 4.15. Point receptance (response of the loading point on the rail). ——, from the multiple beam track model; – – –, from the equivalent single beam model.

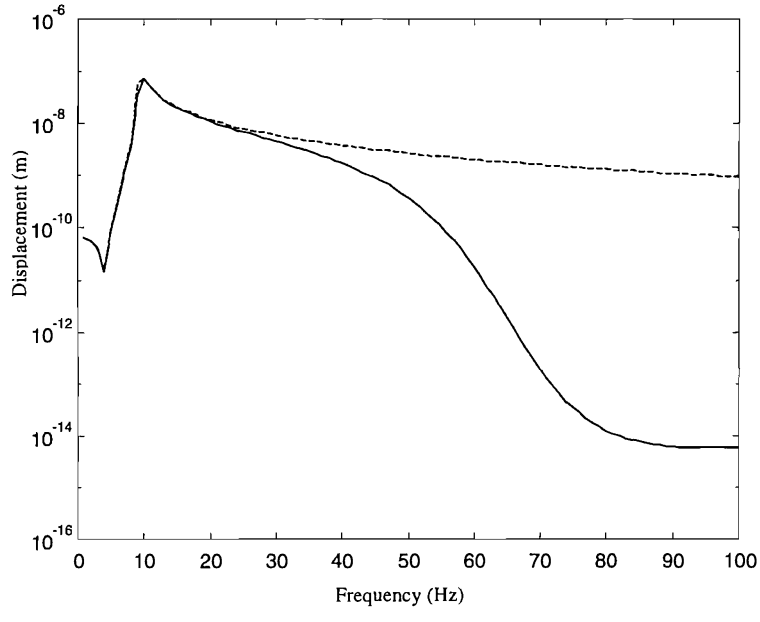

Figure 4.16. Transfer receptance at a point 10 m away from the load on the rail. ——, from the multiple beam track model; – – –, from the equivalent single beam model.

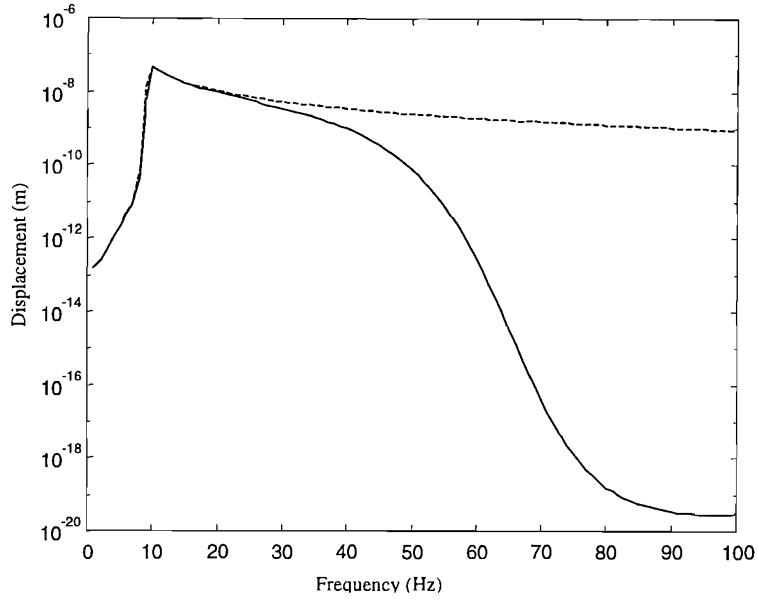

Figure 4.17. Transfer receptance at a point 20 m away from the load on the rail. ——, from the multiple beam track model; – – –, from the equivalent single beam model.

4.7 SUMMARY

In this chapter, the steady state responses have been studied for a track on a Winkler foundation subject to a moving harmonic load. When the viscous damping model is used, the waves in the track can be calculated analytically. This has enabled it to be shown that the FFT approach is capable of achieving a good accuracy.

The dispersion diagram has been shown to be useful in interpreting the excitation of waves by a moving and possibly oscillating load. The dispersion diagram is also helpful to determine the number of points and the spacing in the FFT. A higher damping mechanism increases the efficiency of the FFT method. It has been shown that behind the load, waves in the track can either propagate away from, or towards the load. Comparison has been made between the multiple beam track model and the equivalent single beam track model by calculating the receptance of the rail. It is shown that below the natural frequency of the track, both the models give the same result. However, at frequencies much higher than the natural frequency, the equivalent beam model produces a much higher response than the multiple beam model.

Chapter 5

GROUND VIBRATION GENERATED BY VERTICAL WHEEL-RAIL FORCES

PART I: THEORY AND FORMULATION

5.1 INTRODUCTION

Having investigated the dynamics of a free layered ground and a track on a Winkler foundation, attention is now turned, in this chapter, to a study of the dynamics of a ground coupled with a track structure. The aim of this chapter is to extend the model developed by Sheng, Jones and Petyt [1999 (b)] for predicting ground vibration generated by a single moving harmonic load, so that it accounts for multiple moving forces containing many harmonic components. This chapter is intended to serve two purposes: one is to study ground vibration generated by the quasi-static loads (multiple axle loads) and the other is to form the basis for developing, in Chapter 7, a ground vibration model which comprises vehicles, track and ground. In Section 5.2, the differential equations of motion of the railway track and the ground are presented, for both the time-space domain and the frequency-wavenumber domain. Section 5.3 describes the calculation method for the Fourier-transformed response of the ground surface. The formulae for evaluating response spectra are derived in Section 5.4. A number of results will be presented in the next chapter to investigate the effects of various parameters on the generation and propagation of ground vibration.

5.2 DIFFERENTIAL EQUATIONS OF MOTION OF THE TRACK AND GROUND

Figure 5.1 shows the model of track and ground. The railway is aligned in the x direction and has a contact width $2b$ with the ground. The multiple beam track model developed in Chapter 4 is employed to represent the track. The mass per unit length of track of the rail beam and its bending stiffness are denoted by m_R and EI. The sleeper 'beam' has a mass m_S per unit length of track but no bending stiffness. The complex stiffness of the railpad is denoted by

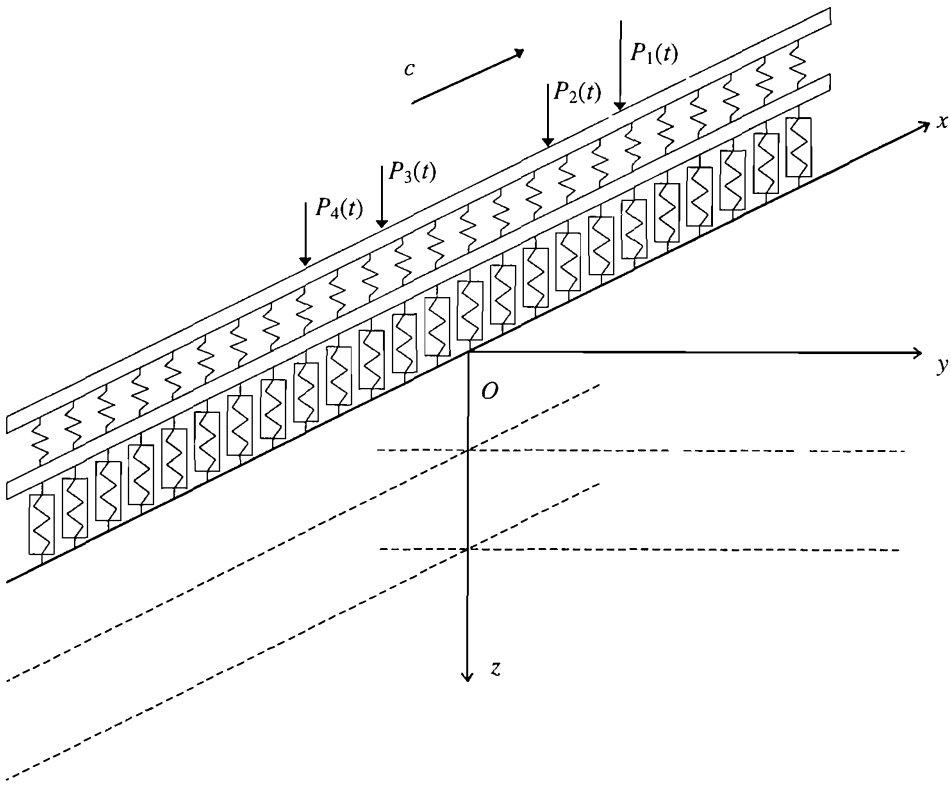

Figure 5.1. Model for the track/ground system

$k_P = k_P^{'}(1+i\eta_P \operatorname{sgn}(\omega))$, where $i=\sqrt{-1}, k_P^{'}$ is the stiffness of rail pad for a unit length of track, η_P is its loss factor and ω is the angular frequency. The mass of the ballast layer per unit length of track is denoted by m_B and its vertical stiffness by $k_B = k_B^{'}(1+i\eta_B \operatorname{sgn}(\omega))$. From right to left, the vertical wheel-rail interaction forces are denoted by $P_1(t), P_2(t), \cdots, P_M(t)$, where M is the number of forces. At time $t = 0$, the corresponding longitudinal coordinates are denoted by $a_1, a_2, \cdots, a_M$. The forces move uniformly along the rail at the train speed c. The vertical displacements of the rail beam and the sleeper beam are denoted by $w_R(x,t)$ and $w_S(x,t)$, respectively, and the vertical displacement of the track centre-line in the plane of contact with the ground (i.e. the x-axis) by $w_C(x,t)$. Further, having considered that the ballast distributes the vertical wheel-rail forces on the ground surface to some extent, it is assumed that there is only a normal contact force in the contact plane which is assumed to be uniformly distributed in the y direction from $y = -b$ to $y = b$ and has a strength of $F_3(x, t)$ for a unit length of track.

The plane *Oxy* forms the ground surface. As in Chapter 2, the ground consists of a number, n, of layers. The nth layer overlies a homogeneous half-space or a rigid foundation, which is numbered as the n+1th layer. The jth layer's material constants are: elastic modulus, E_j, Possion ratio, ν_j, density, ρ_j, loss factor, η_j, and thickness h_j.

Now, the differential equations of motion of the railway track are as follows (see Chapter 4). For the rail beam:

$$EI\frac{\partial^4 w_R(x,t)}{\partial x^4}+m_R\frac{\partial^2 w_R(x,t)}{\partial t^2}+k_P[w_R(x,t)-w_S(x,t)]=\sum_{l=1}^{M}\delta(x-ct-a_l)P_l(t) \qquad (5.1)$$

where $\delta(\cdot)$ is the Dirac-delta function.

For the sleeper 'beam':

$$m_S\frac{\partial^2 w_S(x,t)}{\partial t^2}+k_P[w_S(x,t)-w_R(x,t)]=-F_2(x,t) \qquad (5.2)$$

For the ballast:

$$\frac{m_B}{6}\begin{bmatrix}2 & 1\\ 1 & 2\end{bmatrix}\begin{Bmatrix}\dfrac{\partial^2 w_S(x,t)}{\partial t^2}\\ \dfrac{\partial^2 w_C(x,t)}{\partial t^2}\end{Bmatrix}+k_B\begin{bmatrix}1 & -1\\ -1 & 1\end{bmatrix}\begin{Bmatrix}w_S(x,t)\\ w_C(x,t)\end{Bmatrix}=\begin{Bmatrix}F_2(x,t)\\ -F_3(x,t)\end{Bmatrix} \qquad (5.3)$$

where $F_2(x, t)$ is the longitudinally distributed force between the sleeper 'beam' and the ballast.

As for the ground, its motion is governed by the Navier's equations, which, for the jth layer are (see Chapter 2):

$$\left.\begin{aligned}(\lambda_j+\mu_j)\frac{\partial\Delta_j}{\partial x}+\mu_j\nabla^2 u_j&=\rho_j\frac{\partial^2 u_j}{\partial t^2}\\ (\lambda_j+\mu_j)\frac{\partial\Delta_j}{\partial y}+\mu_j\nabla^2 v_j&=\rho_j\frac{\partial^2 v_j}{\partial t^2}\\ (\lambda_j+\mu_j)\frac{\partial\Delta_j}{\partial z}+\mu_j\nabla^2 w_j&=\rho_j\frac{\partial^2 w_j}{\partial t^2}\end{aligned}\right\}\quad (j=1,2,\cdots,n+1) \qquad (5.4)$$

where, ∇^2 is the Laplace operator, λ_j and μ_j are Lamé constants of the jth layer, determined by

$$\lambda_j = \frac{\nu_j E_j (1+i\eta_j \operatorname{sgn}(\omega))}{(1+\nu_j)(1-2\nu_j)}, \qquad \mu_j = \frac{E_j (1+i\eta_j \operatorname{sgn}(\omega))}{2(1+\nu_j)} \quad (j = 1,2,\cdots,n+1) \tag{5.5}$$

$u_j = u_j(x, y, z, t)$, $\upsilon_j = \upsilon_j(x, y, z, t)$ and $w_j = w_j(x, y, z, t)$ are the longitudinal, lateral and vertical displacements, respectively, of point (x, y, z) in the layer;

$$\Delta_j = \frac{\partial u_j}{\partial x} + \frac{\partial \upsilon_j}{\partial y} + \frac{\partial w_j}{\partial z} \quad (j = 1,2,\cdots,n+1) \tag{5.6}$$

is the dilatation.

Now by applying the one-dimensional Fourier transform pairs

$$\bar{f}(\beta) = \int_{-\infty}^{\infty} f(x) e^{-i\beta x} dx, \qquad f(x) = \frac{1}{2\pi} \int_{-\infty}^{\infty} \bar{f}(\beta) e^{i\beta x} d\beta \tag{5.7}$$

to equations (5.1) to (5.3), and the two-dimensional Fourier transform pairs

$$\bar{f}(\beta,\gamma) = \int_{-\infty}^{\infty}\int_{-\infty}^{\infty} f(x,y) e^{-i(\beta x+\gamma y)} dxdy, \quad f(x,y) = \frac{1}{4\pi^2} \int_{-\infty}^{\infty}\int_{-\infty}^{\infty} \bar{f}(\beta,\gamma) e^{i(\beta x+\gamma y)} d\beta d\gamma \tag{5.8}$$

to equation (5.4), gives

$$EI\beta^4 \overline{w}_R(\beta,t) + m_R \frac{\partial^2 \overline{w}_R(\beta,t)}{\partial t^2} + k_P[\overline{w}_R(\beta,t) - \overline{w}_S(\beta,t)] = e^{-i\beta ct} \sum_{l=1}^{M} P_l(t) e^{-i\beta a_l} \tag{5.9}$$

$$m_S \frac{\partial^2 \overline{w}_S(\beta,t)}{\partial t^2} + k_P[\overline{w}_S(\beta,t) - \overline{w}_R(\beta,t)] = -\overline{F}_2(\beta,t) \tag{5.10}$$

$$\frac{m_B}{6}\begin{bmatrix} 2 & 1 \\ 1 & 2 \end{bmatrix}\begin{Bmatrix} \dfrac{\partial^2 \overline{w}_S(\beta,t)}{\partial t^2} \\ \dfrac{\partial^2 \overline{w}_C(\beta,t)}{\partial t^2} \end{Bmatrix} + k_B\begin{bmatrix} 1 & -1 \\ -1 & 1 \end{bmatrix}\begin{Bmatrix} \overline{w}_S(\beta,t) \\ \overline{w}_C(\beta,t) \end{Bmatrix} = \begin{Bmatrix} \overline{F}_2(\beta,t) \\ -\overline{F}_3(\beta,t) \end{Bmatrix} \tag{5.11}$$

$$\left.\begin{aligned} (\lambda_j+\mu_j) i\beta \overline{\Delta}_j + \mu_j\left(\frac{d^2\overline{u}_j}{dz^2} - \beta^2\overline{u}_j - \gamma^2\overline{u}_j\right) &= \rho_j \frac{\partial^2 \overline{u}_j}{\partial t^2} \\ (\lambda_j+\mu_j) i\gamma \overline{\Delta}_j + \mu_j\left(\frac{d^2\overline{\upsilon}_j}{dz^2} - \beta^2\overline{\upsilon}_j - \gamma^2\overline{\upsilon}_j\right) &= \rho_j \frac{\partial^2 \overline{\upsilon}_j}{\partial t^2} \\ (\lambda_j+\mu_j) \frac{\partial \overline{\Delta}_j}{\partial z} + \mu_j\left(\frac{d^2\overline{w}_j}{dz^2} - \beta^2\overline{w}_j - \gamma^2\overline{w}_j\right) &= \rho_j \frac{\partial^2 \overline{w}_j}{\partial t^2} \end{aligned}\right\} \quad (j = 1,2,\cdots,n+1) \tag{5.12}$$

Each wheel-rail force $P_l(t)$ in equation (5.9) may be expressed in terms of a Fourier integral, i.e.

$$P_l(t) = \int_{-\infty}^{\infty} \tilde{P}_l(\Omega) e^{i\Omega t} d\Omega \quad (l = 1,2,\cdots, M) \tag{5.13}$$

where $\tilde{P}_l(\Omega)$ is the spectrum of the wheel-rail force $P_l(t)$ at frequency Ω. Usually, $\tilde{P}_l(\Omega)$ is a complex number, and there exists a positive number Ω_0 such that when $|\Omega| \geq \Omega_0$, $\tilde{P}_l(\Omega)$ is negligible. Now equation (5.9) becomes

$$\begin{aligned} &EI\beta^4 \overline{w}_R(\beta,t) + m_R \frac{\partial^2 \overline{w}_R(\beta,t)}{\partial t^2} + k_P[\overline{w}_R(\beta,t) - \overline{w}_S(\beta,t)] \\ &= \int_{-\infty}^{\infty} e^{i(\Omega-\beta c)t} \sum_{l=1}^{M} \tilde{P}_l(\Omega) e^{-i\beta a_l} d\Omega \end{aligned} \tag{5.14}$$

Equations (5.14), (5.10), (5.11) and (5.12) are the Fourier transformed differential equations of motion of the track-ground system (or equations of motion of the track-ground system in the wavenumber domain). Having considered the right-hand item in equation (5.14) and the damping existing in the track-ground system, it is reasonable to consider steady state solutions given by

$$\left.\begin{aligned} \overline{w}_R(\beta,t) &= \int_{-\infty}^{\infty} \tilde{w}_R(\beta) e^{i(\Omega-\beta c)t} d\Omega \\ \overline{w}_S(\beta,t) &= \int_{-\infty}^{\infty} \tilde{w}_S(\beta) e^{i(\Omega-\beta c)t} d\Omega \\ \overline{w}_C(\beta,t) &= \int_{-\infty}^{\infty} \tilde{w}_C(\beta) e^{i(\Omega-\beta c)t} d\Omega \\ \overline{F}_2(\beta,t) &= \int_{-\infty}^{\infty} \tilde{F}_2(\beta) e^{i(\Omega-\beta c)t} d\Omega \\ \overline{F}_3(\beta,t) &= \int_{-\infty}^{\infty} \tilde{F}_3(\beta) e^{i(\Omega-\beta c)t} d\Omega \\ \overline{u}_j(\beta,\gamma,z,t) &= \int_{-\infty}^{\infty} \tilde{u}_j(\beta,\gamma,z) e^{i(\Omega-\beta c)t} d\Omega \\ \overline{v}_j(\beta,\gamma,z,t) &= \int_{-\infty}^{\infty} \tilde{v}_j(\beta,\gamma,z) e^{i(\Omega-\beta c)t} d\Omega \\ \overline{w}_j(\beta,\gamma,z,t) &= \int_{-\infty}^{\infty} \tilde{w}_j(\beta,\gamma,z) e^{i(\Omega-\beta c)t} d\Omega \\ \overline{\Delta}_j(\beta,\gamma,z,t) &= \int_{-\infty}^{\infty} \tilde{\Delta}_j(\beta,\gamma,z) e^{i(\Omega-\beta c)t} d\Omega \end{aligned}\right\} \tag{5.15}$$

where $\tilde{u}_j(\beta,\gamma,z)$ denotes the frequency spectrum of the time-varying Fourier transformed displacement $\overline{u}_j(\beta,\gamma,z,t)$ at frequency $\Omega - \beta c$. The existence of steady state motion was

validated by measurements [Madshus and Kaynia 1998(a)]. It will be shown in Section 5.4 that the inverse (spatial) Fourier transform of the spectrum of the (spatial) Fourier transformed displacement gives the spectrum of the actual displacement. The calculation method of $\tilde{w}_R(\beta), \tilde{u}_j(\beta,\gamma,z)$ etc. will be devised in Section 5.3.

If the inverse Fourier transforms of $\tilde{u}_j(\beta,\gamma,z), \tilde{v}_j(\beta,\gamma,z)$ and $\tilde{w}_j(\beta,\gamma,z)$ are denoted by $u_j^*(x,y,z)$, $v_j^*(x,y,z)$ and $w_j^*(x,y,z)$, respectively, from equation (5.15) the actual displacements of the ground are given by

$$\left.\begin{aligned} u_j(x,y,z,t) &= \int_{-\infty}^{\infty} u_j^*(x-ct,y,z)e^{i\Omega t}d\Omega \\ v_j(x,y,z,t) &= \int_{-\infty}^{\infty} v_j^*(x-ct,y,z)e^{i\Omega t}d\Omega \\ w_j(x,y,z,t) &= \int_{-\infty}^{\infty} w_j^*(x-ct,y,z)e^{i\Omega t}d\Omega \end{aligned}\right\} \tag{5.16}$$

It may be useful to express equation (5.16) alternatively. If $u_j^*(x,y,z)$, $v_j^*(x,y,z)$ and $w_j^*(x,y,z)$ are due to a single unit harmonic load of frequency Ω, then they are denoted by $u_j^\Omega(x,y,z)$, $v_j^\Omega(x,y,z)$ and $w_j^\Omega(x,y,z)$, to indicate their dependence on Ω. Equation (5.16) now can be expressed as

$$\left.\begin{aligned} u_j(x,y,z,t) &= \int_{-\infty}^{\infty}\sum_{l=1}^{M}[u_j^\Omega(x-a_l-ct,y,z)\tilde{P}_l(\Omega)]e^{i\Omega t}d\Omega \\ v_j(x,y,z,t) &= \int_{-\infty}^{\infty}\sum_{l=1}^{M}[v_j^\Omega(x-a_l-ct,y,z)\tilde{P}_l(\Omega)]e^{i\Omega t}d\Omega \\ w_j(x,y,z,t) &= \int_{-\infty}^{\infty}\sum_{l=1}^{M}[w_j^\Omega(x-a_l-ct,y,z)\tilde{P}_l(\Omega)]e^{i\Omega t}d\Omega \end{aligned}\right\} \tag{5.17}$$

Equation (5.17) expresses the actual displacements in terms of an infinite integral. However, due to the limited bandwidths of the spectra of the wheel-rail forces, the integration limits in equation (5.17) can be truncated.

With the substitution of equation (5.15) into equations (5.14), (5.10), (5.11) and (5.12) and putting

$$\tilde{P} = \sum_{l=1}^{M}\tilde{P}_l(\Omega)e^{-i\beta a_l} \tag{5.18}$$

$$\omega = \Omega - \beta c \tag{5.19}$$

yields,

$$EI\beta^4\tilde{w}_R(\beta)-\omega^2 m_R\tilde{w}_R(\beta)+k_P[\tilde{w}_R(\beta)-\tilde{w}_S(\beta)]=\tilde{P} \tag{5.20}$$

$$-\omega^2 m_S\tilde{w}_S(\beta)+k_P[\tilde{w}_S(\beta)-\tilde{w}_R(\beta)]=-\tilde{F}_2(\beta) \tag{5.21}$$

$$-\frac{m_B\omega^2}{6}\begin{bmatrix}2 & 1\\ 1 & 2\end{bmatrix}\begin{Bmatrix}\tilde{w}_S(\beta)\\ \tilde{w}_C(\beta)\end{Bmatrix}+k_B\begin{bmatrix}1 & -1\\ -1 & 1\end{bmatrix}\begin{Bmatrix}\tilde{w}_S(\beta)\\ \tilde{w}_C(\beta)\end{Bmatrix}=\begin{Bmatrix}\tilde{F}_2(\beta)\\ -\tilde{F}_3(\beta)\end{Bmatrix} \tag{5.22}$$

$$\left.\begin{aligned}
&(\lambda_j+\mu_j)i\beta\tilde{\Delta}_j+\mu_j[\frac{d^2\tilde{u}_j}{dz^2}-(\beta^2+\gamma^2-\frac{\omega^2\rho_j}{\mu_j})\tilde{u}_j]=0\\
&(\lambda_j+\mu_j)i\gamma\tilde{\Delta}_j+\mu_j[\frac{d^2\tilde{v}_j}{dz^2}-(\beta^2+\gamma^2-\frac{\omega^2\rho_j}{\mu_j})\tilde{v}_j]=0\\
&(\lambda_j+\mu_j)\frac{d\tilde{\Delta}_j}{dz}+\mu_j[\frac{d^2\tilde{w}_j}{dz^2}-(\beta^2+\gamma^2-\frac{\omega^2\rho_j}{\mu_j})\tilde{w}_j]=0
\end{aligned}\right\}\ (j=1,2,\cdots,n+1) \tag{5.23}$$

Equations (5.20) to (5.23) may be termed the equations of motion of the track-ground system in the frequency-wavenumber domain, where the frequency and wavenumber are related to each other through equation (5.19).

Comparing equations (5.20) to (5.23) with reference [Sheng, Jones and Petyt 1999(a)], it can be seen that they are the same as the Fourier transformed equations of motion of the track-ground system when a stationary harmonic load $\tilde{P}e^{i\omega t}$ acts at the head of the rail, where $\tilde{P}$ is given by equation (5.18) as a function of Ω and β, and the angular frequency ω is determined by equation (5.19). Therefore the approach developed to solve these equations in that work, which will be briefly summarised in Section 5.3, can be applied here. Once $\tilde{u}_j(\beta,\gamma,z)$ etc. are calculated, then $\bar{u}_j(\beta,\gamma,z,t)$ etc. are given by equation (5.15).

5.3 DISPLACEMENTS OF THE RAILWAY TRACK AND THE GROUND SURFACE

5.3.1 WHEN THE SPECTRA OF THE WHEEL-RAIL FORCES ARE CONTINUOUS

Denoting the Fourier transformed distributed forces (the term $e^{i\omega t}$ is dropped) on the ground surface by $\tilde{p}_x(\beta,\gamma),\tilde{p}_y(\beta,\gamma),\tilde{p}_z(\beta,\gamma)$ and putting

$$\left.\begin{aligned}\{\tilde{u}\}_{10} &= (\tilde{u}_1(\beta,\gamma,0),\tilde{v}_1(\beta,\gamma,0),\tilde{w}_1(\beta,\gamma,0))^T \\ \{\tilde{p}\} &= (\tilde{p}_x(\beta,\gamma),\tilde{p}_y(\beta,\gamma),\tilde{p}_z(\beta,\gamma))^T\end{aligned}\right\} \tag{5.24}$$

then equation (2.60) in Chapter 2 yields

$$\{\tilde{u}\}_{10} = [\tilde{Q}]\{\tilde{p}\} \tag{5.25}$$

where

$$[\tilde{Q}] = [\tilde{Q}(\beta,\gamma,\Omega-\beta c)] = \begin{bmatrix}\tilde{Q}_{11} & \tilde{Q}_{12} & \tilde{Q}_{13} \\ \tilde{Q}_{21} & \tilde{Q}_{22} & \tilde{Q}_{23} \\ \tilde{Q}_{31} & \tilde{Q}_{32} & \tilde{Q}_{33}\end{bmatrix} \tag{5.26}$$

as defined in Chapter 2, is termed the Fourier transformed moving dynamic flexibility matrix. Its calculation and properties have been discussed in detail in Chapter 2. The force vector $\{\tilde{p}\}$ applied on the ground surface by the track is determined through the coupling of the track with the ground.

To couple the ground with the track, use is made of the continuity of displacement and stress in the contact plane, that is

$$w_1(x,0,0,t) = w_C(x,t) \tag{5.27}$$

$$p_z(x,y,t) = \begin{cases}\dfrac{F_3(x,t)}{2b}, & |y| \le b \\ 0, & \text{elsewhere}\end{cases} \tag{5.28}$$

where

$$\begin{aligned}w_1(x,0,0,t) &= \frac{1}{4\pi^2}\int_{-\infty}^{\infty}\int_{-\infty}^{\infty}\overline{w}_1(\beta,\gamma,0,t)e^{i(\beta x+\gamma y)}d\beta d\gamma\Big|_{y=0} \\ &= \frac{1}{4\pi^2}\int_{-\infty}^{\infty}\int_{-\infty}^{\infty}\overline{w}_1(\beta,\gamma,0,t)e^{i\beta x}d\beta d\gamma\end{aligned} \tag{5.29}$$

Fourier transforming equation (5.29) with respect to x only and taking into account equation (5.27) gives

$$\overline{w}_C(\beta,t) = \frac{1}{2\pi}\int_{-\infty}^{\infty}\overline{w}_1(\beta,\gamma,0,t)d\gamma \tag{5.30}$$

Fourier transforming equation (5.28) with respect to x and y, results in

$$\bar{p}_z(\beta,\gamma,t) = \bar{\bar{F}}_3(\beta,t)\frac{\sin\gamma b}{\gamma b} \tag{5.31}$$

The substitution of equation (5.15) into equations (5.30) and (5.31), yields

$$\tilde{w}_C(\beta) = \frac{1}{2\pi}\int_{-\infty}^{\infty}\tilde{w}_1(\beta,\gamma,0)d\gamma \tag{5.32}$$

$$\tilde{p}_z(\beta,\gamma) = \tilde{F}_3(\beta)\frac{\sin\gamma b}{\gamma b} \tag{5.33}$$

With the substitution of equation (5.33) into equation (5.25) and noting the assumption that in the contact plane there is only normal stress, gives

$$\tilde{w}_1(\beta,\gamma,0) = \tilde{Q}_{33}\tilde{F}_3(\beta)\frac{\sin\gamma b}{\gamma b},$$

and from equation (5.32) this yields

$$\tilde{w}_C(\beta) = (\frac{1}{2\pi}\int_{-\infty}^{\infty}\tilde{Q}_{33}\frac{\sin\gamma b}{\gamma b}d\gamma)\tilde{F}_3(\beta) \tag{5.34}$$

Putting $\tilde{H}(\beta) = \frac{1}{2\pi}\int_{-\infty}^{\infty}\tilde{Q}_{33}\frac{\sin\gamma b}{\gamma b}d\gamma$ and making use of the fact that the integrand is an even function of γ (see Section 2.5.1), results in

$$\tilde{H}(\beta) = \frac{1}{\pi}\int_{0}^{\infty}\tilde{Q}_{33}\frac{\sin\gamma b}{\gamma b}d\gamma \tag{5.35}$$

Thus equation (5.34) may be written as

$$\tilde{w}_C(\beta) = \tilde{H}(\beta)\tilde{F}_3(\beta) \tag{5.36}$$

Equation (5.36) formulates the coupling of the track with the ground. It can be seen from equation (5.35) that $\tilde{H}(\beta)$ is independent of the railway track parameters except for the width of its contact with the ground surface. When the train speed c is set to zero, $\tilde{H}(\beta)$ is an even function of β because $\tilde{Q}_{33}(\beta,\gamma,\Omega-\beta c) = \tilde{Q}_{33}(\beta,\gamma,\Omega)$ but not

otherwise. The physical meaning of $\tilde{H}(\beta)$ can be shown as follows. Suppose a vertical harmonic line-distributed load of frequency Ω and of amplitude

$$p_z(x,y)=\begin{cases}\frac{1}{2b}\delta(x), & |y|\le b\\ 0, & \text{elsewhere}\end{cases} \tag{5.37}$$

the double Fourier transform of which is

$$\tilde{p}_z=\frac{\sin\gamma b}{\gamma b} \tag{5.38}$$

moves along the x-axis over the ground surface at speed c, then the Fourier transformed (with respect to x only) steady state vertical displacements of points on the x-axis can be formulated as

$$\frac{1}{2\pi}\int_{-\infty}^{\infty}\tilde{Q}_{33}(\beta,\gamma,\Omega-\beta c)\frac{\sin\gamma b}{\gamma b}e^{i\gamma y}d\gamma\Big|_{y=0}=\frac{1}{2\pi}\int_{-\infty}^{\infty}\tilde{Q}_{33}(\beta,\gamma,\Omega-\beta c)\frac{\sin\gamma b}{\gamma b}d\gamma$$

(with the term $e^{i(\Omega-\beta c)t}$ dropped) which, as defined above, is identical to $\tilde{H}(\beta)$. More discussion on $\tilde{H}(\beta)$ will be given in Chapter 6.

Using equation (5.36) and equations (5.20) to (5.22), $\tilde{w}_R(\beta)$ and $\tilde{F}_3(\beta)$ can be found as

$$\tilde{w}_R(\beta)=\frac{b_1k_P+(b_1a_{22}-b_2a_{12})\tilde{H}(\beta)}{a_{11}k_P+(a_{11}a_{22}-a_{12}a_{21})\tilde{H}(\beta)}\tilde{P} \tag{5.39}$$

$$\tilde{F}_3(\beta)=\frac{a_{11}b_2-a_{21}b_1}{a_{11}k_P+(a_{11}a_{22}-a_{12}a_{21})\tilde{H}(\beta)}\tilde{P} \tag{5.40}$$

where

$$a_{11}=[k_P+k_B-(m_S+\tfrac{1}{3}m_B)\omega^2](EI\beta^4+k_P-m_R\omega^2)-k_P^2 \tag{5.41}$$

$$a_{12}=-k_P(k_B+\tfrac{1}{6}m_B\omega^2) \tag{5.42}$$

$$a_{21} = -(k_B + \frac{1}{6} m_B \omega^2)(EI\beta^4 + k_P - m_R \omega^2) \tag{5.43}$$

$$a_{22} = k_P (k_B - \frac{1}{3} m_B \omega^2) \tag{5.44}$$

$$b_1 = [k_P + k_B - (m_S + \frac{1}{3} m_B)\omega^2] \tag{5.45}$$

$$b_2 = -(k_B + \frac{1}{6} m_B \omega^2) \tag{5.46}$$

and $\tilde{P}$ is given by equation (5.18).

Combining equations (5.33) and (5.26) gives

$$\left.\begin{aligned} \tilde{u}_1(\beta,\gamma,0) &= \tilde{Q}_{13} \frac{\sin \gamma b}{\gamma b} \tilde{F}_3(\beta) \\ \tilde{v}_1(\beta,\gamma,0) &= \tilde{Q}_{23} \frac{\sin \gamma b}{\gamma b} \tilde{F}_3(\beta) \\ \tilde{w}_1(\beta,\gamma,0) &= \tilde{Q}_{33} \frac{\sin \gamma b}{\gamma b} \tilde{F}_3(\beta) \end{aligned}\right\} \tag{5.47}$$

By performing an inverse Fourier transform on equation (5.47) (usually using an FFT algorithm) and substituting the results into equation (5.17) gives the actual displacement of the ground surface.

5.3.2 WHEN THE SPECTRA OF THE WHEEL-RAIL FORCES ARE DISCRETE

If the spectra of the wheel-rail forces are discrete, the calculation of the actual ground surface displacements can be summarised as follows.

(i) Express $P_l(t)$ in the form of (see equation (5.13))

$$P_l(t) = \sum_k \tilde{P}_{lk}(\Omega_k) e^{i\Omega_k t} \quad (l = 1,2,\cdots,M)$$

where k indicates the kth harmonic component of $P_l(t)$. For various k, carry out (ii) to (vi).

(ii) Put $\tilde{P} = \sum_{l=1}^{M} \tilde{P}_{lk}(\Omega_k) e^{-i\beta a_l}$, $\omega = \Omega_k - \beta c$ (see equations (5.18) and (5.19)).

(iii) Calculate matrix $[\tilde{Q}(\beta,\gamma,\Omega_k - \beta c)]$ (see equation (5.26)).

(iv) Calculate $\tilde{H}(\beta)$ (see equation (5.35)).

(v) By substituting equation (5.36) into equations (5.20) to (5.22), calculate $\tilde{w}_R(\beta),\tilde{w}_S(\beta),\tilde{F}_2(\beta),\tilde{F}_3(\beta)$.

(vi) Calculate $\tilde{u}_1(\beta,\gamma,0),\tilde{v}_1(\beta,\gamma,0),\tilde{w}_1(\beta,\gamma,0)$ (see equation (5.47)). To emphasise their dependence on the *k*th harmonic component, alternative notations, $\tilde{u}_{1k}(\beta,\gamma,0)$, $\tilde{v}_{1k}(\beta,\gamma,0)$ and $\tilde{w}_{1k}(\beta,\gamma,0)$, are used hereinafter.

(vii) Calculate the Fourier transformed displacements of the ground surface (see equation (5.15))

$$\bar{u}_1(\beta,\gamma,0,t) = \sum_k \tilde{u}_{1k}(\beta,\gamma,0)e^{i(\Omega_k-\beta c)t}$$
$$\bar{v}_1(\beta,\gamma,0,t) = \sum_k \tilde{v}_{1k}(\beta,\gamma,0)e^{i(\Omega_k-\beta c)t}$$
$$\bar{w}_1(\beta,\gamma,0,t) = \sum_k \tilde{w}_{1k}(\beta,\gamma,0)e^{i(\Omega_k-\beta c)t}$$

(viii) Calculate the inverse Fourier transforms of $\bar{u}_1(\beta,\gamma,0,t),\bar{v}_1(\beta,\gamma,0,t),\bar{w}_1(\beta,\gamma,0,t)$. The results are actual longitudinal, lateral and vertical displacements, of the ground surface. By denoting the inverse Fourier transforms of $\tilde{u}_{1k}(\beta,\gamma,0)$, $\tilde{v}_{1k}(\beta,\gamma,0)$ and $\tilde{w}_{1k}(\beta,\gamma,0)$ by $u^*_{1k}(x,y)$, $v^*_{1k}(x,y)$ and $w^*_{1k}(x,y)$, then

$$u_1(x,y,0,t) = \sum_k u^*_{1k}(x-ct,y)e^{i\Omega_k t}$$
$$v_1(x,y,0,t) = \sum_k v^*_{1k}(x-ct,y)e^{i\Omega_k t}$$
$$w_1(x,y,0,t) = \sum_k w^*_{1k}(x-ct,y)e^{i\Omega_k t}$$

5.4 DISPLACEMENT SPECTRA OF THE GROUND SURFACE

In previous work [Sheng, Jones and Petyt 1999 (b) and Jones, Sheng and Petyt 2000], results have been produced as displacement response in the moving frame of reference due to a single moving load oscillating at a single frequency. These visualisations of the surface wave-field are instructive, but, now, calculating for the effects

of multiple loads, it is important to derive spectra of vibration response at particular fixed positions. By this means, a presentation of results closer to that obtained by measurements is achieved.

5.4.1 WHEN THE SPECTRA OF THE RAIL-WHEEL FORCES ARE CONTINUOUS

Fourier transforming equation (5.16) with respect to time t, gives the ground surface displacement spectra (put $j = 1$, $z = 0$). The spectra of $u_1(x,y,0,t), v_1(x,y,0,t), w_1(x,y,0,t)$ are denoted by $S_u(x,y,f), S_v(x,y,f), S_w(x,y,f)$, respectively, where f is the frequency at which the spectra are evaluated. Thus

$$S_u(x,y,f) = \int_{-\infty}^{\infty} u_1(x,y,0,t) e^{-i2\pi ft} dt = \int_{-\infty}^{\infty} \left(\int_{-\infty}^{\infty} u_1^*(x-ct,y,0) e^{-i(2\pi f - \Omega)t} dt \right) d\Omega$$

Putting $x\text{-}ct = \xi$, then $dt = -1/c\, d\xi$, yields

$$S_u(x,y,f) = \frac{1}{c} \int_{-\infty}^{\infty} \left(\int_{-\infty}^{\infty} u_1^*(\xi,y,0) e^{-i(2\pi f - \Omega)(x-\xi)/c} d\xi \right) d\Omega$$

Putting

$$\beta = (\Omega - 2\pi f)/c, \quad \Omega = 2\pi f + \beta c, \quad d\Omega = c\, d\beta \tag{5.48}$$

and therefore equation (5.19) becomes

$$\omega = \Omega - \beta c = 2\pi f \tag{5.49}$$

Then

$$S_u(x,y,f) = \int_{-\infty}^{\infty} \left(\int_{-\infty}^{\infty} u_1^*(\xi,y,0) e^{-i\beta\xi} d\xi \right) e^{i\beta x} d\beta$$

Noting that $u_1^*(\xi,y,0) = \frac{1}{4\pi^2} \int_{-\infty}^{\infty} \int_{-\infty}^{\infty} \tilde{u}_1(\beta,\gamma,0) e^{i(\beta\xi+\gamma y)} d\beta d\gamma$

$$S_u(x,y,f) = \frac{1}{2\pi} \int_{-\infty}^{\infty} \int_{-\infty}^{\infty} \tilde{u}_1(\beta,\gamma,0) e^{i\beta x} e^{i\gamma y} d\beta d\gamma \tag{5.50}$$

Similarly,

$$S_v(x,y,f)=\frac{1}{2\pi}\int_{-\infty}^{\infty}\int_{-\infty}^{\infty}\tilde{v}_1(\beta,\gamma,0)e^{i\beta x}e^{i\gamma y}d\beta d\gamma \tag{5.51}$$

$$S_w(x,y,f)=\frac{1}{2\pi}\int_{-\infty}^{\infty}\int_{-\infty}^{\infty}\tilde{w}_1(\beta,\gamma,0)e^{i\beta x}e^{i\gamma y}d\beta d\gamma \tag{5.52}$$

and for the rail and sleeper, the vibration spectra are

$$S_R(x,f)=\int_{-\infty}^{\infty}e^{i\beta x}\tilde{w}_R(\beta)d\beta \tag{5.53}$$

$$S_S(x,f)=\int_{-\infty}^{\infty}e^{i\beta x}\tilde{w}_S(\beta)d\beta \tag{5.54}$$

Equations (5.50) to (5.54) show that, by letting $\Omega=2\pi f+\beta c$ in equation (5.18) and $\omega=2\pi f$ in equation (5.19), calculating $\tilde{u}_1(\beta,\gamma,0),\tilde{v}_1(\beta,\gamma,0)$, and $\tilde{w}_1(\beta,\gamma,0)$ as shown in Section 5.3, then the vibration spectra at frequency f are determined by performing inverse Fourier transform on $\tilde{u}_1(\beta,\gamma,0),\tilde{v}_1(\beta,\gamma,0)$, and $\tilde{w}_1(\beta,\gamma,0)$.

It is worth pointing out that multiplying the displacement spectra by $i2\pi f$ gives the velocity spectra that are more often used in practice.

5.4.2 WHEN THE SPECTRA OF THE RAIL-WHEEL FORCES ARE DISCRETE

If the spectra of the wheel-rail forces are discrete, the calculation of the displacement spectra of the ground surface at frequency f may be summarised as follows.

(i) Express $P_l(t)$ in form of (see equation (5.13))

$$P_l(t)=\sum_k\tilde{P}_{lk}(\Omega_k)e^{i\Omega_k t}\quad(l=1,2,\cdots,M)$$

where k indicates the kth harmonic component of $P_l(t)$. For various k, carry out (ii) to (vi).

(ii) Put $\beta_k=(\Omega_k-2\pi f)/c,\tilde{P}=\sum_{l=1}^{M}\tilde{P}_{lk}(\Omega_k)e^{-i\beta_k a_l},\omega_k=\Omega_k-\beta_k c=2\pi f$ (see equations (5.18), (5.19) and (5.49)).

(iii) Calculate matrix $[\tilde{Q}(\beta_k,\gamma,2\pi f)]$ (see equation (5.26)).

(iv) Calculate $\tilde{H}(\beta_k)$ (see equation (5.35)).

(v) With the substitution of equation (5.35) into equations (5.20) to (5.22), compute $\tilde{w}_R(\beta_k), \tilde{w}_S(\beta_k), \tilde{F}_2(\beta_k), \tilde{F}_3(\beta_k)$.

(vi) Calculate $\tilde{u}_1(\beta_k,\gamma,0), \tilde{v}_1(\beta_k,\gamma,0), \tilde{w}_1(\beta_k,\gamma,0)$ (see equation (5.47)). To emphasise the fact that they are due to the kth harmonic component, alternative notations, $\tilde{u}_{1k}(\beta_k,\gamma,0)$, $\tilde{v}_{1k}(\beta_k,\gamma,0)$ and $\tilde{w}_{1k}(\beta_k,\gamma,0)$, are used hereinafter.

(vii) Calculate the displacement spectra of the ground surface, rail and sleeper

$$\left.\begin{aligned}
S_u(x,y,f) &= \frac{1}{c}\sum_k e^{i\beta_k x}\left(\frac{1}{2\pi}\int_{-\infty}^{\infty}\tilde{u}_{1k}(\beta_k,\gamma,0)e^{i\gamma y}d\gamma\right)\\
S_v(x,y,f) &= \frac{1}{c}\sum_k e^{i\beta_k x}\left(\frac{1}{2\pi}\int_{-\infty}^{\infty}\tilde{v}_{1k}(\beta_k,\gamma,0)e^{i\gamma y}d\gamma\right)\\
S_w(x,y,f) &= \frac{1}{c}\sum_k e^{i\beta_k x}\left(\frac{1}{2\pi}\int_{-\infty}^{\infty}\tilde{w}_{1k}(\beta_k,\gamma,0)e^{i\gamma y}d\gamma\right)\\
S_R(x,f) &= \frac{1}{c}\sum_k e^{i\beta_k x}\tilde{w}_{Rk}(\beta_k)\\
S_S(x,f) &= \frac{1}{c}\sum_k e^{i\beta_k x}\tilde{w}_{Sk}(\beta_k)
\end{aligned}\right\} \qquad (5.55)$$

(see equations (5.50) to (5.54)).

5.4.3 WHEN RAIL-WHEEL FORCES ARE HARMONIC AT A SINGLE FREQUENCY

Assume that all the wheel-rail forces are harmonic at a single frequency Ω. When $\tilde{P}$ in equation (5.20) is replaced by a unit force, the corresponding solutions of equations (5.20) to (5.22) for $\tilde{w}_R(\beta), \tilde{w}_S(\beta), \tilde{F}_3(\beta)$ are denoted by $\tilde{w}_R^0(\beta), \tilde{w}_S^0(\beta), \tilde{F}_3^0(\beta)$. The spectra of the ground surface and the track can be rewritten, according to equations (5.18), (5.33), (5.47) and (5.55), as follows

$$\left.\begin{aligned}
S_u(x,y,f;\Omega) &= S_u^0(x,y,f;\Omega)\left(\sum_{l=1}^{M}\tilde{P}_l e^{-ia_l(\Omega-2\pi f)/c}\right)\\
S_v(x,y,f;\Omega) &= S_v^0(x,y,f;\Omega)\left(\sum_{l=1}^{M}\tilde{P}_l e^{-ia_l(\Omega-2\pi f)/c}\right)\\
S_w(x,y,f;\Omega) &= S_w^0(x,y,f;\Omega)\left(\sum_{l=1}^{M}\tilde{P}_l e^{-ia_l(\Omega-2\pi f)/c}\right)\\
S_R(x,f;\Omega) &= S_R^0(x,y,f;\Omega)\left(\sum_{l=1}^{M}\tilde{P}_l e^{-ia_l(\Omega-2\pi f)/c}\right)\\
S_S(x,f;\Omega) &= S_S^0(x,y,f;\Omega)\left(\sum_{l=1}^{M}\tilde{P}_l e^{-ia_l(\Omega-2\pi f)/c}\right)
\end{aligned}\right\} \qquad (5.56)$$

where, new notations have been introduced for the spectra to indicate their dependence on the load frequency Ω, $\tilde{P}_l$ is the amplitude of the lth wheel-rail force, and

$$\left.\begin{aligned}
S_u^0(x,y,f;\Omega) &= \frac{1}{c}e^{ix(\Omega-2\pi f)/c}\tilde{F}_3^0\left(\tfrac{\Omega-2\pi f}{c}\right)\left(\frac{1}{2\pi}\int_{-\infty}^{\infty}\tilde{Q}_{13}\left(\tfrac{\Omega-2\pi f}{c},\gamma,2\pi f\right)\frac{\sin\gamma b}{\gamma b}e^{iy\gamma}d\gamma\right)\\
S_v^0(x,y,f;\Omega) &= \frac{1}{c}e^{ix(\Omega-2\pi f)/c}\tilde{F}_3^0\left(\tfrac{\Omega-2\pi f}{c}\right)\left(\frac{1}{2\pi}\int_{-\infty}^{\infty}\tilde{Q}_{23}\left(\tfrac{\Omega-2\pi f}{c},\gamma,2\pi f\right)\frac{\sin\gamma b}{\gamma b}e^{iy\gamma}d\gamma\right)\\
S_w^0(x,y,f;\Omega) &= \frac{1}{c}e^{ix(\Omega-2\pi f)/c}\tilde{F}_3^0\left(\tfrac{\Omega-2\pi f}{c}\right)\left(\frac{1}{2\pi}\int_{-\infty}^{\infty}\tilde{Q}_{33}\left(\tfrac{\Omega-2\pi f}{c},\gamma,2\pi f\right)\frac{\sin\gamma b}{\gamma b}e^{iy\gamma}d\gamma\right)\\
S_R^0(x,f;\Omega) &= \frac{1}{c}\tilde{w}_R^0\left(\tfrac{\Omega-2\pi f}{c}\right)e^{ix(\Omega-2\pi f)/c}\\
S_S^0(x,f;\Omega) &= \frac{1}{c}\tilde{w}_S^0\left(\tfrac{\Omega-2\pi f}{c}\right)e^{ix(\Omega-2\pi f)/c}
\end{aligned}\right\} \qquad (5.57)$$

are spectra due to a single unit harmonic force of frequency Ω moving along the rails at speed c.

From equations (5.56) and (5.57) it can be seen that, when $2\pi f = \Omega$, since $\tilde{Q}_{13}(0,\gamma,2\pi f) \equiv 0$ (see Section 2.5.1), $S_u(x,y,f;\Omega) = 0$, i.e. the longitudinal spectrum vanishes at the wheel-rail load frequency. It can also be seen that the modulus of each spectrum is independent of the value of x.

The term

$$S_P(f) = \sum_{l=1}^{M}\tilde{P}_l e^{-ia_l(\Omega-2\pi f)/c} \qquad (5.58)$$

in equation (5.56) may be identified as the load spectrum which reflects the harmonic components of the excitation produced by the passage of the axles of a train. During the passage of a train of many similar wagons, the pattern of axles of the wagons may give rise to strong harmonic components. However, the spectra vanish at frequencies

satisfying $\sum_{l=1}^{M} \tilde{P}_l e^{-ia_l(\Omega-2\pi f)/c} = 0$. In principle, this equation shows that certain frequencies can be eliminated from the excitation of ground vibration by a careful choice of wagon axle spacing. However, this is not likely to be a practical proposition in order to treat problem frequencies that are dependent on the ground and track properties of a particular site. It may, however, offer a choice of speed particular to the vehicle type which reduces a certain (narrow) range of excitation frequency. It is noticed that a shift of x-coordinates does not change the amplitude of the load spectrum. In fact, let $a_l = a_l' + a_0$ in equation (5.58), where, a_l' are the new co-ordinates of the forces at $t = 0$, a_0 is a constant. Then

$$\begin{aligned} |S_P(f)| &= \left| \sum_{l=1}^{M} \tilde{P}_l e^{-i(a_l'+a_0)(\Omega-2\pi f)/c} \right| = \left| \sum_{l=1}^{M} \tilde{P}_l e^{-ia_l'(\Omega-2\pi f)/c} \right| \left| e^{-ia_0(\Omega-2\pi f)/c} \right| \\ &= \left| \sum_{l=1}^{M} \tilde{P}_l e^{-ia_l'(\Omega-2\pi f)/c} \right| \end{aligned}$$

From equation (5.56), for example,

$$|S_w(x, y, f; \Omega)| = |S_w^0(x, y, f; \Omega)| \left| \sum_{l=1}^{M} \tilde{P}_l e^{-ia_l(\Omega-2\pi f)/c} \right| \tag{5.59}$$

This means that when the rail-wheel forces are harmonic at a single frequency, the amplitudes of displacement (velocity, acceleration) spectra are independent not only of x but also of the absolute positions of the wheel-rail forces.

5.5 SUMMARY

In this chapter, a mathematical model, which couples the ground model developed in Chapter 2 and the track model in Chapter 4, has been developed for predicting the ground vibration generated by vertical wheel-rail. Though the equations for only one particular track structure are presented, other types of track structure can be modelled by simple modifications of the track equations. Two purposes are intended to be served by this model: one is to study ground vibration generated by the quasi-static loads (the multiple axle loads) and the other is to develop a ground vibration model which comprises vehicles, track and ground. During the passages of a train of many similar wagons, the pattern of axles of the train may give rise to, or suppress, some harmonic components. These harmonic components are formulated in terms of the dimensions of

the wagons as well as the train speed. A number of results from this model will be presented in the next chapter.

Chapter 6

GROUND VIBRATION GENERATED BY VERTICAL WHEEL-RAIL FORCES

PART II: RESULTS AND DISCUSSIONS

6.1 INTRODUCTION

In Chapter 5, formulae have been developed for calculating ground vibrations generated by vertical wheel-rail forces. These formulae and the relevant program can be used to calculate displacements, either in the wavenumber domain or in the spatial domain, and spectra produced by multiple or single moving (if $c \neq 0$) or stationary (if $c = 0$) harmonic (if $\Omega \neq 0$) or constant (if $\Omega = 0$) load(s). To investigate the effects of various factors involved in the problem, a number of calculations are carried out in the present chapter. The results are presented for two tracks (one is the lighter and the other is the heavier) and two grounds (one is the stiffer layered ground and the other is the softer layered ground). Parameters of the tracks and the grounds are listed in Tables 1.6 to 1.9. First in Section 6.2, some properties of $\tilde{H}(\beta)$ (see equation (5.35)) are discussed. Section 6.3 presents the dispersion curves for the grounds and the tracks. The receptances of the track-ground systems are presented in Section 6.4, which are compared with those when the tracks rest on a rigid foundation. The effect of load speeds on the response of a track-ground system is investigated in Section 6.5. The effect of the pattern of the axles of a train on the response of a track-ground system is investigated in Section 6.6. Finally in Section 6.7, conclusions demonstrated by these calculations are summarised.

6.2 DISCUSSIONS ON $\tilde{H}(\beta)$

Equation (5.36) formulates the coupling of a ground and a track, in which $\tilde{H}(\beta)$ is evaluated by the infinite integral

$$\tilde{H}(\beta) = \frac{1}{\pi}\int_0^\infty \tilde{Q}_{33}(\beta, \gamma, \Omega - \beta c)\frac{\sin \gamma b}{\gamma b} d\gamma \tag{6.1}$$

It has been pointed out that if $c = 0$, $\tilde{H}(\beta)$ is an even function of β and otherwise not. Further, by using similar reasoning to that made in Section 3.4 and Section 3.5 of Chapter 3, it can be shown that, if the damping in the ground can be neglected, $\tilde{H}(\beta)$ will be infinite when a propagating wavenumber in the ground coincides with $\beta = | \Omega - 2\pi f | / c$. In other words, an unbounded $\tilde{H}(\beta)$ will appear at the intersections on the dispersion diagram of the dispersion curves and the 'load speed lines' defined by $\beta = | \Omega - 2\pi f | / c$. When the damping in the ground is considered finite, peaks occur at these values of wavenumber.

Figures 6.1 and 6.2 show $\tilde{H}(\beta)$ calculated at $\Omega / 2\pi = 30$ Hz, for $c = 0$ and $c = 50$ m/s for the softer ground. The P-SV dispersion curves along with the load speed lines are also shown here in Figure 6.3 to indicate the intersections of the dispersion curves and the load speed lines. Figure 6.1, for $c = 0$, shows that the highest peak corresponds to the wavenumber of the first mode at frequency 30 Hz ($\beta \approx 2.4$ rad/m). When $|\beta|$ is larger than this wavenumber, the imaginary part of $\tilde{H}(\beta)$ decays quickly and the real part of $\tilde{H}(\beta)$ is positive. In Figure 6.3 two intersections of the load speed line for $c = 50$ m/s with the first mode are shown as β_1 (≈ 1.1 rad/m) and β_2 (≈ 6.8 rad/m). Figure 6.2 for $c = 50$ m/s, shows that when $\beta \geq \beta_1$ or $\beta \leq -\beta_2$, the imaginary part of $\tilde{H}(\beta)$ also decays quickly and its real part remains positive. Peaks in $\tilde{H}(\beta)$ occurs at β_1 and $-\beta_2$.

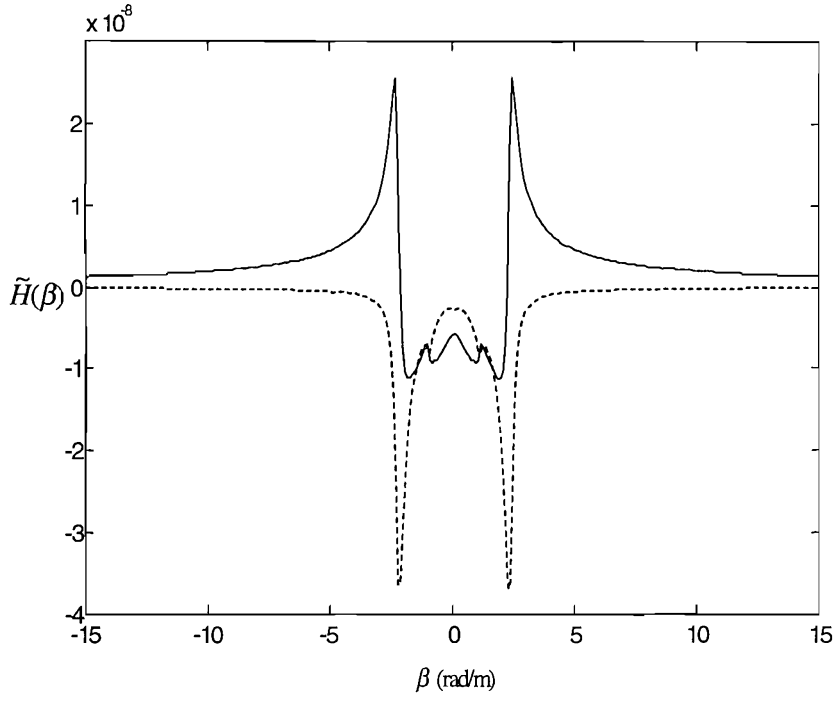

Figure 6.1. $\tilde{H}(\beta)$ calculated for the softer ground with $c = 0$, $\Omega / 2\pi$ = 30 Hz. ——, real part of $\tilde{H}(\beta)$; – – –, imaginary part of $\tilde{H}(\beta)$. When $c = 0$, $\tilde{H}(\beta)$ is an even function of β.

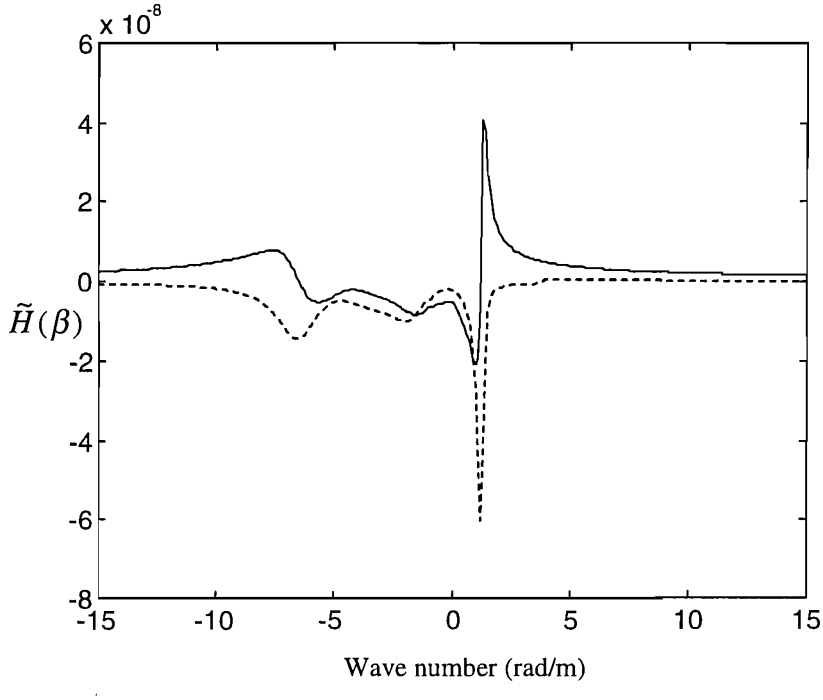

Figure 6.2. $\tilde{H}(\beta)$ calculated for the softer ground with c = 50 m/s, $\Omega / 2\pi$ = 30 Hz. ——, real part of $\tilde{H}(\beta)$; – – –, imaginary part of $\tilde{H}(\beta)$.

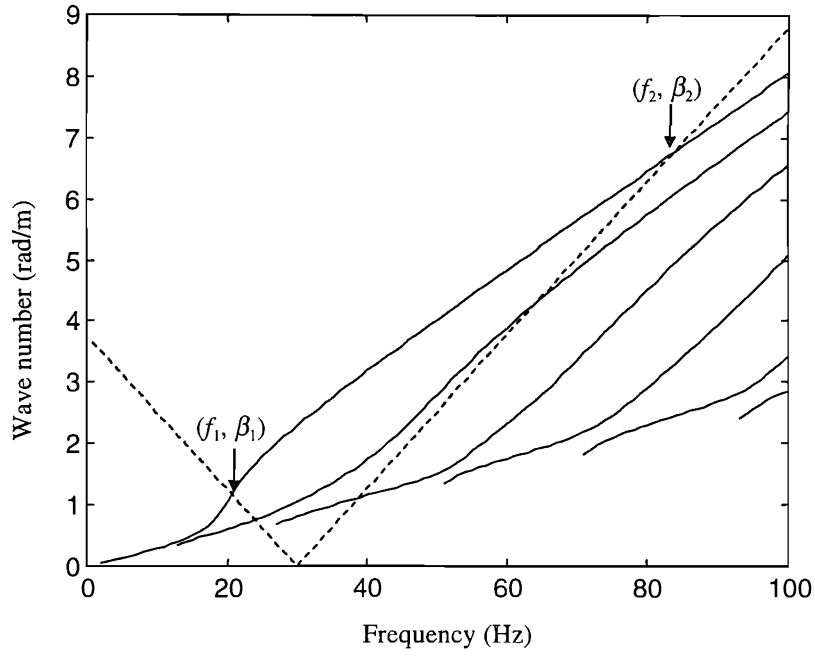

Figure 6.3. P-SV dispersion curves of the softer ground (——) and load speed lines (– – –). Load frequency 30 Hz, load speed 50 m/s.

6.3 DISPERSION CURVES OF THE GROUNDS AND TRACKS

6.3.1 USING FOURIER TRANSFORMED DISPLACEMENTS TO PRODUCE DISPERSION DIAGRAM

The calculation of the dispersion curves of a free ground (a ground without a track structure) has been performed in Chapter 3 by finding the real roots for the dispersion equation. However, for a layered ground with a track, this method is not applicable. An alternative is to calculate the Fourier transformed displacements generated by a surface load for different frequencies and wavenumbers, and then project the displacement peaks on the wavenumber-frequency plane. As an example, the amplitudes of the transformed vertical displacements are calculated for the stiffer ground surface generated by a unit vertical point harmonic load. If the amplitudes are plotted three-dimensionally against wave number β in the x-direction (the wave number γ in the y-direction has been set to zero) and frequency f, then peaks in this plot indicate the propagating wave modes. The projection of these peaks on the (β, f) plane (i.e. the contour plot), as shown in Figure 6.4, gives the P-SV dispersion curves. Figure 6.4 indicates that, in addition to the propagating wave modes shown in Figure 3.1, for some frequencies, an extra mode which has higher wave speed than the shear wave speed in the underlying half-space is also excited by the surface load (see between 40 and 75 Hz). This extra mode is a so-called

'leaky mode' [Jones 1987], and has significant effect on the response of the ground surface as indicated in Figure 3.20.

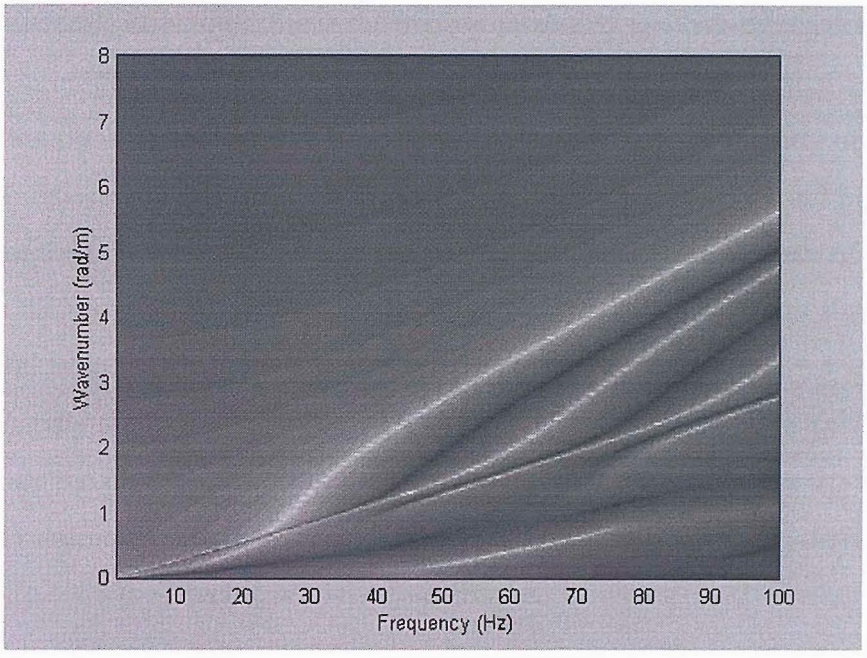

Figure 6.4. Contour plot of the amplitudes of the transformed vertical displacements of the stiffer ground surface (without track) versus wavenumber in the track direction and frequency.

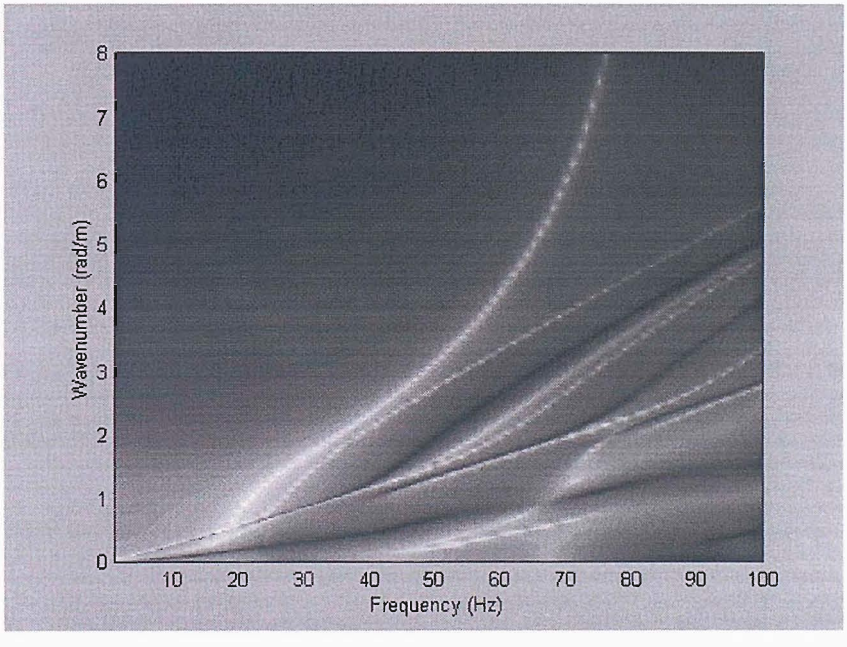

Figure 6.5. Contour plot of the amplitudes of the transformed vertical displacements of the stiffer ground surface with the heavier track versus wavenumber in the track direction and frequency.

6.3.2 A LAYERED GROUND WITH A TRACK STRUCTURE

When a track rests on a ground, the propagation properties of the ground are different in different directions. Since the track is modelled as a two-dimensional structure in the *xz*-plane, the propagation property in the *y*-direction is not affected by the presence of the track. However, in the *x*-direction, the propagation property of the ground will be, to some extent, modified by the track. Figure 6.5 shows the contour plot of the amplitudes of the Fourier transformed vertical displacements of the surface of the stiffer ground with the heavier track. These displacements are produced by a unit stationary harmonic load acting at the head of the rails. Comparing Figures 6.5 and 6.4 it can be seen that, not only the modes of the free ground, but also other modes are excited. These new modes are the propagation modes of the track-ground system. Figure 6.5 also shows that the first mode of the track-ground system has a greater wavenumber, therefore lower phase velocity, than the first mode of the free ground.

Putting $\tilde{P} = 1, \omega = 2\pi f, \gamma = 0$, then equation (5.47) gives the Fourier transformed vertical displacement of the ground surface

$$\tilde{w}_1(\beta,0,0) = \tilde{Q}_{33}(\beta,0,2\pi f)\tilde{F}_3(\beta) = \tilde{Q}_{33}(0,\beta,2\pi f)\tilde{F}_3(\beta) \tag{6.2}$$

According to equations (5.40)

$$\tilde{w}_1(\beta,0,0) = \frac{a_{11}b_2 - a_{21}b_1}{a_{11}k_P/\tilde{H}(\beta) + (a_{11}a_{22} - a_{12}a_{21})} \frac{\tilde{Q}_{33}(\beta,0,2\pi f)}{\tilde{H}(\beta)} \tag{6.3}$$

Equation (5.39) for the transformed displacement of the rails becomes

$$\tilde{w}_R(\beta) = \frac{b_1 k_P + (b_1 a_{22} - b_2 a_{12})\tilde{H}(\beta)}{a_{11}k_P + (a_{11}a_{22} - a_{12}a_{21})\tilde{H}(\beta)} \tag{6.4}$$

where, $a_{11}, a_{12}, a_{21}, a_{22}, b_1, b_2$ are given in equations (5.41) to (5.46).

The wavenumbers of the propagating modes of the track-ground system at frequency f may be identified by the fact that, for no damping, both $\tilde{w}_1(\beta,0,0)$ and $\tilde{w}_R(\beta)$ become infinite. Thus from equations (6.3) and (6.4), the dispersion equation of the track-ground system is given by

$$a_{11}k_P \,/\, \tilde{H}(\beta) + (a_{11}a_{22} - a_{12}a_{21}) = 0 \tag{6.5}$$

If $\tilde{H}(\beta)$ is set to infinity, equation (6.5) gives the dispersion equation of a free track (the lower interface of the track is unrestrained)

$$a_{11}a_{22} - a_{12}a_{21} = 0 \tag{6.6}$$

If $\tilde{H}(\beta)$ is set to zero, equation (6.5) yields the dispersion equation of a track on a rigid foundation (called 'rigid-bed track')

$$a_{11} = 0 \tag{6.7}$$

Finally, if $\tilde{H}(\beta)$ is replaced by a constant $1/k_G$, then equation (6.5) results in the dispersion equation of a track on a Winkler foundation of stiffness k_G. This situation has been discussed in Chapter 4.

Compared to the rigid-bed track, the presence of a ground adds flexibility, mass and radiation damping to the track, as a result, the wave speeds in the track are always much lower than the wave speeds in the 'rigid-bed track', especially for low frequencies.

In the absence of a closed form expression for $\tilde{H}(\beta)$, the analytical formula for the dispersion equation of a track on a ground is not obtainable. As an alternative, the dispersion curves of the free track, the free ground and the rigid-bed track have been produced instead. Figures 6.6 to 6.9 show these dispersion curves. The vertical straight lines in these figures indicate the natural frequencies of the sleeper-ballast-on-supports. From these figures it can be seen that, for a rigid-bed track, a propagating mode exists only at frequencies above the first natural frequency of the track (88 Hz for the lighter track and 51 Hz for the heavy track). For a track with either boundary conditions, propagating modes cease to exist for frequencies lower than the second natural frequency of the track but higher than the natural frequency of the mass of sleeper and ballast vibrating on supports (67 Hz for the lighter free track, 41 Hz for the heavy free track and 92 Hz for the heavier rigid-bed track).

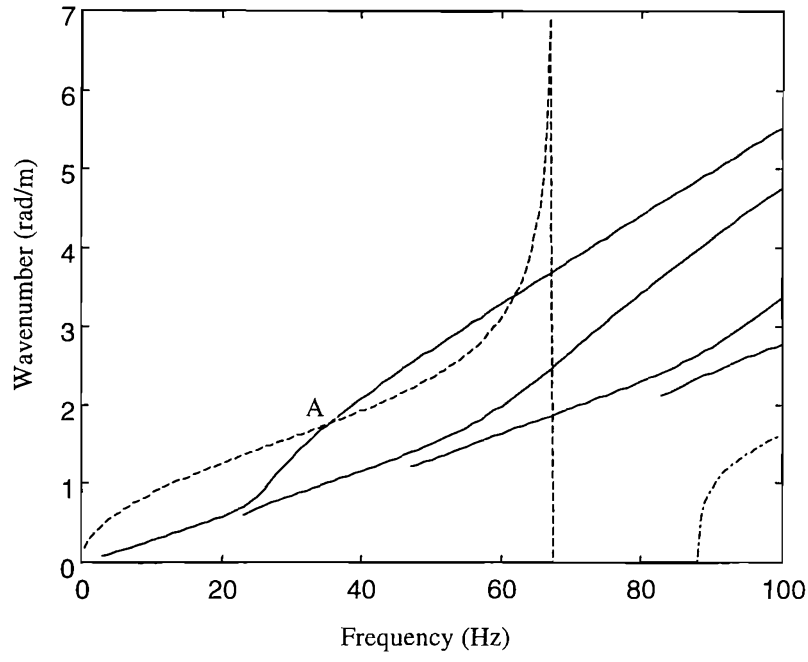

Figure 6.6. Dispersion curves of the stiffer ground (——), the free lighter track (– – –) and the rigid-bed lighter track (– · –).

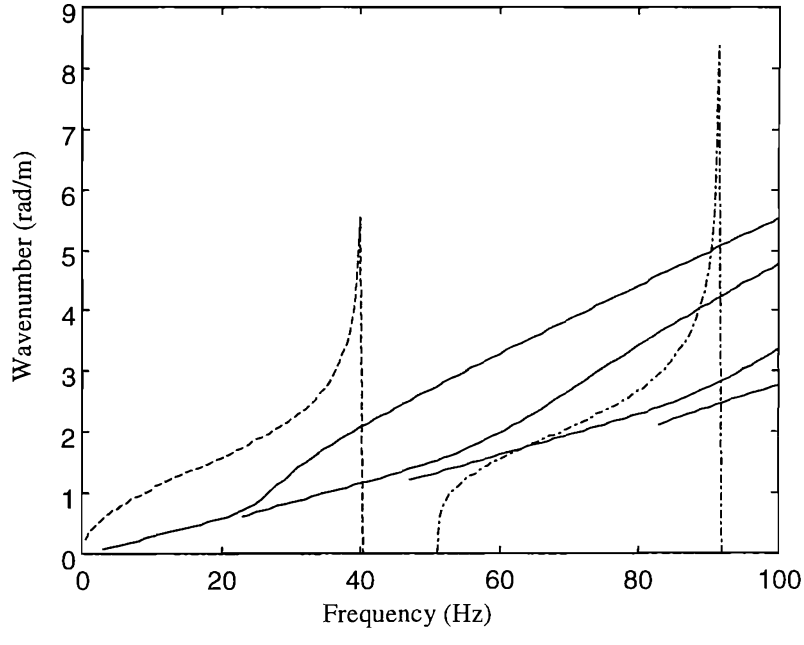

Figure 6.7. Dispersion curves of the stiffer ground (——), the free heavier track (– – –) and the rigid-bed heavier track (– · –).

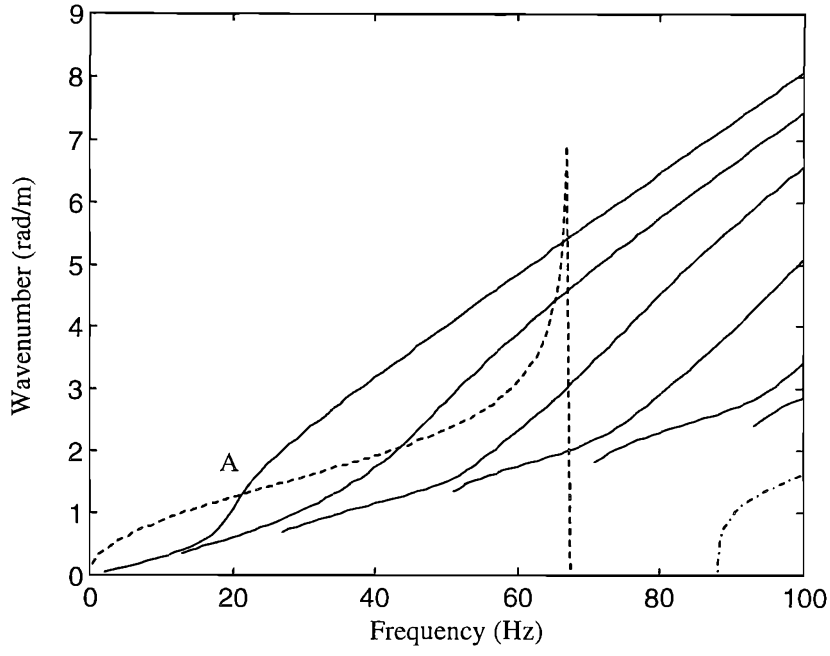

Figure 6.8. Dispersion curves of the softer ground (——), the free lighter track (– – –) and the rigid-bed lighter track (– · –).

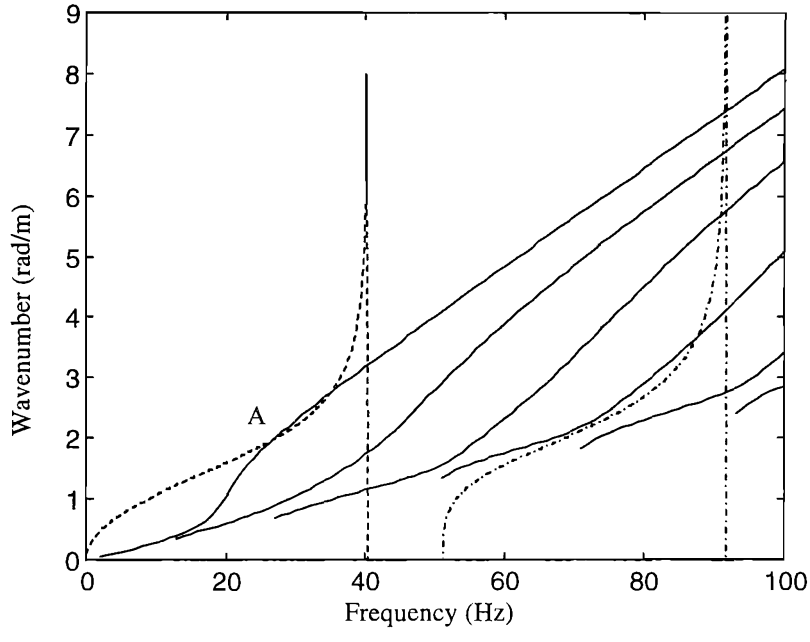

Figure 6.9. Dispersion curves of the softer ground (——), the free heavier track (– – –) and the rigid-bed heavier track (– · –).

If at (f_0, β_0), the dispersion curve of a free track intersects the dispersion curve of a free ground, then since $\tilde{H}(\beta_0) = \infty$, both equations (6.5) and (6.6) hold at this point

(point A in Figures 6.6, 6.8 and 6.9). In other words, a propagating wave can propagate in both the free track and the free ground at speed $2\pi f_0 / \beta_0$.

A general analysis is difficult for the existence of propagating modes in a track-ground system (i.e., the existence of real roots of β in equation (6.5)). However, for a track resting on a homogeneous half-space, some points may be made.

6.3.3 A HOMOGENEOUS HALF-SPACE WITH A TRACK STRUCTURE

For a homogeneous half-space, there is only one straight line on its dispersion diagram, i.e. the Rayleigh wave line. If the Rayleigh wave line is below the dispersion curve of the free track but above the dispersion curve of the rigid-bed track, then for a given frequency, equation (6.5) has a real solution for β, which is greater than the Rayleigh wavenumber but less than the wavenumber of the free track at this frequency. This is because, that below the dispersion curve of the free track but above the Rayleigh wave line, $\tilde{H}(\beta) > 0, a_{11} > 0, a_{11}a_{22} - a_{12}a_{21} < 0$, and when β increases continuously from the Rayleigh wavenumber (at which $\tilde{H}(\beta) = \infty$) to the wavenumber of the free track, $a_{11}k_P / \tilde{H}(\beta) + (a_{11}a_{22} - a_{12}a_{21})$ varies from a negative value to a positive one. Thus, between the Rayleigh wavenumber and the wavenumber of the free track, there exists at least a value of β such that $a_{11}k_P / \tilde{H}(\beta) + (a_{11}a_{22} - a_{12}a_{21}) = 0$.

On the other hand, for a given frequency, if the Rayleigh wavenumber is greater than the wavenumber of the free track (in this case it is definitely greater than the wavenumber of the rigid-bed track), then the only possible real solution to equation (6.5) is a value of β greater than the shear wavenumber but less than the Rayleigh wavenumber in the ground. In fact, if β is greater than the Rayleigh wavenumber then $\tilde{H}(\beta) > 0,\ a_{11} > 0,\ a_{11}a_{22} - a_{12}a_{21} > 0$; if β is less than the shear wavenumber then $\tilde{H}(\beta)$ is not real. For each of these two cases, equation (6.5) does not hold.

It can therefore be concluded that the phase speed of the lowest order in a track resting on a homogeneous half-space does not exceed the shear wave speed in the half-space. A heavy (or less stiff) track may make the wave speed in the track lower than the Rayleigh wave speed in the ground. A demonstration is given in Section 6.5.1.

6.4 RECEPTANCES OF THE TRACKS AND THE GROUNDS

6.4.1 RECEPTANCES OF THE GROUND SURFACES

For the four combinations of the two tracks and the two (layered) grounds, Figures 6.10 and 6.11 show the vertical displacements of the ground surface. The displacements are due to a unit harmonic load of different frequencies acting on the rails. Figure 6.10 is for the displacements of the point just underneath the load while Figure 6.11 for a point 10 m from the track centre-line. It can be seen from these two figures that, resonance also occurs when a track rests on a layered ground. However, the resonance frequency is modified by the presence of the track. As indicated in Figure 6.10, for the stiffer ground with the lighter track, the resonance frequency is 22 Hz, identical to the first cut-on frequency of the ground. However, when the heavier track is present, the resonance frequency is reduced to 18 Hz. As to the softer ground, the lighter track increases the resonance frequency from its first cut-on frequency, 13 Hz, to 16 Hz. It can be concluded that the heavier a track is, the lower is the resonance frequency.

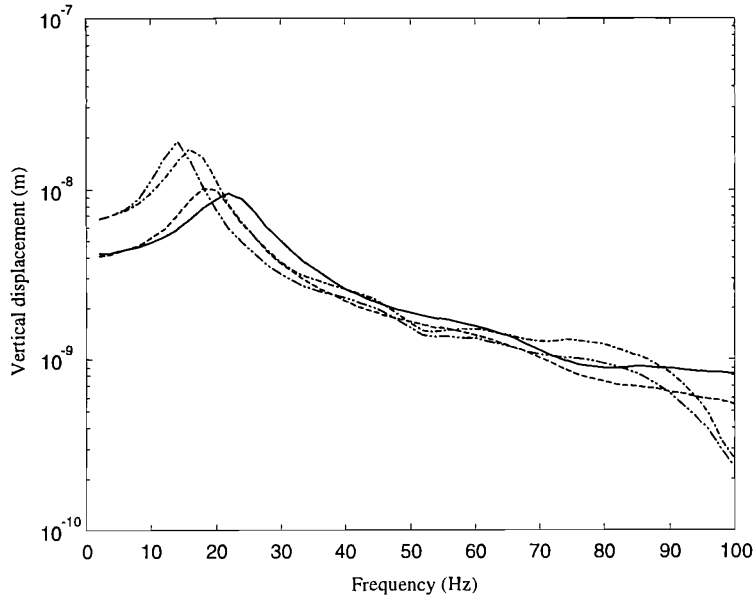

Figure 6.10. Receptances (response of the ground to a force on the rail) at $y = 0$ m. ——, lighter track-stiffer ground system; – – –, heavier track-stiffer ground system; – · – · –, lighter track-softer ground system; – · · –, heavier track-softer ground system.

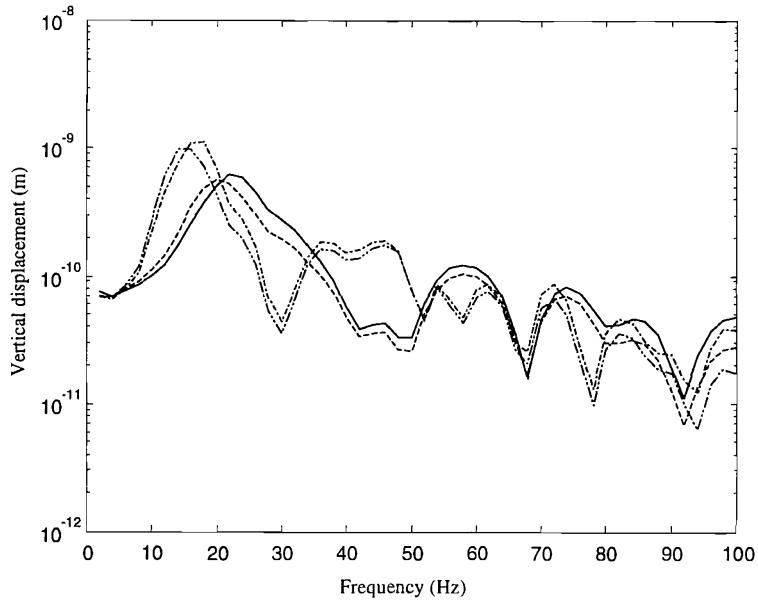

Figure 6.11. Receptances (response of the ground to a force on the rail) at y = 10 m. ——, lighter track-stiffer ground system; – – –, heavier track-stiffer ground system; – · – · –, lighter track-softer ground system; – · · –, heavier track-softer ground system.

It is also seen in Figures 6.10 and 6.11 that, at very low frequencies (below 5 Hz), a change of the mass of the track does not significantly affect the responses of the ground surface. With increasing frequency, the lighter track produces lower responses than the heavier track due to the increase in the resonance frequency. However, for frequencies higher than the resonance frequencies, the heavier track produces less response than the lighter track.

For different distances from the track, the vertical displacements are shown in Figure 6.12 for the stiffer ground with the lighter track and in Figure 6.13 for the softer ground with the heavier track. It can be seen that, in the lateral direction, the attenuation rate near the track is higher than elsewhere. In Figure 6.12, the first trough is identified at 40 Hz while in Figure 6.13 it is at 30 Hz. The low responses at these frequencies are due to the loading width in the track/ground contact plane, which filters the propagating wave of the first mode at a wavelength identical to the loading width. In fact, from equation (5.47), when $\gamma b = \pi$, the Fourier transformed displacements vanish. Since b = 1.35 m, this occurs at γ = 2.327 rad/m. In the dispersion diagrams, Figure 6.6 for the stiffer ground and Figure 6.8 for the softer ground, it can be identified that the frequency corresponding to this wavenumber of the first propagating mode is 40 Hz for the stiffer ground and 30 Hz for the softer ground.

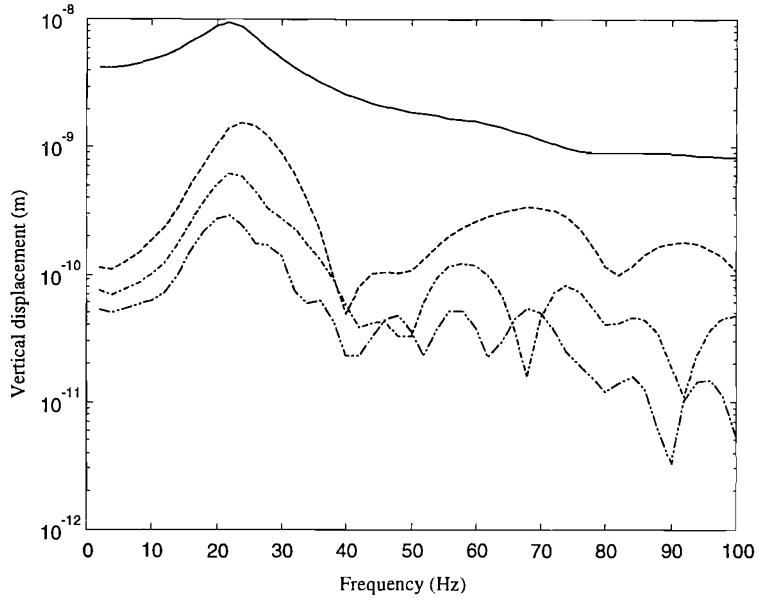

Figure 6.12. Transfer receptances from the lighter track to the stiffer ground surface. ——, y = 0 m; – – –, y = 5 m; – · – · –, y = 10 m; – · · –, y = 15 m.

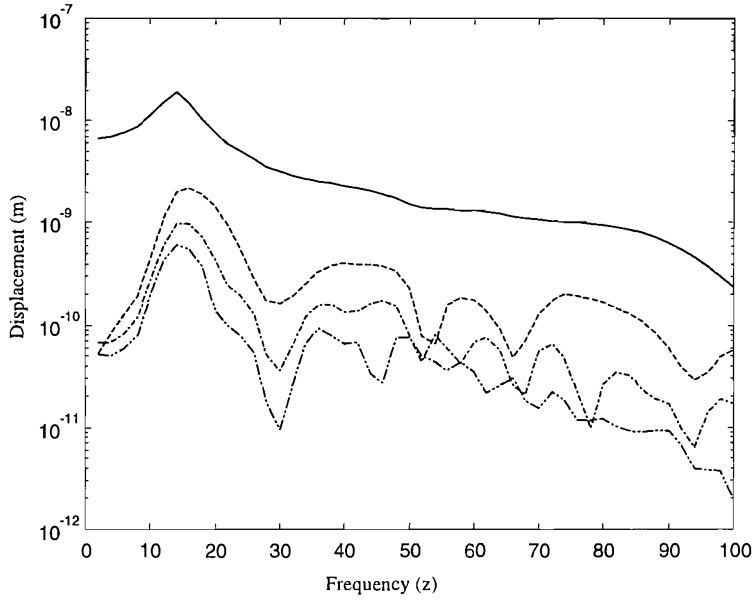

Figure 6.13. Transfer receptances from the heavier track to the softer ground surface. ——, y = 0 m; – – –, y = 5 m; – · – · –, y = 10 m; – · · –, y = 15 m.

6.4.2 RECEPTANCES OF THE TRACKS

Figures 6.14 and 6.15 show the receptances at the loading point on the rails of the tracks. Also shown are results for the tracks resting on a rigid foundation. It is seen that, as for the ground surfaces, the tracks also have a peak response around the first cut-on

frequency of the supporting layered ground. Only at higher frequencies is the difference between a ground and a rigid foundation negligible for the track receptance.

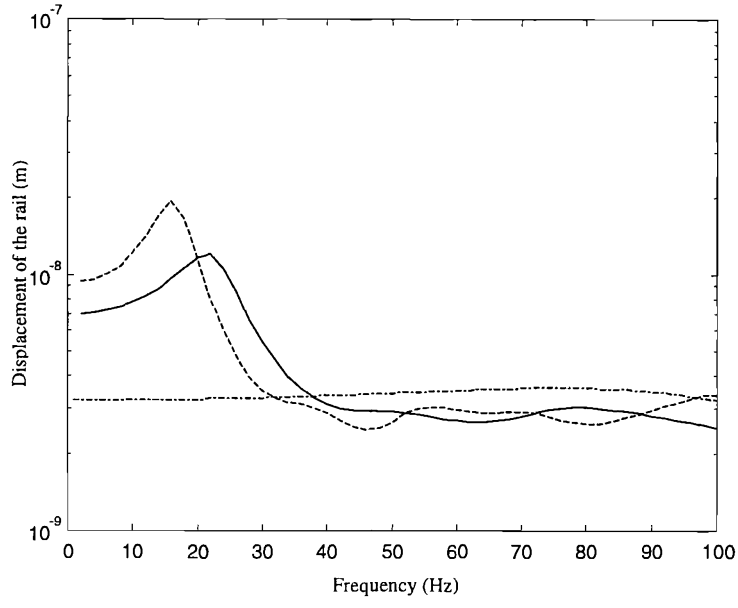

Figure 6.14. Receptances of the loading point on the rail of the lighter track. ——, the track rests on the stiffer ground; – – –, the track rests on the softer ground; – · – · –, the track rests on a rigid foundation.

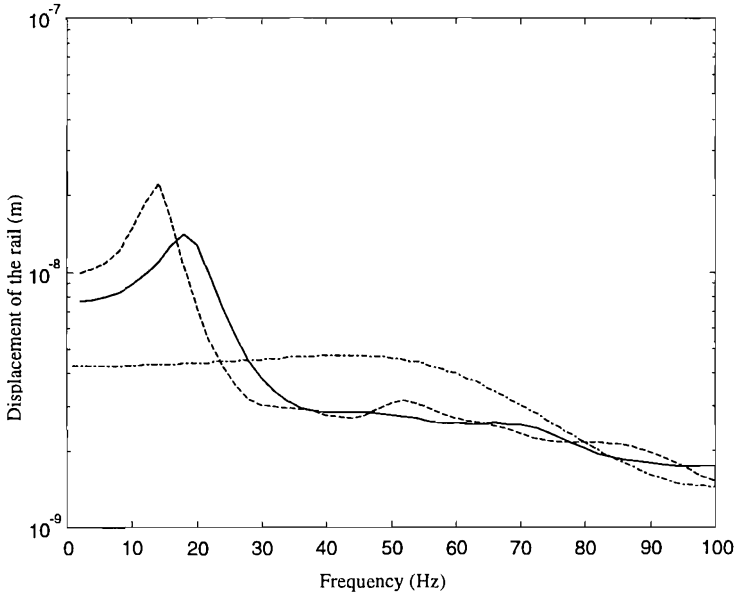

Figure 6.15. Receptances of the loading point on the rail of the heavier track. ——, the track rests on the stiffer ground; – – –, the track rests on the softer ground; – · – · –, the track rests on a rigid foundation.

6.5 EFFECTS OF LOAD SPEEDS ON THE RESPONSES OF TRACK-GROUND SYSTEMS

In this section, the effects of the speed of a quasi-static load on the responses of track-ground systems are investigated. First in Section 6.5.1 the case of a track resting on a homogeneous half-space is treated. The situation of a track resting on a layered ground is considered in Section 6.5.2.

6.5.1 WHEN A TRACK RESTS ON A HOMOGENEOUS HALF-SPACE

Two homogenous half-spaces are considered. One is made of the upper layer material of the softer ground and the other made of the upper layer material of the stiffer ground (see Tables 1.6 and 1.7). The combinations of the lighter track and the heavier track and these two half-spaces give four track-ground systems. Figure 6.16 shows the vertical displacements (amplitude) for the softer half-space with the lighter track due to a unit constant load moving at different speeds. The solid line indicates the maximum displacement along the rail and the dashed line the maximum displacement along the x-axis on the ground surface. The peak occurs at a load speed of 77 m/s, equal to the Rayleigh wave speed of the half-space. This load speed is termed the *peak response load speed.*

Figure 6.17 shows the maximum displacements of the softer half-space with the heavier track. The peak occurs again at 77 m/s, i.e. the Rayleigh wave speed of the half-space.

For the stiffer homogeneous half-space, results are presented in Figures 6.18 and 6.19. It can be seen that with the lighter track, the peak response load speed is 110 m/s, close to the Rayleigh wave speed of the half-space; with the heavier track, the peak response load speed is 105 m/s, slightly lower than the Rayleigh wave speed.

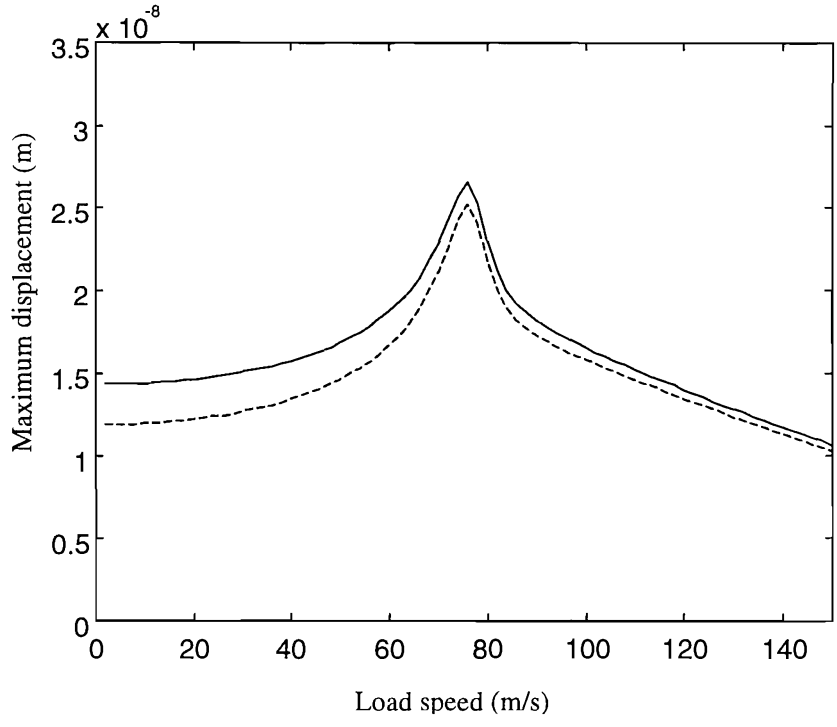

Figure 6.16. Maximum displacements of the softer half-space with the lighter track due to a unit constant load moving at different speeds. ——, the maximum displacement along the rail; – – –, the maximum displacement along the x-axis on the ground surface. The peak occurs at 77 m/s, the Rayleigh wave speed.

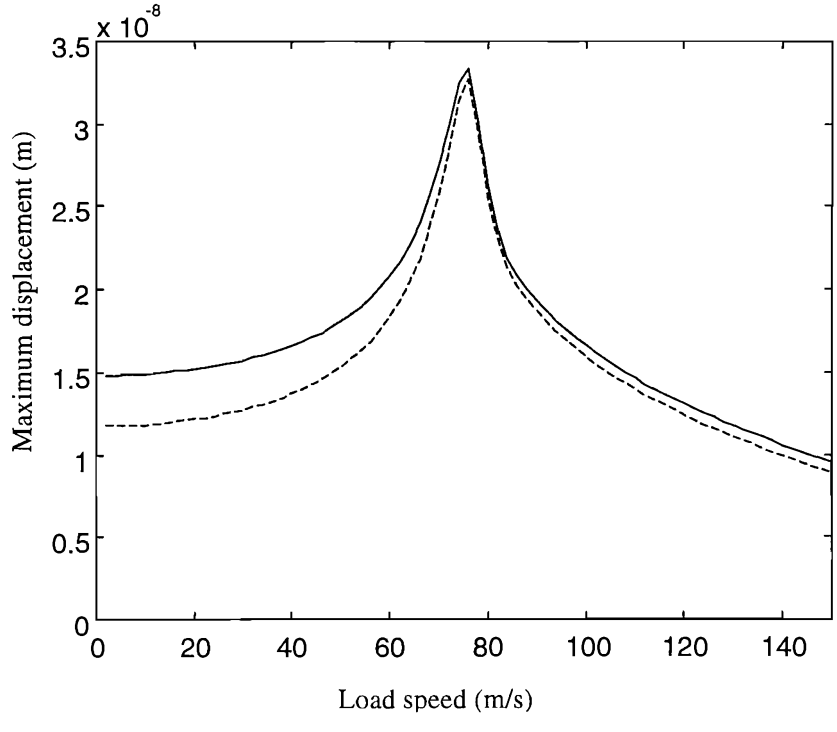

Figure 6.17. Maximum displacements of the softer half-space with the heavier track due to a unit constant load moving at different speeds. ——, the maximum displacement along the rail; – – –, the maximum displacement along the x-axis on the ground surface. The peak occurs at 77 m/s, the Rayleigh wave speed.

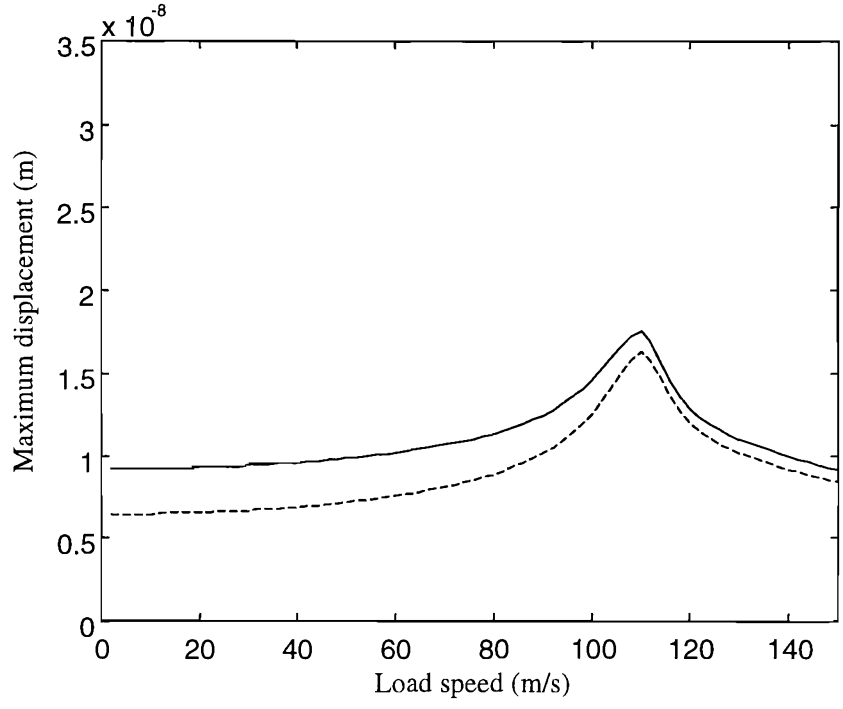

Figure 6.18. Maximum displacements of the stiffer half-space with the lighter track due to a unit constant load moving at different speeds. ——, the maximum displacement along the rail; – – –, the maximum displacement along the x-axis on the ground surface. The peak occurs at 110 m/s, close to the Rayleigh wave speed of the ground.

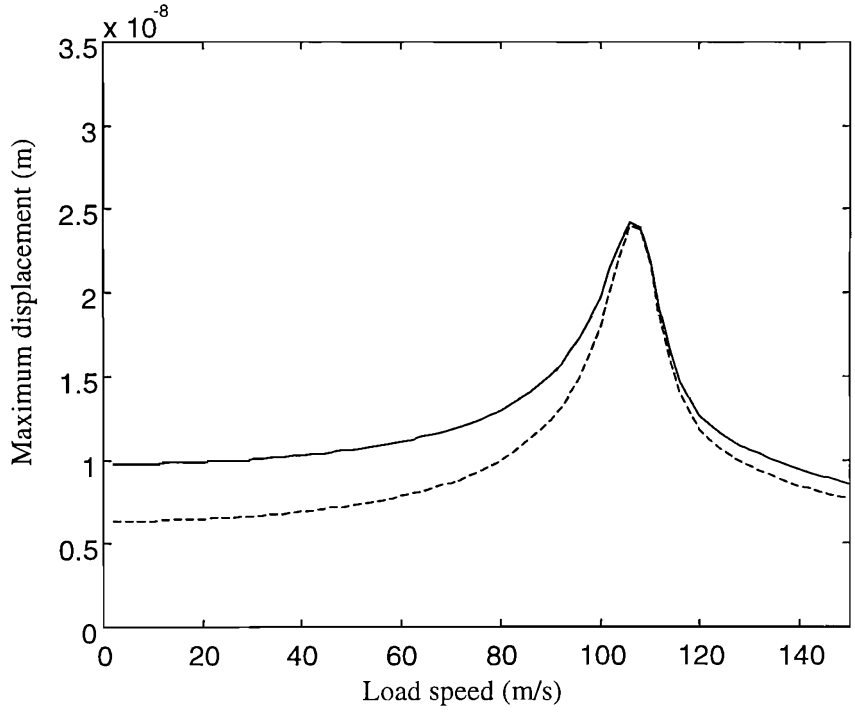

Figure 6.19. Maximum displacements of the stiffer half-space with the heavier track due to a unit constant load moving at different speeds. ——, the maximum displacement along the rail; – – –, the maximum displacement along the x-axis on the ground surface. The peak occurs at 105 m/s, lower than the Rayleigh wave speed of the ground.

The results of the four cases are compared in Figure 6.20. Figure 6.21 shows the dispersion curves of the free tracks and the homogeneous half-spaces. From Figures 6.20 and 6.21 it can concluded that, for a track resting on a homogeneous half-space, if the propagating wavenumber in the free track is greater than the Rayleigh wavenumber of the half-space at all frequencies, then the peak response load speed is lower than the Rayleigh wave speed. However, if the propagating wavenumber in the free track is equal to the Rayleigh wavenumber at a particular frequency, then the peak response load speed equals the Rayleigh wave speed, and decreasing the mass of the track or increasing its bending stiffness further does not increase the peak response load speed. This demonstrates the upper limit of the track-ground wave speed indicated above in Section 6.3.3. The same points were also observed by Dieterman and Metrikine [1997(a)] when they investigated the responses of an Euler-Bernoulli beam resting on a homogeneous half-space to a moving constant load.

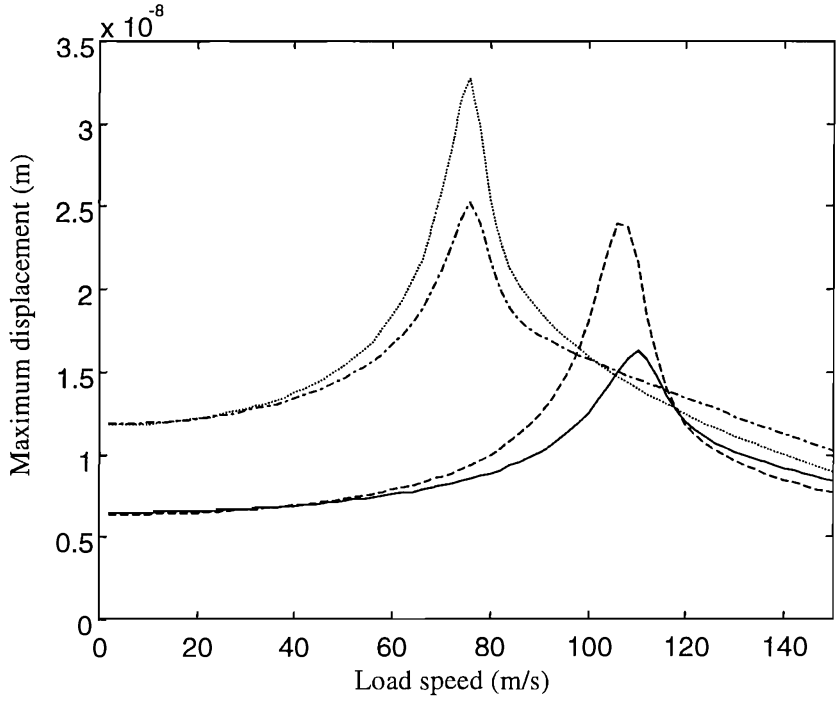

Figure 6.20. Maximum displacements along the x-axis on the ground surfaces. ——, for the stiffer homogeneous half-space with the lighter track; – – –, for the stiffer homogeneous half-space with the heavier track; – · –, for the softer homogeneous half-space with the lighter track; · · · ·, for the softer homogeneous half-space with the heavier track.

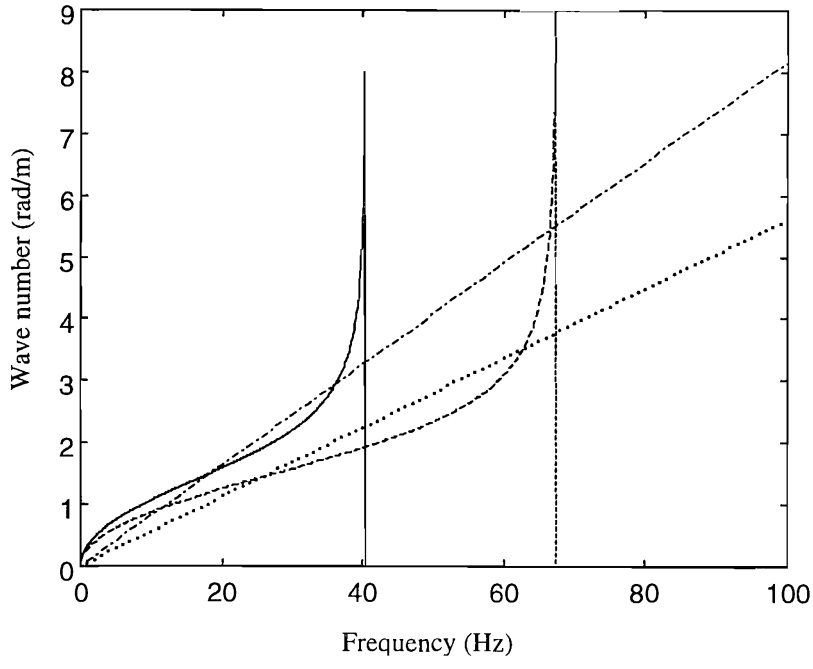

Figure 6.21. Dispersion curves of the free tracks and the homogeneous half-spaces. ——, for the free heavier track; – – –, for the free lighter track; – · –, for the softer homogeneous half-space; · · · ·, for the stiffer homogeneous half-space.

6.5.2 WHEN A TRACK RESTS ON A LAYERED GROUND

When a track rests on a layered ground, since there are several propagating modes existing in the system, the effect of the load speed on the response becomes much more complicated to analyse.

Figure 6.22 shows the maximum displacements of different track and layered ground combinations (Tables 1.6 to 1.9) due to a unit constant load moving at different speeds. For the stiffer ground with the lighter track, the peak response load speed is 130 m/s, greater than the Rayleigh wave speed of the upper layer (112 m/s). On Figure 6.6, a line may be drawn going through the origin point and the first intersection, A, of the free-track dispersion curve and the free-ground dispersion curve. This line represents the excitation due to a constant load travelling at 130 m/s, i.e. the speed at which the peak response is shown in Figure 6.22.

For the heavy track on the stiffer ground, the peak occurs at 110 m/s, a little less than the Rayleigh wave speed of the upper layer of the ground. From Figure 6.7, the dispersion curve of the free track is seen to have no intersection with the first dispersion curve of the ground.

For the softer ground with the lighter track, the peak response load speed is 105 m/s, much greater than the Rayleigh wave speed of the upper layer (77 m/s). For the heavier track resting on the softer ground, the peak load speed is 90 m/s, also greater than the Rayleigh wave speed. The correspondence observed for the stiffer ground between the peak response load speed and the dispersion curves of the track/ground structure is also valid for the softer ground, i.e. these speeds correspond to a load speed line through the point A in Figures 6.8 and 6.9.

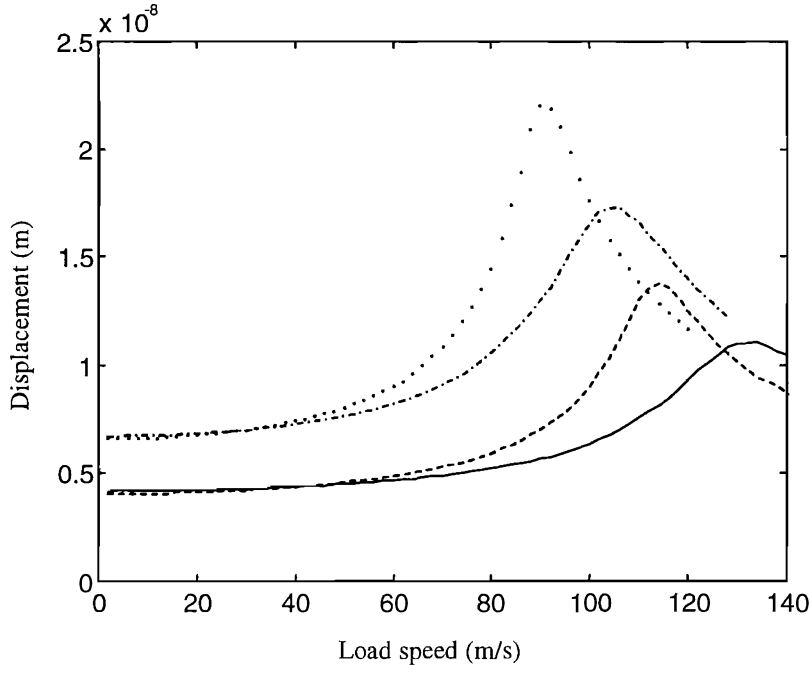

Figure 6.22. Maximum displacements along the x-axis on the ground. ——, the lighter track resting on the stiffer ground; – – –, the heavier track resting on the stiffer ground; – · –, the lighter track resting on the softer ground; · · ·, the heavier track resting on the softer ground

The above observations reveal that, when a track rests on a layered ground, the peak response load speed may be determined by the first intersection of the free-track dispersion curve and the ground dispersion curve of the first mode. Denoting the wave number and the frequency at this intersection by β_0 and f_0, then the peak response load speed for a constant load is determined by $c = 2\pi f_0 / \beta_0$. If there is no such intersection, because the free track wave speed is lower than that of the first mode in the ground, then the peak response load speed is lower than the Rayleigh wave speed in the upper layer.

It can also be seen in Figures 6.20 and 6.22 that, when the load speed is well below their peak response load speeds, the heavier track and the lighter track make little

difference to the ground responses. However, the peak response of the ground with the lighter track is much lower than that of the ground with the heavier track.

6.6 EFFECTS OF MULTIPLE AXLE LOADS

This section investigates the effects of multiple axle loads on the responses of track-ground systems. The investigations are based on equations (5.17) and (5.56). From equation (5.17), the displacement of the ground surface is given by

$$w_1(x, y,0,t) = \sum_{l=1}^{M} w_1^0(x - a_l - ct, y,0)\tilde{P}_l \tag{6.8}$$

where, $\tilde{P}_l$ denotes the magnitude of the lth axle load, $w_1(x, y,0,t)$ the ground surface vertical displacement and $w_1^0(x, y,0)$ represents the vertical displacement on the ground surface generated by a single unit constant force moving at speed c. When the load speed is well below the lowest phase speed in the track-ground system, the displacement produced by a single force is attenuated quickly (evanescent wave) and is confined near to the position of the force. In this case, the maximum displacement produced by the multiple axle loads is not so different from that produced by each single axle load. The situation may be different when the load speed is high enough to excite one of the propagating wave modes of the track-ground system. In this case, if the distances between adjacent axles are almost the same and close to the wavelength of that propagating mode, then as indicated by equation (6.8), the responses produced by each axle load are 'in phase' with each other, and add together to give a higher total response.

However, whatever the train speed is, during the passage of a train of many similar wagons, the pattern of axles of the wagons may give rise to strong harmonic components. Equation (5.56) shows that the spectra produced by multiple forces of a single frequency (for the quasi-static loads, the frequency is equal to zero) are equal to those produced by a moving unit force of that frequency, times the load spectrum. The load spectrum is given by equation (5.58). The spectra vanish at frequencies satisfying $\sum_{l=1}^{M} \tilde{P}_l(\Omega) e^{-ia_l(\Omega - 2\pi f)/c} = 0$. In principle, this equation shows that certain frequencies can be eliminated from the excitation of ground vibration by a careful choice of wagon axle spacing. However, this is not likely to be a practical proposition in order to treat problem frequencies that are dependent on the ground and track properties of a

particular site. It may, however, offer a choice of speed particular to the vehicle type which reduces a certain (narrow) range of excitation frequency.

To represent a train consisting of similar two-axle wagons, $\tilde{P}_l = P, l = 1,2,\cdots,M$, $a_1 = 0$, $a_2 = -b$, $a_3 = -a$, $a_4 = -a-b$, $a_5 = -2a$, $a_6 = -2a-b$ etc., where, a is the length of each wagon, and b the distance between two axles within a wagon. Thus equation (5.58) becomes

$$\begin{aligned} S_P(f) &= \sum_{l=1}^{M} P e^{i2\pi f a_l / c} = P\sum_{k=1}^{N} e^{-i2\pi f(k-1)a/c} + P\sum_{k=1}^{N} e^{-i2\pi f[(k-1)a+b]/c} \\ &= P(1+e^{-i2\pi f b/c})\sum_{k=1}^{N} e^{-i2\pi f(k-1)a/c} \end{aligned} \tag{6.9}$$

where N denotes the number of the wagons. Equation (6.9) shows that, (1) at $f = 0$, the magnitude of the load spectrum is equal to $2PN$; (2) at frequencies $f = c/(2b)$ and $f = c/(2a)$ (if N is even) the load spectrum vanishes; (3) at frequency $f = c/a$, the passing frequency of each wagon, the magnitude of the load spectrum increases linearly with the number of wagons and (4) when $a = 2b$, i.e. the distance between two adjacent axles either within a wagon or in two adjacent wagons is identical, then at the passing frequency of axles, $f = c/b$, the load spectrum is $2NP$. Through equation (5.56), the spectrum of the ground increases linearly with the number of wagons in cases (1), (3) and (4).

In what follows, the vertical velocity spectra are presented for six quasi-static loads ($M = 6$), of three two-axle wagons ($N = 3$) [Jonsson 2000, Sheng, Jones, Petyt and Thompson 2000], which move on the lighter track on the softer ground. The axle spacing b within a vehicle is 8.96 m and the length of a wagon, a, is 13.82 m. The magnitude of each axle force is set to unity.

Figure 6.23 shows the vertical velocity spectra of the ground surface at various distances produced by the six loads moving at $c = 40$ m/s. The vertical velocity spectra produced by a single unit constant force moving at speed 40 m/s are shown in Figure 6.24. The load spectrum of the six axle loads, defined by equation (5.58), is shown in Figure 6.25.

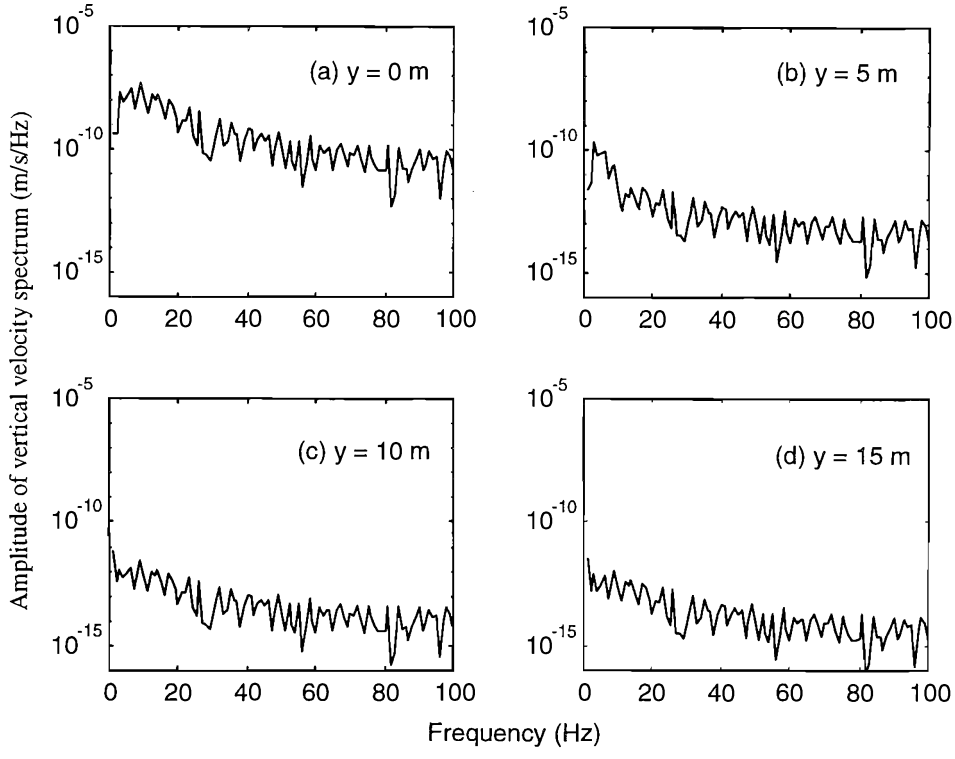

Figure 6.23. Vertical velocity spectra of points on the ground surface produced by the six loads moving at 40 m/s. (a) at the track centre-line; (b) at 5 m; (c) at 10 m; (d) at 15 m.

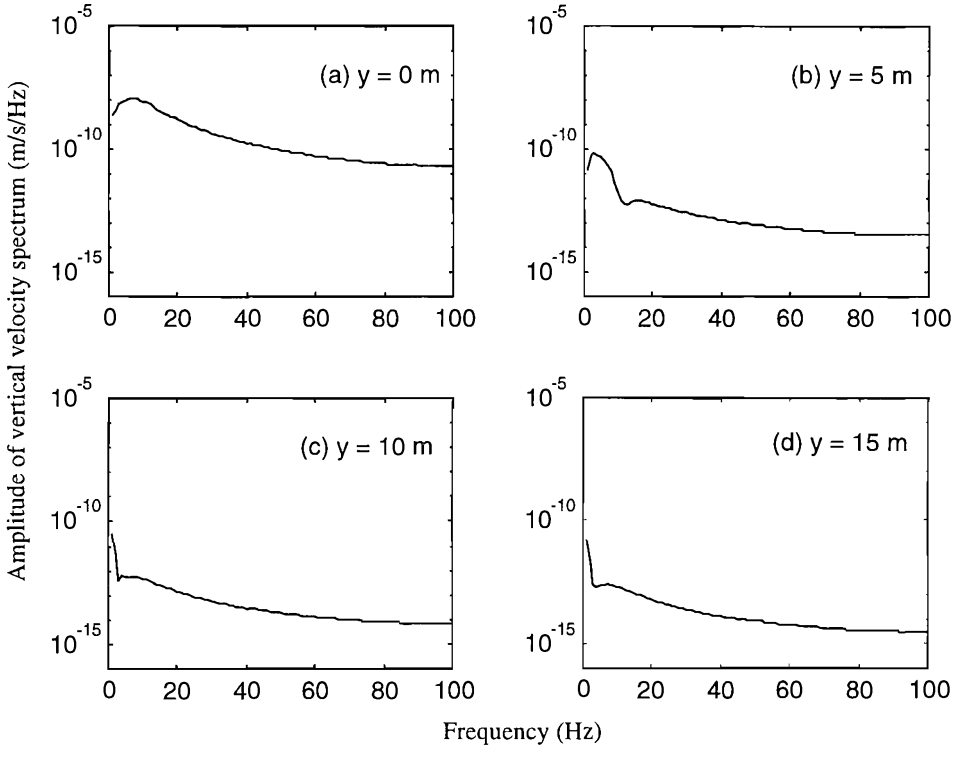

Figure 6.24. Vertical displacement spectra of points on the ground surface produced by a single unit constant force moving at 40 m/s. (a) at the track centre-line; (b) at 5 m; (c) at 10 m; (d) at 15 m.

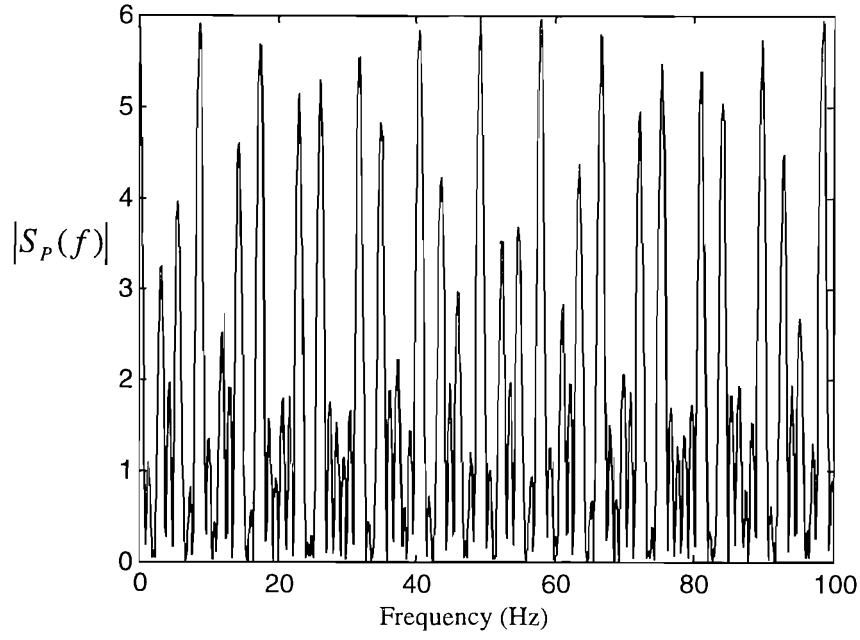

Figure 6.25. The 'load spectrum' of the six axle loads moving at 40 m/s

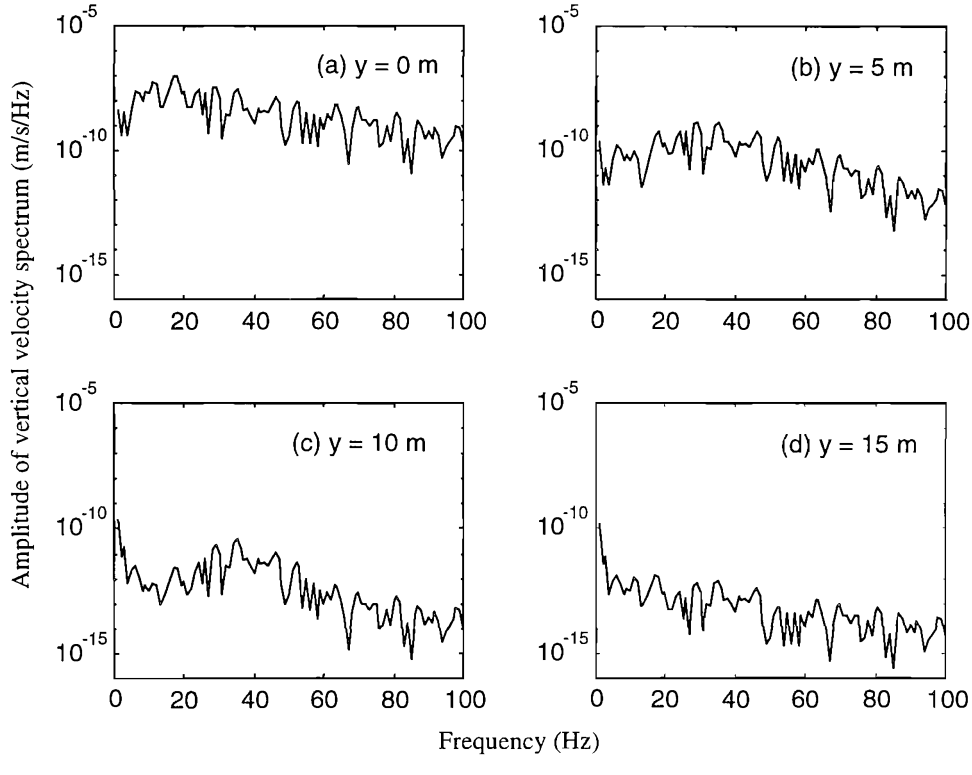

Figure 6.26. Vertical velocity spectra of points on the ground surface by the six loads moving at 80 m/s. (a) at the track centre-line; (b) at 5 m; (c) at 10 m; (d) at 15 m.

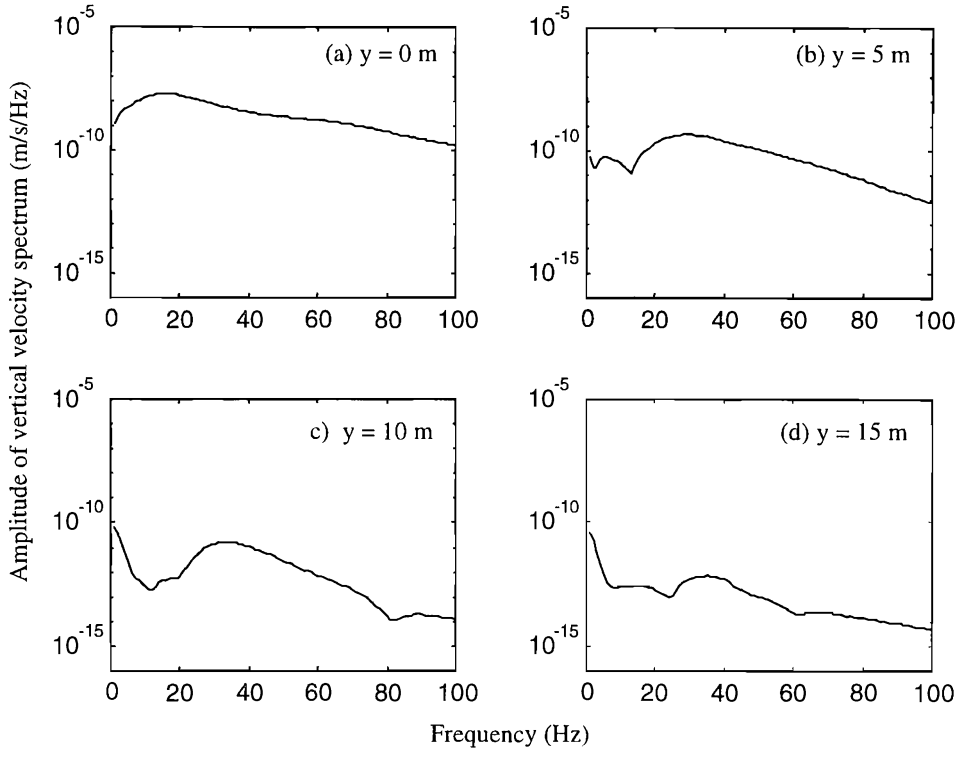

Figure 6.27. Vertical velocity spectra of points on the ground surface produced by a single unit constant load moving at 80 m/s. (a) at the track centre-line; (b) at 5 m; (c) at 10 m; (d) at 15 m.

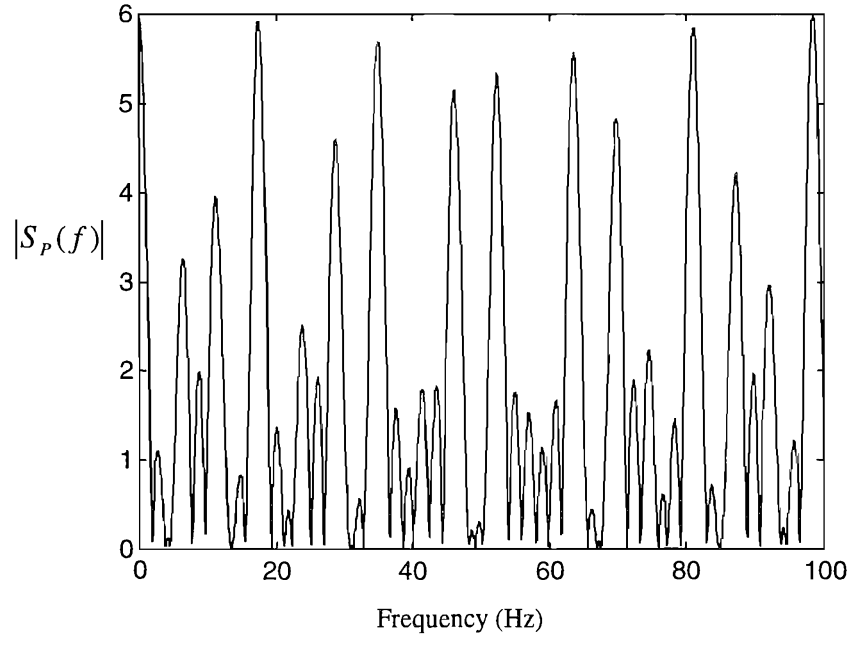

Figure 6.28. The 'load spectrum' of the six axle loads moving 80 m/s.

Comparison of Figures 6.23 and 6.25 indicates the harmonic nature of the excitation introduced by the multiple axles.

Figures 6.26 to 6.28 give equivalent results for a train speed of 80 m/s, which exceeds the Rayleigh wave speed in the upper layer of the ground. Compared with the case of low load speed, the responses are higher due to the higher load speed, especially for the frequencies 20 to 40 Hz. The harmonic components in this frequency range are due to the excitation of the first propagating mode of the ground by the moving loads.

6.7 SUMMARY

A number of results are produced using the model presented in Chapter 5 in order to investigate the effects of the track structure and the distribution of axles in a train. The concepts of free track, 'fixed-bed' track and free ground are defined. From the example results presented here some conclusions have been demonstrated, amongst others, relating to the peak response load speed which track designers may seek to control using a high bending stiffness and low mass per unit length of track/embankment structure.

(1) For a track on a ground, a harmonic surface load may excite not only the propagating modes of the track-ground system but also the modes of the free ground.

(2) For a track on a layered ground, near the first cut-on frequency of the free ground, both the track and the ground have maximum (resonant) responses. The presence of a track may increase or decrease the resonance frequency depending on the combination of the ground and the track parameters. The existence of a resonance frequency indicates the layered structure of the ground.

(3) At very low frequencies, change of the mass of a track does not significantly affect the responses of the ground surface. With increasing frequency, a lighter track produces lower responses than a heavier track due to its higher resonance frequency. However, for frequencies higher than the resonance frequencies, a heavier track produces less response than a lighter track.

(4) The ground may have a great effect on the track response compared to the response of the same track on a rigid foundation, especially for frequencies near the cut-on frequency of the ground. For the dynamics of a track at low frequencies (e.g. below 250 Hz), consideration of the elasticity and energy radiation of the supporting ground is necessary.

(5) For a track on a homogeneous half-space, the peak response load speed of a constant load will not be greater than the Rayleigh wave speed in the half-space. In the dispersion diagram, if the dispersion curve of the free track is above the Rayleigh wave line of the ground, then the peak load speed is lower than the Rayleigh wave speed. If the dispersion curve of the free track intersects the Rayleigh wave line, then the peak load speed is equal to the Rayleigh wave speed. Further increasing the track bending stiffness, or decreasing the track mass, does not increase the peak response load speed. When the load speed is well below the peak response load speed, modification to the track mass leads to a small reduction of vibration. However, when the load speed approaches the peak response load speed, decreasing the track mass has a much greater effect on reducing the level of vibration.

(6) For a track on a layered ground consisting of a single layer on a deep, stiffer substratum which is modelled as a homogeneous half-space, the peak response load speed may be greater than the Rayleigh wave speed in the upper layer of the ground. The peak response load speed may be determined by the first intersection of the free-track dispersion curve and the dispersion curve of the first mode of the ground, i.e. it is given by $2\pi f_0 / \beta_0$, where β_0 and f_0 are the wavenumber and frequency corresponding to this intersection. Since for low frequency, the dispersion curve of the first mode of the ground is close to the Rayleigh wave line of the underlying half-space, increasing the track bending stiffness or decreasing the track mass can increase the peak response load speed for the track-ground system so that the peak response load speed is much higher than the Rayleigh wave speed in the upper layer.

(7) During the passage of a train of many similar wagons, the pattern of axles of the wagons may give rise to, or suppress, some harmonic components. For example at the wagon passing frequency, the spectrum is proportional to the number of the wagons. These harmonic components are formulated using the dimensions of the wagons as well as the train speed. When the load speed is beyond the phase wave speeds in the ground, due to the excitation of the first propagating mode in the ground, vibration at certain frequencies is much stronger and less attenuated with distance than vibration in the case of low load speed.

Chapter 7

GROUND VIBRATIONS GENERATED BY WHEEL/RAIL IRREGULARITIES

7.1 INTRODUCTION

In Chapter 5, a model has been developed for predicting ground vibrations generated by vertical wheel-rail forces. This model assumes that the wheel-rail forces are known in advance. Using this model, a number of calculations have been performed in Chapter 6, providing some insights into the problem.

The vertical wheel-rail forces may be calculated using a vehicle dynamics model. A number of vehicle dynamics models have been developed [Zai, 1997]. The main aims of these models are to analyse ride quality, running safety, hunting motion, curving etc., rather than ground vibration. In these models, however, the ground is modelled as either a rigid base or a Winkler foundation, and the track is often truncated into a finite length. As a result, waves, which actually propagate away along the track and into the ground, would be reflected into the 'finite system'.

Each vertical wheel-rail force consists of two components: a quasi-static component, which is equal to the axle load, and a dynamic component. It is demonstrated by Lai et al [2000] that, the dynamic component can give rise to high levels of ground vibration and may dominate over the quasi-static component. The dynamic excitations at wheel-rail contact points come from the irregular vertical profiles of the wheel and rail running surfaces. The rail irregularities include dipped joints, corrugations as well as the general undulation in the 'track top'. The wheel irregularities can be wheel flats, surface irregularities and wheel eccentricity. The variations in the vertical profiles of either surface (wheel and rail) introduce a relative displacement input to the system, as shown in Section 7.3. The process is usually assumed to be linear, so that for a given wavelength λ, a displacement input is generated at the passing frequency $f = c/\lambda$, where c denotes the vehicle speed.

Comprehensive analysis requires realistic models of ground vibration generation and propagation. This model should be able to account for the interactions between vehicles, track and ground. This chapter is devoted to the development of such a model.

In the frequency range of interest, a vehicle is modelled as a multi-body system. A rigid body, e.g., the car body in a vehicle, may have six degrees of freedom, accounting for three displacements of the centre of mass and three rotations. However, since only the motion in the vertical plane (xz plane) is considered, each body has only two degrees of freedom, i.e., the vertical displacement of its centre of mass and its pitch motion. The suspensions in a vehicle may have non-linear behaviour. To make it possible to analyse in the frequency domain, each non-linear suspension is replaced by a linearised equivalent. As a result, the differential equation of motion for a vehicle is linear and with constant coefficients. It is specified by a mass matrix and a complex stiffness matrix. Damping is introduced and included in the stiffness matrix. The mass and the stiffness matrices of several types of vehicle are presented in Section 7.6.

From the first wheelset of the first vehicle to the last wheelset of the last vehicle, the vertical wheel-rail forces are denoted by $P_1(t), P_2(t), \cdots, P_M(t)$, where M is the number of the forces. At time $t = 0$, the longitudinal co-ordinates of these forces are denoted by $a_1, a_2, \cdots, a_M$. The forces move along the rails uniformly at the train speed c. For each wheel-rail force, there are two components: one is a static load, i.e. the axle load, and the other is a dynamic load. The responses to the axle loads may be calculated using the model developed in Chapter 5. Therefore in this chapter only the dynamic wheel-rail forces are considered and still denoted by $P_1(t), P_2(t), \cdots, P_M(t)$. The vertical displacement of the rail is denoted by $w_R(x,t)$.

The plane Oxy is located on the ground surface. For a particle in the jth layer, its longitudinal, lateral and vertical displacements are, as in the previous chapters, denoted by $u_j(x, y, z, t)$, $v_j(x, y, z, t)$ and $w_j(x, y, z, t)$. Especially, the displacements $u_j(x, y, 0, t)$, $v_j(x, y, 0, t)$ and $w_j(x, y, 0, t)$ on the ground surface are denoted alternatively by $u_{10}(x, y, t)$, $v_{10}(x, y, t)$ and $w_{10}(x, y, t)$.

In Section 7.2, the receptances of the vehicles, track and ground are derived. Compatibility of displacements at the wheel-rail contact points couples the vehicles and the track-ground system, and yield equations for the wheel-rail contact forces. The detail is presented in Section 7.3. Having worked out the wheel-rail contact forces, the ground vibration can be evaluated by employing the formulae developed in Chapter 5. In Section 7.4, a relationship is sought between the displacement power spectrum of the ground surface and the power spectral density of the vertical profile of the rails. The Hertzian

contact springs between the wheelsets and the rail are introduced in the model and a formula for evaluating the stiffness of a Hertzian contact spring is given in Section 7.5. Results from the model are presented and discussed in Section 7.7. Conclusions based these results are summarised in Section 7.8.

7.2 RECEPTANCES OF A VEHICLE AND A TRACK-GROUND SYSTEM

7.2.1 RECEPTANCES OF A VEHICLE AT THE WHEELSETS

The differential equation of motion of a vehicle is given by

$$[M_V]\{\ddot{z}_V(t)\}+[K_V]\{z_V(t)\}=\{F_V(t)\}=[B](\{F(t)\}-\{P(t)\}) \tag{7.1}$$

where, $[M_V]$ and $[K_V]$ ('V' means vehicle) denote the mass and stiffness matrices of the vehicle (not including the Hertzian contact spring), $\{z_V(t)\}$ denotes the (generalised) displacement vector, $\{F(t)\}$ denotes the generalised force vector applied at the wheelsets excluding the wheel-rail interaction force vector which is denoted by $\{P(t)\}$, and $[B]$ is a constant matrix. A minus sign before $\{P(t)\}$ indicates that the positive wheel-rail forces are of compression. The detailed expressions for matrices $[M_V]$, $[K_V]$ and $[B]$ are derived in Section 7.6.

To derive the receptances of the vehicle at the wheelsets, let $\{F(t)\}=\{\tilde{F}(\Omega)\}e^{i\Omega t}$, $\{P(t)\}=\{\tilde{P}(\Omega)\}e^{i\Omega t}$, $\{z_V(t)\}=\{\tilde{z}_V(\Omega)\}e^{i\Omega t}$, where Ω denotes the angular frequency. Then equation (7.1) becomes

$$\{\tilde{z}_V(\Omega)\}=([K_V]-\Omega^2[M_V])^{-1}[B](\{\tilde{F}(\Omega)\}-\{\tilde{P}(\Omega)\})=[\Sigma_V](\{\tilde{F}(\Omega)\}-\{\tilde{P}(\Omega)\}) \tag{7.2}$$

where

$$[\Sigma_V]=([K_V]-\Omega^2[M_V])^{-1}[B] \tag{7.3}$$

For the vehicle, the receptance between the jth and the kth wheelsets is denoted by σ^W_{jk}, ('W' means wheelset) where, $j,k=1,2,\cdots,N$, N being the number of the wheelsets of the vehicle (for a two-axle wagon, $N=2$ and for a four-axle coach, $N=4$). In other words, σ^W_{jk} denotes the amplitude of the displacement of the jth wheelset due to

a unit vertical harmonic load acting at the kth wheelset. Thus the complex amplitudes of the displacements of the wheelsets produced by the vertical loads acting at the wheelsets are given by

$$\{\tilde{z}_W(\Omega)\} = [\Sigma_W](\{\tilde{F}(\Omega)\} - \{\tilde{P}(\Omega)\}) \tag{7.4}$$

where,

$$[\Sigma_W] = (\sigma^W_{jk})_{j,k=1,2,\cdots N} = \begin{bmatrix} \sigma^W_{11} & \cdots & \sigma^W_{1N} \\ \vdots & \cdots & \vdots \\ \sigma^W_{N1} & \cdots & \sigma^W_{NN} \end{bmatrix} \tag{7.5}$$

denotes the receptance matrix of the vehicle at the wheelsets. This matrix is dependent on the vehicle parameters and Ω and is symmetric. In equation (7.4)

$$\{\tilde{z}_W(\Omega)\} = (\tilde{z}_{W1}(\Omega), \tilde{z}_{W2}(\Omega), \tilde{z}_{W3}(\Omega), \cdots, \tilde{z}_{WN}(\Omega))^T \tag{7.6}$$

is the displacement vector of the wheelsets, and

$$\{\tilde{P}(\Omega)\} = (\tilde{P}_1(\Omega), \tilde{P}_2(\Omega), \tilde{P}_3(\Omega), \cdots, \tilde{P}_N(\Omega))^T \tag{7.7}$$

is the vector of forces exerted on the wheelsets by the rail.

The displacement vector of the wheelsets forms part of that of the vehicle, therefore, it may be written that

$$\{\tilde{z}_W(\Omega)\} = [A]\{\tilde{z}_V(\Omega)\} \tag{7.8}$$

where $[A]$ is a constant matrix and $[A] = [B]^T$ (see Section 7.6). Thus equations (7.3) and (7.4) give

$$[\Sigma_W] = [A][\Sigma_V] = [A]([K_V] - \Omega^2[M_V])^{-1}[B] \tag{7.9}$$

Equation (7.9) gives the receptance matrix at the wheelsets of one vehicle. Supposing that N_1 vehicles are being considered, then the total number of the wheel-rail forces $M = N_1 N$. For the present model, it is assumed that these vehicles are only coupled by the rails, thus the receptance matrix at the wheelsets for the 'train', denoted by $[\Sigma_T]$ ('T' means train), is given by

$$[\Sigma_T] = \mathrm{diag}([\Sigma_W],\cdots,[\Sigma_W]) = \begin{bmatrix} [\Sigma_W] & \cdots & 0 \\ \vdots & \vdots & \vdots \\ 0 & \cdots & [\Sigma_W] \end{bmatrix} \tag{7.10}$$

The elements of matrix $[\Sigma_T]$ are denoted by σ_{lk}^T, where, $k,l = 1,2,\cdots,M$.

7.2.2 RECEPTANCES OF A TRACK-GROUND SYSTEM AT WHEEL/RAIL CONTACT POINTS

Suppose a unit vertical harmonic load $e^{i\Omega t}$, which is pointing downwards and located at $x = 0$ when $t = 0$, moves at speed c along the rails. The steady state displacements of the rails and the ground surface, denoted by $w_R(x,t)$, $u_{10}(x,y,t)$, $v_{10}(x,y,t)$ and $w_{10}(x,y,t)$, may be expressed as (see equation (5.17))

$$\left.\begin{aligned} w_R(x,t) &= w_R^{\Omega}(x-ct)e^{i\Omega t} \\ u_{10}(x,y,t) &= u_{10}^{\Omega}(x-ct,y)e^{i\Omega t} \\ v_{10}(x,y,t) &= v_{10}^{\Omega}(x-ct,y)e^{i\Omega t} \\ w_{10}(x,y,t) &= w_{10}^{\Omega}(x-ct,y)e^{i\Omega t} \end{aligned}\right\} \tag{7.11}$$

where the calculation of $w_R^{\Omega}(r)$ $(r = x - ct)$ etc., has been described in Chapter 5. Thus, the receptance at the jth wheel/rail contact point due to a unit load at the kth wheel/rail contact point (both of these two points are moving at speed c) on the rail is determined by

$$\sigma_{jk}^R = w_R^{\Omega}(l_{jk}) \tag{7.12}$$

where

$$l_{jk} = a_j - a_k \tag{7.13}$$

is the distance between these two contact points, and when the jth contact point is ahead the kth one, $l_{jk} > 0$.

The amplitudes of the displacements of the wheel-rail contact points on the rails may now be written

$$\{\tilde{z}_R(\Omega)\} = [\Sigma_R]\{\tilde{P}(\Omega)\} \tag{7.14}$$

where,

$$[\Sigma_R] = \begin{bmatrix} \sigma_{11}^R & \sigma_{12}^R & \cdots & \sigma_{1M}^R \\ \sigma_{21}^R & \sigma_{22}^R & \cdots & \sigma_{2M}^R \\ \vdots & \vdots & \vdots & \vdots \\ \sigma_{M1}^R & \sigma_{M2}^R & \cdots & \sigma_{MM}^R \end{bmatrix} \tag{7.15}$$

is the receptance matrix of the track-ground system at the wheel/rail contact points on the rail. Notice that when the train speed does not vanish, this matrix is non-symmetric due to the motion of the loads. In equation (7.14)

$$\{\tilde{z}_R(\Omega)\} = (\tilde{z}_{R1}(\Omega), \tilde{z}_{R2}(\Omega), \cdots, \tilde{z}_{RM}(\Omega))^T \tag{7.16}$$

represents the displacement vector of the rail at the wheel-rail contact points.

7.3 COUPLING OF THE VEHICLES AND THE TRACK-GROUND SYSTEM

For a single wavelength, the vertical profile of the rails can be expressed as $z(x) = Ae^{i\frac{2\pi}{\lambda}x}$, where λ denotes the wavelength and A the amplitude (which may be complex). At the instant t, the lth wheelset arrives at $x = a_l + ct$, thus the displacement input at the lth wheel/rail contact point is

$$z_l(t) = \tilde{z}_l(\Omega)e^{i\Omega t} = Ae^{i\frac{2\pi}{\lambda}(a_l+ct)} = Ae^{i\frac{2\pi}{\lambda}a_l}e^{i2\pi\frac{c}{\lambda}t} \tag{7.17}$$

where, $\tilde{z}_l(\Omega) = Ae^{i\frac{2\pi}{\lambda}a_l}$, $\Omega = 2\pi c / \lambda$..

See Figure 7.1, where $\tilde{z}_{Wl}(\Omega)e^{i\Omega t}$ denotes the displacement of the lth wheelset. A Hertzian contact spring is inserted between the wheel and the rails. The calculation formula for the stiffness of the Hertzian contact spring, denoted by k_{Hl}, is given in Section 7.5. Suppose the wheelset is always in contact with the rails. Then

$$\tilde{z}_{Wl}(\Omega) = \tilde{z}_{Rl}(\Omega) + \tilde{z}_l(\Omega) + \tilde{P}_l(\Omega) / k_{Hl} \tag{7.18}$$

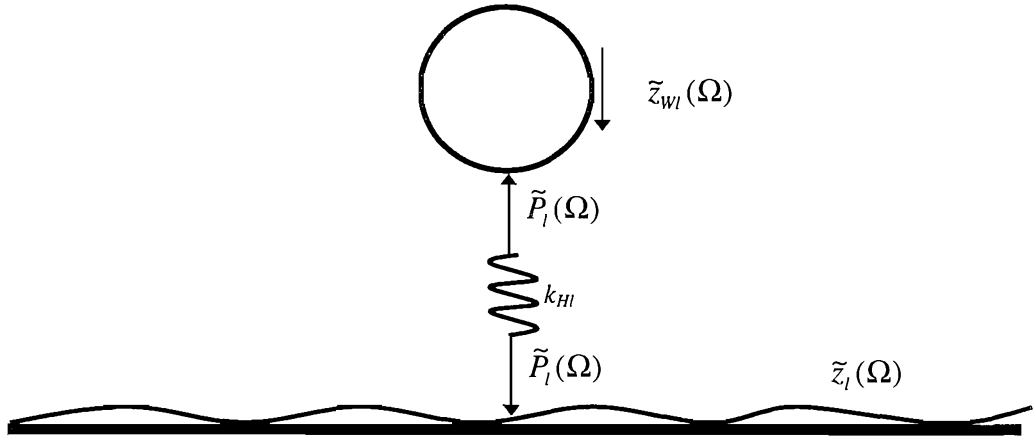

Figure 7.1. Coupling of the lth wheelset with the rail

From equations (7.4) and (7.14)

$$\tilde{z}_{Wl}(\Omega) = \sum_{k=1}^{M} \sigma_{lk}^{T} [\tilde{F}_k(\Omega) - \tilde{P}_k(\Omega)] \tag{7.19}$$

$$\tilde{z}_{Rl}(\Omega) = \sum_{k=1}^{M} \sigma_{lk}^{R} \tilde{P}_k(\Omega) \tag{7.20}$$

Inserting these two equations into equation (7.18) yields

$$\sum_{k=1}^{M} (\sigma_{lk}^{T} + \sigma_{lk}^{R}) \tilde{P}_k(\Omega) + \frac{1}{k_{Hl}} \tilde{P}_l(\Omega) = \sum_{k=1}^{M} \sigma_{lk}^{T} \tilde{F}_k(\Omega) - \tilde{z}_l(\Omega) \quad (l = 1,2,\cdots,M) \tag{7.21}$$

Equation (7.21) is a set of linear algebraic equations with unknowns $\tilde{P}_k(\Omega)$, where $k = 1,2,\cdots,M$. Once $\{\tilde{P}(\Omega)\}$ has been determined from equation (7.21), the displacements of the rails and ground surface are given by

$$\left.\begin{aligned}
w_R(x,t) &= \sum_{l=1}^{M} w_R^{\Omega}(x - a_l - ct) \tilde{P}_l(\Omega) e^{i\Omega t} \\
u_{10}(x,y,t) &= \sum_{l=1}^{M} u_{10}^{\Omega}(x - a_l - ct, y) \tilde{P}_l(\Omega) e^{i\Omega t} \\
v_{10}(x,y,t) &= \sum_{l=1}^{M} v_{10}^{\Omega}(x - a_l - ct, y) \tilde{P}_l(\Omega) e^{i\Omega t} \\
w_{10}(x,y,t) &= \sum_{l=1}^{M} w_{10}^{\Omega}(x - a_l - ct, y) \tilde{P}_l(\Omega) e^{i\Omega t}
\end{aligned}\right\} \tag{7.22}$$

7.4 RESPONSE POWER SPECTRA OF THE GROUND SURFACE

Once the wheel-rail forces have been evaluated, the displacement spectra of the ground surface can be evaluated using the formulae developed in Section 5.4. In this section, formulae are derived for the response power spectra of the ground surface. To do so, the longitudinal, lateral and vertical displacement spectra of point (x, y) on the ground surface due to a unit rail irregularity of wavelength λ , $z(x) = e^{i\frac{2\pi}{\lambda}x} = e^{i\beta x}$, are denoted by $S_u^0(x, y, f; \Omega), S_v^0(x, y, f; \Omega), S_w^0(x, y, f; \Omega)$, respectively (Note: in Section 5.4.3, they are used to represent the displacement spectra due to a single unit harmonic load of frequency Ω moving at c), where f is the frequency at which the spectra are evaluated, Ω is the excitation angular frequency in the vehicle frame of reference, determined by

$$\Omega = 2\pi c / \lambda = c\beta \tag{7.23}$$

A complete vertical rail profile may be described by

$$z(x) = \frac{1}{2\pi} \sum_{k=-\infty}^{\infty} \tilde{z}(\beta_k) e^{i\beta_k x} \Delta\beta \tag{7.24}$$

where $\beta_k = k\Delta\beta$, $\Delta\beta$ denotes the spacing of the discrete wavenumbers. With this input, the displacement spectra are given by (taking the vertical one as an example)

$$S_w(x, y, f) = \frac{\Delta\beta}{2\pi} \sum_{k=-\infty}^{\infty} S_w^0(x, y, f; \Omega_k) \tilde{z}(\beta_k) \tag{7.25}$$

where, according to equation (7.23), $\Omega_k = c\beta_k$. Equation (7.25) yields,

$$\begin{aligned} |S_w(x, y, f)|^2 &= \frac{(\Delta\beta)^2}{4\pi^2} \sum_{k=-\infty}^{\infty} S_w^0(x, y, f; \Omega_k) \tilde{z}_k \sum_{j=-\infty}^{\infty} S_w^{0*}(x, y, f; \Omega_j) \tilde{z}_j^* \\ &= \frac{(\Delta\beta)^2}{4\pi^2} \sum_{j=-\infty}^{\infty} \sum_{k=-\infty}^{\infty} S_w^0(x, y, f; \Omega_k) S_w^{0*}(x, y, f; \Omega_j) \tilde{z}_k \tilde{z}_j^* \end{aligned} \tag{7.26}$$

where, $\tilde{z}_j = \tilde{z}(\beta_j)$ and $\tilde{z}_j^*$ denotes the conjugate of $\tilde{z}_j$.

Denoting the ensemble average operator by E, and assuming that each harmonic component of the rail vertical profile is independent of others, i.e.

$$E[\tilde{z}_k \tilde{z}_j^*] = \begin{cases} 0, \text{if } k \neq j \\ E[|\tilde{z}_k|^2], \text{if } k = j \end{cases} \tag{7.27}$$

then equation (7.26) yields,

$$E[|S_w(x,y,f)|^2] = \frac{(\Delta\beta)^2}{4\pi^2} \sum_{k=-\infty}^{\infty} |S_w^0(x,y,f;\Omega_k)|^2 \; E[|\tilde{z}_k|^2] \tag{7.28}$$

The assumption made in equation (7.27) is based on the idea that the irregularities of different wavelengths are not correlated, i.e. that the irregularity may be treated as a random process.

$E[|S_w(x,y,f)|^2]$ gives the vertical displacement power spectrum of point (x, y) on the ground surface and is denoted by $P_w(x,y,f)$. Thus from equation (7.28),

$$\begin{aligned} P_w(x,y,f) &= \frac{L}{L}\frac{(\Delta\beta)^2}{4\pi^2} \sum_{k=-\infty}^{\infty} |S_w^0(x,y,f;\Omega_k)|^2 \; E[|\tilde{z}_k|^2] \\ &= \frac{(\Delta\beta)^2 L}{4\pi^2} \sum_{k=-\infty}^{\infty} |S_w^0(x,y,f;\Omega_k)|^2 \; \frac{1}{L} E[|\tilde{z}_k|^2] \end{aligned}$$

where L is a distance over which the power spectral density (PSD), denoted by $P_z(\beta)$, of the vertical profile of the rails is estimated, and $\Delta\beta L = 2\pi$. It is known that $\frac{1}{L} E[|\tilde{z}_k|^2] \approx P_z(\beta_k)$. Thus

$$P_w(x,y,f) = \frac{1}{2\pi} \sum_{k=-\infty}^{\infty} |S_w^0(x,y,f;\Omega_k)|^2 \; P_z(\beta_k)\Delta\beta \tag{7.29}$$

Since the vertical profile of the rails, described by $z(x)$, is a real function of x, its power spectral density $P_z(\beta)$ is an even function of β. Thus equation (7.29) can be written as

$$\begin{aligned} P_w(x,y,f) = \frac{1}{2\pi} \sum_{k=1}^{\infty} [&|S_w^0(x,y,f;\Omega_k)|^2 + |S_w^0(x,y,f;-\Omega_k)|^2] P_z(\beta_k)\Delta\beta \\ &+ \frac{1}{2\pi} |S_w^0(x,y,f;0)|^2 \; P_z(0)\Delta\beta \end{aligned} \tag{7.30}$$

It can be shown that $S_w^0(x,y,-f;\Omega_k) = S_w^{0*}(x,y,f;-\Omega_k)$ which implies that $P_w(x,y,f)$ is an even function of frequency f. However, it should be noticed that, in general $S_w^0(x,y,f;\Omega_k) \neq S_w^{0*}(x,y,f;-\Omega_k)$.

In equation (7.30), the last term should be zero since it corresponds to an excitation of zero frequency at which the dynamic wheel-rail forces vanish.

Now the power spectrum due to the moving axle loads is added to equation (7.30) to give the total power spectrum. If $S_w^0(x, y, f;0)$ is now made to refer to the vertical displacement spectrum produced by the moving axle loads, then the associated power spectrum is $|S_w^0(x, y, f;0)|^2$. Thus the total power spectrum, also denoted by $P_w(x, y, f)$, is given by

$$P_w(x, y, f) = \frac{1}{2\pi}\sum_{k=1}^{\infty}[|S_w^0(x, y, f;\Omega_k)|^2 + |S_w^0(x, y, f;-\Omega_k)|^2]P_z(\beta_k)\Delta\beta + |S_w^0(x, y, f;0)|^2 \tag{7.31}$$

Equation (7.31) gives the relationship between the displacement power spectrum of the ground surface and the power spectral density of the vertical profile of the rails. In international standards, the units of the former are $m^2/(Hz)^2$, and that of the latter are m^2/(cycle/m). Since $|S_w^0(x, y, f;\Omega_k)|^2$ is independent of x as well as the position of the train (see Section 5.4.3, Chapter 5), the total power spectrum of the ground surface is independent of x and also of the train position.

The velocity power spectrum, $P_{\dot{w}}(x, y, f)$, and the acceleration power spectrum, $P_{\ddot{w}}(x, y, f)$, of the ground surface are given by

$$P_{\dot{w}}(x, y, f) = (2\pi f)^2 P_w(x, y, f) \tag{7.32}$$

$$P_{\ddot{w}}(x, y, f) = (2\pi f)^2 P_{\dot{w}}(x, y, f) = (2\pi f)^4 P_w(x, y, f) \tag{7.33}$$

When divided by a chosen period of time, which normally is the time needed for a train to pass a fixed point, equations (7.31), (7.32) and (7.33) give the response power spectral density of the ground surface.

7.5 STIFFNESS OF THE HERTZIAN CONTACT SPRING

The relationship between the vertical wheel-rail interaction force P and the compression δz at the contact point is given by [see e.g. Jenkins, Stephenson et al 1974 and Zai 1997]

$$P = (\delta z / G)^{3/2} \tag{7.34}$$

where δz refers to the compression between the wheel and rail, and G the wheel-rail contact constant. For a wheel with a coned tyre, an approximation for G is

$$G = 4.57R^{-0.149} \times 10^{-8} \ (\text{m/N}^{2/3}) \tag{7.35}$$

whereas for a wheel with a worn tyre

$$G = 3.86R^{-0.115} \times 10^{-8} \ (\text{m/N}^{2/3}) \tag{7.36}$$

where R denotes the rolling radius of the wheel.

From equation (7.34),

$$\frac{dP}{d(\delta z)} = \frac{3}{2G}(P)^{1/3}$$

The Hertzian contact stiffness for each wheelset is determined by

$$k_H = 2\frac{dP}{d(\delta z)}\Big|_{P=P_0/2} = \frac{3}{G}(P_0/2)^{1/3} \tag{7.37}$$

where P_0 is the static load applied on the rails by the wheelset, equal to the axle load.

7.6 MASS AND STIFFNESS MATRICES OF VEHICLES

In this section, the mass and stiffness matrices for several types of vehicle are derived. As shown in Figures 7.3 to 7.6, a vehicle consists in general of a car body, two bogies and four or two wheelsets. The mass and the pitch inertia of the car body are denoted by M_C and J_C. The vertical displacement and the pitch angle of the car body are denoted by $z_C(t)$ and $\varphi_C(t)$. The mass and the pitch inertia of each bogie are denoted by M_B and J_B. The vertical displacement and the pitch angle of the jth bogie are denoted by $z_{Bj}(t)$ and $\varphi_{Bj}(t)$. The mass of each wheelset is denoted by M_W, and the vertical displacement of the lth wheelset is denoted by $z_{Wl}(t)$. For a vertical displacement, the positive direction is downwards, while for a pitch angle, the positive direction is clockwise. The dynamic stiffness of the primary suspension (between wheelset and bogie) per axle is denoted by k_1, and that of the secondary suspension (between bogie and car body) per bogie is denoted by k_2. For any other notation, its meaning will be defined where it appears. For different types of suspension, k_1 and k_2 are different

functions of frequency, stiffness and damping of the suspension. When a suspension, for example a primary suspension, consists of a spring and a viscous damper which are connected in parallel, as shown in Figure 7.2(a), then

$$k_1 = k_{S1} + i\Omega c_{S1} \tag{7.38}$$

where, k_{S1} denotes the stiffness of the spring, c_{S1} the viscous damping coefficient of the damper, and Ω the angular frequency. If the suspension has a structure shown in Figure 7.2(b), in which an extra spring is connected in series with the damper, then

$$k_1 = \frac{k_{S1}k_{S1}^{'} + i\Omega c_{S1}(k_{S1} + k_{S1}^{'})}{k_{S1}^{'} + i\Omega c_{S1}} \tag{7.39}$$

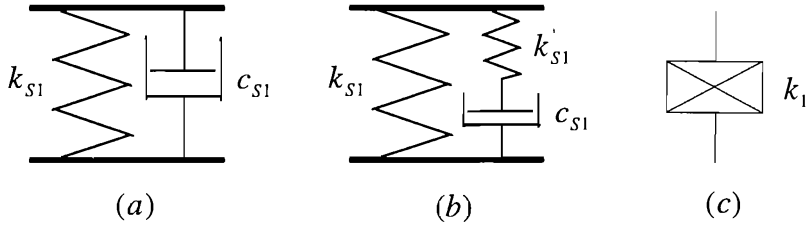

Figure 7.2. Structure of suspensions.

A symbol, shown in Figure 7.2(c), is used to represent a suspension of any type. The hysteretic damping may also be incorporated into the suspension by introducing a complex spring stiffness.

7.6.1 FOR VEHICLE TYPE I

Vehicle type I, which is shown in Figure 7.3, represents a passenger car which has two levels of suspension (primary and secondary). The displacement vector of the vehicle is defined as

$$\{z_V(t)\} = (z_C(t), \varphi_C(t), z_{B1}(t), \varphi_{B1}(t), z_{B2}(t), \varphi_{B2}(t), z_{W1}(t), z_{W2}(t), z_{W3}(t), z_{W4}(t))^T \tag{7.40}$$

Corresponding to this displacement vector, the external force vector is determined as

$$\begin{aligned}\{F_V(t)\} &= (0,0,0,0,0,0, F_1(t) - P_1(t), F_2(t) - P_2(t), F_3(t) - P_3(t), F_4(t) - P_4(t))^T \\ &= [B](\{F(t)\} - \{P(t)\})\end{aligned} \tag{7.41}$$

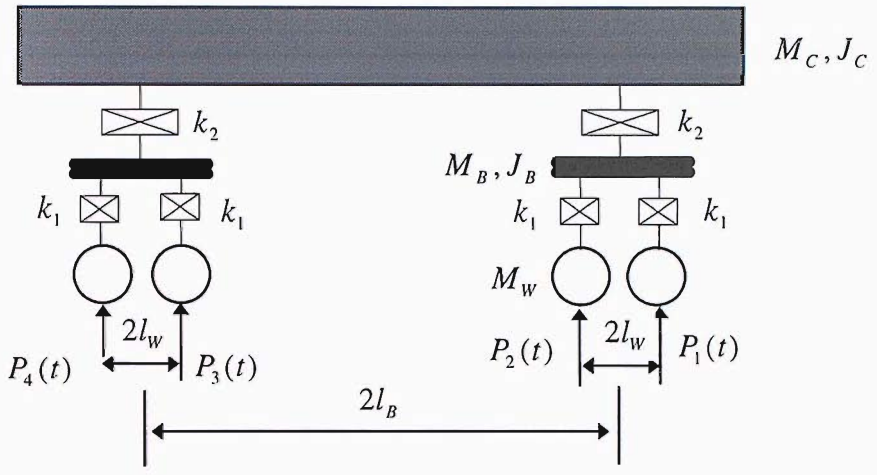

Figure 7.3. Type I: A vehicle system with primary and secondary suspensions.

where

$$[B] = \begin{bmatrix} [0]_{6\times4} \\ [I]_{4\times4} \end{bmatrix} \tag{7.42}$$

$$\{P(t)\} = (P_1(t), P_2(t), P_3(t), P_4(t))^T \tag{7.43}$$

is the vertical wheel-rail force vector, and

$$\{F(t)\} = (F_1(t), F_2(t), F_3(t), F_4(t))^T \tag{7.44}$$

is a vertical external force vector exerted at the wheelsets (not shown in Figure 7.3).

The wheelset displacement vector can be written as (see Equation (7.8))

$$\{z_W(t)\} = [A]\{z_V(t)\} \tag{7.45}$$

where

$$[A] = \begin{bmatrix} [0]_{4\times6} & [I]_{4\times4} \end{bmatrix} = [B]^T \tag{7.46}$$

The mass matrix is given by

$$[M_V] = \text{diag}(M_C, J_C, M_B, J_B, M_B, J_B, M_W, M_W, M_W, M_W) \tag{7.47}$$

and the stiffness matrix by

$$[K_V] =$$

$$\begin{bmatrix}
2k_2 & 0 & -k_2 & 0 & -k_2 & 0 & 0 & 0 & 0 & 0 \\
0 & 2k_2 l_B^2 & -k_2 l_B & 0 & k_2 l_B & 0 & 0 & 0 & 0 & 0 \\
-k_2 & -k_2 l_B & k_2 + 2k_1 & 0 & 0 & 0 & -k_1 & -k_1 & 0 & 0 \\
0 & 0 & 0 & 2k_1 l_W^2 & 0 & 0 & -k_1 l_W & k_1 l_W & 0 & 0 \\
-k_2 & k_2 l_B & 0 & 0 & k_2 + 2k_1 & 0 & 0 & 0 & -k_1 & -k_1 \\
0 & 0 & 0 & 0 & 0 & 2k_1 l_W^2 & 0 & 0 & -k_1 l_W & k_1 l_W \\
0 & 0 & -k_1 & -k_1 l_W & 0 & 0 & k_1 & 0 & 0 & 0 \\
0 & 0 & -k_1 & k_1 l_W & 0 & 0 & 0 & k_1 & 0 & 0 \\
0 & 0 & 0 & 0 & -k_1 & -k_1 l_W & 0 & 0 & k_1 & 0 \\
0 & 0 & 0 & 0 & -k_1 & k_1 l_W & 0 & 0 & 0 & k_1
\end{bmatrix} \quad (7.48)$$

7.6.2 FOR VEHICLE TYPE II

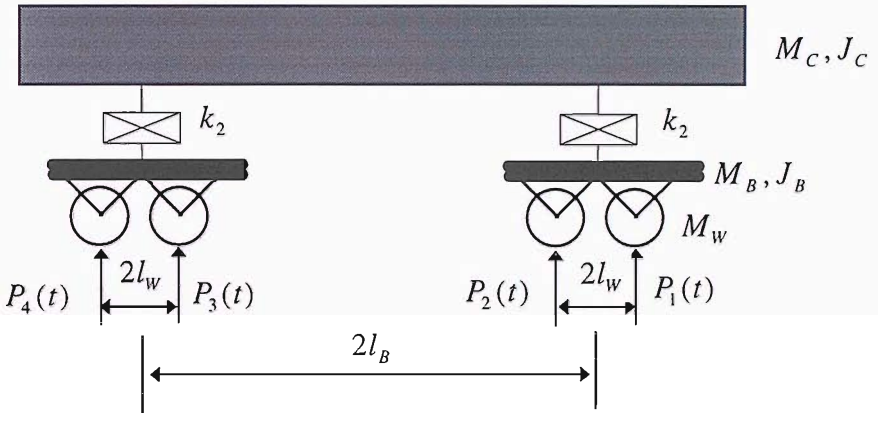

Figure 7.4. Type II: A vehicle system with only secondary suspensions.

Figure 7.4 (type II) shows a freight vehicle with only one level of suspension which is installed between the car body and the bogies. The displacement vector is defined as

$$\{z_V(t)\} = (z_C(t), \varphi_C(t), z_{B1}(t), \varphi_{B1}(t), z_{B2}(t), \varphi_{B2}(t))^T \quad (7.49)$$

Thus the external force vector is determined as

$$\{F_V(t)\} = [B](\{F(t)\} - \{P(t)\}) \quad (7.50)$$

where

$$[B] = \begin{bmatrix} 0 & 0 & 0 & 0 \\ 0 & 0 & 0 & 0 \\ 1 & 1 & 0 & 0 \\ l_W & -l_W & 0 & 0 \\ 0 & 0 & 1 & 1 \\ 0 & 0 & l_W & -l_W \end{bmatrix} \tag{7.51}$$

The wheelset displacement vector is given by

$$\{z_W(t)\} = [A]\{z_V(t)\} \tag{7.52}$$

where

$$[A] = \begin{bmatrix} 0 & 0 & 1 & l_W & 0 & 0 \\ 0 & 0 & 1 & -l_W & 0 & 0 \\ 0 & 0 & 0 & 0 & 1 & l_W \\ 0 & 0 & 0 & 0 & 1 & -l_W \end{bmatrix} = [B]^T \tag{7.53}$$

The mass matrix is given by

$$[M_V] = \text{diag}(M_C, J_C, M_B + 2M_W, J_B + 2M_W l_W^2, M_B + 2M_W, J_B + 2M_W l_W^2) \tag{7.54}$$

and the stiffness matrix by

$$[K_V] = \begin{bmatrix} 2k_2 & 0 & -k_2 & 0 & -k_2 & 0 \\ 0 & 2k_2 l_B^2 & -k_2 l_B & 0 & k_2 l_B & 0 \\ -k_2 & -k_2 l_B & k_2 & 0 & 0 & 0 \\ 0 & 0 & 0 & 0 & 0 & 0 \\ -k_2 & k_2 l_B & 0 & 0 & k_2 & 0 \\ 0 & 0 & 0 & 0 & 0 & 0 \end{bmatrix} \tag{7.55}$$

7.6.3 FOR VEHICLE TYPE III

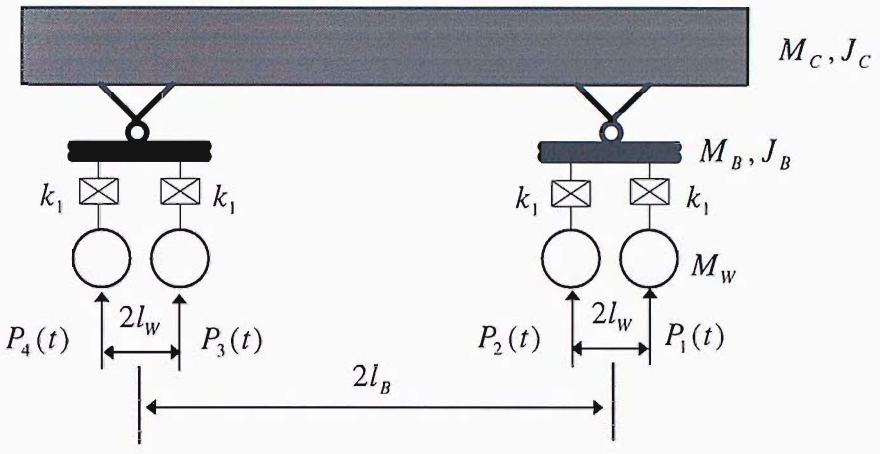

Figure 7.5. Type III: A vehicle system with only primary suspensions.

The third type (type III) shown in Figure 7.5 is also a freight vehicle with only one level of suspension which is between the axle boxes and the bogies. The displacement vector is defined as

$$\{z_V(t)\} = (z_C(t), \varphi_C(t), \varphi_{B1}(t), \varphi_{B2}(t), z_{W1}(t), z_{W2}(t), z_{W3}(t), z_{W4}(t))^T \tag{7.56}$$

Thus the external force vector is determined as

$$\begin{aligned}\{F_V(t)\} &= (0,0,0,0, F_1(t) - P_1(t), F_2(t) - P_2(t), F_3(t) - P_3(t), F_4(t) - P_4(t))^T \\ &= [B](\{F(t)\} - \{P(t)\})\end{aligned} \tag{7.57}$$

where

$$[B] = \begin{bmatrix} [0]_{4\times4} \\ [I]_{4\times4} \end{bmatrix} \tag{7.58}$$

The wheelset displacement vector can be expressed as

$$\{z_W(t)\} = [A]\{z_V(t)\} \tag{7.59}$$

where

$$[A] = \begin{bmatrix} [0]_{4\times4} & [I]_{4\times4} \end{bmatrix} = [B]^T \tag{7.60}$$

The mass matrix is given by

$$[M_V] = \text{diag}(M_C + 2M_B, J_C + 2M_B l_B^2, J_B, J_B, M_W, M_W, M_W, M_W) \tag{7.61}$$

and the stiffness matrix is given by

$$[K_V]=\begin{bmatrix} 4k_1 & 0 & 0 & 0 & -k_1 & -k_1 & -k_1 & -k_1 \\ 0 & 4k_1 l_B^2 & 0 & 0 & -k_1 l_B & -k_1 l_B & k_1 l_B & k_1 l_B \\ 0 & 0 & 2k_1 l_W^2 & 0 & -k_1 l_W & k_1 l_W & 0 & 0 \\ 0 & 0 & 0 & 2k_1 l_W^2 & 0 & 0 & -k_1 l_W & k_1 l_W \\ -k_1 & -k_1 l_B & -k_1 l_W & 0 & k_1 & 0 & 0 & 0 \\ -k_1 & -k_1 l_B & k_1 l_W & 0 & 0 & k_1 & 0 & 0 \\ -k_1 & k_1 l_B & 0 & -k_1 l_W & 0 & 0 & k_1 & 0 \\ -k_1 & k_1 l_B & 0 & k_1 l_W & 0 & 0 & 0 & k_1 \end{bmatrix} \tag{7.62}$$

7.6.4. FOR VEHICLE TYPE IV

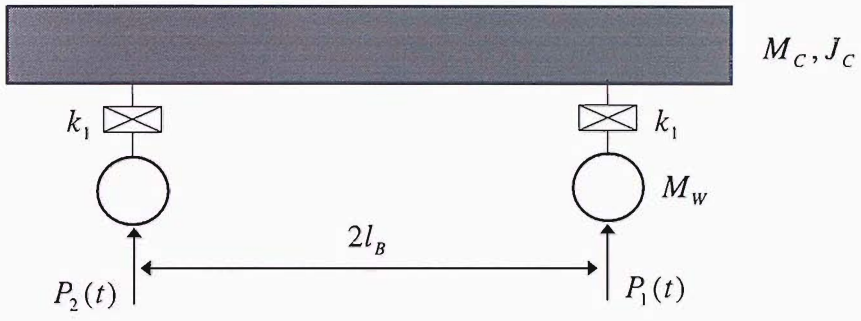

Figure 7.6. Type IV: A two-axle vehicle

Figure 7.6 (type IV) shows a freight vehicle with two axles. The displacement vector is defined as

$$\{z_V(t)\}=(z_C(t),\varphi_C(t),z_{W1}(t),z_{W2}(t))^T \tag{7.63}$$

Thus the external force vector is determined as

$$\{F_V(t)\}=[B](\{F(t)\}-\{P(t)\}) \tag{7.64}$$

where

$$[B]=\begin{bmatrix} 0 & 0 \\ 0 & 0 \\ 1 & 0 \\ 0 & 1 \end{bmatrix} \tag{7.65}$$

The wheelset displacement vector is given by

$$\{z_W(t)\} = [A]\{z_V(t)\} \tag{7.66}$$

where

$$[A] = \begin{bmatrix} 0 & 0 & 1 & 0 \\ 0 & 0 & 0 & 1 \end{bmatrix} = [B]^T \tag{7.67}$$

The mass matrix is given by

$$[M_V] = \text{diag}(M_C, J_C, M_W, M_W) \tag{7.68}$$

and the stiffness matrix by

$$[K_V] = \begin{bmatrix} 2k_1 & 0 & -k_1 & -k_1 \\ 0 & 2k_1 l_B^2 & -k_1 l_B & k_1 l_B \\ -k_1 & -k_1 l_B & k_1 & 0 \\ -k_1 & k_1 l_B & 0 & k_1 \end{bmatrix} \tag{7.69}$$

7.7 RESULTS AND DISCUSSION

7.7.1 RESULTS FOR A ONE-AXLE VEHICLE MODEL

To make discussion simpler, in this sub-section, a calculation is performed for a one-axle vehicle model comprising a suspended mass M_C and an unsprung mass M_W. Each mass only has one degree of freedom in the vertical direction. The parameters for this vehicle model are deduced from the parameters of a freight car of type II (C_{62A} in Table 1.1) and are listed in Table 7.1. From Table 7.1 the axle load is 205800 N. The radius of the wheel is 0.42 m, thus from equations (7.36) and (7.37) the Hertzian contact stiffness is evaluated as 2.7×10^9 N/m. The natural frequency of the suspended mass on the suspension is evaluated as $\frac{1}{2\pi}\sqrt{k_{S1}/M_C} = 1.87$ Hz.

TABLE 7.1

Parameters for the one-axle vehicle model

Suspended mass (kg)	Unsprung mass (kg)	k_{S1} (N/m)	c_{S1} (Ns/m)	$k_{S1}^{'}$ (N/m)
19250	1750	2.66×10^6	3.5×10^4	3×10^6

The ballasted tracks specified by Tables 1.8 (the lighter track) and 1.9 (the heavier track), and the layered ground specified by Table 1.7 (the softer ground), are used

in the calculation. A vertical irregular rail profile with amplitude of 0.1 mm but varying wavelengths is introduced as the excitation.

7.7.1.1 *WHEN THE VEHICLE IS RUNNING ON THE LIGHTER TRACK ON THE GROUND*

Figure 7.7 shows the magnitude of the dynamic wheel-rail force plotted against excitation frequency (speed divided by wavelength) for three travelling speeds, 0, 30 m/s (108 km/h) and 60 m/s (216 km/h). Figures 7.8 and 7.9 show the magnitudes of the displacements of the contact points on the wheel and on the rail.

At $f = 2$ Hz, Figures 7.7 and 7.9 indicate a very small peak, while Figure 7.8 shows a local minimum. This frequency is close to the natural frequency of the suspended mass on the suspension. The magnitude of the wheel-rail force increases with frequency and achieves a maximum at a particular frequency (around 80 Hz) within the frequency range shown. As the travelling speed increases, this frequency decreases and the maximum wheel-rail force decreases. Previously, the wheel-rail force was calculated without considering the vehicle motion, as indicated here, the effect of the vehicle motion is negligible for low frequencies and low vehicle speeds.

The effect of the layered structure of the ground on the wheel-rail force is not noticeable, compared to those on the displacements of the wheel/rail contact points. As shown in Figure 7.9, for low vehicle speed, around the first cut-on frequency of the track-ground system (16 Hz), the displacement at the wheel-rail contact point on the rail has a peak and this peak is flattened when the vehicle speed increases. This peak is also seen on the wheel, Figure 7.8.

Now in equation (7.21) let $M = 1, \tilde{F}_1(\Omega) = 0$, so that

$$\tilde{P}_1(\Omega) = -\frac{\tilde{z}_1(\Omega)}{\sigma_{11}^T + \sigma_{11}^R + 1/k_{H1}} \tag{7.70}$$

where, σ_{11}^R denotes the receptance of the rail at the wheel/rail contact point, σ_{11}^T the receptance of the vehicle at the wheelset, given by

$$\sigma_{11}^T = \frac{1-(\Omega/\omega_0)^2}{\omega_0^2(\Omega/\omega_0)^2[M_W(\Omega/\omega_0)^2-(M_C+M_W)]} \tag{7.71}$$

where, $\omega_0 = \sqrt{k_1 / M_C}$ denotes the damped natural frequency of the suspended mass on the suspension. From equations (7.19) and (7.20),

$$\tilde{z}_{W1}(\Omega) = \frac{\sigma_{11}^T \tilde{z}_1(\Omega)}{\sigma_{11}^T + \sigma_{11}^R + 1/k_{H1}} \tag{7.72}$$

$$\tilde{z}_{R1}(\Omega) = -\frac{\sigma_{11}^R \tilde{z}_1(\Omega)}{\sigma_{11}^T + \sigma_{11}^R + 1/k_{H1}} \tag{7.73}$$

It can be seen from equations (7.71), (7.72) and (7.73) that, when $\Omega \to 0, \sigma_{11}^T \to \infty$, $\tilde{z}_{W1} \to \tilde{z}_1$, and $\tilde{z}_{R1} \to 0$. This low frequency feature is illustrated in Figures 7.8 and 7.9. At the natural frequency of the suspended mass on the suspension, $\sigma_{11}^T = 0$ (if there is no damping), thus, both the wheel-rail force and the displacement of the contact point on the rail have a peak while the displacement of the wheel has a local minimum.

For frequencies much higher than the natural frequency of the suspended mass on the suspension, the displacement of the suspended mass is negligible. Thus the receptance of the vehicle at a wheelset can be approximated by

$$\sigma_{11}^T = \frac{1}{k_1 - M_W \Omega^2} \tag{7.74}$$

which implies that, when $\Omega^2 = k_1 / M_W$, i.e., around the natural frequency of the unsprung mass on suspended mass (which is much higher than the natural frequency of the suspended mass on the suspension, since the unsprung mass is much smaller), $\sigma_{11}^T \to \infty$, $\tilde{P}_1 \to 0$, $\tilde{z}_{W1} \to \tilde{z}_1$, and $\tilde{z}_{R1} \to 0$. The presence of damping in the suspension of the vehicle produces a local minimum in the wheel-rail force and a local minimum in the rail displacement at this frequency. For the present vehicle parameters, this frequency is evaluated as 9.2 Hz.

When $\Omega \to \infty$, then $\sigma_{11}^T \to 0, \sigma_{11}^R \to 0$, thus the wheel-rail force is bounded, as indicated by equation (7.70).

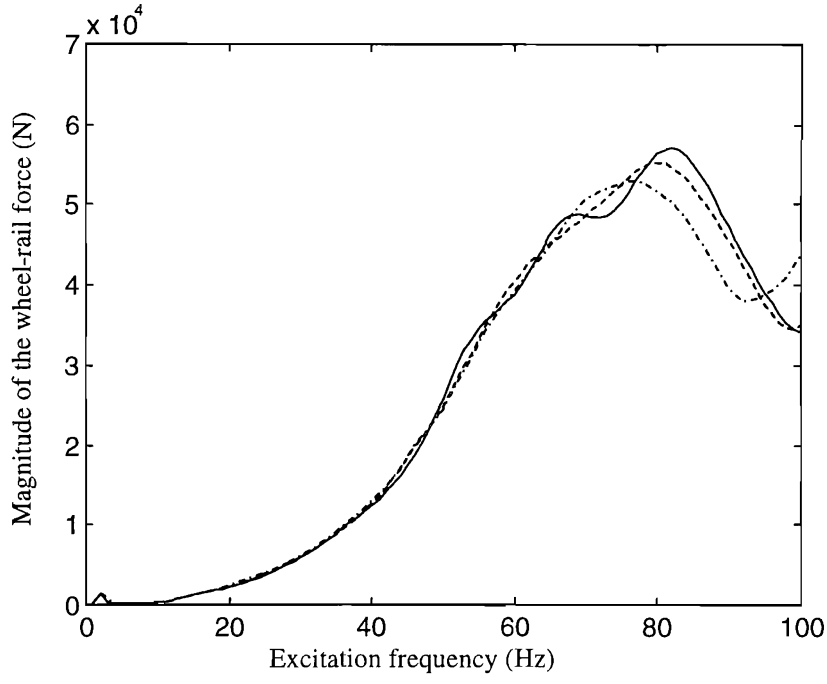

Figure 7.7. Magnitude of the wheel-rail force plotted against frequency of excitation. ——, for vehicle running at 0 m/s; – – –, for vehicle running at 30 m/s; – · –, for vehicle running at 60 m/s.

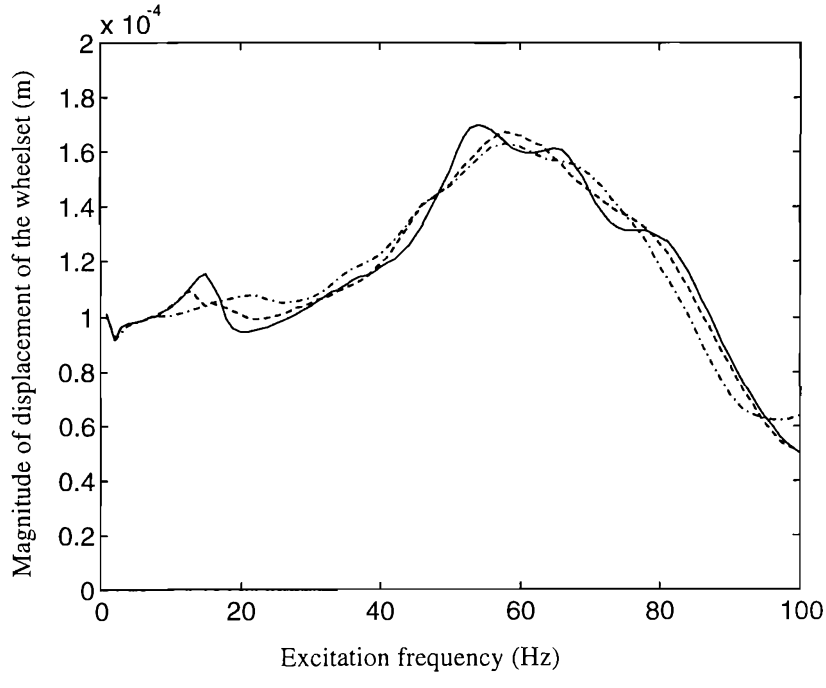

Figure 7.8. Magnitude of displacement of the wheelset plotted against frequency of excitation. ——, for vehicle running at 0 m/s; – – –, for vehicle running at 30 m/s; – · –, for vehicle running at 60 m/s.

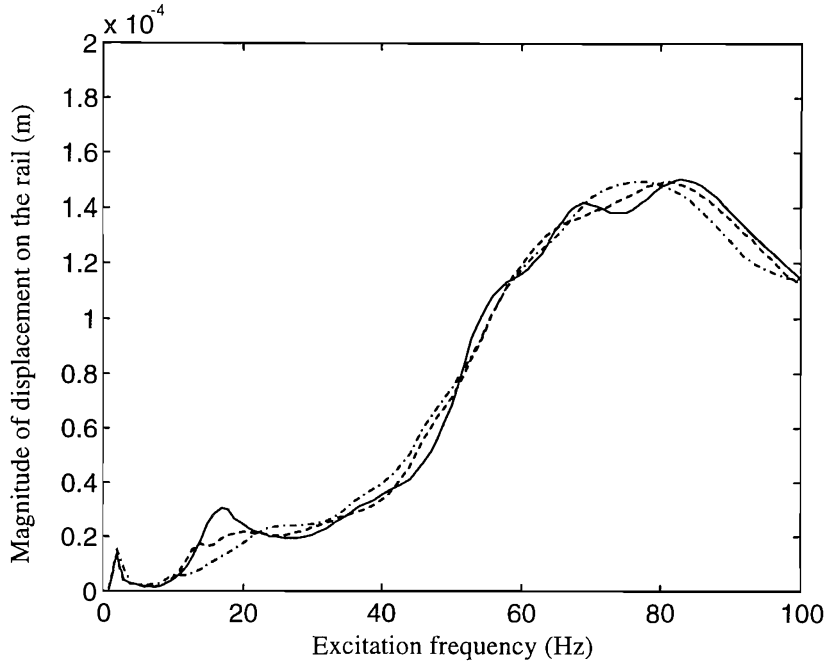

Figure 7.9. Magnitude of the displacement of the wheel/rail contact point on the rail plotted against frequency of excitation. ——, for vehicle running at 0 m/s; – – –, for vehicle running at 30 m/s; – · –, for vehicle running at 60 m/s.

Figure 7.9 shows that the vehicle speed does not have a significant effect on the displacement of the wheel/rail contact point on the rail. However, the vibration propagation in the track direction is strongly influenced by the vehicle travelling speed. To show this, the magnitudes of the vertical displacement along the x-axis on the ground surface for different excitation frequencies are shown in Figures 7.10 to 7.12 for the three vehicle speeds. It can be seen that around the natural frequency of the suspended mass on the suspension, the ground surface has a peak response. Figure 7.10 shows that when the excitation frequency is about 16 Hz, i.e. the first track-modified cut-on frequency of the soft layered ground, strong vibration propagation occurs in the track direction. As the vehicle speed increases, this vibration propagation is greatly enhanced in the reverse direction of the vehicle motion in a wider frequency range consisting of higher frequencies, as can be seen in Figures 7.11 and 7.12.

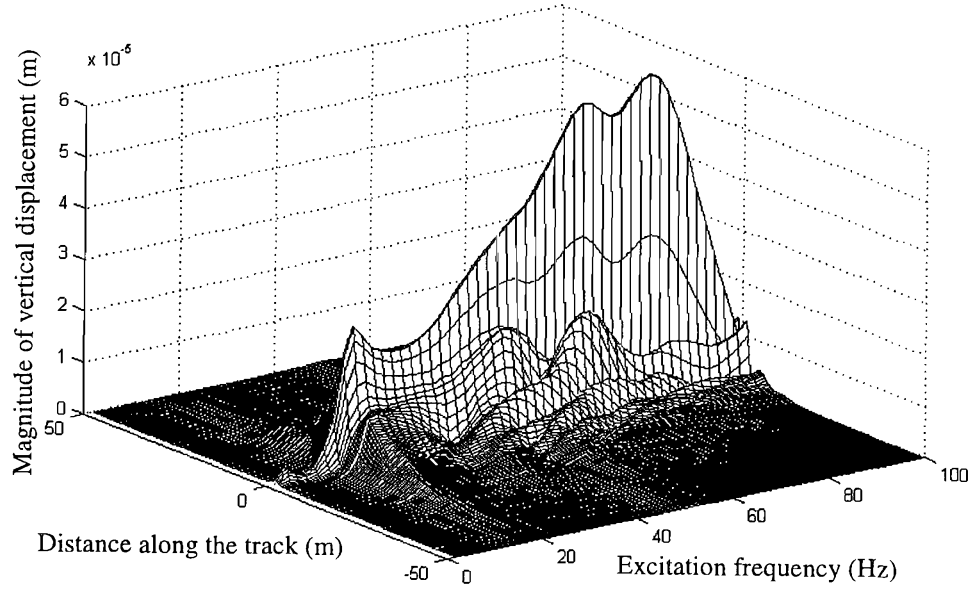

Figure 7.10. Vertical displacement along x-axis on the ground surface for $c = 0$ m/s.

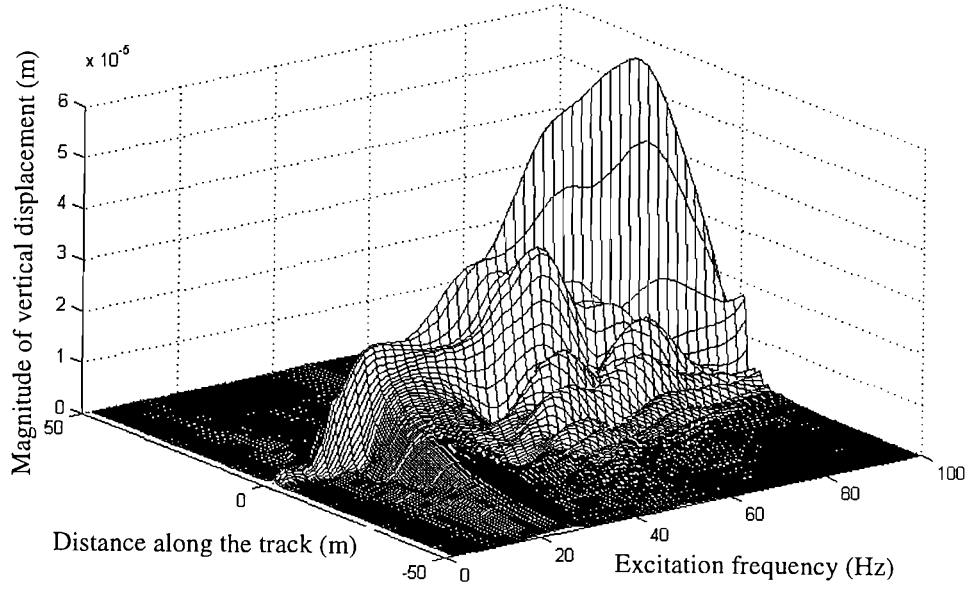

Figure 7.11. Vertical displacement along x-axis on the ground surface for $c = 30$ m/s.

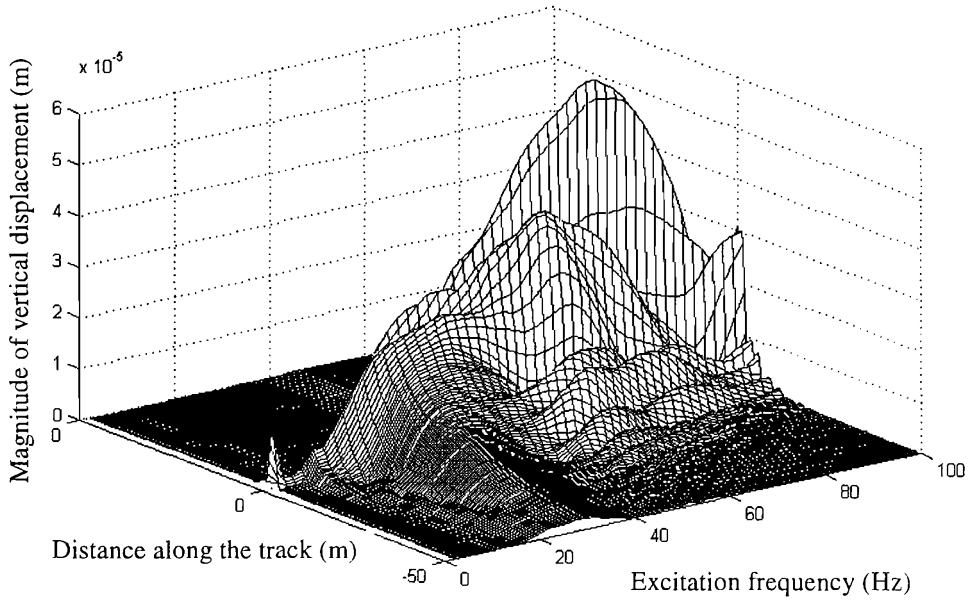

Figure 7.12. Vertical displacement along x-axis on the ground surface for c = 60 m/s.

7.7.1.2 *WHEN THE VEHICLE IS RUNNING ON THE HEAVIER TRACK ON THE GROUND*

Compared with the lighter track, the heavier track (Table 1.9) has more ballast mass and less ballast stiffness. Some results for the heavier track on the ground are shown in Figures 7.13 to 7.16, with comparison made with those for the lighter track.

Figure 7.13 shows the magnitude of the wheel-rail force for the vehicle running at 60 m/s. It can be seen that for excitation frequencies lower than 67 Hz, the heavier track produces slightly less wheel-rail force than the lighter track. However, for higher excitation frequencies, the heavier track produces much greater wheel-rail force. Figure 7.14 shows the displacement of the wheelset plotted against excitation frequency and indicates that for excitation frequencies higher than 67 Hz, the displacement of the wheelset is greater when it runs on the heavier track. Figures 7.15 and 7.16 present the maximum displacements along the rail and along the track centre-line on the ground surface. Both of these figures indicate that the heavier track produces less vibration for frequencies lower than 85 Hz.

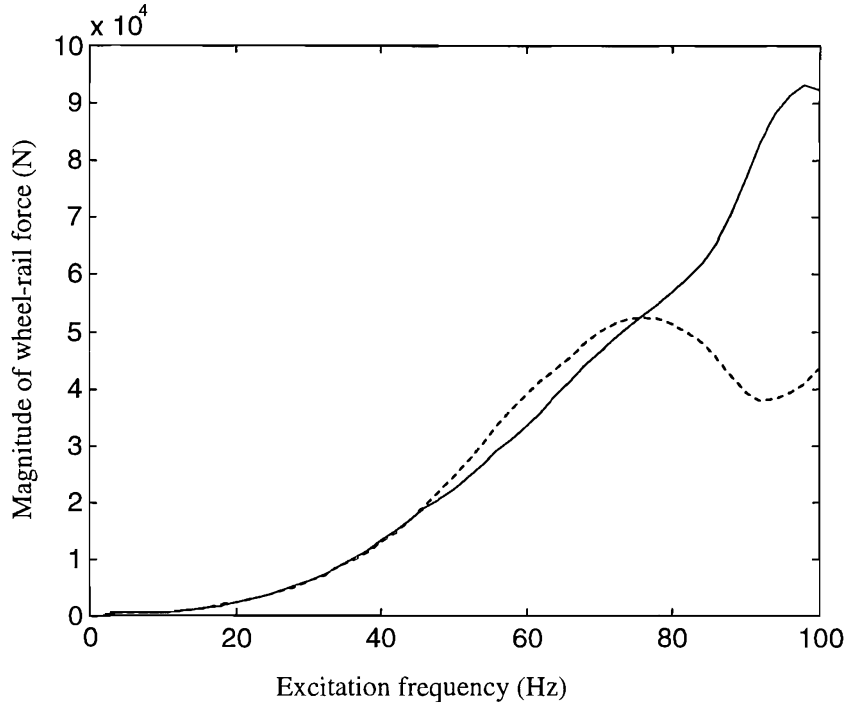

Figure 7.13. Magnitude of the wheel-rail force plotted against excitation frequency for the vehicle running at 60 m/s. ——, for the vehicle running on the heavier track; – – –, for the vehicle on the lighter track.

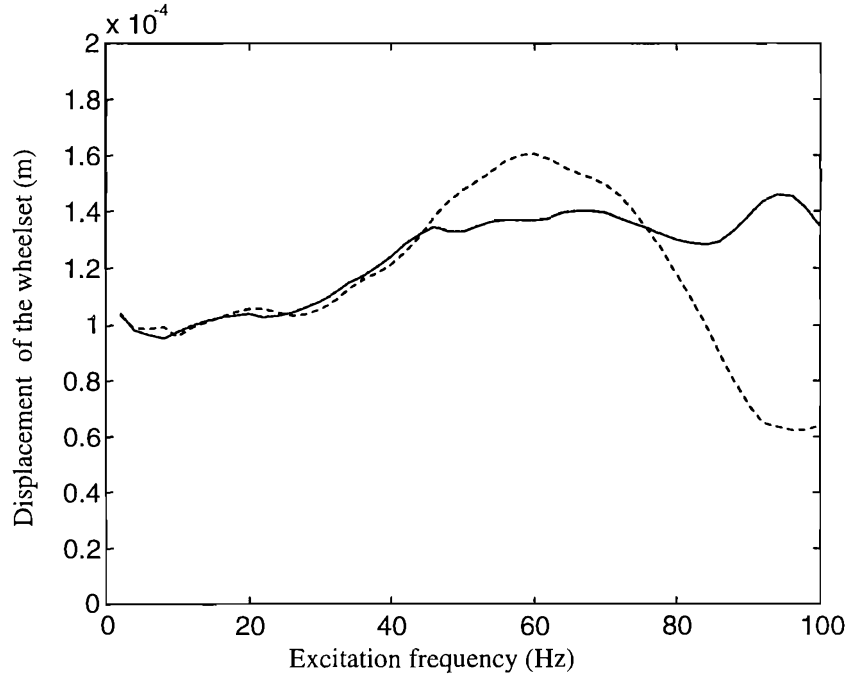

Figure 7.14. Magnitude of the displacement of the wheelset plotted against excitation frequency for the vehicle running at 60 m/s. ——, for the vehicle running on the heavier track; – – –, for the vehicle on the lighter track.

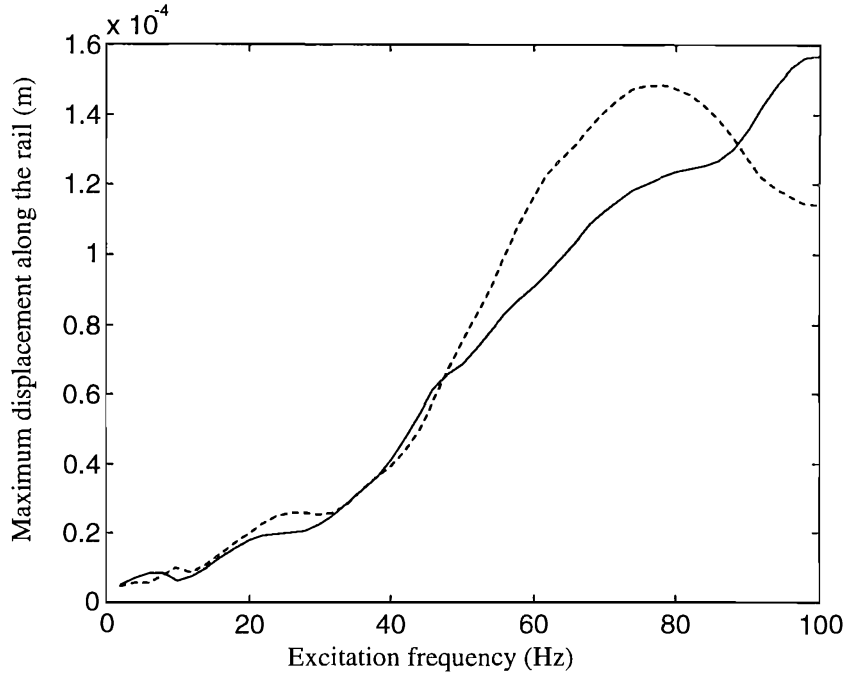

Figure 7.15. Maximum displacement along the rails plotted against excitation frequency for the vehicle running at 60 m/s. ——, for the vehicle running on the heavier track; – – –, for the vehicle on the lighter track.

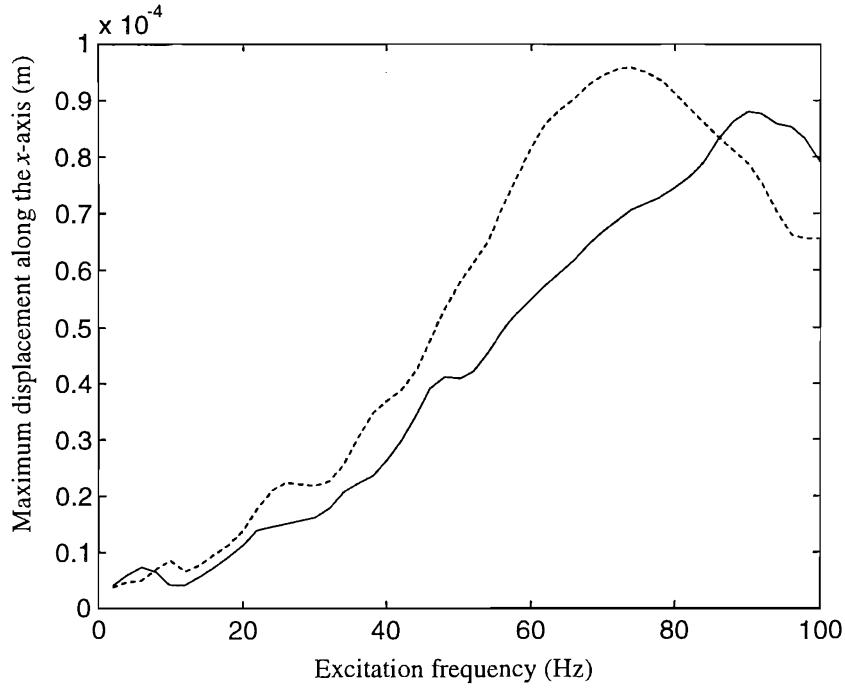

Figure 7.16. Maximum displacement along the x-axis on the ground surface plotted against excitation frequency for the vehicle running at 60 m/s. ——, for the vehicle running on the heavier track; – – –, for the vehicle on the lighter track.

7.7.2 RESULTS FOR A MK 3 PASSENGER COACH

In this sub-section, the vertical velocity levels of the surface of the softer ground with different tracks are calculated using equation (7.32) for a single Mk 3 passenger coach (vehicle type I) running at different speeds. The parameters for this vehicle are listed in Table 1.1. In addition to the lighter track and the heavier track (both are ballasted track) used in the last sub-section, calculations are also performed for a slab track. The width and the thickness of the slab are 2.5 m and 0.25 m. Other parameters of the slab track are listed in Table 7.2. The slab track has almost the same mass as the heavier ballasted track. The difference between the heavier track and the slab track is that the slab track has nearly ten times the bending stiffness and twice the vertical stiffness of the heavier track. For these analyses, the vertical rail-head profile for a nominally 'good' track measured on a 200 km/h mixed traffic main line in England is used in the calculation. The power spectral density of this profile is shown in Figure 8.19 in the next chapter.

TABLE 7.2

Parameters for a slab railway track

Mass of rail beam per unit length of track	120 kg/m
Bending stiffness of rail beam	1.26×10^{7} Nm^2
Loss factor of the rail	0.01
Rail pad stiffness	2×10^{8} N/m^2
Rail pad loss factor	0.25
Mass of slab per unit length of track	(2.5×0.25×2400)=1500 kg/m
Bending stiffness of slab	1.11×10^{8} Nm^2
Loss factor of slab material	0.03
Contact width of track and ground	2.7m

Predictions of the vibration velocity spectra of the ground surface are shown in Figures 7.17 to 7.29 for three points on the ground surface and for three vehicle speeds, 25 m/s, 60 m/s and 83 m/s. The distances from these three points to the track centre-line are 5 m, 10 m and 20 m. Also shown are the vertical velocity levels due to the quasi-static loads only. Discussion based on these figures is carried out on three aspects.

7.7.2.1 *LEVELS OBSERVED AT DIFFERENT DISTANCES FROM THE TRACK*

Three frequency ranges may be identified in these figures (approximately): 1.6 to 6 Hz, 6 to 20 Hz and 20 to 80 Hz. These approximate ranges will be referred to as the *low*, *middle* and *upper* frequency ranges in this discussion. As seen in Figure 7.17 to Figure 7.25, the response level is dominated by the quasi-static loads for low frequencies

only up to a few Hertz. The lower the vehicle speed or the further the observer from the track, the more important is the dynamic component of excitation. For example, as shown in Figure 7.18 for a vehicle speed of 60 m/s, the quasi-static loads are the dominant source for frequencies below 8 Hz at 5 m, 5 Hz at 10 m and 3.2 Hz at 20 m. In the *low* frequency range, which is dominated by the quasi-static loads, the attenuation rate with distance from the track is much higher than those in the *middle* and *upper* frequency ranges. In the *middle* frequency range, a strong rise in the total response level is observed due to the cut-on of the first propagating wave mode in the track-ground system. In this frequency range, the vibration has least attenuation rate compared to the *low* and the *upper* frequency ranges.

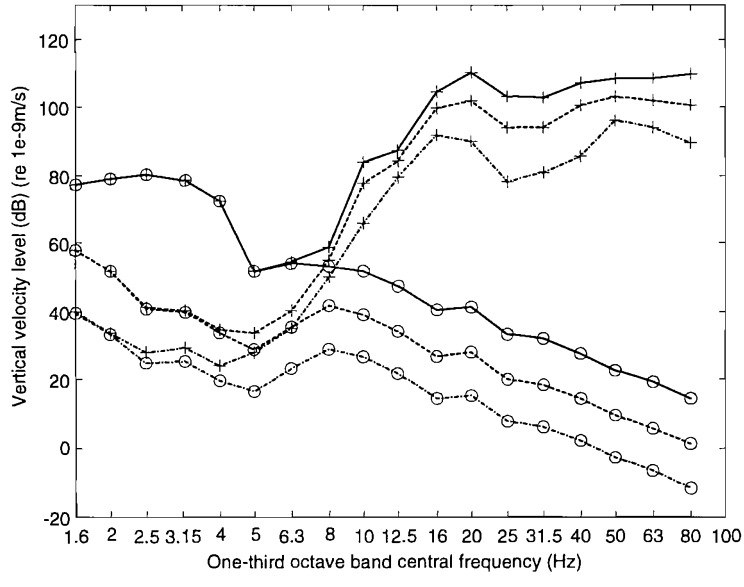

Figure 7.17. Vertical velocity levels for points at 5 m (——), 10 m (– – –) and 20 m (– · –) from the track centre-line when a Mk 3 coach runs on the lighter track at 25 m/s. +: total level , ○: level due the quasi-static loads.

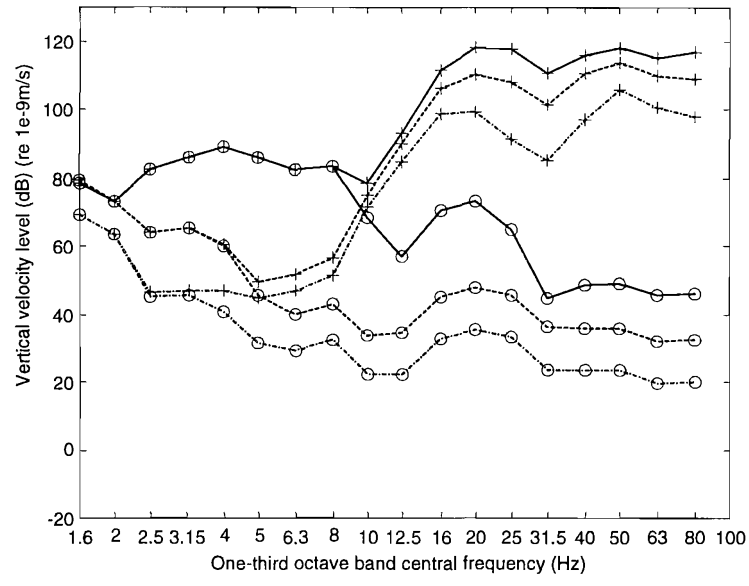

Figure 7.18. Vertical velocity levels for points at 5 m (——), 10 m (– – –) and 20 m (– · –) from the track centre-line when a Mk 3 coach runs on the lighter track at 60 m/s. +: total level; ○: level due to the quasi-static loads.

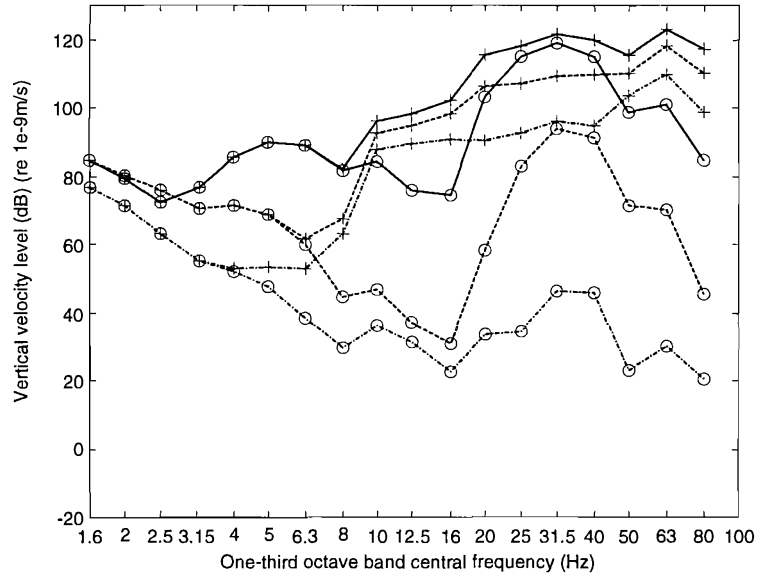

Figure 7.19. Vertical velocity levels for points at 5 m (——), 10 m (– – –) and 20 m (– · –) from the track centre-line when a Mk 3 coach runs on the lighter track at 83 m/s. +: total level; ○: level due to the quasi-static loads.

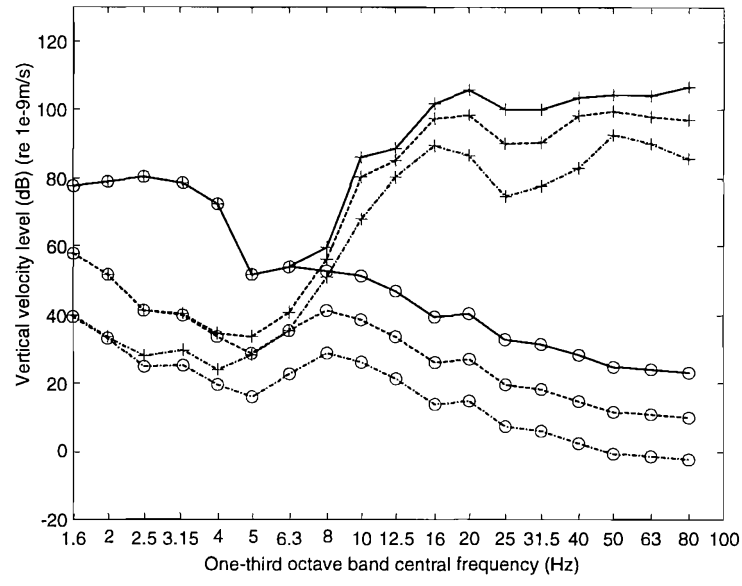

Figure 7.20. Vertical velocity levels for points at 5 m (——), 10 m (– – –) and 20 m (– · –) from the track centre-line when a Mk 3 coach runs on the heavier track at 25 m/s. +: total level; o: level due to the quasi-static loads.

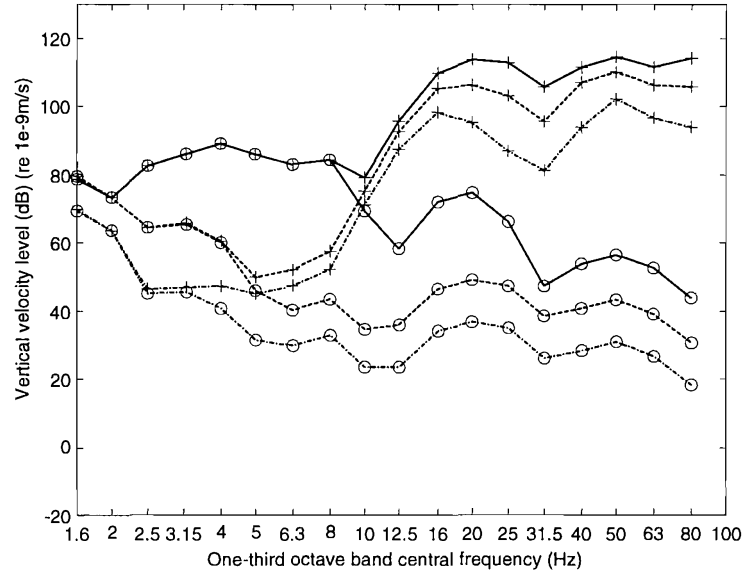

Figure 7.21. Vertical velocity levels for points at 5 m (——), 10 m (– – –) and 20 m (– · –) from the track centre-line when a Mk 3 coach runs on the heavier track at 60 m/s. +: total level; o: level due to the quasi-static loads.

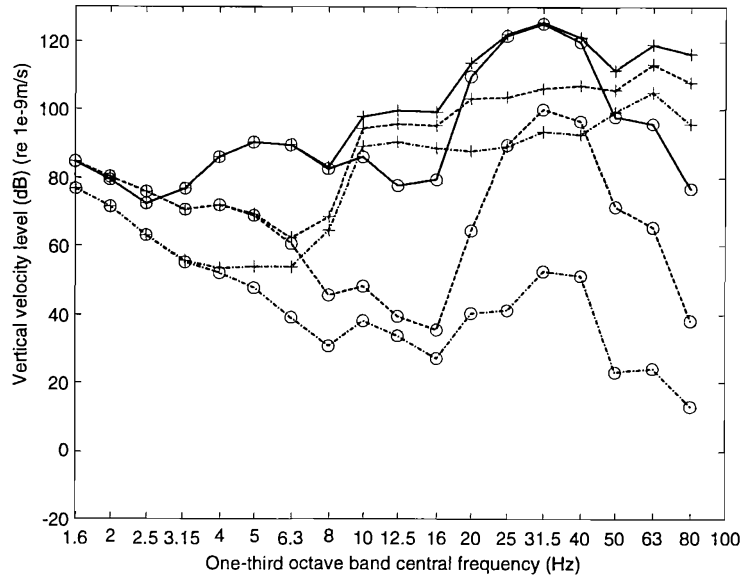

Figure 7.22. Vertical velocity levels for points at 5 m (——), 10 m (– – –) and 20 m (– · –) from the track centre-line when a Mk 3 coach runs on the heavier track at 83 m/s. +: total level; ○: level due to the quasi-static loads.

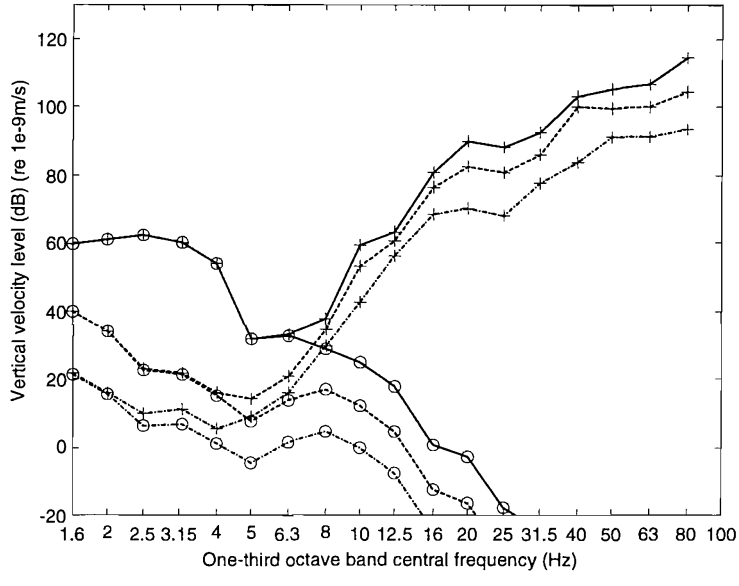

Figure 7.23. Vertical velocity levels for points at 5 m (——), 10 m (– – –) and 20 m (– · –) from the track centre-line when a Mk 3 coach runs on the slab track at 25 m/s. +: total level; ○: level due to the quasi-static loads.

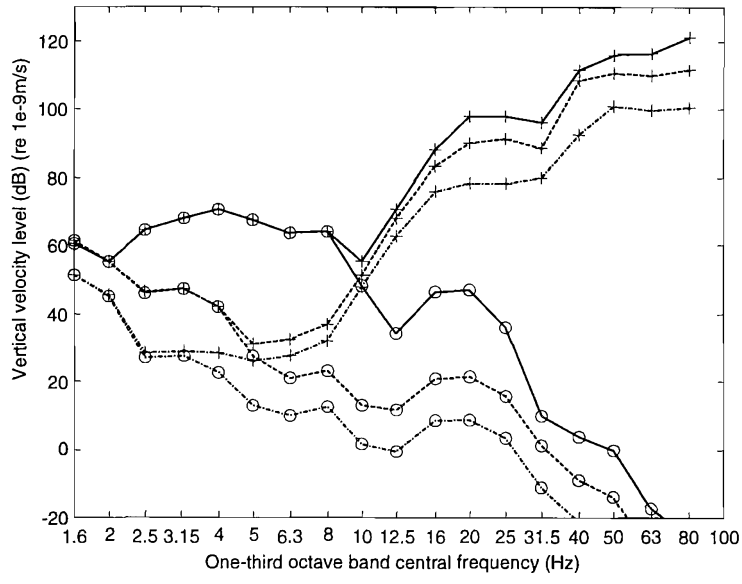

Figure 7.24. Vertical velocity levels for points at 5 m (——), 10 m (– – –) and 20 m (– · –) from the track centre-line when a Mk 3 coach runs on the slab track at 60 m/s. +: total level; ○: level due to the quasi-static loads.

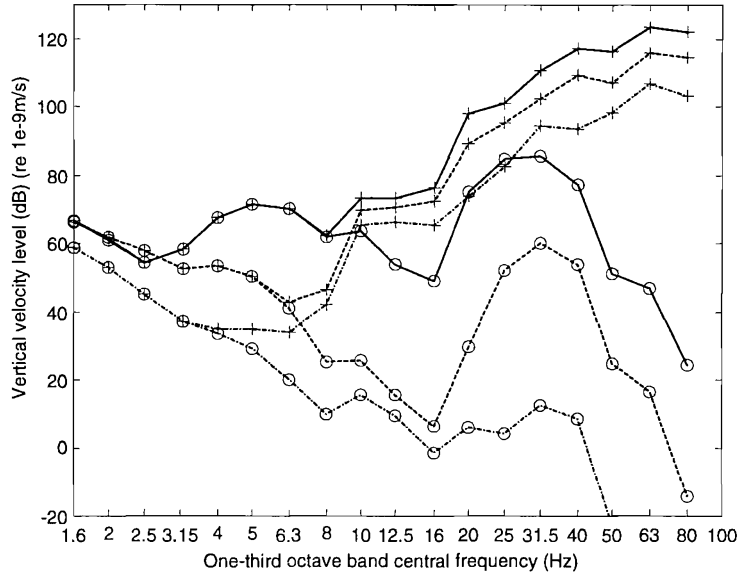

Figure 7.25. Vertical velocity levels for points at 5 m (——), 10 m (– – –) and 20 m (– · –) from the track centre-line when a Mk 3 coach runs on the slab track at 83 m/s. +: total level; ○: level due to the quasi-static loads.

7.7.2.2 *EFFECT OF TRACK STRUCTURE ON THE RESPONSE LEVEL*

A comparison between the three tracks is presented in Figures 7.26 to 7.28 for the three travelling speeds, 25 m/s, 60 m/s and 83 m/s. In these figures only the vertical

velocity levels at 10 m on the ground surface are shown. Since the heavier ballasted track produces less vibration from the dynamic wheel-rail forces (Figure 7.16) but greater vibration from the quasi-static loads (Figure 6.22) than the lighter track, the heavier track only gives a little reduction in vibration level in the *upper* frequency range (Figures 7.26 to 7.28). However, the slab track has a quite different behaviour. Due to its much greater bending stiffness, the slab track produces about 20 dB lower vibration level than either of the ballasted tracks for frequencies up to 25 Hz. Compared to the ballasted tracks, the slab track greatly reduces the vibration level due to the quasi-static loads, since the peak response load speed of the ground with the slab track is significantly increased by the bending stiffness of the track; therefore it is more effective for low frequencies. For high frequencies, it may increase the level due to dynamic wheel-rail forces, as can be seen, for frequencies higher than 40 Hz, the response levels for the three tracks are close to each other.

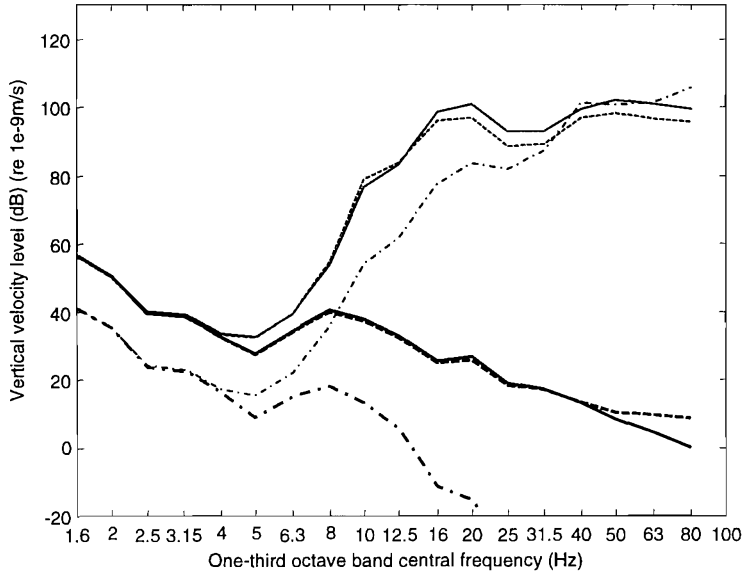

Figure 7.26. Vertical velocity level at 10 m on the ground surface for vehicle speed 25 m/s. ——, for the lighter track; – – –, for the heavier track; – · –, for the slab track. Thicker lines are for the levels due to the quasi-static loads.

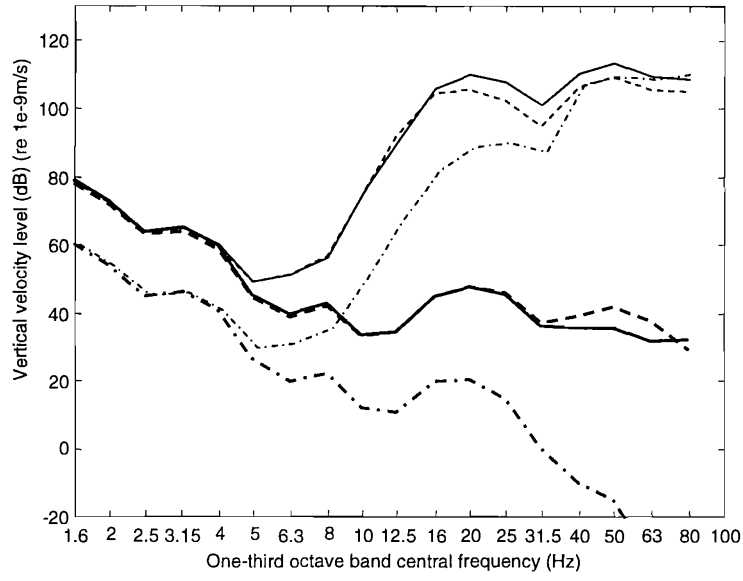

Figure 7.27. Vertical velocity level at 10 m on the ground surface for vehicle speed 60 m/s. ——, for the lighter track; – – –, for the heavier track; – · –, for the slab track. Thicker lines are for the levels due to the quasi-static loads.

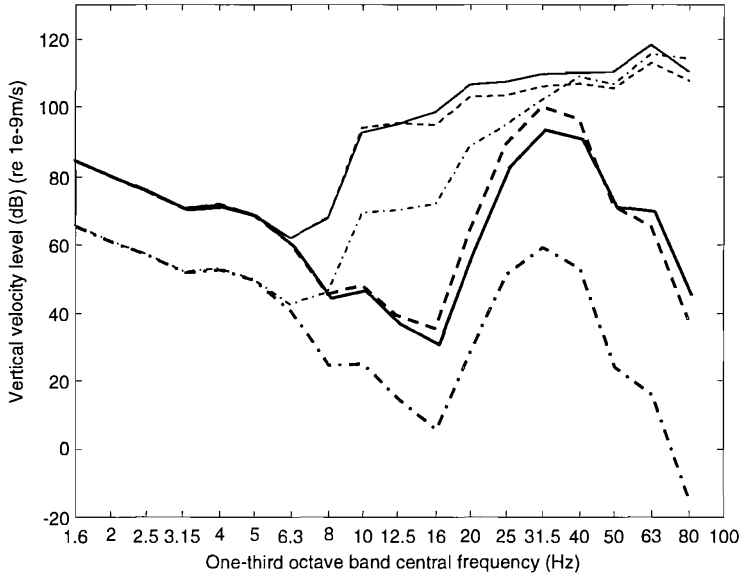

Figure 7.28. Vertical velocity level at 10 m on the ground surface for vehicle speed 83 m/s. ——, for the lighter track; – – –, for the heavier track; – · –, for the slab track. Thicker lines are for the levels due to the quasi-static loads.

7.7.2.3 *EFFECT OF VEHICLE SPEED ON RESPONSE LEVEL*

The effect of vehicle travelling speeds on the response level is shown in Figure 7.29 for a point at 10 m on the ground surface with the heavier track. With increasing

vehicle speed, the upper limit of frequency at which the quasi-static loads are the dominant source is slightly increased, from 3.2 Hz for 25 m/s to 6 Hz for 83 m/s. From 6 to 16 Hz, a strong rise in the total response level is shown in the figure due to the cut-on of the first propagating wave mode in the track-ground system. Since the quasi-static loads are the dominating mechanism of excitation for frequencies below the cut-on frequency, the vehicle travelling speed has a greater effect on the response level for this frequency range. For higher frequencies, though the response level due to the quasi-static loads is strongly dependant on the vehicle speed, the dynamic response and, therefore, the total response level is far less dependant on this. This is still more the case at further distances, see Figures 7.19, 7.22 and 7.25.

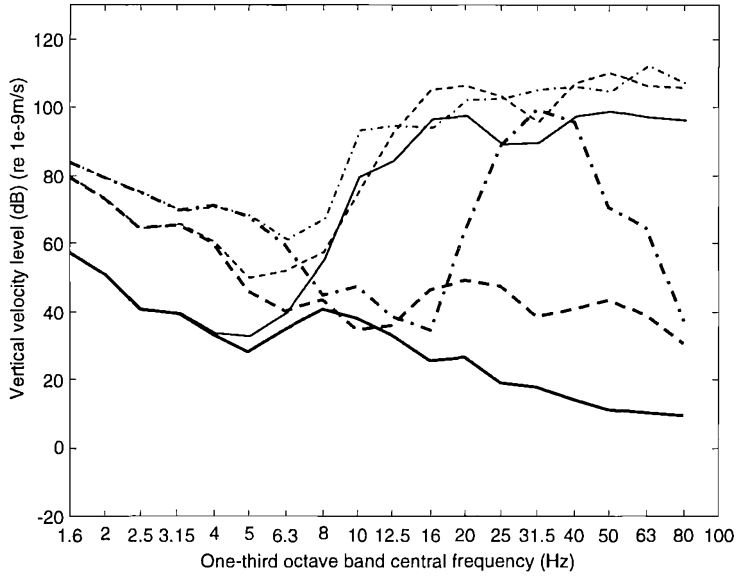

Figure 7.29. Vertical velocity level at 10 m on the ground surface with the heavier track for different vehicle speeds. ——, 25 m/s; – – –, 60 m/s; – · –, 83 m/s. Thicker lines are for the levels due to the quasi-static loads.

7.8 SUMMARY

In this chapter, the vertical dynamics of vehicles running uniformly on a track has been coupled with the track-ground model developed in Chapter 5, producing a whole model incorporating vehicles, track and ground. A relationship is derived between the rail irregularity spectral density and the ground vibration power spectra. This relationship makes the prediction from the model comparable to measured data as shown in the next chapter, Chapter 8.

From this model, the wheel-rail dynamic force and the maximum displacement along the track centre-line on the ground surface are calculated for a one-axle vehicle model and for the lighter and heavier tracks. It is shown that, for a large range of frequencies, the layered structure of the ground and the vehicle speed have little effect on the wheel-rail force and the displacements of the wheel/rail contact points. However, the wave propagation in the track direction is strongly enhanced by the motion of the vehicle. The heavier track may reduce the vibration due to the dynamic wheel-rail force.

Also produced from this model are vertical velocity levels of the softer ground surface for a Mk 3 passenger coach running, respectively, on the lighter ballasted track, the heavier ballasted track and a slab track. Three frequency ranges are identified by these results: frequencies much below the cut-on frequency of the track-ground system (*low* frequency range), frequencies around the cut-on frequency (*middle* frequency range) and frequencies above this (*upper* frequency range). Only in the *low* frequency range is the response level dominated by the quasi-static loads. The lower the vehicle speed or the further the observer from the track, the more important is the dynamic component of excitation. In the *low* frequency range, the attenuation rate with distance from the track is much higher than those in the other two frequency ranges. In the *middle* frequency range, a strong rise in the total response level is observed due to the cut-on of the first propagating wave mode in the track-ground system. In this frequency range, the vibration has the lowest attenuation rate compared to the *low* and the *upper* frequency ranges. Since the heavier ballasted track produces less vibration from the dynamic wheel-rail forces but greater vibration from the quasi-static loads than the lighter track, the heavier track only gives a little reduction in vibration level in the *upper* frequency range.

Due to its much greater bending stiffness, the slab track produces about 20 dB lower vibration level than either of the ballasted tracks for frequencies up to 25 Hz. Compared to the ballasted tracks, the slab track greatly reduces the vibration level due to the quasi-static loads, since the peak response load speed of the ground with the slab track is significantly increased by the bending stiffness of the track; it is therefore more effective for low frequencies. For high frequencies, it may increase the observed vibration level due to the increased dynamic wheel-rail forces.

With increasing vehicle speed, the upper limit of frequency at which the quasi-static loads are the dominant source is slightly increased. Since the quasi-static loads are the dominant mechanism of excitation for frequencies below the cut-on frequency, the

vehicle travelling speed has a greater effect on the response level for this frequency range. For higher frequencies, though the response level due to the quasi-static loads is greatly dependant on the vehicle speed, the total response level is much less sensitive to vehicle speed.

It should be remembered that, at this stage, only a single ground model has been examined. Ground conditions and embankments vary over a wide range. This issue is addressed in the next chapter. Therefore, the conclusions of the present chapter may not be universal in application.

Chapter 8

COMPARISON OF THE VEHICLE-TRACK-GROUND MODEL WITH MEASUREMENTS

8.1 INTRODUCTION

In Chapter 7, a model for predicting ground vibration and propagation is developed. In this model the vertical dynamics of a number of types of vehicles travelling at a constant speed on an infinite track are coupled to a semi-analytic model for a three dimensional layered ground. A relationship is established between the response power spectra of the ground and the power spectral density of the combined wheel/rail irregularities. In the present chapter, ground vibrations at three sites are predicted using this vehicle-track-ground model and compared with measured data, providing validation for the model. The predictions and comparisons for the three sites are performed in Sections 8.2, 8.3 and 8.4 respectively.

8.2 SIMULATIONS AND COMPARISON FOR SITE I: LEDSGÅRD

First the model is applied to predict the train-induced vibration for the X2000 high-speed train. The Swedish National Rail Administration (BANVERKET) encountered very large vibrations when its X2000 high-speed trains (Figure 8.1) were operated at 200 km/h at a site called Ledsgård. This site is located on the West Coast line south of Gothenburg. BANVERKET carried out an extensive programme of measurements with a test train in order to investigate the causes of the high level of vibrations. It was observed that when the train speed approached the 'Rayleigh wave' velocity of the ground, an extraordinarily strong response occurs [BANVERKET 2000]. The soil properties of the site are listed in Table 8.1, the track parameters are in Table 8.2 and the axle loads and their locations of the test train are in Table 8.3. The values of parameters in these three tables have all been taken to be those identified by BANVERKET in its measurement programme [BANVERKET 1998]. As indicated in Table 8.1, the ground at this site is modelled as two layers on a homogeneous half-space, and the second layer, consisting of organic clay, is very soft.

TABLE 8.1
Ground parameters for the Ledsgård site (in Sweden) [BANVERKET 1998]

Layer	Depth (m)	Young's modulus (10^6 Nm^{-2})	Poisson's ratio	Density (kg/m^3)	Loss factor	P-wave speed (m/s)	S-wave speed (m/s)	Rayleigh wave speed (m/s)
1	1.6	19.0	0.491	1500	0.15	500	65	62
2	3.0	3.84	0.498	1250	0.15	500	32	30.5
Half-space		31.82	0.498	1470	0.15	1500	85	81

TABLE 8.2
Track parameters at the Ledsgård site (in Sweden) [BANVERKET 1998]

Mass of rail beam per unit length of track	120 kg/m
Bending stiffness of rail beam	1.26×10^7 Nm^2
Loss factor of the rail	0.01
Rail pad stiffness per unit length of track	3.5×10^8 N/m^2
Rail pad loss factor	0.15
Mass of sleepers per unit length of track	490 kg/m
Mass of ballast per unit length of track	1200 kg/m
Ballast stiffness per unit length of track	3.15×10^8 N/m^2
Loss factor of ballast	0.2
Density of the embankment	1800 kg/m^3
Young's Modulus of the embankment	2.95×10^8
Loss factor of the embankment	0.3
Top width of the embankment	2.7 m
Height of the embankment	0.9 m
Contact width of railway and ground	3 m

TABLE 8.3
Axle locations and axle loads of the X2000 *test train* [BANVERKET 1998]

No.	1	2	3	4	5	6	7	8	9	10
a_j (m)	50.00	47.10	35.50	32.60	28.25	25.35	10.60	7.65	3.30	0.40
P_j (kN)	167.50	119.00	143.25	143.25	122.00	122.00	122.00	122.00	125.50	125.50
No.	11	12	13	14	15	16	17	18	19	20
a_j (m)	-14.40	-17.30	-21.65	-24.54	-39.35	-42.25	-46.60	-49.50	-56.10	-59.00
P_j (kN)	125.50	125.50	122.00	122.00	122.00	122.00	185.75	185.75	183.00	188.50

In Section 8.2.1 below, the calculated dispersion curves of the ground are presented. Mode shapes are plotted in Section 8.2.2 for propagating wave modes of the ground at several frequencies. In Section 8.2.3, the predicted displacements of the embankment under the action of the test train at two speeds, 70 km/h and 200 km/h, are compared with measured data. Predicted and measured velocity spectra of the ground surface are compared in Section 8.2.4.

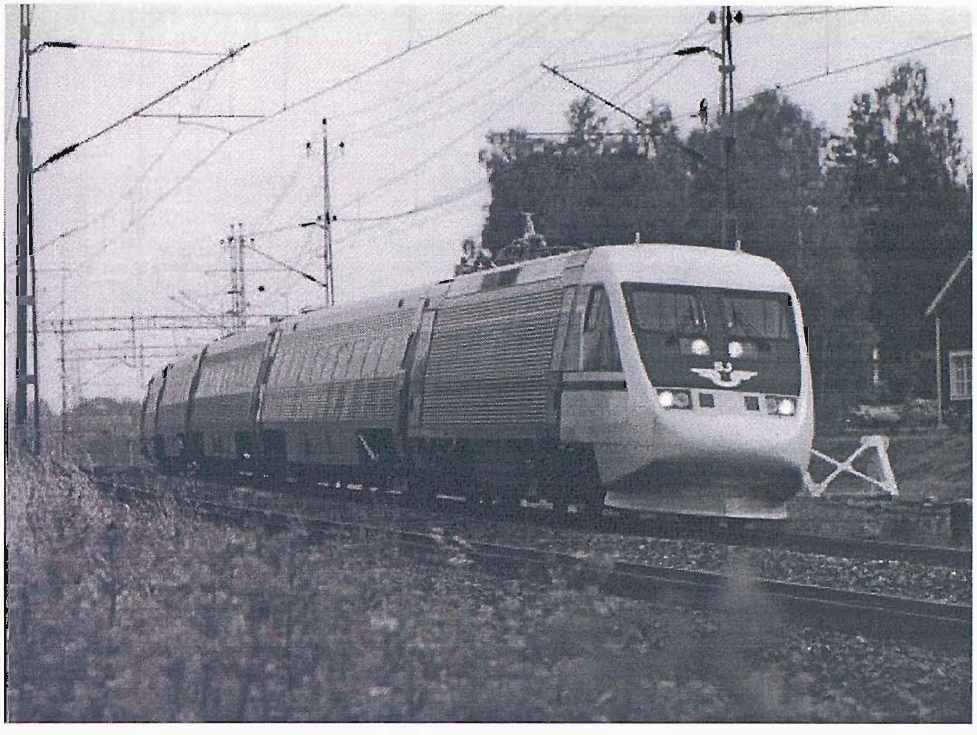

Figure 8.1. The X2000 high-speed train

8.2.1 DISPERSION CURVES OF THE GROUND

Figure 8.2 shows the P-SV dispersion curves of the ground at Ledsgård for a frequency range of 0 to 50 Hz. It can be seen that: (1) the cut-on points are always on the shear wave line of the underlying half-space; (2) for higher frequencies, the wave of the first mode (i.e. the mode with the highest wavenumber at a given frequency) approaches the shear wave of the second layer; (3) the shear wave line of the first layer intersects the dispersion curves at their inflection points.

An enlargement of the dispersion curve diagram for a small range of frequency up to 10 Hz is shown in Figure 8.3. A complex characteristic of the ground is revealed by this figure. Below 2 Hz, three wave modes are available while between 2 and 3.3 Hz, only one wave mode is present. Also shown in this figure is a 'load speed line', indicating the excitation of modes by a constant load moving at 200 km/h (55.6 m/s).

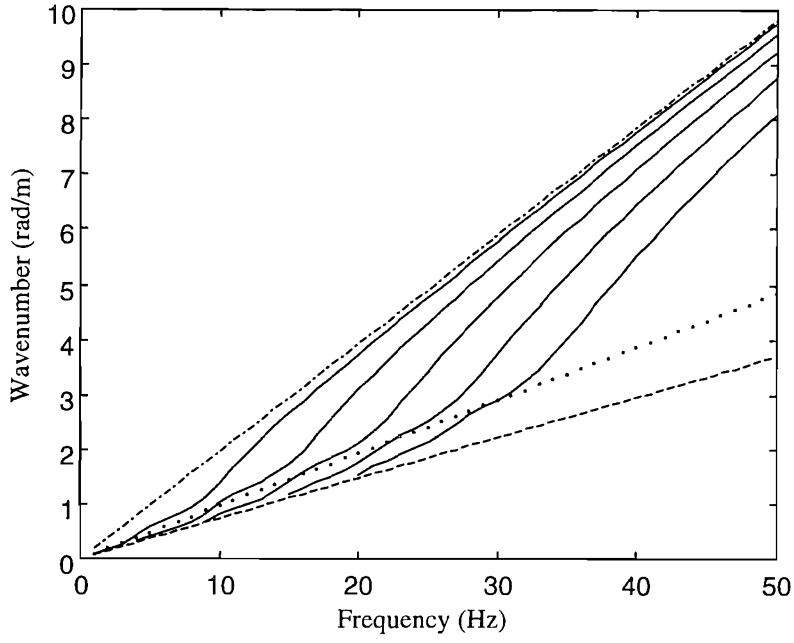

Figure 8.2. Dispersion curves for the ground at Ledsgård site. ——, P-SV modes; – – –, shear wave of the underlying half-space; · · · · · ·, shear wave of the upper layer; – · – · –, shear wave of the second layer.

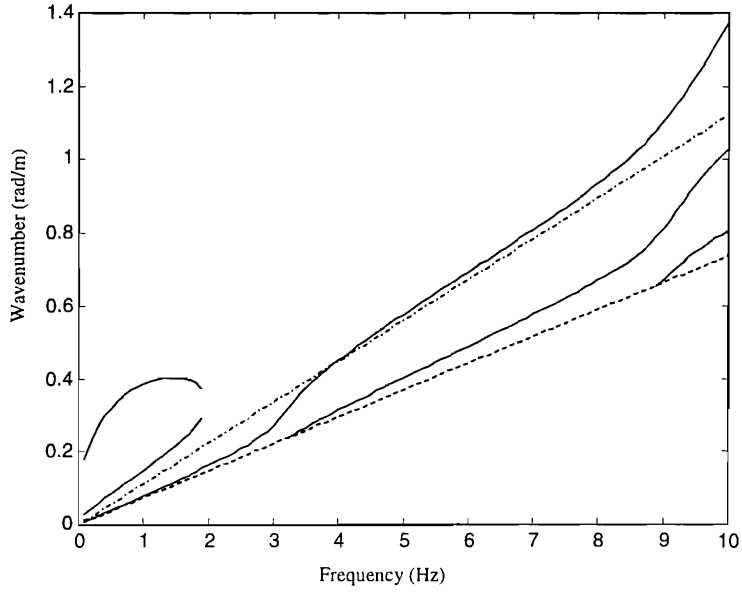

Figure 8.3. P-SV dispersion curves of the ground at Ledsgård site. ——, P-SV modes; – – –, shear wave of the half-space; – · – · –, the load speed line for a speed of 55.6 m/s.

To show which wave is excited by a surface load, the Fourier transformed displacements on the ground surface due to a vertical unit point load of different frequencies is presented in Figure 8.4. This plot has a speckled appearance because of the discrete frequencies of excitation applied in the calculation (1 Hz spacing). This figure indicates that only modes with a wave speed higher than the Rayleigh speed in the first

layer (62 m/s) but less than the shear wave speed in the underlying half-space are excited at the ground surface. Other waves propagate along the interface of the second layer and the half-space and decay rapidly with vertical distance away from the interface so that they do not contribute significantly to the surface response. Therefore only when a load moves at a speed close to the Rayleigh wave speed of the surface layer is the ground surface expected to have a strong response.

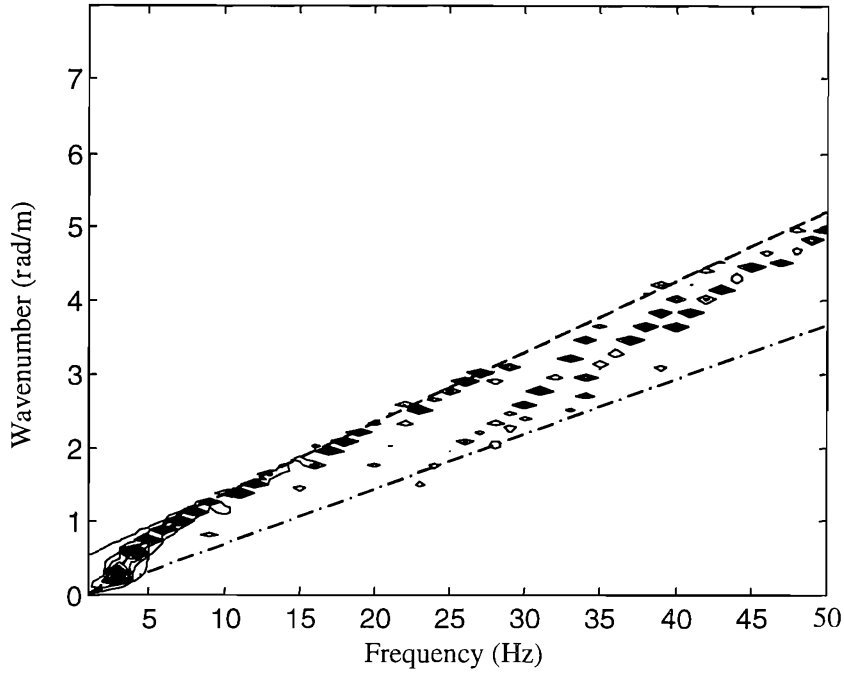

Figure 8.4. Contour plot of the Fourier transformed vertical displacement on the ground surface. Also shown are the Rayleigh wave in the first layer (– – –) and shear wave in the half-space (– · – · –).

8.2.2 MODE SHAPES OF THE GROUND

The P-SV mode shapes are calculated and shown in Figures 8.5 to 8.8 for the first mode at frequencies 1.4 Hz, 1.9 Hz, 3 Hz and 20 Hz. The layer interfaces are also indicated by using horizontal dash-dotted lines. The vertical component is a real number while the horizontal component is a purely imaginary number. As shown in Figures 8.5 and 8.6, the mode shapes in the underlying half-space resemble the mode shape of the Rayleigh wave in the same half-space, and the ground surface has minimum displacement. In Figure 8.8, the first mode at 20 Hz only propagates near the interface of the second layer and the half-space. However, as can be seen in Figure 8.7, at 3 Hz, the ground has maximum displacement at its surface.

When a load speed is just over the shear wave speed of the second layer, the load speed line would intersect the dispersion curve of the first mode at high frequencies (see

Figure 8.2). Because of the mode shapes at high frequencies (Figure 8.8), the ground surface response induced by this moving load is not expected to be very large. On the other hand, when the load speed is close to the shear wave speed of the first layer, the load speed line intersects, or is very close to, the dispersion curve of the first mode at about 3 to 8 Hz. In this case, the ground surface response is expected to be very strong. Both measurement and simulation show this, as presented in the following sections.

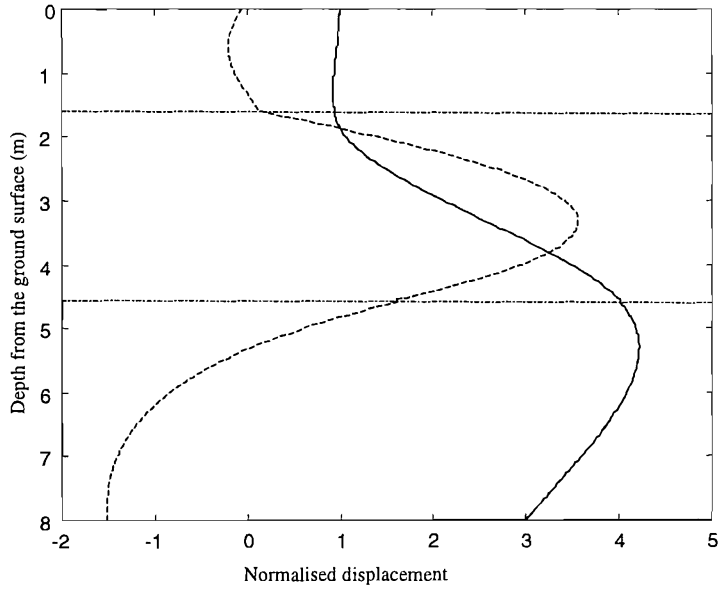

Figure 8.5. The first P-SV mode shape (frequency = 1.4 Hz, wavenumber = 0.4 rad/m) for the ground at Ledsgård site. ——, vertical component; – – –, horizontal component.

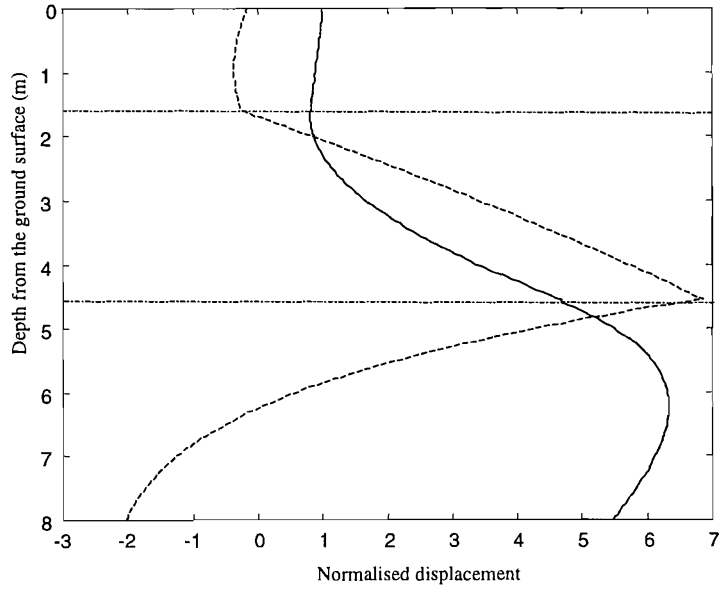

Figure 8.6. The P-SV mode shape (frequency = 1.9 Hz, wavenumber = 0.375 rad/m) for the ground at Ledsgård site. ——, vertical component; – – –, horizontal component.

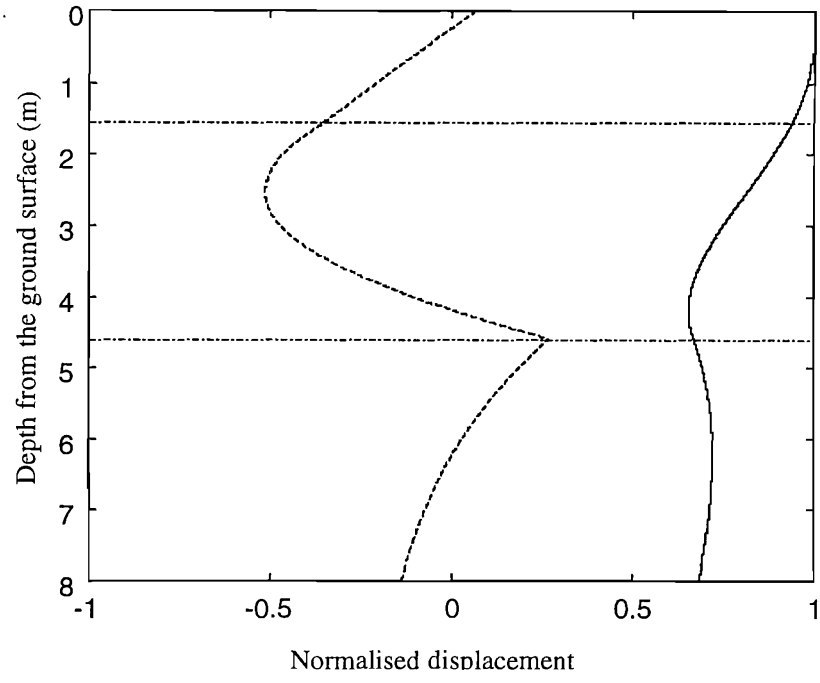

Figure 8.7. The P-SV mode shape (frequency = 3 Hz, wavenumber = 0.272 rad/m) for the ground at Ledsgård site. ——, vertical component; – – –, horizontal component.

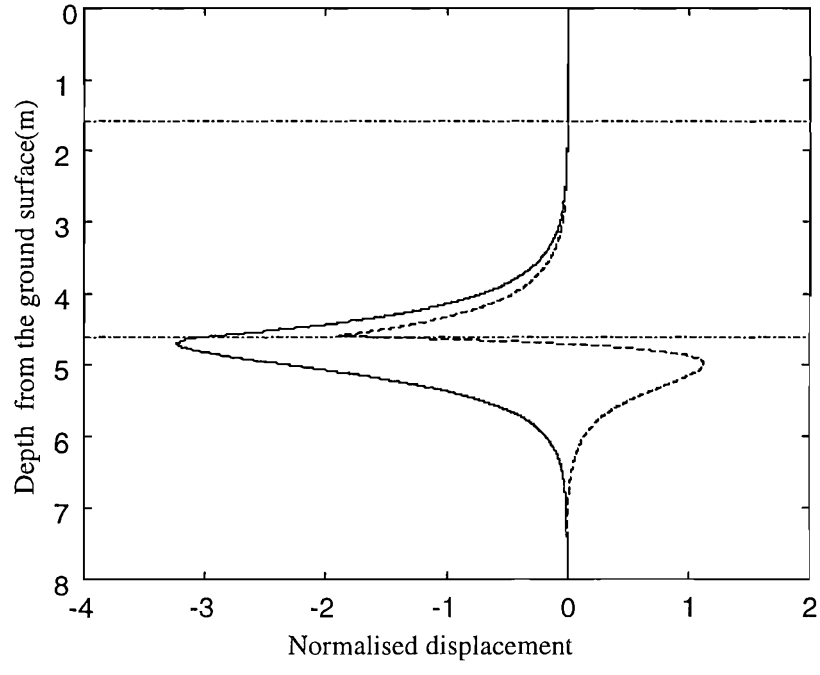

Figure 8.8. The P-SV mode shape of the first mode (frequency = 20 Hz, wavenumber = 3.74 rad/m) for the ground at Ledsgård site. ——, vertical component; – – –, horizontal component.

8.2.3 DISPLACEMENTS OF THE TRACK GENERATED BY THE QUASI-STATIC LOADS

Simulations are performed for the displacements generated by the X2000 test train. Two train speeds, 70 km/h (19.4 m/s) and 200 km/h (55.6 m/s), are considered. In

these predictions, only the quasi-static loads are taken into account. At the track the response to the dynamic wheel-rail forces is expected to be small compared to the moving axle loads. The magnitudes and locations of the axle loads are shown in Table 8.3. The instantaneous displacements of the embankment are shown in Figure 8.9 for 70 km/h and Figure 8.10 for 200 km/h. The success of the prediction indicates the accuracy of the ground and track parameters derived by BANVERKET. For the low speed case shown in Figure 8.9, a quasi-static loading state is clearly indicated. However, in the high-speed case, a propagating wave mode is excited and a large oscillating response appears because of the excitation of this propagating wave mode. As shown in Figure 8.3, the load speed line for a load speed equal to 200 km/h (55.6 m/s) has an intersection with the dispersion curve of the first mode at wavenumber 0.4 rad/m. The presence of the mass of the track (including an embankment) will decrease this wavenumber to some extent. As a result, a propagating wave of more than 16 m wavelength is excited and propagates away from each load in the opposite direction to that of the train motion (compare results shown in reference [Sheng, Jones and Petyt 1999(b)]). Behind the last axle load, a wave 'tail' of this wavelength is clearly visible in Figure 8.10.

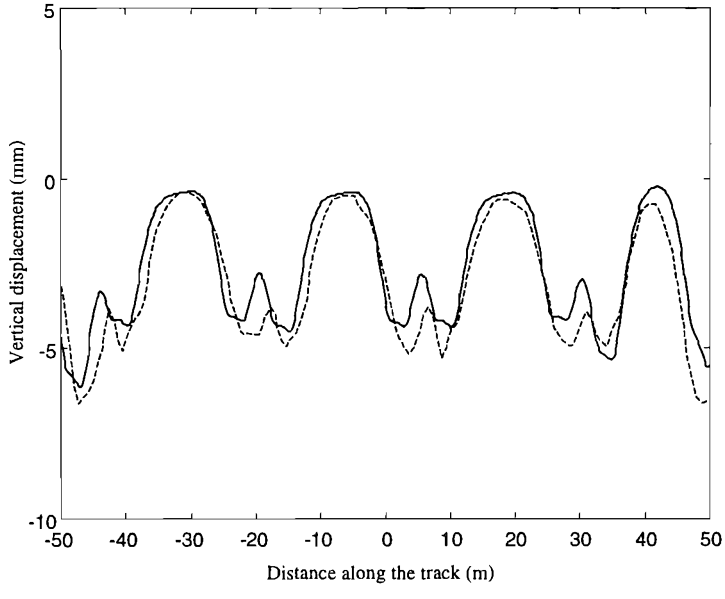

Figure 8.9. Predicted (——) and measured (– – –) vertical displacement of the embankment for train speed equal to 70 km/h (19.4 m/s).

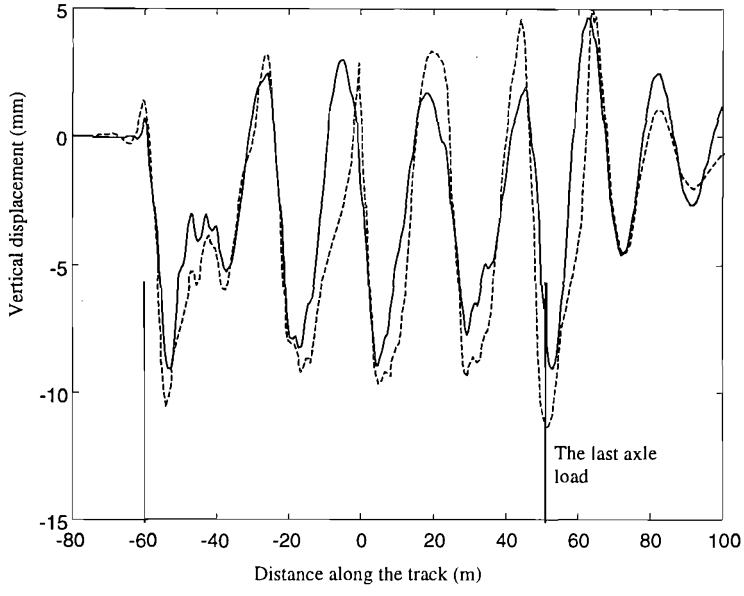

Figure 8.10. Predicted (——) and measured (– – –) vertical displacement of the embankment at 200 km/h (55.6 m/s).

8.2.4 VELOCITY SPECTRA OF THE GROUND SURFACE GENERATED BY THE QUASI-STATIC LOADS

8.2.4.1 *FOR TRAIN SPEED* 70 km/h

The predicted load spectrum, given by equation (5.58), for the X2000 test train at 70 km/h is shown in Figure 8.11. Predicted and measured velocity spectra of vibration on the track are compared in Figure 8.12. Figures 8.13 and 8.14 present results for two positions on the ground surface. One position is 7.5 m and the other 15 m away from the track centre-line. The measurements were carried out using seismometers with a natural frequency of 2.0 Hz. It can be seen from Figure 8.12 that on the embankment, for frequencies higher than 5 Hz and lower than 22 Hz, the prediction reproduces the measurement quite well. This indicates that for the response of the track, the quasi-static loads are the dominant sources compared with the dynamic loads. However, as shown in Figures 8.13 and 8.14, away from the track on the ground surface, the predicted response is much lower than the measured one.

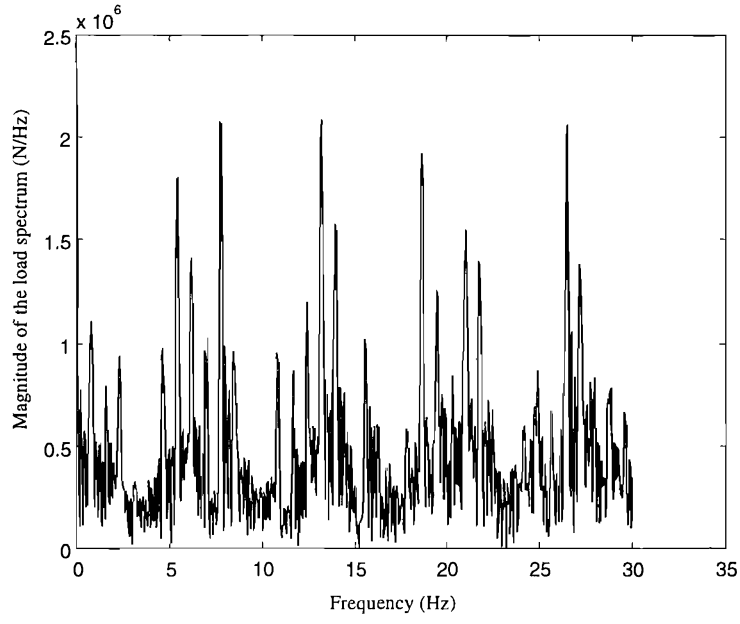

Figure 8.11. Load spectrum of the multiple quasi-static loads for train speed 70 km/h (19.4 m/ s) calculated from equation (5.65) with $\Omega = 0$.

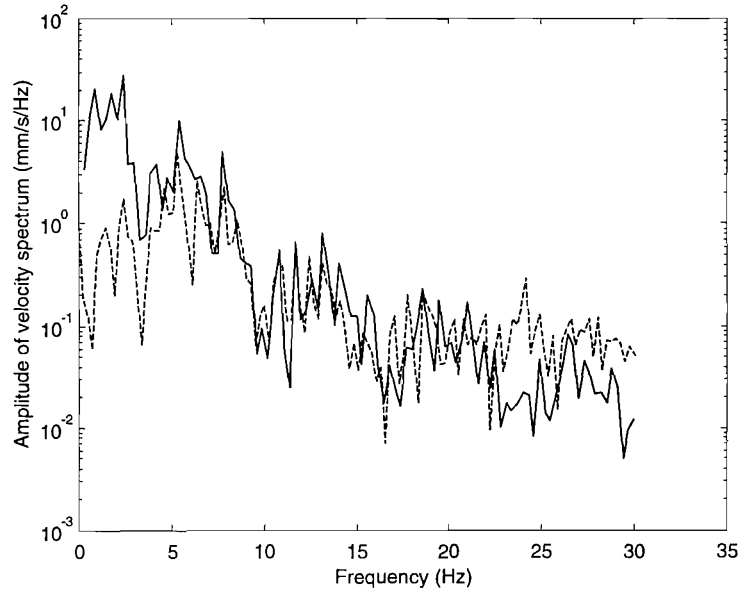

Figure 8.12. Vertical velocity spectrum of the embankment. ——, prediced; – – –, measured. Train speed: 70 km/h (19.4 m/s).

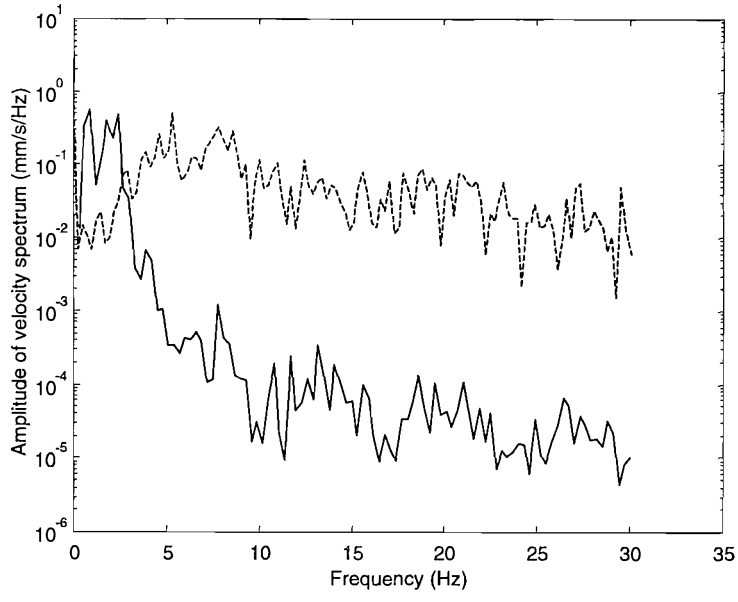

Figure 8.13. Vertical velocity spectrum for a point 7.5 m away from the track centre line on the ground surface. ——, predicted; – – –, measured. Train speed: 70 km/h (19.4 m/s).

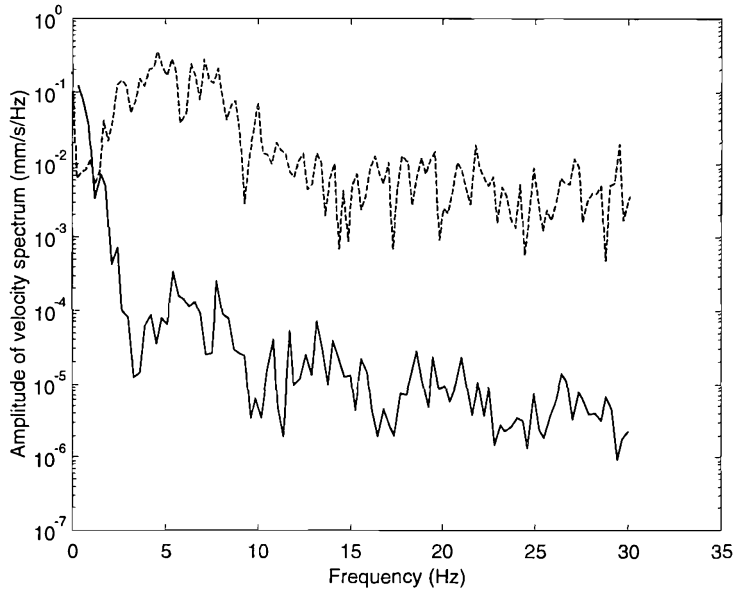

Figure 8.14. Vertical velocity spectrum for a point 15 m away from the track centre line on the ground surface. ——, predicted; – – –, measured. Train speed: 70 km/h (19.4 m/s).

8.2.4.2 *FOR TRAIN SPEED* 200 km/h

Figures 8.15 to 8.18 show the predicted and measured vertical velocity spectra at different points on the ground surface for the test train running at 200 km/h. It can be seen that at low frequencies and for points near the track, for example the point 7.5 m away from the track, the predicted responses are quite close to the measured ones. This is

quite different from the low speed case shown in Figure 8.13, where the predicted response is much lower than that measured. However, at higher frequencies, especially at further distances from the track, the simulations underestimate the response. At frequencies around 3 to 8 Hz, even for points far from the track, the predicted responses are close to those measured. The harmonic components of such frequencies are due to the first propagating wave mode excited by the moving quasi-static loads and corresponds to the range of frequency at which the load speed line for 200 km/h (55.6 m/s) intersects, or, is very close to the dispersion curve of first mode (Figure 8.3).

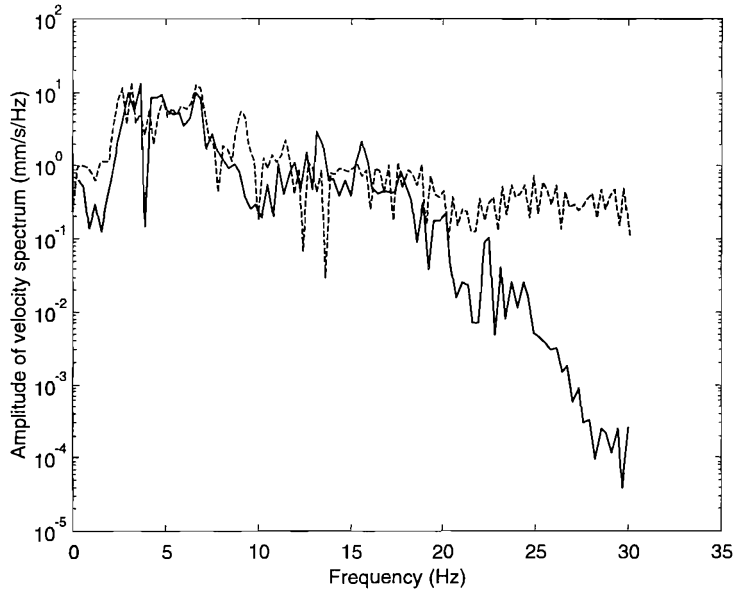

Figure 8.15. Vertical velocity spectrum for a point 7.5 m away from the track on the ground surface. ——, predicted; – – –, measured. Train speed: 200 km/h (55.6 m/s).

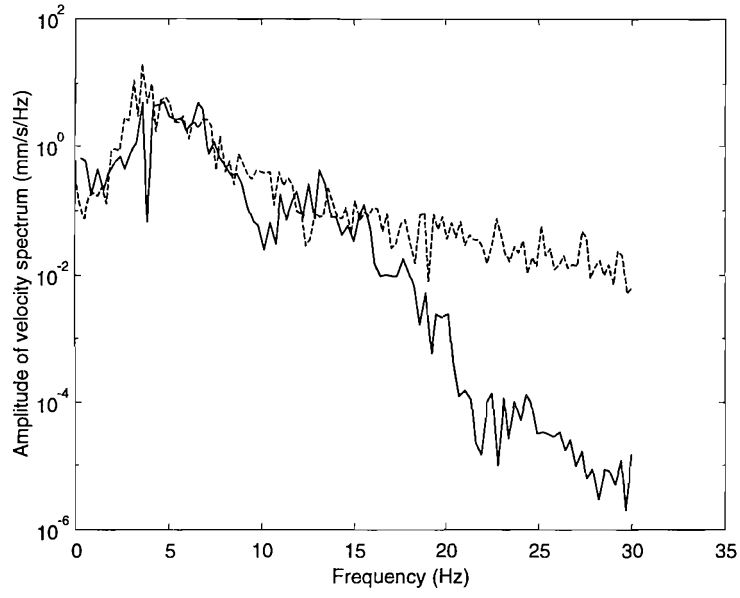

Figure 8.16. Vertical velocity spectrum for a point 15 m away from the track on the ground surface. ——, predicted; – – –, measured. Train speed: 200 km/h (55.6 m/s).

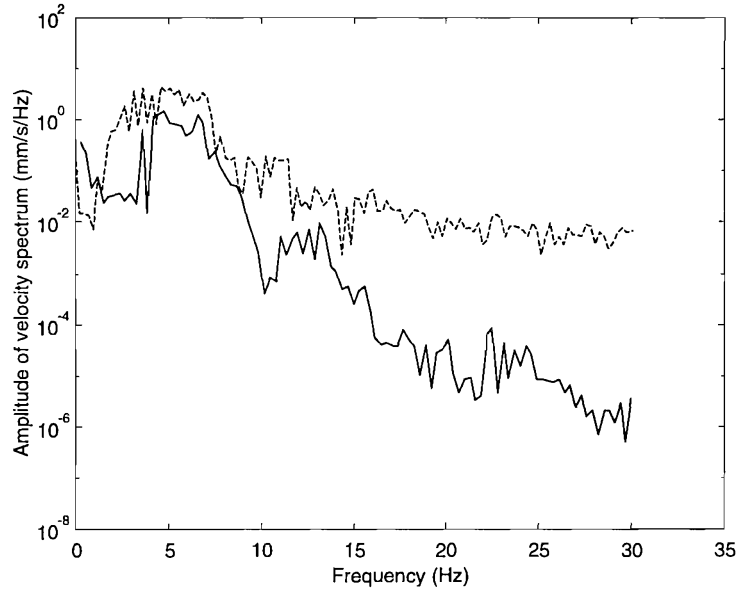

Figure 8.17. Vertical velocity spectrum for a point 30 m away from the track on the ground surface. ——, predicted; – – –, measured. Train speed: 200 km/h (55.6 m/s).

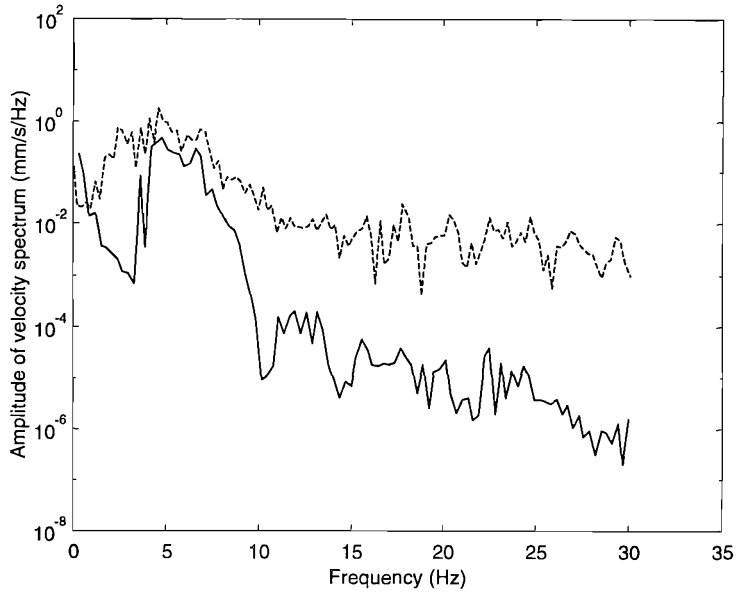

Figure 8.18. Vertical velocity spectrum for a point 45 m away from the track on the ground surface. ——, predicted; – – –, measured. Train speed: 200 km/h (55.6 m/s).

8.2.5 TOTAL VELOCITY SPECTRA GENERATED BY THE QUASI-STATIC AS WELL AS DYNAMIC LOADS

As shown in Section 8.2.4, the dynamic wheel-rail forces contribute a large proportion to the ground response. To predict the total response generated by the test train, the vehicle parameters for the X2000 train have been provided by BANVERKET (in confidence). In the absence of the rail irregularity data specific to this site, the vertical rail-top profile used in Section 7.7.2 is also applied here. The power spectral density of the profile is shown 8.19, in which the decibel is defined as $10\log_{10}(P_z(\beta))$. The levels of the profile expressed in terms of one-third octave band centre wavelengths are shown in Figure 1.5.

The vertical velocity levels of two points, at 7.5 m and 15 m, on the ground surface for two train speeds, 70 km/h and 200 km/h, are shown in Figures 8.20 to 8.23. Although the prediction does not reproduce the measurement precisely, it is clearly shown that for train speeds lower than the wave speeds in the ground at this site, the dynamic components of the wheel-rail forces are dominant over the quasi-static loads, even for very low frequencies. However, for train speeds exceeding the wave speeds in the ground, the quasi-static loads are dominant for frequencies up to more than 10 Hz.

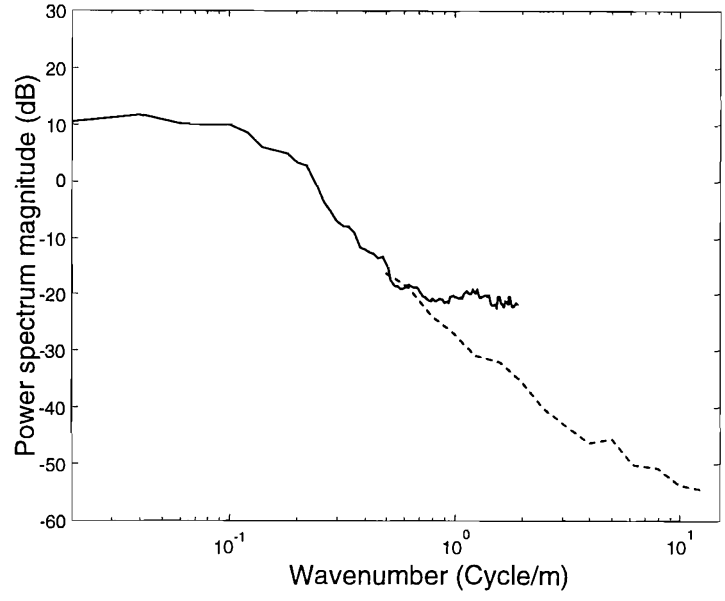

Figure 8.19. The power spectral density of the vertical rail profile used in the prediction. ——, calculated from measured data; – – –, from [Jones 1996].

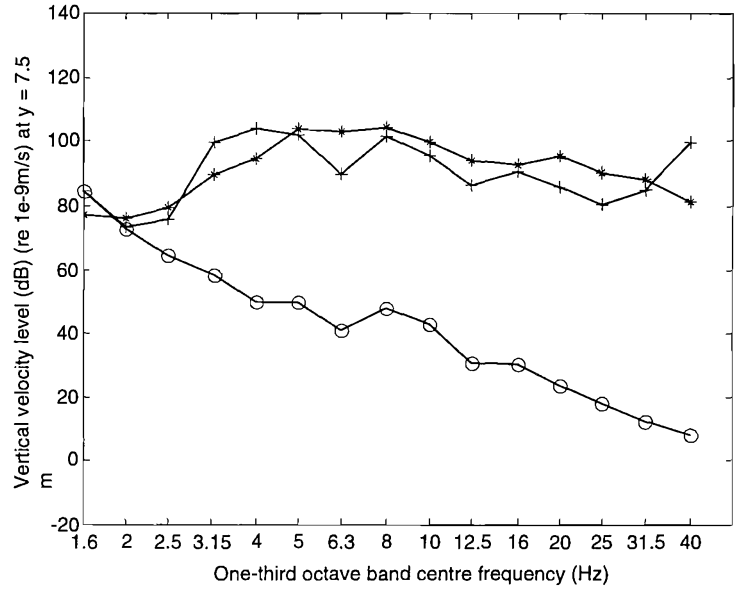

Figure 8.20. Vertical velocity level for a point 7.5 m from the track on the ground surface. o: predicted level due to quasi-static loads; +: total predicted level; *: measured level. Train speed: 70 km/h (19.4 m/s).

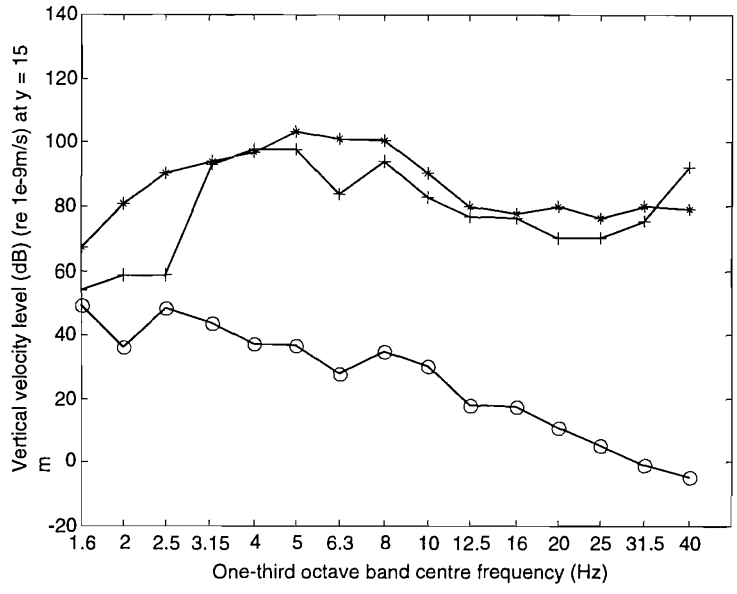

Figure 8.21. Vertical velocity level for a point 15 m from the track on the ground surface. o: predicted level due to quasi-static loads; +: total predicted level; *: measured level. Train speed: 70 km/h (19.4 m/s).

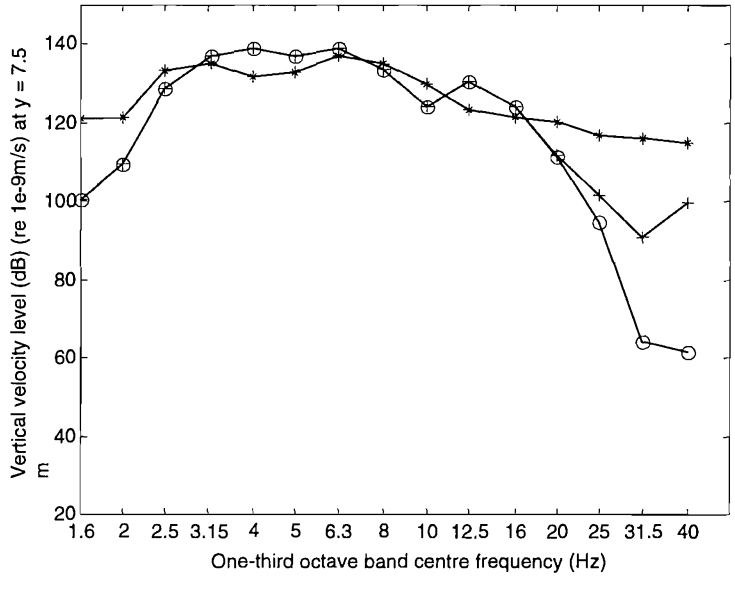

Figure 8.22. Vertical velocity level for a point 7.5 m from the track on the ground surface. o: predicted level due to quasi-static loads; +: total predicted level; *: measured level. Train speed: 200 km/h (55.6 m/s).

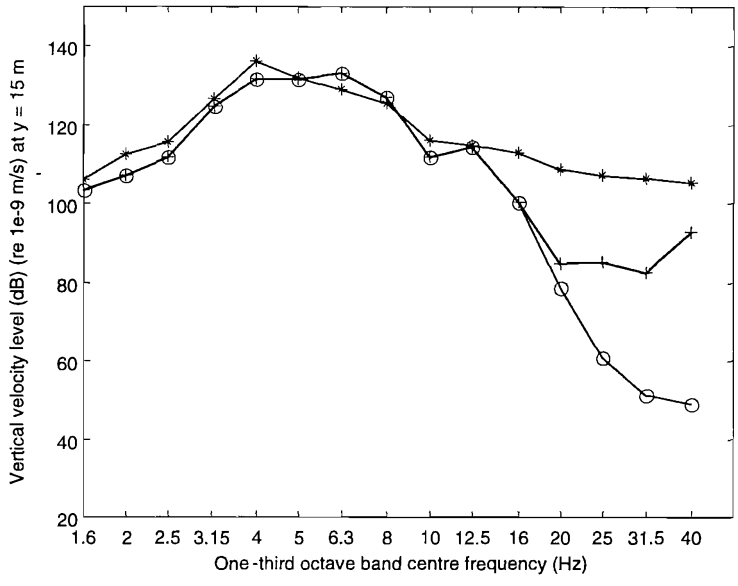

Figure 8.23. Vertical velocity level for a point 15 m from the track on the ground surface. o: predicted level due to quasi-static loads; +: total predicted level; *: measured level. Train speed: 200 km/h (55.6 m/s).

8.3 SIMULATIONS AND COMPARISON FOR SITE II: VIA-TEDALDA

In this section, the model is applied to ground vibrations induced by the ETR500 high-speed train. A picture of the ETR500 train is shown in Figure 8.24. Predicted vibration spectra are compared with the measured data reported in reference [Lai et al 2000]. In November 1999 a series of vibration measurements were carried out in Florence, Italy during the passages of the ETR500 high-speed train. The transducers used in the measurements are geophones with a natural frequency of 2.0 Hz. The average speed of the train passages during the measurement is about 70 to 80 km/h. The data measured at a site called Via Tedalda are used here for comparison. The parameters of the vehicle are provided by Alstom Transport in confidence and those of the soil and the track are listed in Tables 8.4 and 8.5. According to Figure 5 in reference [Lai et al 2000], the ground is modelled as one layer of 10 m depth which overlies a homogeneous half-space. The shear wave speeds in the layer and in the half-space are 300 m/s and 600 m/s, respectively. In the absence of specific parameters, the track structure, other than the embankment, has been assigned parameters typical of a monobloc sleeper, ballasted track. As advised by Lai, the embankment is 1.5 m high, and its density has been estimated as 1800 kg/m^3. Since the Young's modulus of the embankment is uncertain, several values have been tested. It was found that the value (2.0×10^7 N/m^2) giving the closest correspondence with the measurement is that derived from the total vertical

stiffness of the track, 50500 kN/m^2, suggested in reference [Lai et al 2000]. In the simulations, five ETR500 passenger cars running at 25 m/s are coupled with the track-ground system and, again in the absence of specific data, the rail roughness data shown in Figure 8.19 is used.

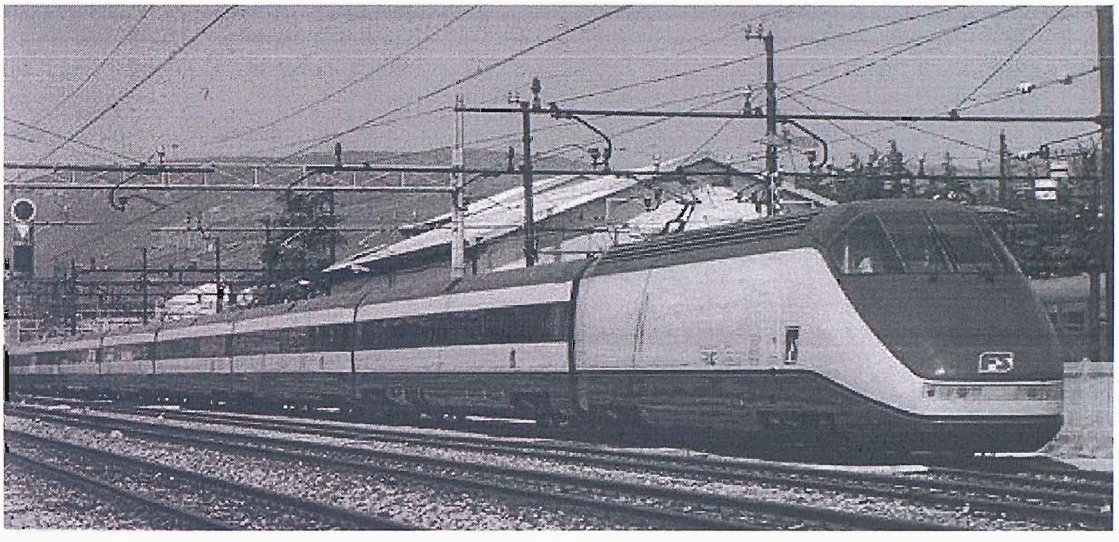

Figure 8.24. The ETR500 high-speed train.

The dispersion curves of the ground are shown in Figure 8.25. As indicated in this figure, the cut-on frequency of the first propagating wave in the layer is 11.2 Hz.

Figures 8.26 and 8.27 show the amplitude spectra of the vertical component of the acceleration at distances of 13 m and 26.2 m from the track. The measured data are available as one-third octave spectra. The comparative predictions have therefore been band-averaged and are presented in the same way.

TABLE 8.4

Ground parameters at the Via Tedalda site (in Italy) [Lai et al 2000]

Layer	Depth (m)	Young's modulus (10^6 Nm^{-2})	Poisson's ratio	Density (kg/m^3)	Loss factor	P-wave speed (m/s)	S-wave speed (m/s)	Rayleigh wave speed (m/s)
1	10	469.8	0.45	1800	0.1	995	300	284
Half-space		1879.2	0.45	1800	0.1	1989.97	600	568.55

TABLE 8.5

Track parameters at the Via Tedalda site (in Italy) [Lai et al 2000, but some parameters are assumed]

Mass of rail beam per unit length of track	120 kg/m
Bending stiffness of rail beam	1.26×10^{7} Nm^2
Loss factor of the rail	0.01
Rail pad stiffness per unit length of track	3.5×10^{8} N/m^2
Rail pad loss factor	0.15
Mass of sleepers per unit length of track	490 kg/m
Mass of ballast per unit length of track	1200 kg/m
Ballast stiffness per unit length of track	3.15×10^{8} N/m^2
Loss factor of ballast	0.2
Density of the embankment	1800 kg/m^3
Young's modulus of the embankment	2.0×10^{7} N/m^2
Loss factor of the embankment	0.05
Top width of the embankment	2.7m
Height of the embankment	1.5m
Contact width of railway and ground	4m

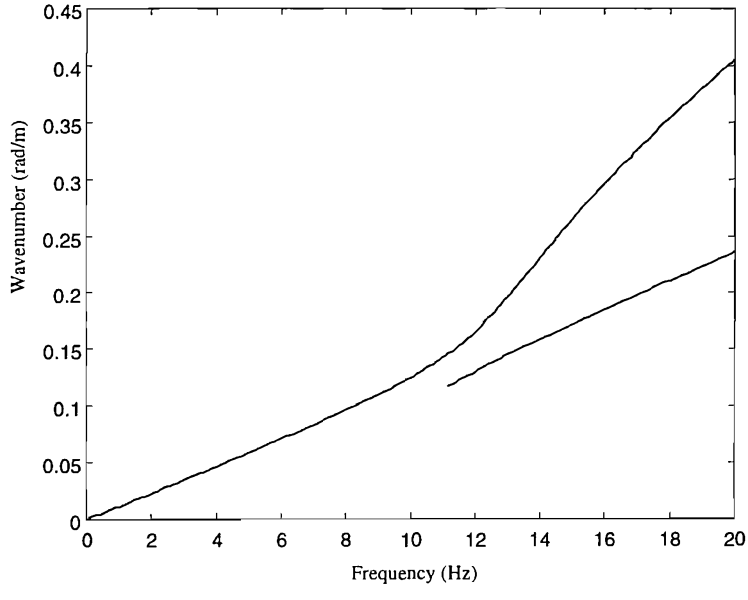

Figure 8.25. Dispersion curves of P-SV waves in the ground. Cut-on frequency is 11.2 Hz.

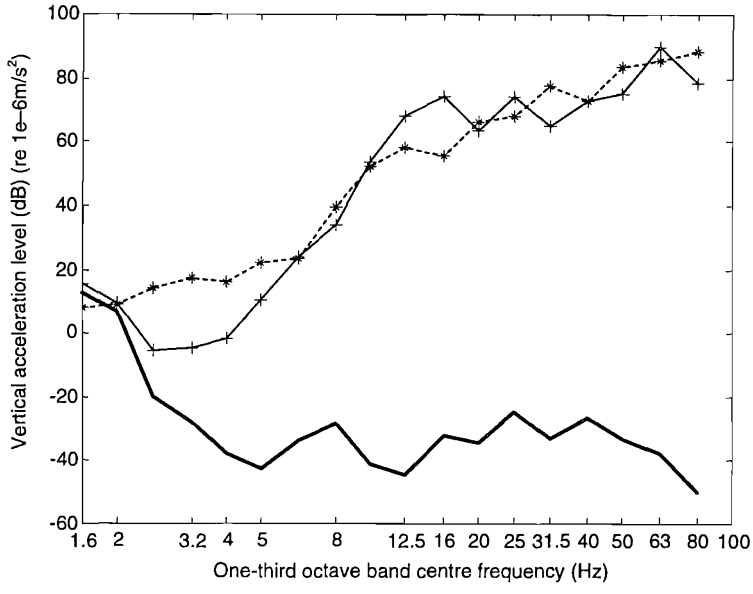

Figure 8.26. Vertical acceleration levels for a point 13 m from the track at Via Tedalda when five ETR 500 passenger cars pass at 25 m/s. + : predicted ; *: measured [Lai et al 2000]; —: predicted level due to quasi-static loads.

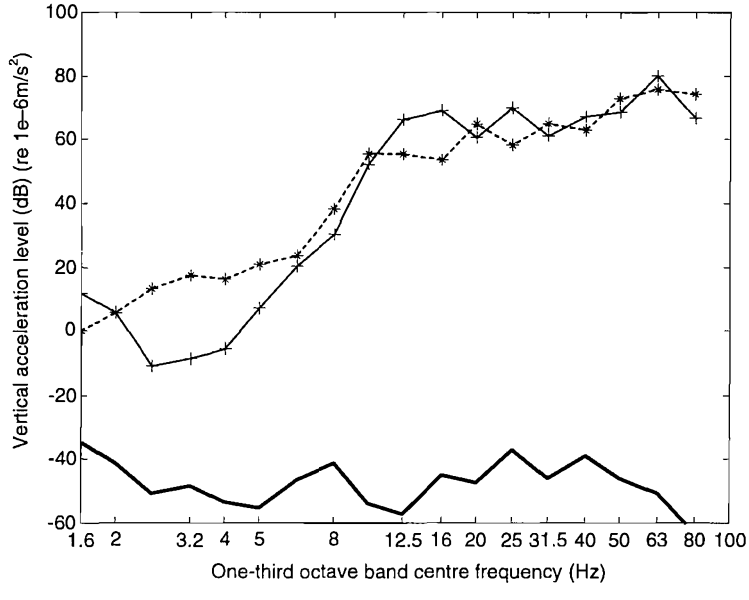

Figure 8.27 Vertical acceleration levels for a point 26.2 m from the track at Via Tedalda when five ETR 500 passenger cars pass at speed c = 25 m/s. + : predicted ; *: measured [Lai et al 2000]; —: predicted level due to quasi-static loads.

As seen in Figures 8.26 and 8.27, both the prediction and the measurement show a strong rise in vibration level corresponding to the cut-on at about 12 Hz. This cut-on is due to the layered structure of the ground, as indicated by the dispersion diagram of the ground in Figure 8.25. It is also shown that good correspondence is achieved between the

predicted response levels and the measured levels for frequencies higher than 5 Hz. However for frequencies of 2 to 5 Hz, the predicted levels are much lower than the measured ones. It is possible that this is due, in part, to a building near the track (Figure 4 in reference [Lai et al 2000]). Since the point 26.2 m away from the track is nearer the building, its effect may be stronger as shown in Figure 8.27.

Figures 8.26 and 8.27 also show the predicted response due to the quasi-static loads without the dynamic mechanism. Clearly, in this case, the dynamic components of the wheel-rail forces dominate the response.

The effects of the variation in the Young's modulus of the embankment are shown in Figures 8.28 and 8.29. Three values are tested: 2.0×10^7 N/m^2, 5.0×10^7 N/m^2 and 10.0×10^7 N/m^2. Three frequency ranges are identified in Figures 8.28 and 8.29: 1.6 to 5 Hz, 5 to 16 Hz and 16 to 80 Hz. It can be seen that as the Young's modulus of the embankment is increased, the change in the response levels in the first frequency range is negligible. However, in the second frequency range, the response levels decrease with increasing stiffness of the embankment while in the third frequency range, they increase.

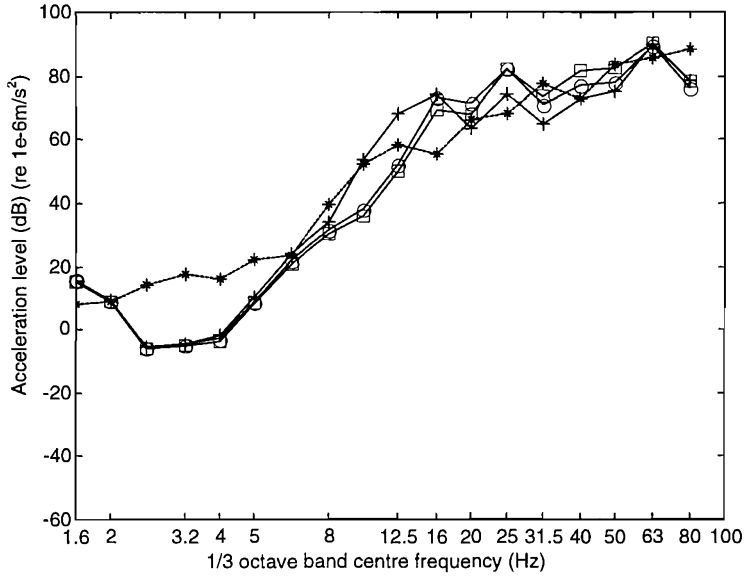

Figure 8.28. Effect of embankment Young's modulus on vertical acceleration levels at 13 m from the track at Via Tedalda when five ETR 500 cars run at 25 m/s. + : 2.0×10^7 N/m^2; ○: 5.0×10^7 N/m^2; □: 10.0×10^7 N/m^2 ; *: measured [Lai et al 2000]

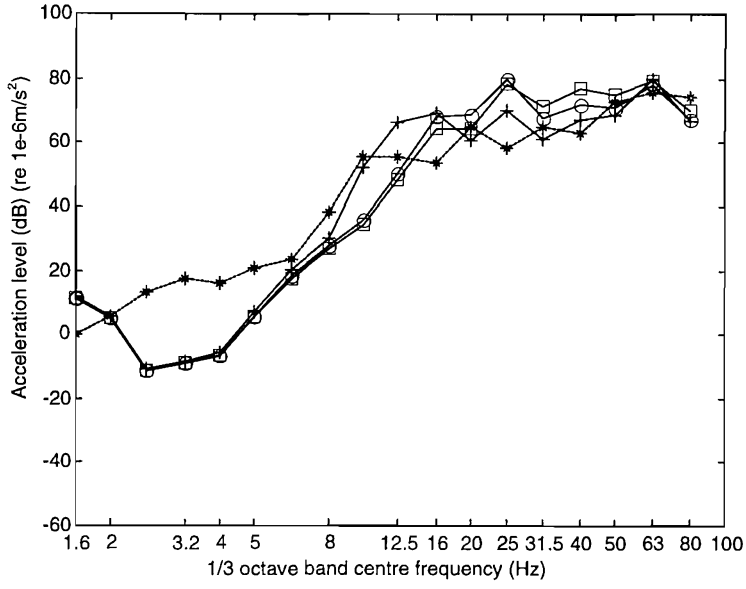

Figure 8.29. Effect of embankment Young's modulus on vertical acceleration levels at 26.2 m from the track at Via Tedalda when five ETR 500 cars run at 25 m/s. + : 2.0×10^7 N/m^2; ○: 5.0×10^7 N/m^2; □: 10.0×10^7 N/m^2 ; *: measured [Lai et al 2000].

8.4 SIMULATIONS AND COMPARISON FOR SITE III: BURTON-JOYCE

In this section, the model is applied to predict the vibration spectra induced by a train of two-axle freight wagons (type HAA, Figure 8.30). Again the prediction is compared with measured data at a site called Burton Joyce. Information on the measurement at Burton Joyce in Nottinghamshire, England, is reported in reference [Jones and Block 1996]. The average speed of the train during the measurement is about 14 m/s. The parameters for an HAA wagon are shown in Table 1.1 and those of the soil and track are listed in Tables 8.6 to 8.7. According to reference [Jones and Block 1996], the ground is modelled as a single layer of 1.8 m depth, which overlies a homogeneous half-space. The shear wave speeds in the layer and in the half-space are 81 m/s and 216 m/s, respectively. The track is ballasted, with an embankment of 1.3 m thickness. The rail roughness data specific to this site are available and shown in Figures 8.31 and 8.32.

TABLE 8.6

Ground parameters at the Burton Joyce site (in England) [Jones and Block 1996]

Layer	Depth (m)	Young's modulus (10^6 Nm^{-2})	Poisson's ratio	Density (kg/m^3)	Loss factor	P-wave speed (m/s)	S-wave speed (m/s)	Rayleigh wave speed (m/s)
1	1.8	29.3	0.47	1520	0.1	341	81	77
Half-space		286	0.49	2060	0.1	1700	216	206

TABLE 8.7

Track parameters at the Burton Joyce site (in England) [Jones and Block 1996]

Mass of rail beam per unit length of track (BS 113A rail)	112 kg/m
Bending stiffness of rail beam	9.68×10^{6} Nm^2
Loss factor of the rail	0.01
Rail pad stiffness per unit length of track	3.5×10^{8} N/m^2
Rail pad loss factor	0.15
Mass of sleepers per unit length of track	396 kg/m
Mass of ballast per unit length of track	760 kg/m
Ballast stiffness per unit length of track	3.0×10^{8} N/m^2
Loss factor of ballast	0.2
Density of the embankment	1800 kg/m^3
Young's modulus of the embankment	1.5×10^{7} N/m^2
Loss factor of the embankment	0.1
Top width of the embankment	2.7 m
Height of the embankment	1.3 m
Contact width of railway and ground	4 m

The P-SV dispersion diagram of the ground is calculated and shown in Figure 8.33. As indicated, the first cut-on frequency is 15 Hz. The transfer mobility (vertical velocity due to vertical load) for the ground itself and from track to ground was measured by British Rail Research (now AEAT Rail) and is shown in Figures 8.34 and 8.35. The measured responses in Figure 8.34 show the variation due to moving the loading point and the measurement point within a small area on the ground surface. Using the parameters in Tables 8.6 and 8.7, the transfer mobility is predicted and the results are also shown in these two figures. Both the prediction and measurement show a strong rise at frequency about 15 Hz. A discrepancy is observed at around 20 Hz between the model and the measurements, similar to that observed at the Via Tedalda site (Figures 8.26 and 8.27), because of the unrealistic sudden change in soil properties at the layer interface.

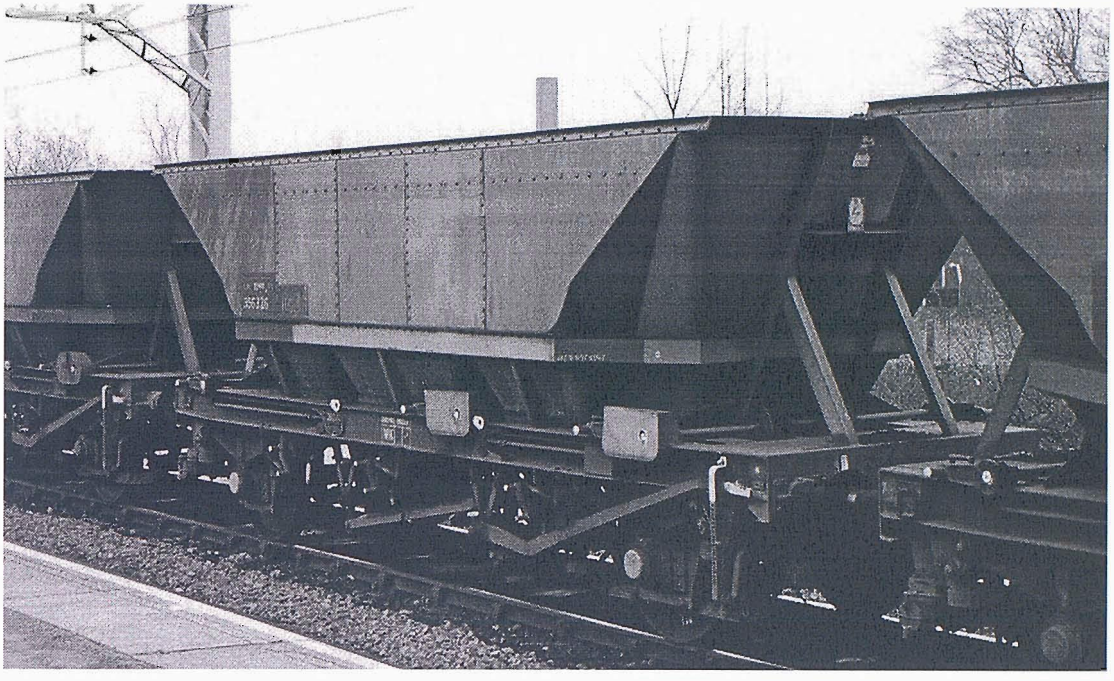

Figure 8.30. The HAA coal freight wagons

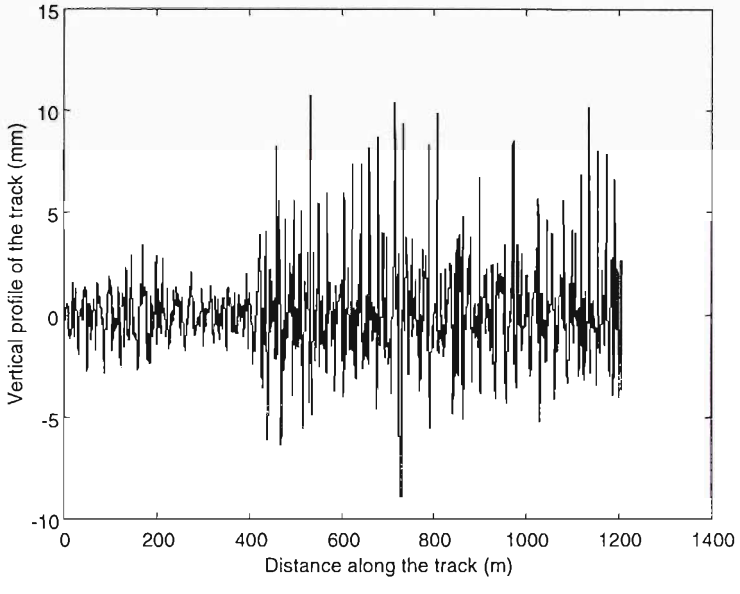

Figure 8.31. Vertical profile of the rail at Burton Joyce site.

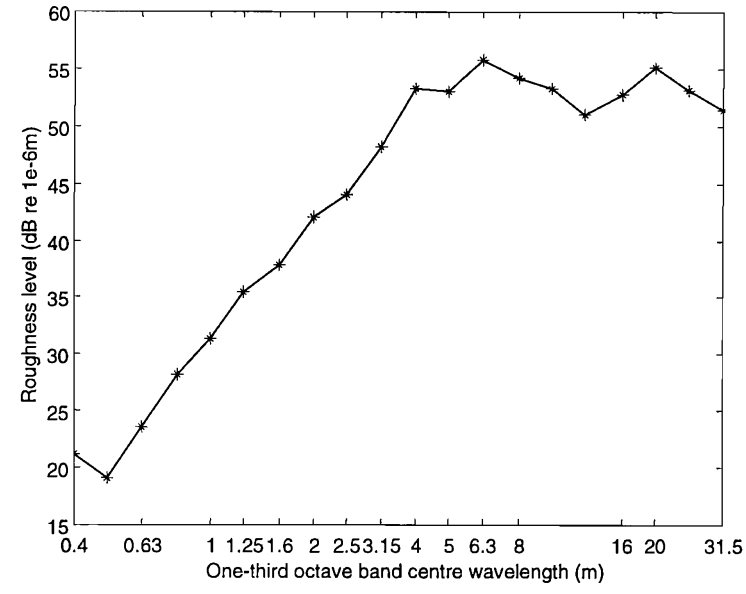

Figure 8.32. Spectrum of roughness of the rails at Burton Joyce site.

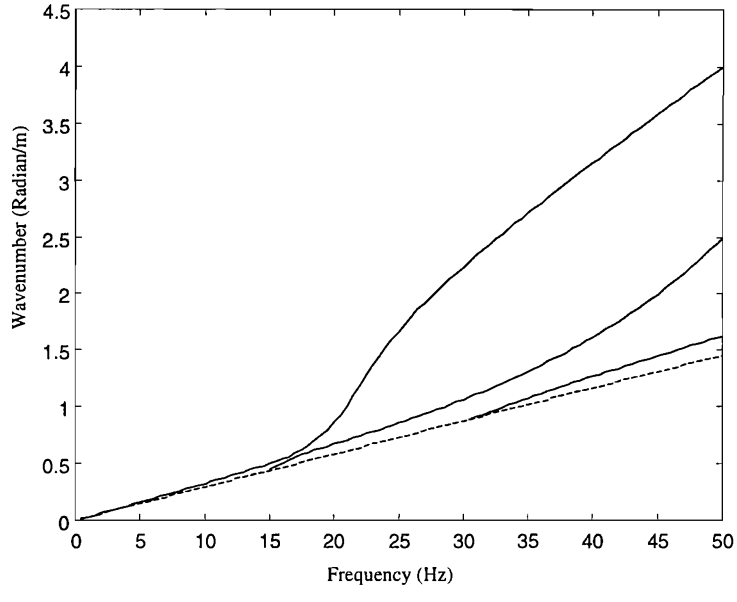

Figure 8.33. Dispersion curves of P-SV (——) waves in the ground. Cut-on frequencies are 15 Hz and 30 Hz. Also shown is the shear wave of the underlying half-space (– – –).

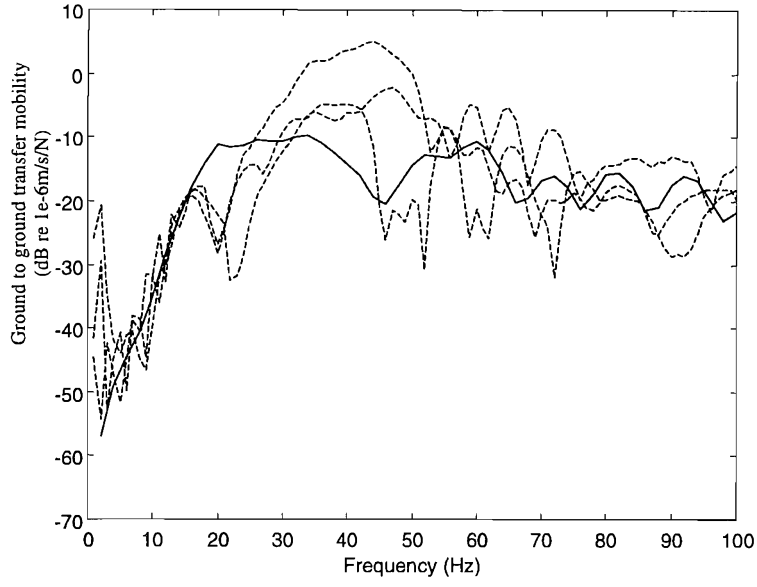

Figure 8.34. Transfer mobility of the ground surface (vertical component) at a distance of 10 m from the loading point on the ground surface. ——— , predicted; – – –, measured.

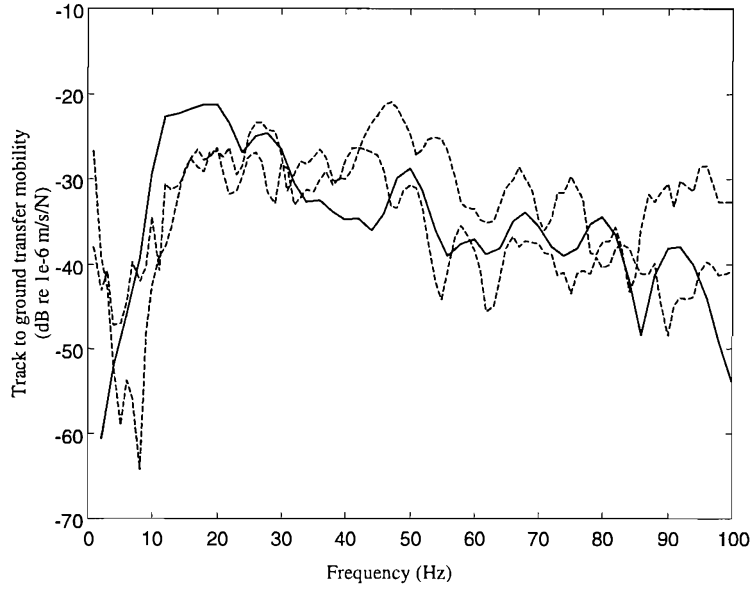

Figure 8.35. Transfer mobility from track to ground surface (vertical component) at a distance of 10 m from the near rail. ———, predicted; – – –, measured.

Figure 8.36 shows the predicted vertical velocity levels at a distance of 10 m from the track, for different embankment Young's moduli and different track/ground contact widths. Also shown in bold lines are the maximum and minimum levels derived from the measurements of vibration from HAA wagons reported in reference [Jones and Block 1996]. Since the ground is relatively soft, the modification to the track parameters has a great effect on the response level for frequencies higher than 10 Hz. The level of

response due to the quasi-static loads is less than 40 dB and therefore not shown in the figure.

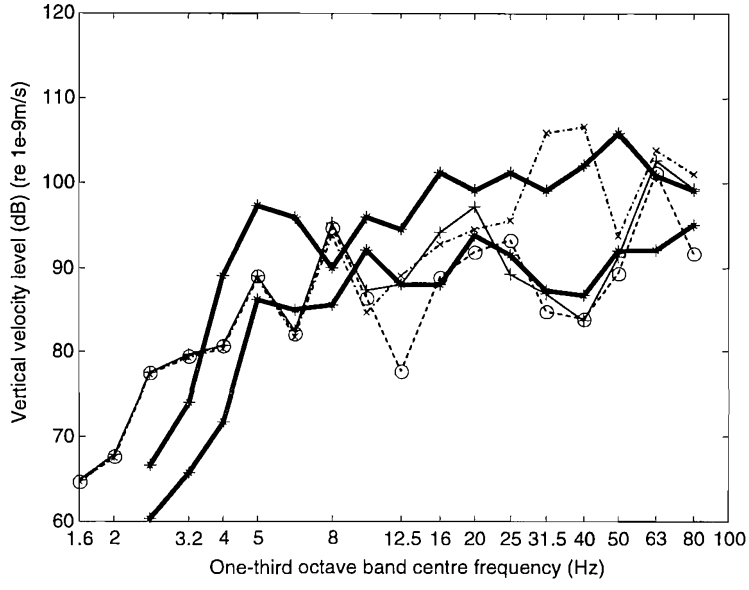

Figure 8.36. Vertical velocity levels at 10 m from the track at site Burton Joyce when five HAA wagons run at 14 m/s. + : the Young's modulus of the embankment is 1.5×10^7 N/m^2 and the track/ground contact width is 4 m; ○: the Young's modulus of the embankment is 1.5×10^7 N/m^2 and the track/ground contact width is 5 m; ×: the Young's modulus of the embankment is 3.0×10^7 N/m^2 and the track/ground contact width is 4 m; thick line: maximum and minimum measured levels.

8.5 DISCUSSION

The prediction of the quasi-statically and dynamically induced vibration components has been carried out for three sites. The dynamically induced vibration prediction requires the knowledge of the vehicle dynamics and measurements of the vertical profile of the track. Site-specific data for the latter was only available to the author for the third site. For the first two sites typical data has been used.

In the case of the first site, Ledsgård, the ground is not only unusually soft, but also unusual in that the second layer is softer than the surface layer. The measured displacement at the track has been shown to be close to that predicted for the quasi-static axle loads of the train both in the case of the train speed below, and above, the speed of the wave in the ground/embankment (Figures 8.9 and 9.10). For the lower train speed (70 km/h), the dynamically induced vibration dominates the spectrum of vibration on the ground surface away from the track (Figures 8.20 and 8.21). However, when the train speed exceeds the speed of the ground wave, a high level of vibration is observed in

which is predominantly due to the quasi-statically induced vibration. At 7.5 metres from the track, this vibration is approximately 25 dB higher than the vibration observed for the lower speed. Vibration that is observed at large distances from the track has strongest components in the frequency range from about 3 to 8 Hz (e.g. Figure 8.18). This is due to a combination of the facts (1) that at 200 km/h (55.6 m/s) the axle-loads excite the first mode of propagation at these frequencies (Figure 8.3) and (2) that the mode shape of the first propagating wave changes considerably with frequency. Close to 3 Hz it has its maximum at the ground surface. But at frequencies significantly below or above this frequency, the displacement is strongest at the second layer interface below the surface (Figures 8.5 to 8.8). The predicted level of the dynamically induced vibration appears to be too low (see Figures 8.22 and 8.23). However, this prediction is based on vertical profile data taken from a good track that may not be appropriate for a track that has been subjected to high dynamic displacements.

The second site, Via Tedalda, comprises a relatively stiff soil and therefore is very different from Ledsgård. As a consequence, the measured levels of vibration are much lower. The model predicts the rise in the measured vibration level that occurs in the frequency range from about 8 to 16 Hz (Figures 8.26 and 8.27). This is due to the cut-on of the propagating mode of vibration at 12 Hz (Figure 8.25). Although the train is capable of high speed, the measurements at this site are for a train speed that is much lower than the first mode of propagation in the ground. For the measurement distances at 13 m and 26 m from the track, the observed vibration is demonstrated to be due to the dynamic generation mechanism. An over-prediction of the dynamically induced vibration occurs near to the cut-on frequency of vibration in the layer. This is due to the fact that the ground is modelled as a distinct layer with a change of stiffness at exactly 10 m depth, whereas in practice the transition will be less precise. The stiffness of the embankment is not known. Results show that the predicted levels are sensitive to this parameter for the frequency range in which propagation takes place in the upper layer (and the track). Notwithstanding the uncertainty in the embankment stiffness and the vertical track profile data that has been used, the model predicts the vibration level well for most of the frequency range, except for 2.5 Hz to 5 Hz (Figures 8.26 and 8.27). No satisfactory explanation for the under-prediction in this range has been found.

At the first two sites, measurements were made for high-speed passenger rolling stock. Measurements for two-axle freight wagons were made at the third site, Burton Joyce. Here there are fairly soft soil conditions with the speed of the first propagating

wave in the ground tending towards 77 m/s at high frequency (i.e. the 'Rayleigh' wave speed). As well as the specifically measured vertical profile of the track, measured data consisting of transfer mobility measurements for the ground only, and from the track to the ground, are available. These have also been used to validate the ground model and track/ground model. Additionally, at this site, some indication of the range of measurement levels for different trains is available. This variation, in itself, suggests that a much closer correspondence with predictions than has been obtained from the model would not be significant. In the present analysis no variation between trains has been included since wheel irregularity data (and other variation, e.g. loading, vehicle condition) has not been available. With some uncertainty in the parameters for the embankment and the effective width that should be used for the contact of the track structure with the ground, the levels predicted are close to, or within, the band of levels of the measurements (Figure 8.36). The predicted level due to the quasi-static loads is much lower than this band. Thus in the vibration observed at this site, the dynamic component of vibration is, once more, the dominant one.

The comparisons of measured and predicted vibration at the first site show that the model may be used to study the effects of high-speed trains running on very soft soils. The comparison at the second site extends the validation to a relatively stiff soil site and, despite the discrepancy at the low end of the frequency range of interest, shows that the model predicts vibration levels relatively well. Uncertainties in the stiffness of the embankment lead to uncertainty in the prediction for frequencies above the cut-on of vibration in the soil layer that are of the same order of magnitude as the differences between the prediction and measurement. The third site extends the validation to freight rolling stock and confirms the role of uncertainties in the parameters. Apart from the case of the X2000 train travelling near to the speed of wave propagation in the ground, the results presented here show that the dynamic mechanism of vibration generation is the most important. For the X2000 train at 200 km/h at Ledsgård, the excitation of a propagating wave by the quasi-static axle loads is confirmed.

8.6 SUMMARY

Using the vehicle-track-ground model developed in Chapter 7, ground vibration at three sites is predicted and compared with measured data. The comparisons show a reasonable correspondence although due to the inherent uncertainty in some parameters, the quality of such a comparison is bound to be limited.

From the predictions for the three sites, the roles are demonstrated of the two components of vibration at different frequencies and for train speeds below and above the lowest ground wave speed. It is found that, in most practical cases, the dynamic components gives rise to higher levels of vibration than the quasi-static components. It is also demonstrated that the response level is sensitive to the track parameters for frequencies above the cut-on frequency of the ground.

Chapter 9

CONCLUSIONS AND POSSIBLE FURTHER WORK

9.1 CONCLUSIONS

In this thesis, a semi-analytical model has been developed for the prediction of ground vibrations generated by surface trains. This model incorporates the necessary components of the mechanism and propagation of vibration in railway traffic. The vehicles, track and ground are described in a sufficiently detailed manner. The vehicles are described as multi-rigid body systems and only the vertical dynamics is considered. The track is modelled as multiple beams supported by vertical springs with consistent mass. The ground is represented by horizontal layers on a homogeneous half-space or a rigid foundation. The governing equations of the vehicles are solved in the frequency domain and those of the track-ground system in the frequency-wavenumber domain. The FFT technique is used to convert the responses of the track and the ground from the frequency-wavenumber domain into the time-space domain. This model uses the moving axle loads and/or the wheel/rail combined irregularities as its inputs. Outputs include the dynamic wheel-rail forces, the displacements and displacement spectra of the track and the ground (on the surface or within the ground). The model has been validated using measured data at three sites. These sites present different ground conditions (very soft, fairly soft and hard) and different train-traffic operations (high-speed passenger trains and freight trains of two-axle wagons). For typical parameters of vehicle, track and ground, various aspects involved in the problem of train-induced ground vibration have been investigated at each stage of the development of the model. A number of findings have been obtained from the investigations and are summarised below.

In Chapter 1, impacts of ground vibration on the environment and on hi-tech manufacturing facility are stressed. The frequency range of interest and sources of ground vibration are identified. Different approaches used to model the ground vibration problem are reviewed. Parameters for vehicles, railway tracks and grounds are collected. Tasks for the present PhD project are defined.

In Chapter 2, effort is made to formulate the steady state displacements and stresses (Green's functions) of a layered ground due to stationary and moving harmonic loads. This is similar to work by Barros and Luco [1994]; however, the properties of

these Green's functions, such as the reciprocity relations, are explored, and are used to improve the computational efficiency of these Green's functions.

In Chapter 3, a study is carried out for vibration propagation in a layered ground. Results are produced for dispersion curves, mode shapes, cut-on (natural) frequencies, receptances, displacement spectra due to a moving harmonic load and critical load speeds. These results are presented for two idealised sets of ground parameters, namely the stiffer layered ground (Table 1.6) and the softer layered ground (Table 1.7). It is shown that: (1) a layered ground will be resonant at its cut-on frequencies; (2) for low frequencies and an observer far away from a surface harmonic load (such that both the distance of the observer and the wavelength are greater than the depth of the layer and the dimensions of the load), the responses are mainly determined by the underlying half-space; (3) for high frequencies and an observer close to the load (such that both the distance of the observer and the wavelength are shorter than the depth of the layer), the layered ground behaves as a homogeneous half-space of the layer material; (4) for some frequencies, there is a P-SV mode, the wave speed of which is greater that that of the shear wave in the underlying half-space; this type of wave may be excited by a surface load and propagate far away over the ground surface and is dominant over other waves; (5) the displacement spectrum of the ground due to a moving harmonic load has peaks at frequencies corresponding to the intersections of the dispersion curves and the load speed line; (6) for a constant load, the critical load speed is identical to the Rayleigh wave speed of the upper layer.

It is expected that the presence of a track will modify these features to some extent, thus this study will be helpful in the understanding of dynamics of a track-ground system.

To derive an understanding of the track dynamics itself, an investigation is carried out in Chapter 4 into the steady state responses of a railway track on a Winkler foundation to a moving harmonic load. It is shown that: (1) when the viscous damping model is used, the waves in the track can be calculated analytically; (2) the FFT approach has been illustrated to be able to achieve a good accuracy and higher damping values increases the accuracy of the FFT; (3) behind the load, waves in the track may either propagate away from or towards the load; (4) below the natural frequency of the track, both the multiple beam track model and the equivalent beam track model give almost the

same result, however, at frequencies much higher than the natural frequency, the equivalent beam model produces a much higher response than the multiple beam model.

In Chapter 5, a model to predict ground vibrations generated by vertical wheel-rail forces is developed. This model is intended to serve two purposes: one is to study ground vibration generated by moving quasi-static loads (multiple axle loads) and the other is to form part of a ground vibration model which comprises vehicles, track and ground. A number of results from this model are presented in Chapter 6 in order to investigate the effects of the track structure and the distribution of axles in a train. The concepts of 'free track', 'fixed-bed track' and 'free ground' are defined. It is shown that: (1) for a track on a ground, a harmonic surface load may excite not only the propagating modes of the track-ground system but also the modes of the free ground; (2) for a track on a layered ground, near the first cut-on frequency of the free ground, both the track and the ground have maximum (resonant) responses. The presence of a track may increase or decrease the resonance frequency depending on the combination of the ground and the track parameters. (3) For very low frequencies, a change in the mass of the track does not significantly affect the responses of the ground surface. With increasing frequency, a lighter track produces lower responses than a heavier track. However, for frequencies higher than the resonance frequencies, a heavier track produces less response than a lighter track. (4) A ground may greatly modify the track response from that of the same track on a Winkler foundation, especially for frequencies near the cut-on frequency of the ground. In this case, consideration of the elasticity and energy radiation of the supporting ground is necessary. (5) For a track on a homogeneous half-space, the peak response load speed of a constant load will not be greater than the Rayleigh wave speed in the half-space. In the dispersion diagram, if the dispersion curve of the free track is above the Rayleigh wave line of the ground, then the peak load speed is lower than the Rayleigh wave speed. If the dispersion curve of the free track intersects the Rayleigh wave line, then the peak load speed is equal to the Rayleigh wave speed. Further increasing the track bending stiffness, or decreasing the track mass, does not increase the peak response load speed. When load speed is well below the peak response load speed, such modifications to the track mass lead to a small reduction of vibration. However, when the load speed approaches the peak response load speed, a decrease in the track mass causes a much greater reduction in the level of vibration. (6) For a track on a layered ground consisting of a single layer on a deep, stiffer substratum which is modelled as a homogeneous half-space, the peak response load speed may be greater than the Rayleigh

wave speed in the upper layer of the ground. The peak response load speed may be determined by the first intersection of the free-track dispersion curve and the dispersion curve of the first mode of the ground, i.e. it is given by $2\pi f_0 / \beta_0$, where β_0 and f_0 are the wavenumber and frequency corresponding to this intersection. Since for low frequency, the dispersion curve of the first mode of the ground is close to the Rayleigh wave line of the underlying half-space, increasing the track bending stiffness or decreasing the track mass can increase the peak response load speed for the track-ground system so that the peak response load speed is much higher than the Rayleigh wave speed in the upper layer. (7) During the passage of a train of many similar wagons, the pattern of axles of the wagons may give rise to, or suppress, some harmonic components of excitation. For example, at the wagon passing frequency, the response spectrum of the track-ground system is proportional to the number of the wagons. These harmonic components are formulated in terms of the dimensions of the wagons as well as the train speed. When the load speed is beyond the phase wave speeds in the ground, due to the excitation of the first propagating mode in the ground, vibration at certain frequencies is much stronger and less attenuated than those in the case of low load speed.

In Chapter 7, the vertical dynamics of vehicles running uniformly on a track is coupled with the track-ground model developed in Chapter 5, producing a complete model incorporating vehicles, track and ground. A relationship is derived between the rail irregularity spectral density and the ground vibration power spectra. This relationship makes the response predicted from the model comparable to that measured. From this vehicle-track-ground model, the wheel-rail dynamic force and the maximum displacement along the track centre-line on the ground surface are calculated for a one-axle vehicle model and for the lighter and heavier tracks. It is shown that for a large range of frequency, the layered structure of the ground and the vehicle speed have little effect on the wheel-rail force and the displacements of the wheel/rail contact points. However, the wave propagation in the track direction is strongly enhanced by the motion of the vehicle. The heavier track reduces the vibration due to the dynamic wheel-rail force compared to the lighter track. Also produced from this model are vertical velocity levels of the softer ground surface for a Mk 3 passenger carriage running, in turn, on the lighter ballasted track, the heavier ballasted track and a slab track (Table 7.2). Three frequency ranges are identified by these results: frequencies below the cut-on frequency of the track-ground system, frequencies around the cut-on frequency and frequencies above this. Only in the first frequency range is the response level dominated by the quasi-

static loads. The lower the vehicle speed or the further the observer from the track, the more important is the dynamic component of excitation. In the first frequency range, the attenuation rate with distance from the track is much higher than those in the other two frequency ranges. In the second frequency range, a strong rise with frequency in the total response level is observed due to the cut-on of the first propagating wave mode in the track-ground system. In this frequency range, the vibration has the smallest attenuation rate compared to the first and the third frequency ranges. Since the heavier ballasted track produces less vibration from the dynamic wheel-rail forces but greater vibration from the quasi-static loads than the lighter track, the heavier track gives only a little reduction in vibration level in the third frequency range. However, due to its much higher bending stiffness, the slab track produces about 20 dB lower vibration level than both the ballasted tracks for frequencies up to 25 Hz. Compared to the ballasted tracks, the slab track greatly reduces the vibration level due to the quasi-static loads, since the peak response load speed of the ground with the slab track is significantly increased by the bending stiffness of the track; therefore it is more effective for low frequencies. For high frequencies, it may raise the level due to dynamic wheel-rail forces. With increasing vehicle speed, the upper limit of frequency for which the quasi-static loads is the dominant source is slightly increased. Since the quasi-static loads are the dominating mechanism of excitation for frequencies below the cut-on frequency, the vehicle travelling speed has a greater effect on the response level for this frequency range. For higher frequencies, though the response level due to the quasi-static loads is greatly dependant on the vehicle speed, the total response level does not change so much with increasing speed.

Ground vibration at three sites is predicted and compared with measured data using the model developed in Chapter 7. This is presented in Chapter 8. The comparisons show a reasonable correspondence although due to the inherent uncertainty in some parameters, the quality of such a comparison is bound to be limited. It has been demonstrated that the response level is sensitive to the track parameters only for frequencies higher than the first cut-on frequency of the ground. From the predictions for the three sites, the roles are demonstrated of the two components of vibration at different frequencies and for train speeds below and above the lowest ground wave speed. It is found that, in most practical cases, the dynamic component gives rise to the higher level of vibration. The validation of the model also suggests that this model can be used as a tool for predicting the ground vibration levels of new lines as well as for studying

vibration reduction measures and to investigate the nature of vibration observed at particular sites.

9.2 POSSIBLE FURTHER WORK

The frequency-wavenumber domain approach may be used in the following ways, further to investigate and improve the models for vibration from trains.

(1) POWER ANALYSIS. Using the concept of power flow it would be possible to study the vibration power distribution between the track and the ground; the power in each subsystem may be used as a measure of vibration strength in that subsystem.

(2) INCLUDING THE BENDING STIFFNESS OF THE EMBANKMENT IN THE TRACK MODEL. As has been shown, the embankment has great effect on ground vibration. So far, only the vertical stiffness and the mass of the embankment are included in the model. The bending stiffness of the embankment is ignored and no wave propagation can be developed in the embankment in the longitudinal direction. A three-dimensional elasto-dynamic analysis may be necessary for the embankment and suitable parameters will be required.

(3) IMPROVING THE COUPLING OF THE TRACK AND THE GROUND. In the model, only the normal stress in the track-ground contact plane is considered and this is assumed to be distributed uniformly over the contact width. The knowledge of the stress distribution in the contact plane and its dependence on the frequency of excitation is very limited. An *in situ* measurement would be useful to acquire such knowledge. Improved models of load distribution between the ballast and embankment should be also developed.

(4) THE EFFECT OF DISCRETE SUPPORTS OF THE SLEEPERS. For a low speed freight train, the sleeper-passing frequency is a few tens of Hertz, and may be close to the cut-on frequency of a layered ground. In that case the discrete supports of the sleepers may have a significant effect on the ground vibration level. Periodic structure theory [e.g. Mead 1996, Belotserkovskiy 1996] may be used to improve the model to account for the discrete supports of the sleepers.

(5) THE EFFECT OF THE LATERAL DYNAMICS OF VEHICLES ON GROUND VIBRATION. As has been shown that, in many practical cases, the vertical dynamic wheel-rail forces are dominant over the quasi-static loads. The vehicles also apply lateral and rotational (roll) dynamic forces excited by track irregularities on the rails, in addition to the vertical wheel-rail forces. The ground vibration due to these lateral and rotational wheel-rail forces may contribute significantly to the total vibration. For such an analysis the lateral dynamics of the vehicle and track would have to be added to the model.

(6) INTERACTIONS BETWEEN A BUILDING AND THE GROUND. It would be possible to use the wavenumber-frequency domain approach to investigate the interaction between the ground and a building represented by a multi-degree-of-freedom system on the ground surface, under the action of a moving train.

(7) GROUND VIBRATION FROM TUNNEL TRAINS. The wavenumber-frequency approach can be applied to study ground vibrations for a layered ground with a tunnel of infinite length, as demonstrated by Luco and Barros [1993]. In this application, use should be made of the homogeneity of the tunnel in the longitudinal direction. A BEM model can be also developed in the wavenumber-frequency domain.

Appendix 1

NON-CAUSALITY IN VIBRATIONS INDUCED BY THE ASSUMPTION OF CONSTANT LOSS FACTORS

A1.1 INTRODUCTION

There are several mathematical damping models used to describe the damping mechanism of materials [Bert 1973]. Of those, two are most widely used: the linear viscous damping model in which the resistance force applied to a moving particle is proportional to the particle's velocity in magnitude and opposite in direction and the linear hysteretic damping model specified by a loss factor. By letting a material experience harmonic deformation, the loss factor is defined as $\eta = \frac{W}{2\pi V}$, where, W denotes the energy lost per cycle and V the peak potential energy stored in the material during that cycle. Many materials possess a hysteretic damping mechanism rather than a viscous damping mechanism. In general, loss factors are dependent on frequency, though for some materials, for example rubber, from which railpads are made, and some kinds of soils, this dependence is very slight [Fenander 1996]. For simplicity, many researchers use constant loss factors for soils in their applications [e.g., Barros and Luco 1994, Lefeuve-Mesgouez, Le Houédec and Peplow 2000] (the first reference has been widely cited by people working on soil-structure interactions). However, it has been pointed out [Crandall, 1970] that the assumption of constant loss factors in a linear vibration system will produce non-causal response, i.e., a response that appears before the excitation starts. The non-causality comes from three approximations, namely, linearity, constant loss factor and property of wave propagation [Aki and Richards 1980, pp. 167-180]. In this appendix, to examine the magnitude of the non-causal response, the impulse response functions of four systems are examined: a one-degree-of-freedom system, a railway track on a Winkler foundation, an elastic medium occupying the entire space and an elastic half-space. The second and the last systems are subsystems of the vehicle-track-ground system studied in this thesis.

A1.2 A ONE-DEGREE-OF FREEDOM SYSTEM

For a one-degree-of-freedom system, its frequency response function is given by

$$H(\omega)=\frac{1}{k+i\omega c-m\omega^2} \tag{A1.1}$$

for the viscous damping model, where ω is the angular frequency, m is the mass, k is the stiffness and c the damping coefficient. For the hysteretic damping model it is given by

$$H(\omega)=\frac{1}{k(1+i\eta\,\mathrm{sgn}(\omega))-m\omega^2} \tag{A1.2}$$

where, η is the loss factor and 'sgn' represents the sign function. Equations (A1.1) and (A1.2) are two special cases of the general form

$$H(\omega)=\frac{1}{k(\omega)[1+i\eta(\omega)]-m\omega^2} \tag{A1.3}$$

where, as functions of frequency ω, the stiffness and the loss factor have the property of

$$k(-\omega)=k(\omega),\ \eta(-\omega)=-\eta(\omega) \tag{A1.4}$$

For a linear system, the inverse Fourier transforms of the frequency response function give the unit impulse response function $h(t)$ of the system, i.e.

$$h(t)=\frac{1}{2\pi}\int_{-\infty}^{\infty}\frac{1}{k(\omega)[(1+i\eta(\omega)]-m\omega^2}e^{i\omega t}\,d\omega \tag{A1.5}$$

Having considered equation (A1.4), equation (A1.5) can be written

$$h(t)=\frac{1}{\pi}\int_{0}^{\infty}\frac{[k(\omega)-m\omega^2]\cos\omega t+k(\omega)\eta(\omega)\sin\omega t}{[k(\omega)-m\omega^2]^2+k^2(\omega)\eta^2(\omega)}d\omega \tag{A1.6}$$

$k(\omega)$ and $\eta(\omega)$ can be measured by experiment. In general, both $k(\omega)$ and $\eta(\omega)$ are dependent on both the amplitude and the frequency of oscillation. However, for many materials, $k(\omega),\eta(\omega)$ are nearly independent of ω, i.e., it may be assumed that, $k(\omega)\equiv k,\eta(\omega)\equiv\eta$. Thus equation (A1.6) becomes

$$h(t)=\frac{1}{\pi}\int_{0}^{\infty}\frac{(k-m\omega^2)\cos\omega t+k\eta\sin\omega t}{(k-m\omega^2)^2+k^2\eta^2}d\omega \tag{A1.7}$$

However, as noted in reference [Crandall 1970], equation (A1.7) will produce a non-causal response, i.e., mathematically, $h(t)\neq 0$ for $t\leq 0$. To check how large the effect of

the non-causality would be, the integral in equation (A1.7) has to be evaluated. From equation (A1.7),

$$h(t)=\frac{1}{\pi\sqrt{mk}}\int_0^\infty \frac{(1-\lambda^2)\cos\lambda\omega_n t+\eta\sin\lambda\omega_n t}{(1-\lambda^2)^2+\eta^2}d\lambda \tag{A1.8}$$

where ω_n is the undamped natural frequency of the system, i.e., $\omega_n=\sqrt{k/m}$, and $\lambda=\omega/\omega_n$. It is difficult to evaluate this integral if $t\neq 0$ and so for the present purpose, it is evaluated only at $t=0$. It can be shown, from equation (A1.8) that

$$h(0)=\frac{i}{4\sqrt{mk}}\left[\frac{1}{\sqrt{1-i\eta}}-\frac{1}{\sqrt{1+i\eta}}\right] \tag{A1.9}$$

The unit impulse response function $g(t)$ for a viscously damped single degree of freedom system for $t\geq 0$, is given by

$$g(t)=\begin{cases}\dfrac{1}{\sqrt{1-\zeta^2}\sqrt{mk}}e^{-\zeta\omega_n t}\sin(\sqrt{1-\zeta^2}\omega_n t), \text{ if } \zeta<1;\\ \dfrac{1}{2\sqrt{\zeta^2-1}\sqrt{mk}}e^{-\zeta\omega_n t}[e^{\sqrt{\zeta^2-1}\omega_n t}-e^{-\sqrt{\zeta^2-1}\omega_n t}], \text{ if } \zeta>1;\\ \dfrac{t}{m}e^{-\omega_n t}, \text{ if } \zeta=1\end{cases} \tag{A1.10}$$

and for $t\leq 0$, $g(t)\equiv 0$, where, ζ is the viscous damping ratio. The maximum displacement, $g_{\max}$, occurs at t such that $g'(t)=0$. From equation (A1.10)

$$g_{\max}=\frac{1}{\sqrt{mk}\sqrt{1-\zeta^2}}e^{-(\zeta/\sqrt{1-\zeta^2})T}\sin T,\ T=\arctan(\sqrt{1-\zeta^2}/\zeta),\ \zeta<1, \tag{A1.11a}$$

$$g_{\max}=\frac{1}{2\sqrt{mk}\sqrt{\zeta^2-1}}e^{-(\zeta/\sqrt{1-\zeta^2})T}(e^T-e^{-T}),\ T=\frac{1}{2}\ln\left(\frac{\zeta+\sqrt{\zeta^2-1}}{\zeta-\sqrt{\zeta^2-1}}\right),\zeta>1, \tag{A1.11b}$$

$$g_{\max}=\frac{1}{\sqrt{mk}}e^{-1},\zeta=1 \tag{A1.11c}$$

For a given system, the non-causality of equation (A1.8) may be measured by $h(0)/g_{\max}$, where, $g_{\max}$ takes the value given by equation (A1.11) for $\zeta=\eta/2$. From equations (A1.9) and (A1.11) this ratio is independent of the mass and stiffness of the system but not its damping. Figure A1.1 shows $h(0)/g_{\max}$ varying with loss factor η. It

can be seen, for $\eta < 0.3$, $| h(0) / g_{max} | < 0.1$. Figures A1.2 and A1.3 show g_{max} and $h(0)$ plotted against η with $\sqrt{mk} = 1$.

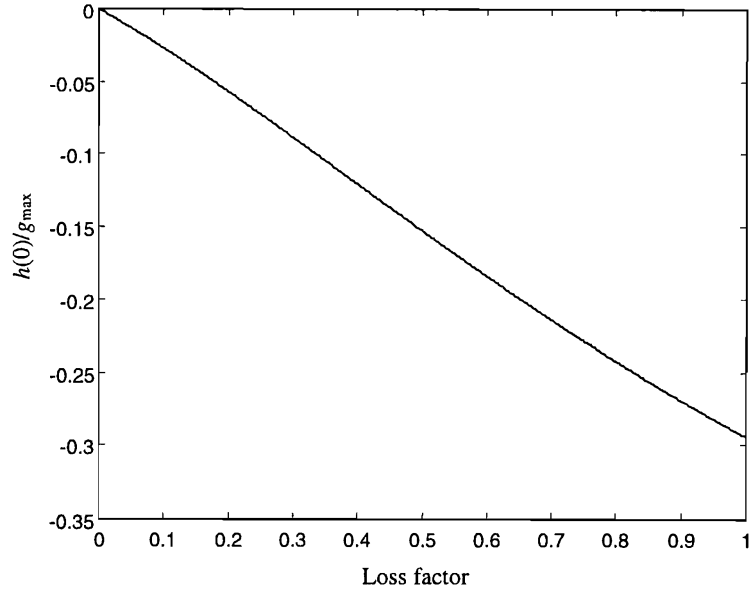

Figure A1.1. $h(0) / g_{max}$ plotted against factor η.

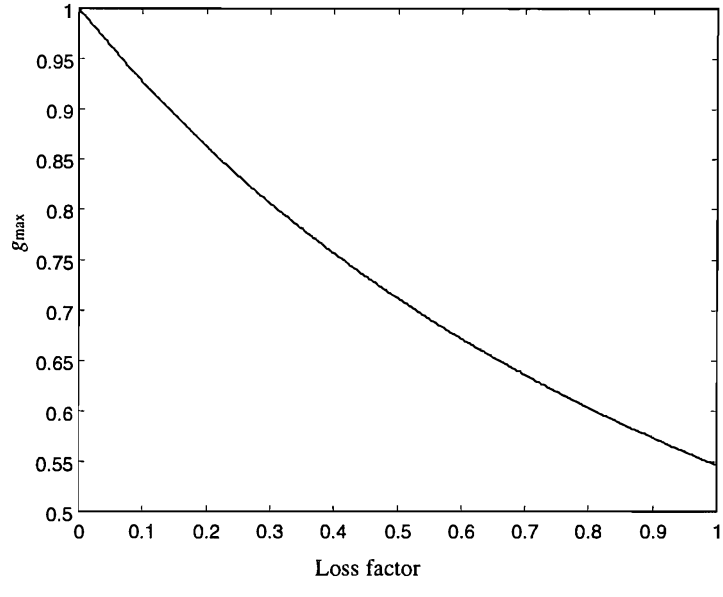

Figure A1.2. g_{max} plotted against factor η.

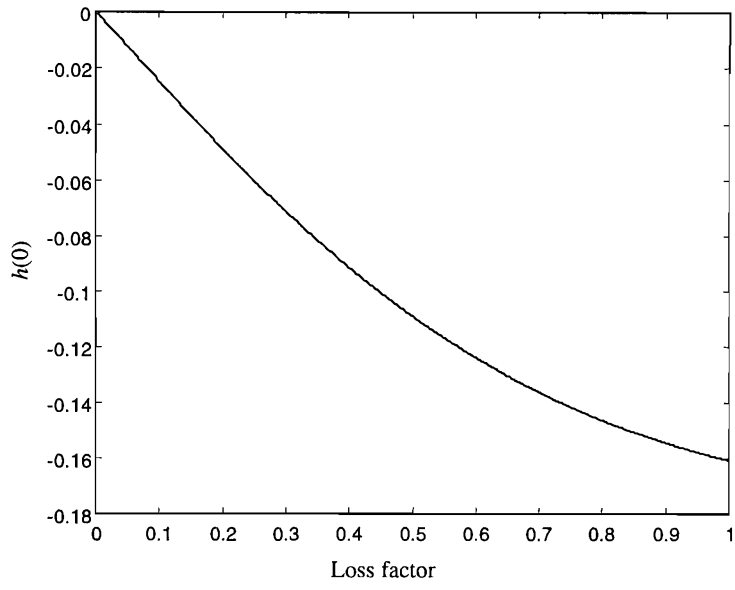

Figure A1.3. $h(0)$ plotted against factor η.

Figures A1.4 to A1.6 show the unit impulse response functions calculated using equations (A1.8) and (A1.10) for a normalised single degree of freedom system with m = 1 kg, and k = 1 N/m, and so having a natural frequency $\omega_n = 1$. In Figure A1.4, the solid line is calculated from equation (A1.10) using the viscous damping model with a damping ratio of $\zeta = 0.1$; while the dashed line is computed from equation (A1.8) using the hysteretic damping model with an equivalent loss factor at the viscous damped natural frequency, i.e. $\eta = 2\zeta\sqrt{1-\zeta^2}\omega_n = 0.199$. For the hysteretic damping model, the time response is calculated from the frequency response using an FFT. In this and other FFT-calculations, 4096 samples are used with a frequency spacing of 0.00125 Hz, thus the time history within the range of -400 to 400 s is produced. In Figure A1.5 the solid line is for the viscous damping model with a damping ratio of $\zeta = 0.25$ while the dashed line is for the hysteretic damping model with an equivalent loss factor 0.4841. Figure A1.6 accounts for a higher damping with $\zeta = 0.4$ and $\eta = 2\zeta\sqrt{1-\zeta^2}\omega_n = 0.7332$.

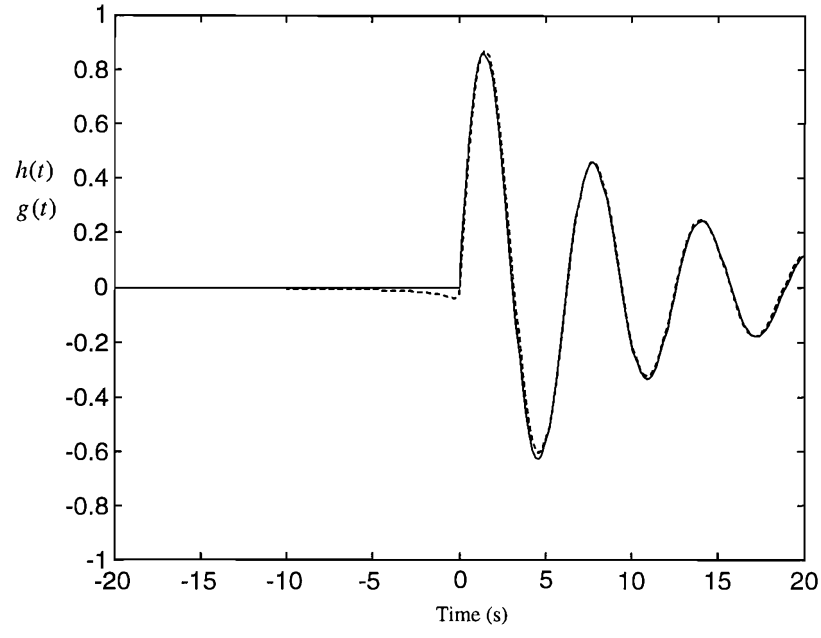

Figure A1.4. The unit impulse response function of a single-degree-of-freedom system with m = 1 kg, k = 1 N/m. ——, for the viscous damping model with a damping ratio of 0.1; – – –, for the hysteretic damping model with an equivalent loss factor to the viscous damping.

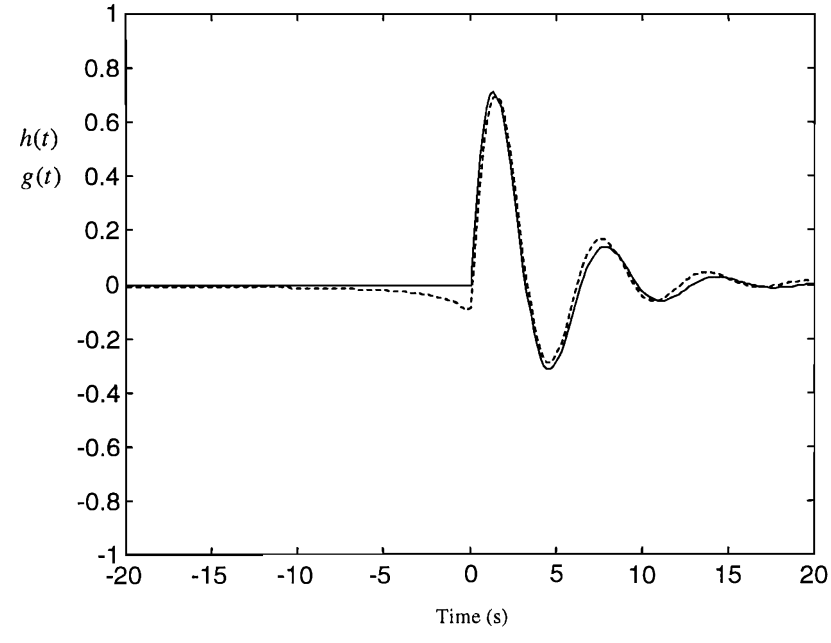

Figure A1.5. The unit impulse response function of a single-degree-of-freedom system with m = 1 kg, k = 1 N/m. ——, for the viscous damping model with a damping ratio of 0.25; – – –, for the hysteretic damping model with an equivalent loss factor to the viscous damping.

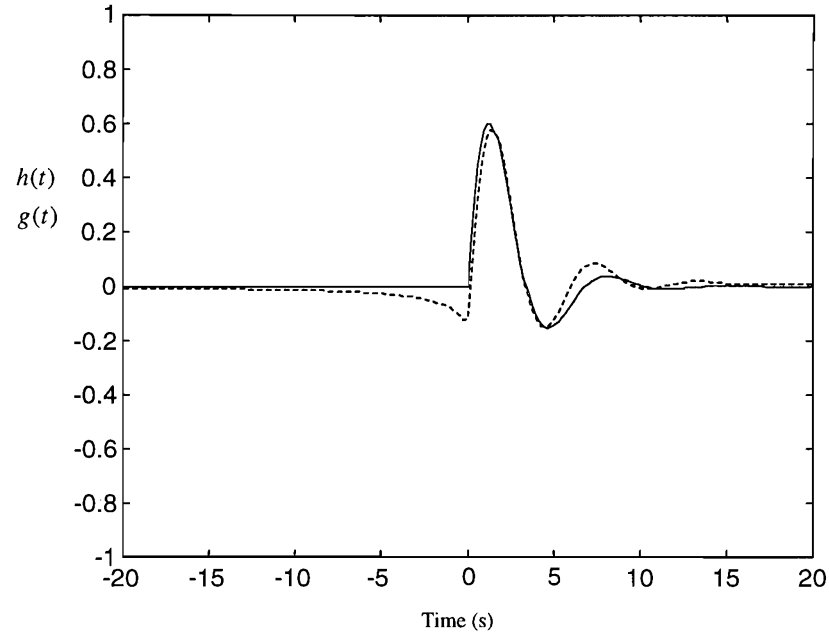

Figure A1.6. The unit impulse response function of a single-degree-of-freedom system with m = 1 kg, k = 1 N/m. ——, for the viscous damping model with a damping ratio of 0.4; – – –, for the hysteretic damping model with an equivalent loss factor to the viscous damping.

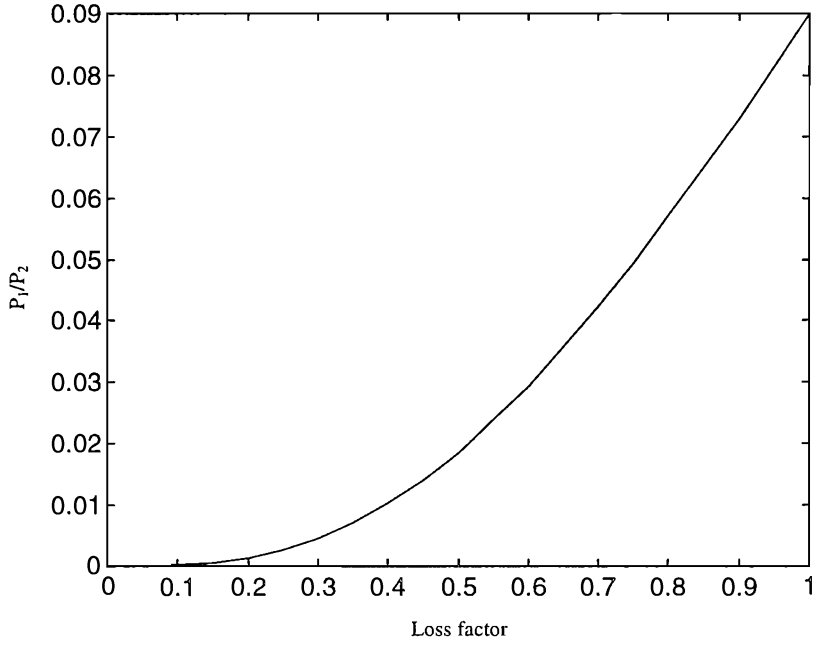

Figure A1.7. The ratio of the pre-impulse power to the post-impulse power for a single-degree-of-freedom system with m = 1 kg, k = 1 N/m and different loss factors.

For a given system, an alternative measure of the non-causality of equation (A1.8) is to compare the pre-impulse power P_1 and the post-impulse power P_2, where, P_1 and P_2 are defined as $P_1 = \int_{-\infty}^{0} h^2(t)dt$ and $P_2 = \int_{0}^{\infty} h^2(t)dt$. In this measurement, the infinite

integrations are required to be convergent, and the post-impulse response is assumed to be an approximation of the true response. Figure A1.7 shows the ratio of the pre-impulse power to the post-impulse power for the normalized single-degree-of-freedom system for different loss factors.

From the above calculations, a point may be made that for low damping, the pre-impulse response is small. For example for loss factor $\eta \leq 0.4$, it is less than 1% of the post-impulse response. In this case the post-impulse response of the hysteretically damped system is closely similar to that for the viscously damped system.

A1.3 A RAILWAY TRACK ON A WINKLER FOUNDATION

For a structure like a railway track, a damping model not only affects the energy loss with time, but also affects the energy loss due to radiation. In Chapter 4, a track is modelled as a system of multiple beams supported by the Winkler foundation. It is shown that, for a stationary harmonic load applied on the rail beam, the response of the rail beam can be obtained analytically (the damping model can be either viscous or hysteretic). Thus the frequency response function (FRF) of any point on the rail can be computed exactly. The inverse Fourier transform of the FRF gives the unit impulse response function of this point. All the parameters of the track listed in Table 4.1 are used in this section except for the loss factors of the railpad, ballast and the foundation.

Figure A1.8 shows the amplitude of the driving point FRF. The loss factors of the railpad, ballast and foundation are set to be 0.1. The peak occurs at about 9 Hz which is the natural frequency of the track on the Winkler foundation (see Figure 4.5). Using the FFT technique with a length of 8192 and a frequency spacing of 0.025 Hz, the impulse response functions are computed for the driving point and for points at 50 m and 100 m from the loading point. For the loss factors equal to 0.1, these impulse functions are shown in Figures A1.9 to A1.11. If the loss factors are increased to 0.4, the impulse response functions of the three points are shown in Figures A1.12 to A1.14.
Figure A1.15 shows the ratio of the pre-impulse power to the post-impulse power for the loading point on the rail for different loss factors. Compared with Figure A1.7, it can be seen that the track presents a similar non-causality to that for a one-degree-of-freedom system. This is because the track has a resonance frequency which is dominant over other frequencies.

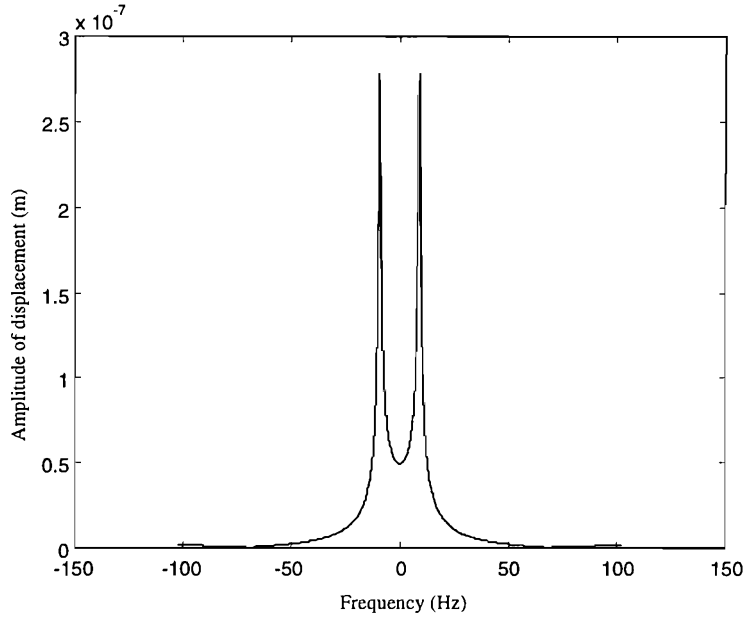

Figure A1.8. The amplitude of the driving point FRF for loss factors equal to 0.1.

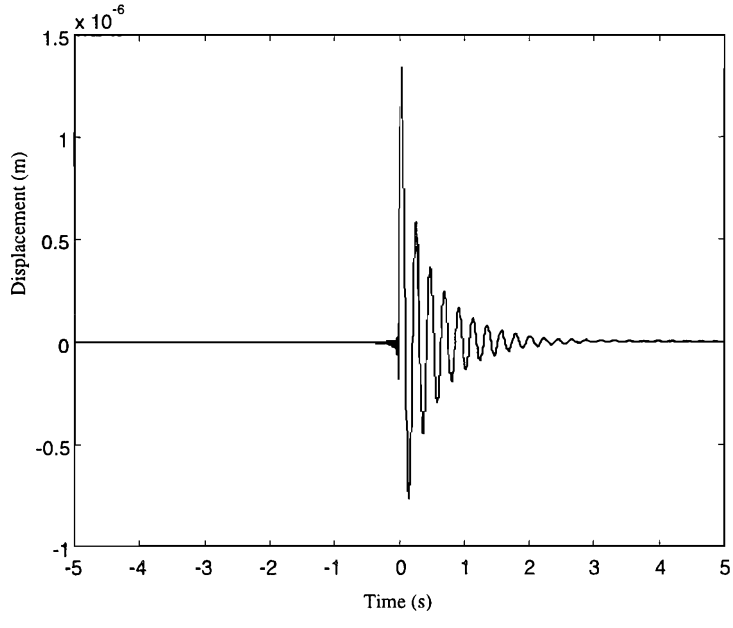

Figure A1.9. Impulse response function of the loading point on the rail, loss factors equal to 0.1.

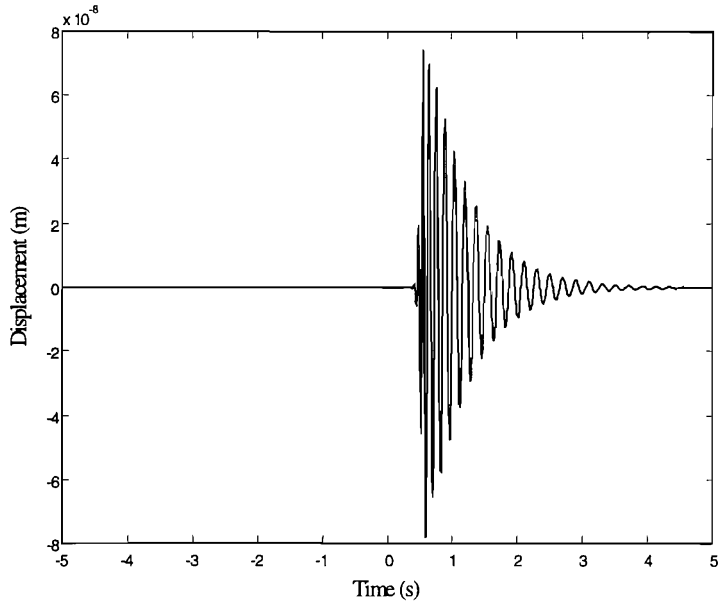

Figure A1.10. Impulse response function of a point at 50 m from the loading point on the rail, loss factors equal to 0.1.

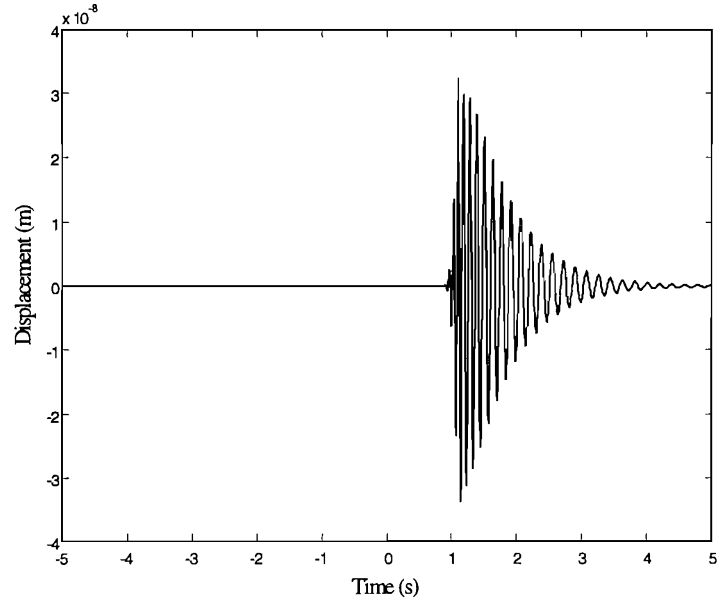

Figure A1.11. Impulse response function of a point at 100 m from the loading point on the rail, loss factors equal to 0.1.

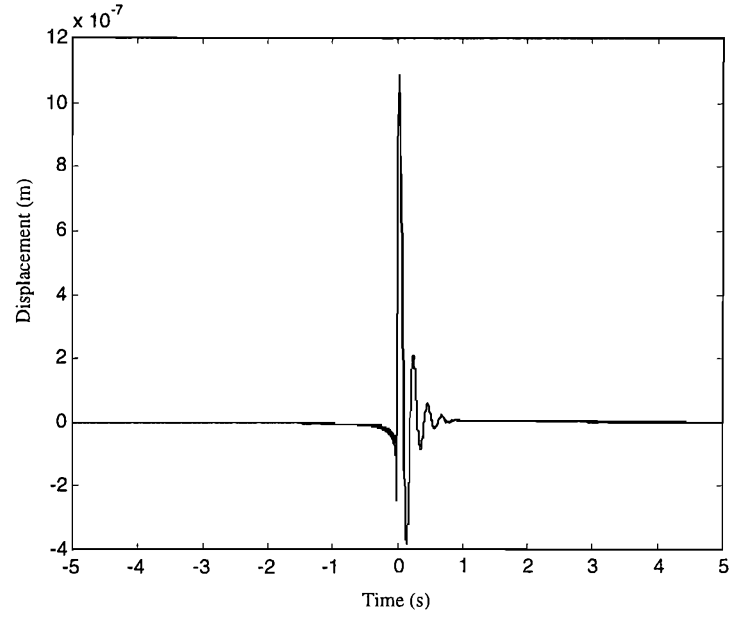

Figure A1.12. Impulse response function of the loading point on the rail, loss factors equal to 0.4.

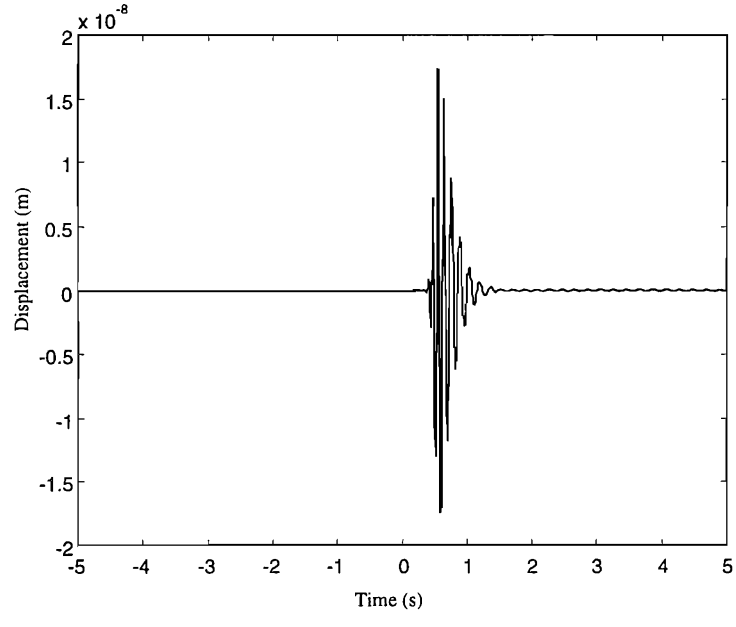

Figure A1.13. Impulse response function of a point at 50 m from the loading point on the rail, loss factors equal to 0.4.

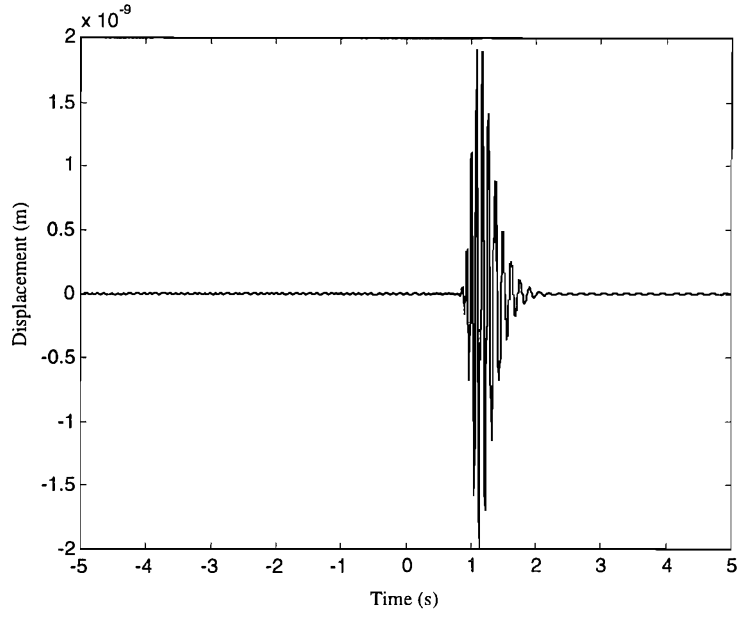

Figure A1.14. Impulse response function of a point at 100 m from the loading point on the rail, loss factors equal to 0.4.

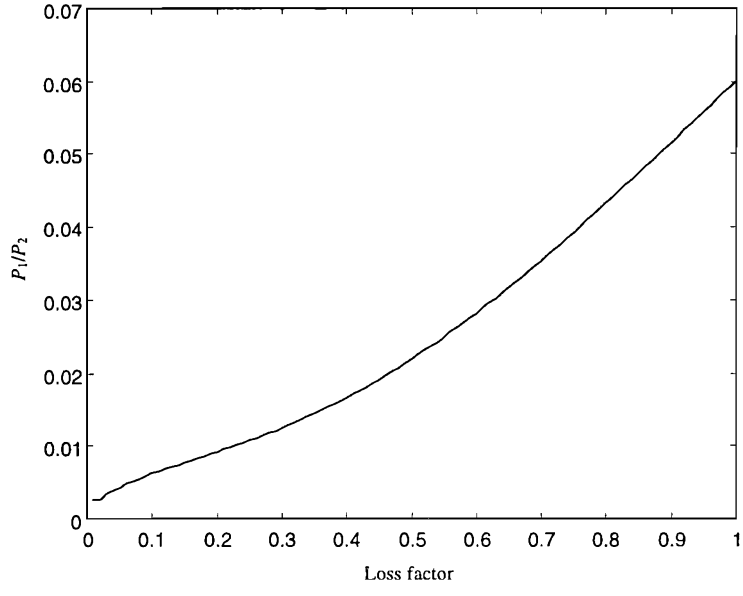

Figure A1.15. The ratio of the pre-impulse power to the post-impulse power at the loading point on the rail for different loss factors.

A1.4 A WHOLE SPACE OF ELASTIC MEDIUM

For an infinite elastic medium (i.e. occupying a whole space), the Cartesian coordinates are denoted by x_1, x_2 and x_3. The axes x_1 and x_2 form the horizontal plane and the axis x_3 is in the vertical direction. Material properties of this medium are denoted by E for its Young's modulus, ν for its Possion ratio, ρ for its density and η for its loss

factor. For a unit point harmonic load of radian frequency ω applied at the origin in the x_k-direction, the following formulae give the amplitude of the steady-state displacement in the x_l-direction of point (x_1, x_2, x_3) [Dominguez, 1993]:

$$w_{lk}(x_1, x_2, x_3) = \frac{1}{4\pi\rho c_2^2}[\psi\delta_{lk} - \chi \frac{\partial r}{\partial x_l}\frac{\partial r}{\partial x_k}] \tag{A1.12}$$

where, $r = \sqrt{x_1^2 + x_2^2 + x_3^2}$,

$$\psi = \frac{1}{r}e^{-k_2 r}[1 + (1 + \frac{1}{k_2 r})\frac{1}{k_2 r}] - \frac{1}{r}e^{-k_1 r}\frac{c_2^2}{c_1^2}(1 + \frac{1}{k_1 r})\frac{1}{k_1 r} \tag{A1.13}$$

$$\chi = \frac{1}{r}e^{-k_2 r}[1 + (1 + \frac{1}{k_2 r})\frac{3}{k_2 r}] - \frac{1}{r}e^{-k_1 r}\frac{c_2^2}{c_1^2}[1 + (1 + \frac{1}{k_1 r})\frac{3}{k_1 r}] \tag{A1.14}$$

$$k_1 = i\omega / c_1, k_2 = i\omega / c_2 \tag{A1.15, A1.16}$$

$$c_1 = \sqrt{(\lambda + 2\mu)/\rho}, c_2 = \sqrt{\mu/\rho} \tag{A1.17, A1.18}$$

$$\lambda = \frac{\nu E(1+i\eta\,\mathrm{sgn}(\omega))}{(1+\nu)(1-2\nu)}, \mu = \frac{E(1+i\eta\,\mathrm{sgn}(\omega))}{2(1+\nu)} \tag{A1.19, A1.20}$$

The inverse Fourier transform of equation (A1.12) gives the impulse response function of point (x_1, x_2, x_3) in the x_l-direction, i.e.,

$$h_{lk}(x_1, x_2, x_3; t) = \frac{1}{2\pi}\frac{1}{4\pi\rho}\int_{-\infty}^{\infty}\frac{1}{c_2^2}[\psi\delta_{lk} - \chi\frac{\partial r}{\partial x_l}\frac{\partial r}{\partial x_k}]e^{i\omega t}\,d\omega \tag{A1.21}$$

In the absence of damping, the impulse response function of point (x_1, x_2, x_3) in the x_l-direction, denoted by $g_{lk}(x_1, x_2, x_3; t)$, can be expressed analytically as [Dominguez, 1993]:

$$\begin{aligned} g_{lk}(x_1, x_2, x_3; t) = \frac{1}{4\pi\rho}\{&\frac{t}{r^3}(3\frac{\partial r}{\partial x_l}\frac{\partial r}{\partial x_k} - \delta_{lk})[H(t - \frac{r}{c_1}) - H(t - \frac{r}{c_2})] \\ &+ \frac{1}{r}\frac{\partial r}{\partial x_l}\frac{\partial r}{\partial x_k}[\frac{1}{c_1^2}\delta(t - \frac{r}{c_1}) - \frac{1}{c_2^2}\delta(t - \frac{r}{c_2})] + \frac{\delta_{lk}}{rc_2^2}\delta(t - \frac{r}{c_2})\} \end{aligned} \tag{A1.22}$$

Equation (A1.22) shows that the disturbance emitted from the origin at $t = 0$ is felt at point (x_1, x_2, x_3) from the arrival of the longitudinal wave ($t = r/c_1$) up to the arrival of the shear wave ($t = r/c_2$). Impulses are received at $t = r/c_1$ and at $t = r/c_2$.

In the presence of damping, the integrals $\int_{-\infty}^{\infty} \frac{1}{c_2^2} \psi e^{i\omega t} d\omega$ and $\int_{-\infty}^{\infty} \frac{1}{c_2^2} \chi e^{i\omega t} d\omega$ in equation (A1.21) are evaluated as follows:

$$\begin{aligned}\int_{-\infty}^{\infty} \frac{1}{c_2^2} \psi e^{i\omega t} d\omega &= \int_{-\infty}^{\infty} \frac{1}{c_2^2} \{\frac{1}{r} e^{-i\omega r/c_2} [1 + (1 + \frac{c_2}{i\omega r}) \frac{c_2}{i\omega r}] - \frac{1}{r} e^{-i\omega r/c_1} \frac{c_2^2}{c_1^2} (1 + \frac{c_1}{i\omega r}) \frac{c_1}{i\omega r}\} e^{i\omega t} d\omega \\ &= \frac{1}{r} \int_{-\infty}^{\infty} \frac{1}{c_2^2} e^{i(t - r/c_2)\omega} d\omega + \frac{1}{r^2} \int_{-\infty}^{\infty} \frac{1}{ic_2\omega} e^{i(t - r/c_2)\omega} d\omega + \frac{1}{r^3} \int_{-\infty}^{\infty} \frac{1}{(i\omega)^2} e^{i(t - r/c_2)\omega} d\omega \\ &\quad - \frac{1}{r^2} \int_{-\infty}^{\infty} \frac{1}{ic_1\omega} e^{i(t - r/c_1)\omega} d\omega - \frac{1}{r^3} \int_{-\infty}^{\infty} \frac{1}{(i\omega)^2} e^{i(t - r/c_1)\omega} d\omega\end{aligned} \tag{A1.23}$$

If a constant loss factor is used, then the dilatational and the shear wave speeds, c_1 and c_2, are complex, and can be expressed in terms of their real and imaginary parts:

$$c_1 = \begin{cases} c_{1R} + ic_{1I}, \text{ if } \omega > 0; \\ c_{1R} - ic_{1I}, \text{ if } \omega < 0; \end{cases} \tag{A1.24}$$

$$c_2 = \begin{cases} c_{2R} + ic_{2I}, \text{ if } \omega > 0; \\ c_{2R} - ic_{2I}, \text{ if } \omega < 0; \end{cases} \tag{A1.25}$$

Since

$$\begin{aligned}\frac{1}{r^3} \int_{-\infty}^{0} \frac{1}{(i\omega)^2} e^{i(t - r/c_2)\omega} d\omega &= -\frac{1}{r^3} [-\frac{1}{\omega} e^{i(t - r/c_2)\omega} |_{-\infty}^{0} + i(t - r/c_2) \int_{-\infty}^{0} \frac{1}{\omega} e^{i(t - r/c_2)\omega} d\omega] \\ &= \frac{1}{r^3} \frac{1}{\omega} |_{\omega=0} - \frac{1}{r^3} i(t - r/c_2) \int_{-\infty}^{0} \frac{1}{\omega} e^{i(t - r/c_2)\omega} d\omega\end{aligned}$$

$$\frac{1}{r^3} \int_{0}^{\infty} \frac{1}{(i\omega)^2} e^{i(t - r/c_2)\omega} d\omega = -\frac{1}{r^3} \frac{1}{\omega} |_{\omega=0} - \frac{1}{r^3} i(t - r/c_2) \int_{0}^{\infty} \frac{1}{\omega} e^{i(t - r/c_2)\omega} d\omega$$

$$\frac{1}{r^3} \int_{-\infty}^{0} \frac{1}{(i\omega)^2} e^{i(t - r/c_1)\omega} d\omega = \frac{1}{r^3} \frac{1}{\omega} |_{\omega=0} - \frac{1}{r^3} i(t - r/c_1) \int_{-\infty}^{0} \frac{1}{\omega} e^{i(t - r/c_1)\omega} d\omega$$

$$\frac{1}{r^3} \int_{0}^{\infty} \frac{1}{(i\omega)^2} e^{i(t - r/c_1)\omega} d\omega = -\frac{1}{r^3} \frac{1}{\omega} |_{\omega=0} - \frac{1}{r^3} i(t - r/c_1) \int_{0}^{\infty} \frac{1}{\omega} e^{i(t - r/c_1)\omega} d\omega$$

thus

$$\int_{-\infty}^{\infty}\frac{1}{c_2^2}\psi e^{i\omega t}d\omega=\frac{1}{r}\int_{-\infty}^{\infty}\frac{1}{c_2^2}e^{i(t-r/c_2)\omega}d\omega+\frac{t}{r^3}\int_{-\infty}^{\infty}\frac{1}{i\omega}e^{i(t-r/c_2)\omega}d\omega-\frac{t}{r^3}\int_{-\infty}^{\infty}\frac{1}{i\omega}e^{i(t-r/c_1)\omega}d\omega \quad \text{(A1.26)}$$

Denoting $1/c_2^2=\alpha_2+i\beta_2$, for $\omega>0$, where,

$$\alpha_2=\frac{c_{2R}^2-c_{2I}^2}{(c_{2R}^2-c_{2I}^2)^2+4c_{2R}^2c_{2I}^2},\ \beta_2=\frac{-2c_{2R}c_{2I}}{(c_{2R}^2-c_{2I}^2)^2+4c_{2R}^2c_{2I}^2} \quad \text{(A1.27)}$$

then the integration in the first term on the right-hand side of equation (A1.26),

$$\int_{-\infty}^{\infty}\frac{1}{c_2^2}e^{i(t-r/c_2)\omega}d\omega=2\int_0^{\infty}\{\alpha_2\cos[(t-\frac{c_{2R}r}{c_{2R}^2+c_{2I}^2})\omega]-\beta_2\sin[(t-\frac{c_{2R}r}{c_{2R}^2+c_{2I}^2})\omega]\}\exp[(-\frac{c_{2I}r}{c_{2R}^2+c_{2I}^2})\omega]d\omega \quad \text{(A1.28)}$$

Using the formulae

$$\int_0^{\infty}e^{-ax}\cos bxdx=\frac{a}{a^2+b^2},\ (a>0) \quad \text{(A1.29)}$$

$$\int_0^{\infty}e^{-ax}\sin bxdx=\frac{b}{a^2+b^2},\ (a>0) \quad \text{(A1.30)}$$

yields

$$\int_{-\infty}^{\infty}\frac{1}{c_2^2}e^{i(t-r/c_2)\omega}d\omega=\frac{2r\alpha_2c_{2I}(c_{2R}^2+c_{2I}^2)}{(rc_{2I})^2+[(c_{2R}^2+c_{2I}^2)t-rc_{2R}]^2}-2\beta_2\frac{(c_{2R}^2+c_{2I}^2)^2t-rc_{2R}(c_{2R}^2+c_{2I}^2)}{(rc_{2I})^2+[(c_{2R}^2+c_{2I}^2)t-rc_{2R}]^2} \quad \text{(A1.31)}$$

The integration in the second term on the right-hand side of equation (A1.26),

$$\int_{-\infty}^{\infty}\frac{1}{i\omega}e^{i(t-r/c_2)\omega}d\omega=2\int_0^{\infty}\frac{1}{\omega}\sin[(t-\frac{c_{2R}r}{c_{2R}^2+c_{2I}^2})\omega]\exp[(-\frac{c_{2I}r}{c_{2R}^2+c_{2I}^2})\omega]d\omega$$

Using the formula

$$\int_0^{\infty}\frac{1}{x}e^{-ax}\sin bxdx=\arctan\frac{b}{a},\ (a>0) \quad \text{(A1.32)}$$

gives

$$\int_{-\infty}^{\infty}\frac{1}{i\omega}e^{i(t-r/c_2)\omega}d\omega=2\arctan[\frac{(c_{2R}^2+c_{2I}^2)t-rc_{2R}}{rc_{2I}}] \quad \text{(A1.33)}$$

Similarly,

$$\int_{-\infty}^{\infty} \frac{1}{i\omega} e^{i(t-r/c_1)\omega} d\omega = 2\arctan[\frac{(c_{1R}^2+c_{1I}^2)t-rc_{1R}}{rc_{1I}}] \tag{A1.34}$$

Inserting equations (A1.31), (A1.33) and (A1.34) into equation (A1.26) yields

$$\begin{aligned}\int_{-\infty}^{\infty} \frac{1}{c_2^2} \psi e^{i\omega t} d\omega = &\frac{2\alpha_2 c_{2I}(c_{2R}^2+c_{2I}^2)}{(rc_{2I})^2+[(c_{2R}^2+c_{2I}^2)t-rc_{2R}]^2} - \frac{2\beta_2}{r}\frac{(c_{2R}^2+c_{2I}^2)^2 t-rc_{2R}(c_{2R}^2+c_{2I}^2)}{(rc_{2I})^2+[(c_{2R}^2+c_{2I}^2)t-rc_{2R}]^2} \\ &+ 2\frac{t}{r^3}\{\arctan[\frac{(c_{2R}^2+c_{2I}^2)t-rc_{2R}}{rc_{2I}}] - \arctan[\frac{(c_{1R}^2+c_{1I}^2)t-rc_{1R}}{rc_{1I}}]\}\end{aligned} \tag{A1.35}$$

Now it is shown that

$$\begin{aligned}\int_{-\infty}^{\infty} \frac{1}{c_2^2} \chi e^{i\omega t} d\omega &= \int_{-\infty}^{\infty} \frac{1}{c_2^2}\{\frac{1}{r} e^{-i\omega r/c_2}[1+(1+\frac{c_2}{i\omega r})\frac{3c_2}{i\omega r}] - \frac{1}{r} e^{-i\omega r/c_1}\frac{c_2^2}{c_1^2}[1+(1+\frac{c_1}{i\omega r})\frac{3c_1}{i\omega r}\}e^{i\omega t} d\omega \\ &= \frac{1}{r}\int_{-\infty}^{\infty} \frac{1}{c_2^2} e^{i(t-r/c_2)\omega} d\omega + \frac{3}{r^2}\int_{-\infty}^{\infty} \frac{1}{ic_2\omega} e^{i(t-r/c_2)\omega} d\omega + \frac{3}{r^3}\int_{-\infty}^{\infty} \frac{1}{(i\omega)^2} e^{i(t-r/c_2)\omega} d\omega \\ &\quad - \frac{1}{r}\int_{-\infty}^{\infty} \frac{1}{c_1^2} e^{i(t-r/c_1)\omega} d\omega - \frac{3}{r^2}\int_{-\infty}^{\infty} \frac{1}{ic_1\omega} e^{i(t-r/c_1)\omega} d\omega - \frac{3}{r^3}\int_{-\infty}^{\infty} \frac{1}{(i\omega)^2} e^{i(t-r/c_1)\omega} d\omega\end{aligned}$$

i.e.,

$$\begin{aligned}\int_{-\infty}^{\infty} \frac{1}{c_2^2} \chi e^{i\omega t} d\omega = &\frac{1}{r}\int_{-\infty}^{\infty} \frac{1}{c_2^2} e^{i(t-r/c_2)\omega} d\omega + \frac{3t}{r^3}\int_{-\infty}^{\infty} \frac{1}{i\omega} e^{i(t-r/c_2)\omega} d\omega \\ &- \frac{1}{r}\int_{-\infty}^{\infty} \frac{1}{c_1^2} e^{i(t-r/c_1)\omega} d\omega - \frac{3t}{r^3}\int_{-\infty}^{\infty} \frac{1}{i\omega} e^{i(t-r/c_1)\omega} d\omega\end{aligned} \tag{A1.36}$$

Denoting $1/c_1^2 = \alpha_1 + i\beta_1$, for $\omega > 0$, where,

$$\alpha_1 = \frac{c_{1R}^2-c_{1I}^2}{(c_{1R}^2-c_{1I}^2)^2+4c_{1R}^2c_{1I}^2},\ \beta_1 = \frac{-2c_{1R}c_{1I}}{(c_{1R}^2-c_{1I}^2)^2+4c_{1R}^2c_{1I}^2} \tag{A1.37}$$

and using equations (A1.31), (A1.33) and (A1.34), yileds

$$\begin{aligned}\int_{-\infty}^{\infty} \frac{1}{c_2^2} \chi e^{i\omega t} d\omega = &\frac{2\alpha_2 c_{2I}(c_{2R}^2+c_{2I}^2)}{(rc_{2I})^2+[(c_{2R}^2+c_{2I}^2)t-rc_{2R}]^2} - \frac{2\beta_2}{r}\frac{(c_{2R}^2+c_{2I}^2)^2 t-rc_{2R}(c_{2R}^2+c_{2I}^2)}{(rc_{2I})^2+[(c_{2R}^2+c_{2I}^2)t-rc_{2R}]^2} \\ &- \frac{2\alpha_1 c_{1I}(c_{1R}^2+c_{1I}^2)}{(rc_{1I})^2+[(c_{1R}^2+c_{1I}^2)t-rc_{1R}]^2} + \frac{2\beta_1}{r}\frac{(c_{1R}^2+c_{1I}^2)^2 t-rc_{1R}(c_{1R}^2+c_{1I}^2)}{(rc_{1I})^2+[(c_{1R}^2+c_{1I}^2)t-rc_{1R}]^2} \\ &+ 6\frac{t}{r^3}\{\arctan[\frac{(c_{2R}^2+c_{2I}^2)t-rc_{2R}}{rc_{2I}}] - \arctan[\frac{(c_{1R}^2+c_{1I}^2)t-rc_{1R}}{rc_{1I}}]\}\end{aligned} \tag{A1.38}$$

The substitution of equations (A1.35) and (A1.38) into equation (A1.21) yields the impulse response functions for a constant loss factor.

The following figures show the vertical (i.e., $l = 3$) impulse response functions of three points for different values of loss factor, due to a vertical (i.e., $k = 3$) impulse applied at the origin. The first point is located in the horizontal plane including the origin and is at 10 m from the origin, i.e., $x_1 = 10, x_2 = 0, x_3 = 0$. The second point is located in the same plane but at 50 m, i.e., $x_1 = 50, x_2 = 0, x_3 = 0$. For these two points, equation (A1.22) becomes

$$g_{lk}(x_1, x_2, x_3; t) = \frac{1}{4\pi\rho}\{-\frac{t}{r^3}[H(t-\frac{r}{c_1}) - H(t-\frac{r}{c_2})] + \frac{1}{rc_2^2}\delta(t-\frac{r}{c_2})\} \qquad \text{(A1.39)}$$

This shows that, from the arrival of the dilational wave, the displacement increases proportionally with time, until the arrival of the shear wave (as an impulse).

The third point is at 50 m below the origin, i.e., $x_1 = 0, x_2 = 0, x_3 = 50$. For this point, equation (A1.22) becomes

$$g_{lk}(x_1, x_2, x_3; t) = \frac{1}{4\pi\rho}\{\frac{2t}{r^3}[H(t-\frac{r}{c_1}) - H(t-\frac{r}{c_2})] + \frac{1}{rc_1^2}\delta(t-\frac{r}{c_1})\} \qquad \text{(A1.40)}$$

This shows that, also at this point, from the arrival of the dilatational wave (as an impulse), the displacement increases proportionally with time, until the arrival of the shear wave.

The shear (S-) and dilatational (P-) wave speeds of the elastic medium are 118 m/s and 360 m/s, respectively. For a distance of 50 m, the travel time of these two waves are 0.42 s and 0.14 s (ignoring the effect of the damping). Figures A1.16 to A1.27 show the calculated pulses arriving at various points either 10 m or 50 m from the origin. The vertical dashed line in each figure indicates the arrival time of the P-wave. Physically, before the arrival of the P-wave, no vibration would be excited. The constant loss factor model does not exactly reproduce this. From Figures A1.16 to A1.23 it can be seen that the pre-impulse response decays slowly with increasing negative time. Even worse, as shown in Figures A1.24 to A1.27, the pre-impulse response increases with increasing negative time for the third point.

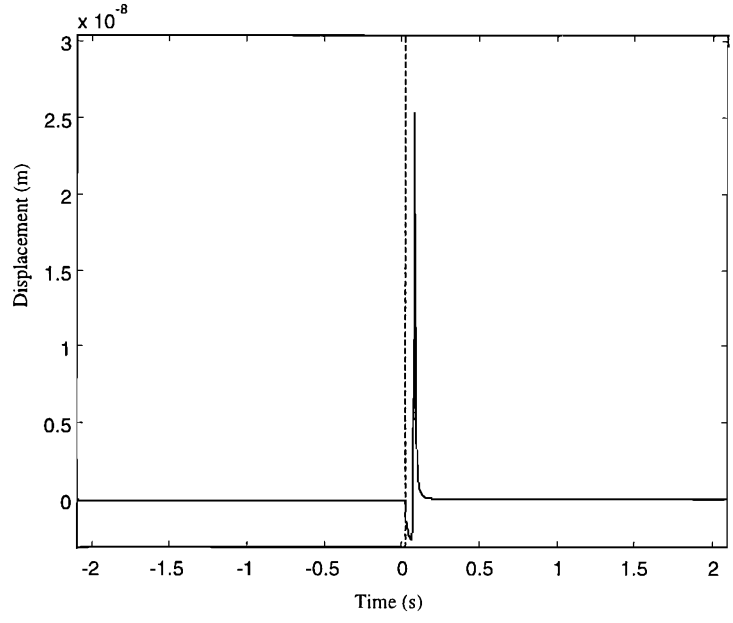

Figure A1.16. The vertical impulse response function of point (10 m, 0, 0) for loss factor equal to 0.1.

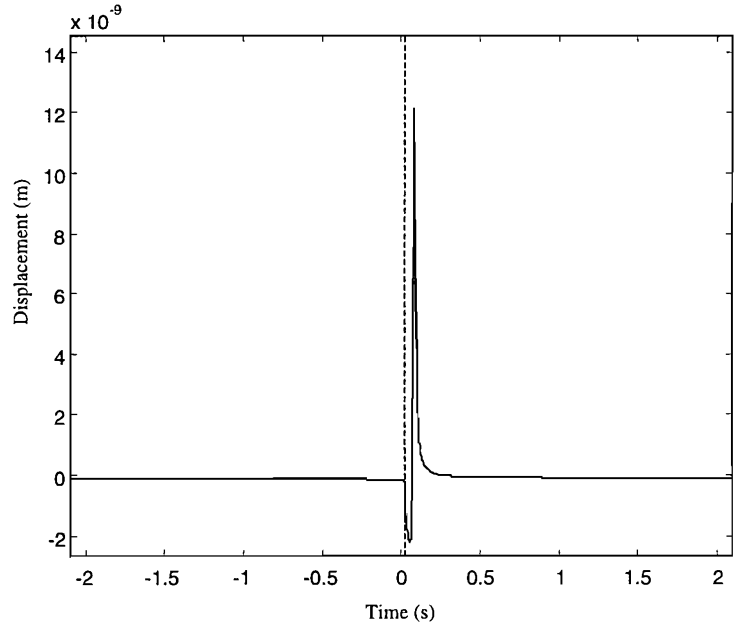

Figure A1.17. The vertical impulse response function of point (10 m, 0, 0) for loss factor equal to 0.2.

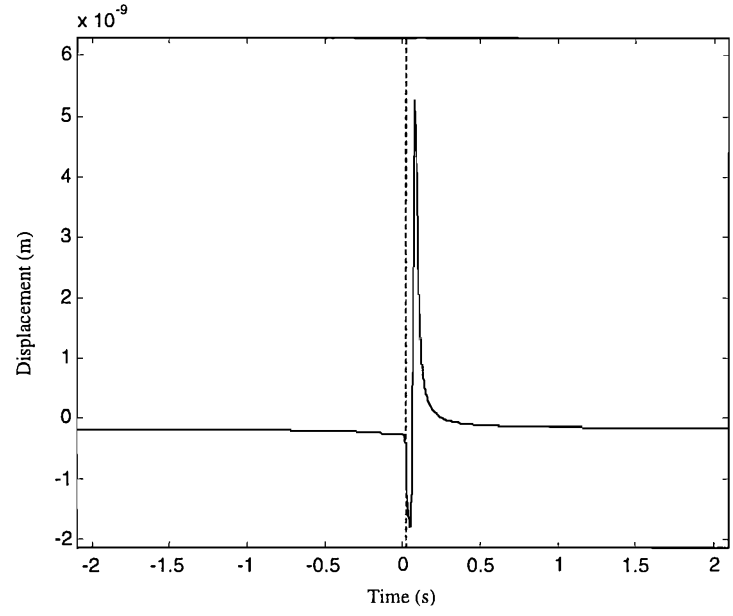

Figure A1.18. The vertical impulse response function of point (10 m, 0, 0) for loss factor equal to 0.4.

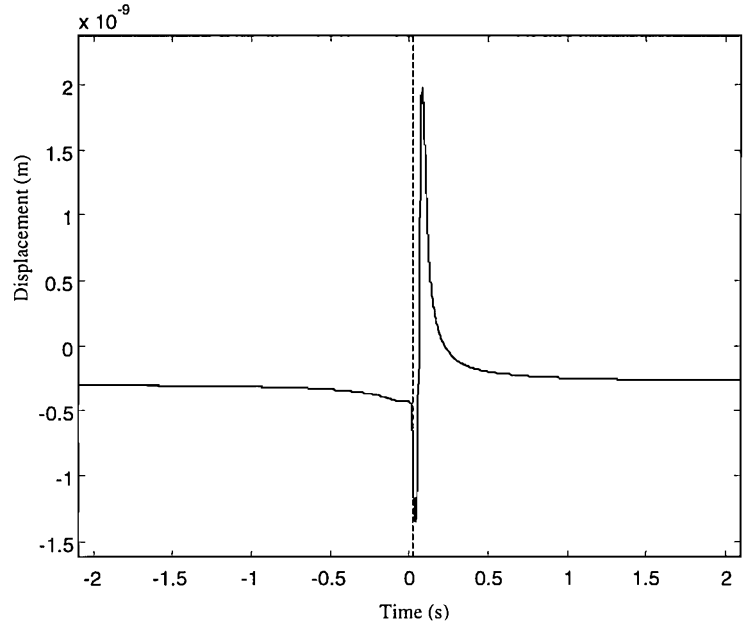

Figure A1.19. The vertical impulse response function of point (10 m, 0, 0) for loss factor equal to 0.8.

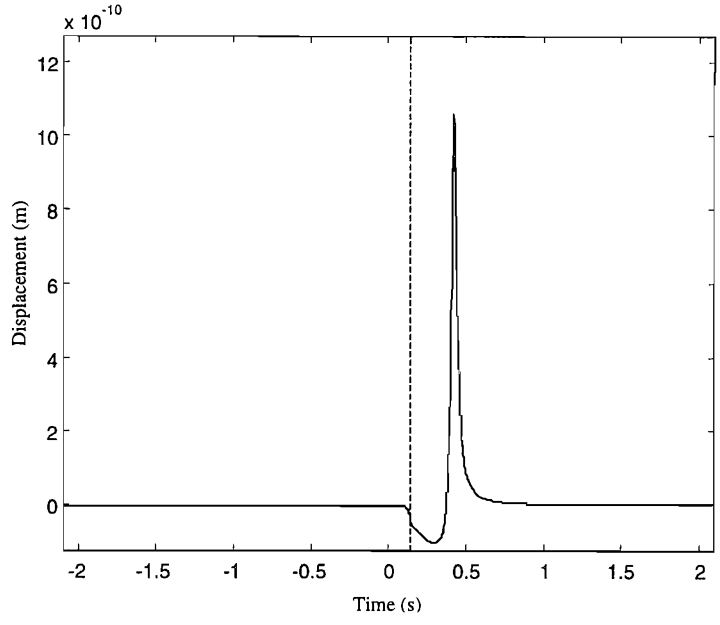

Figure A1.20. The vertical impulse response function of point (50 m, 0, 0) for loss factor equal to 0.1.

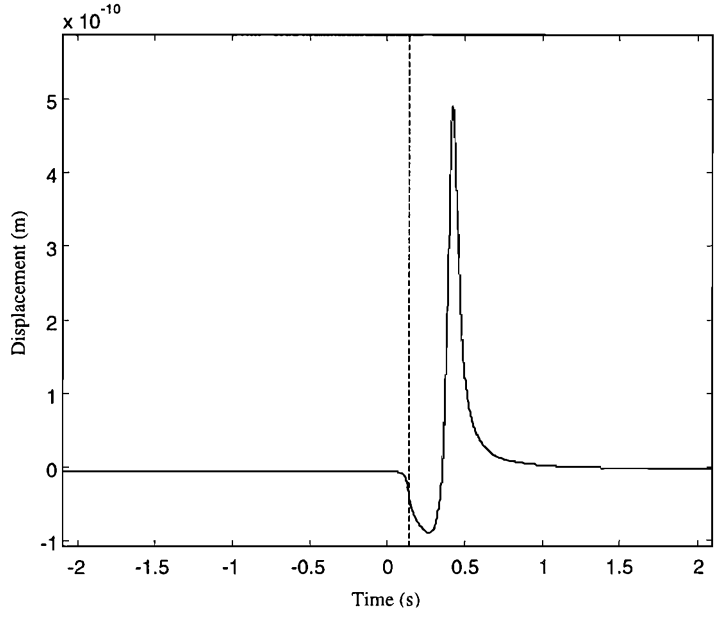

Figure A1.21. The vertical impulse response function of point (50 m, 0, 0) for loss factor equal to 0.2.

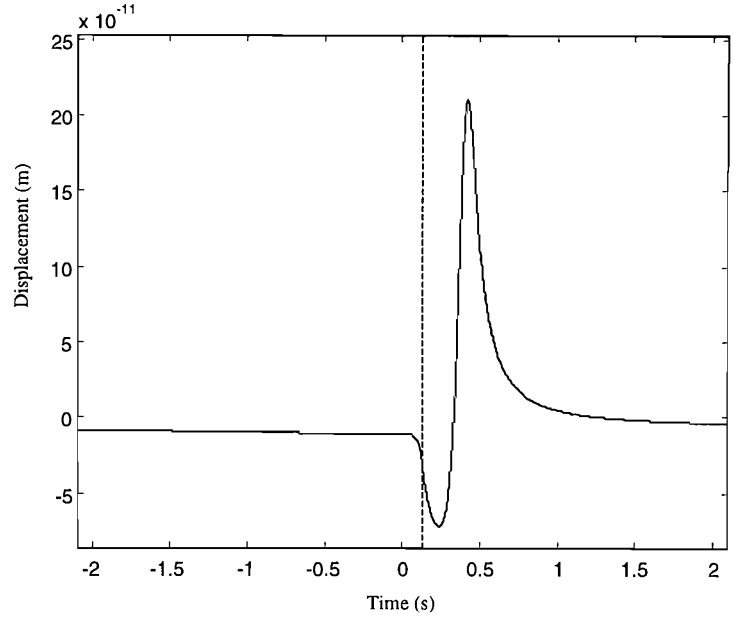

Figure A1.22. The vertical impulse response function of point (50 m, 0, 0) for loss factor equal to 0.4.

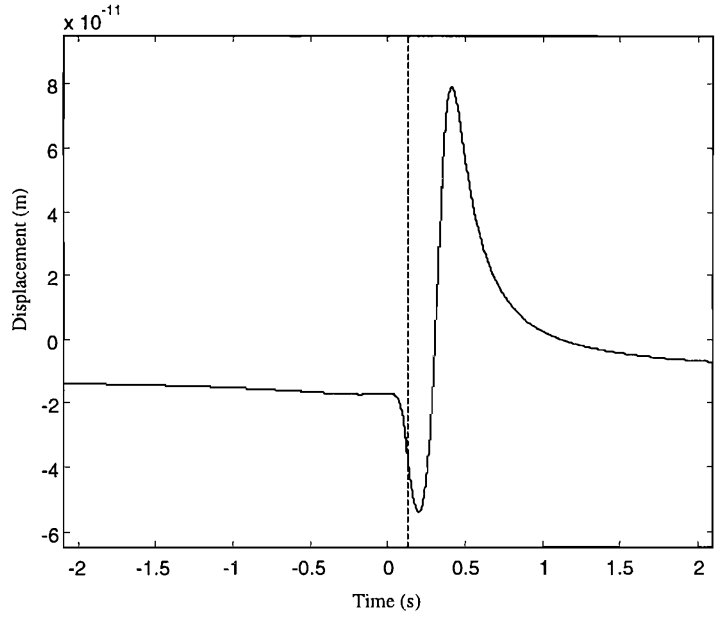

Figure A1.23. The vertical impulse response function of point (50 m, 0, 0) for loss factor equal to 0.8.

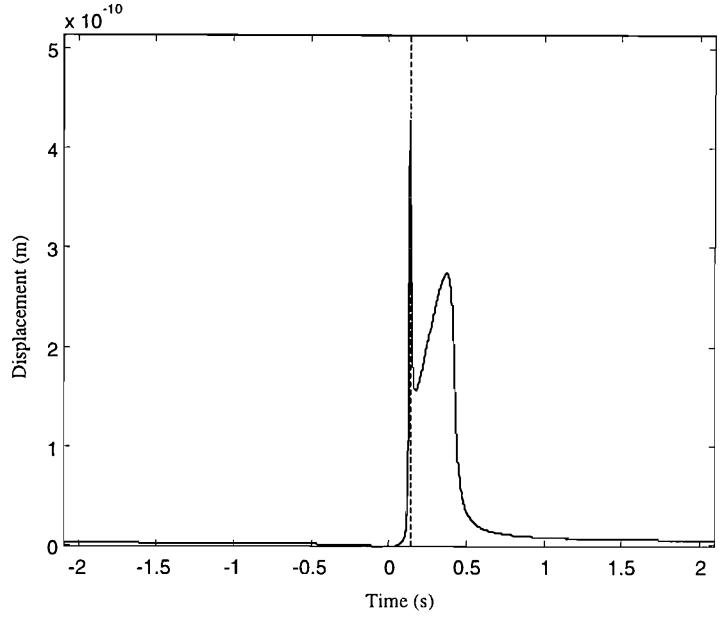

Figure A1.24. The vertical impulse response function of point (0 , 0, 50 m) for loss factor equal to 0.1.

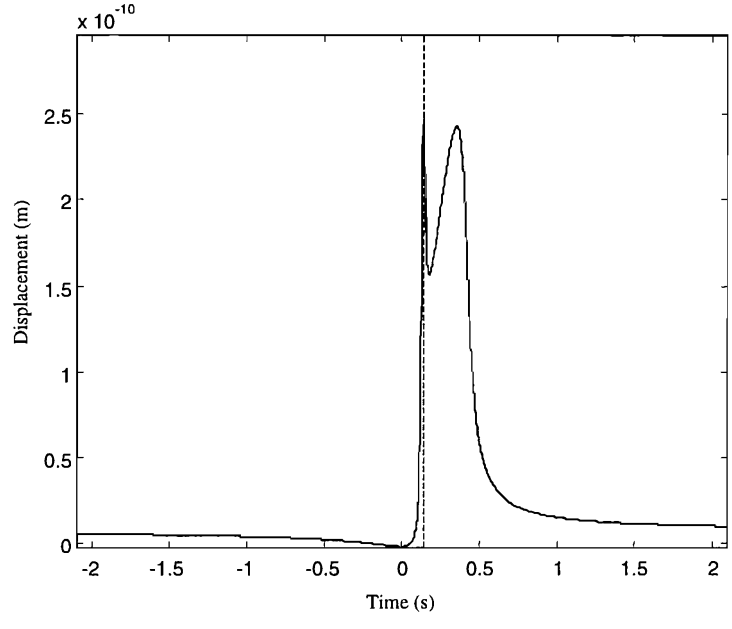

Figure A1.25. The vertical impulse response function of point (0 , 0, 50 m) for loss factor equal to 0.2.

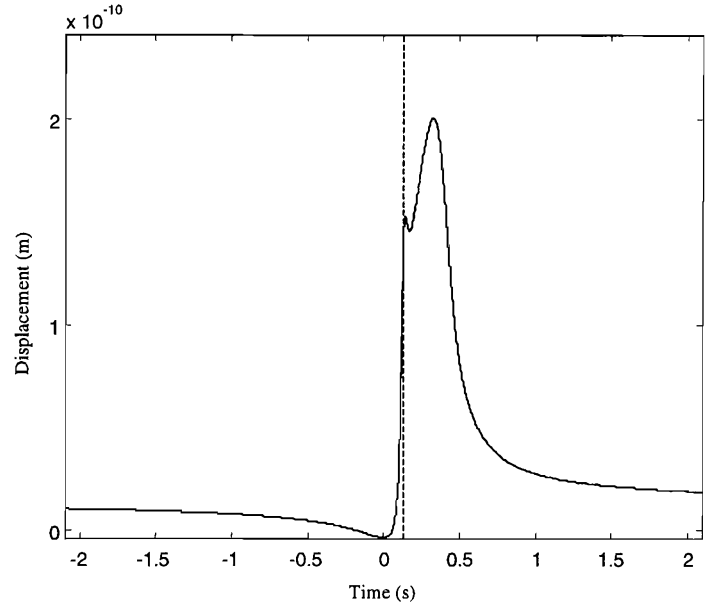

Figure A1.26. The vertical impulse response function of point (0 , 0, 50 m) for loss factor equal to 0.4.

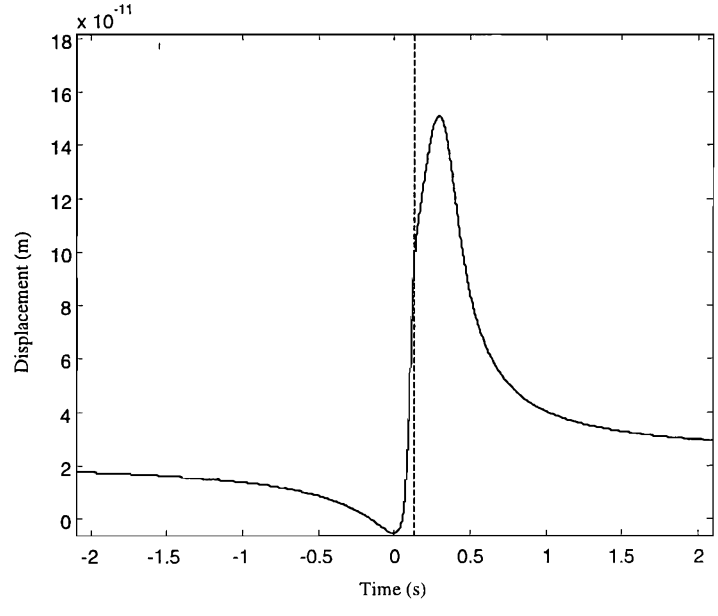

Figure A1.27. The vertical impulse response function of point (0 , 0, 50 m) for loss factor equal to 0.8.

A1.5 AN ELASTIC HALF-SPACE

Reference [Sheng, Jones and Petyt 1999(a)] has given the formula to calculate the steady state response of a ground (an elastic half-space) excited by a point harmonic load. Using this formula, the frequency response function of a point on the ground surface can be obtained. The inverse Fourier transform of this FRF gives the impulse response function of this point. Figures A1.28 to A1.31 show the vertical impulse response

function of a point 10 m away from the loading point due to a vertical impulse, for the loss factor of the soil equal to 0.1, 0.2, 0.4 and 0.8, respectively. Other material properties of the half-space are the same as those of the whole space employed in the last section, and the dilatational (P-), shear (S-) and Rayleigh (R-) wave speeds of the soil are, respectively, 360 m/s, 118 m/s and 112 m/s. Figures A1.28 to A1.31 show the response at 10 m on the surface of the half-space for different values of loss factor. The arrival times of the P-, S- and R-waves are 0.03 s, 0.08 s and 0.09 s. The vertical dashed line in these figures indicates the arrival time of the P-wave. For low loss factor, the arrival of the three waves is clearly identified and the response prior to the arrival of the P-wave is small.

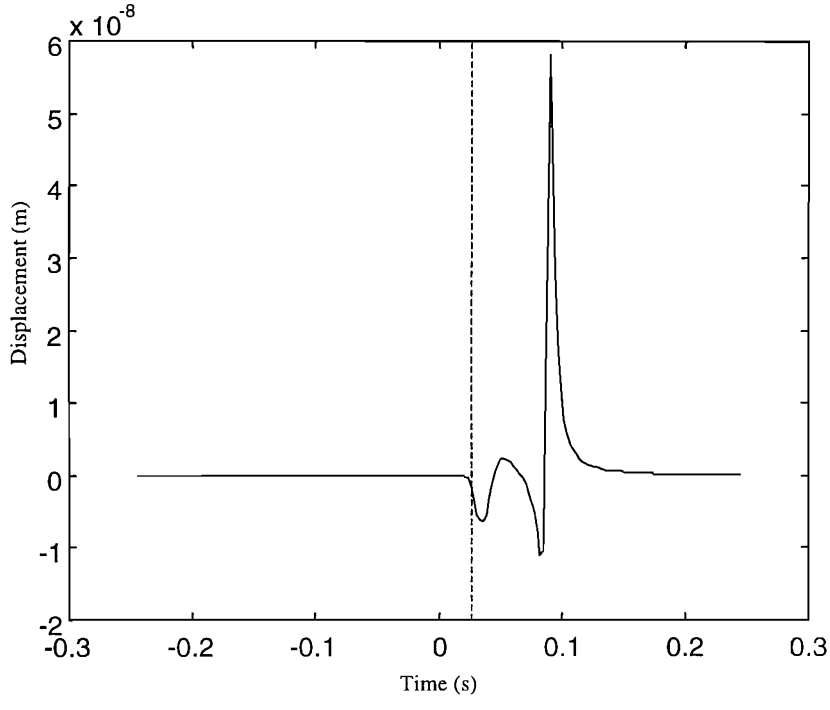

Figure A1.28. The vertical impulse response function of a point at 10 m on the ground surface for loss factor equal to 0.1. The arrival time of the P-, S- and R-waves would be 0.03 s, 0.08 s and 0.09 s if ignoring the damping in the half-space.

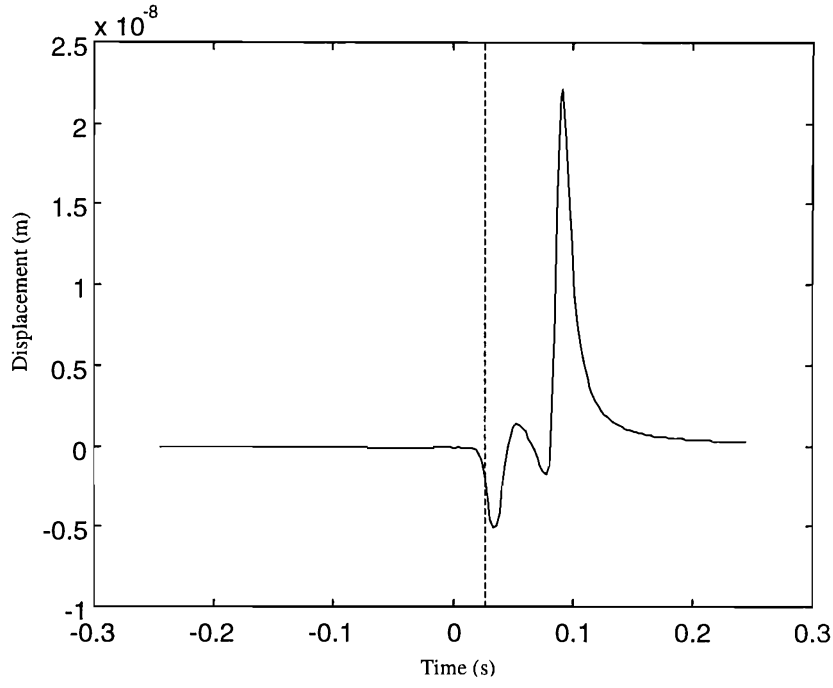

Figure A1.29. The vertical impulse response function of a point at 10 m on the ground surface for loss factor equal to 0.2.

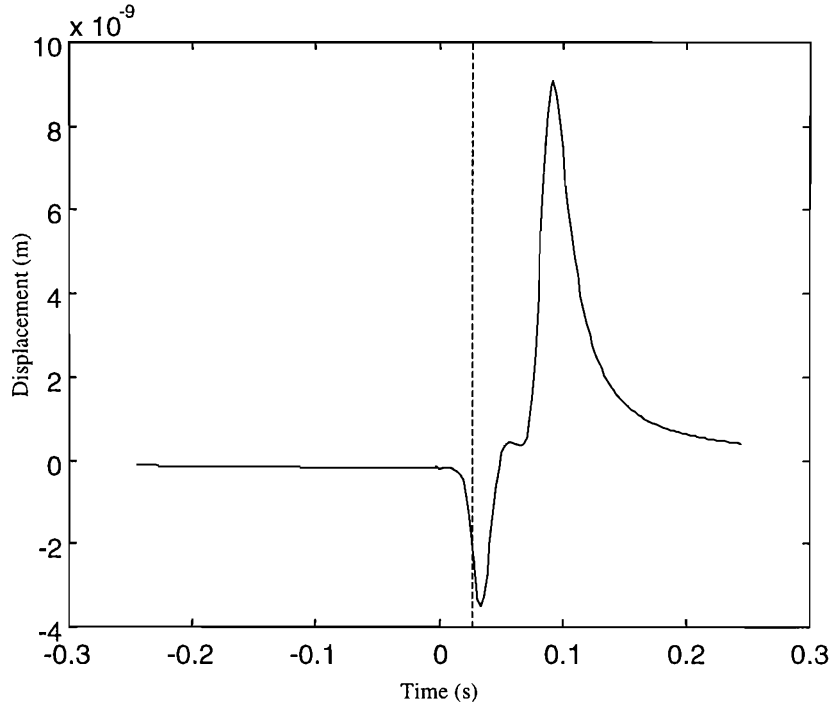

Figure A1.30. The vertical impulse response function of a point at 10 m on the ground surface for loss factor equal to 0.4.

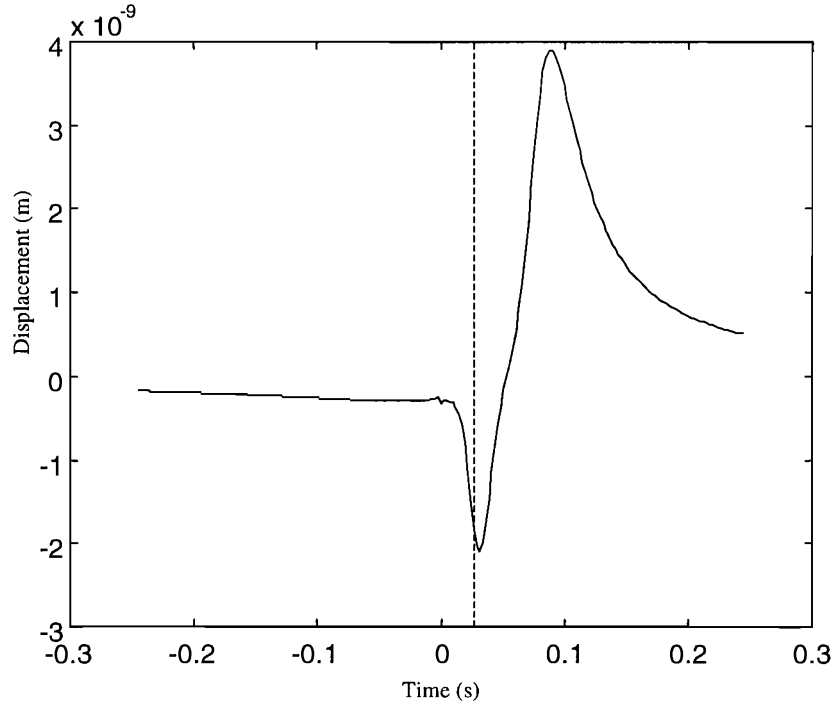

Figure A1.31. The vertical impulse response function of a point at 10 m on the ground surface for loss factor equal to 0.8.

A1.6 SUMMARY

The non-causality in the displacement responses, induced by the assumption of constant loss factors, is examined by calculating the impulse response function for four vibration systems: a one-degree-of-freedom system, a railway track on a Winkler foundation, an elastic medium occupying the entire space and an elastic half-space. It is shown that for low loss factor (e.g. less than 0.2), the pre-impulse response is small enough to be negligible. Further, if a system has a dominating component of a particular frequency, and if the loss factor in the constant hysteretic damping model is selected as the same as the actual loss factor at this frequency, the response of the model will be sufficiently close to that of the actual system. At most frequencies the model will have an incorrect damping but the effect on the dynamic response will not be significant if the damping is light. It is found that the non-causality is more serious in a continuous system where wave propagation is allowed than in a resonant system where only one frequency dominates the response. Nevertheless, the existence of the pre-impulse response does not mean that the post-impulse response is significantly in error. However, the accuracy of the post-impulse response resulting from the constant loss factor model may only be identified by measurement, rather than by mathematical models. On the other hand, an impulse is an idealised loading condition which contains every frequency and the

strength of each frequency component is the same. For a real load, its frequency range is limited. In that frequency range, if the actual loss factor of the material is nearly independent of frequency, then the constant loss factor model should give reasonable results.

Appendix 2

THEOREMS ON THE DIVERGENCE OF IMPROPER INTEGRALS

The following theorems on the divergence of an integral over an infinite interval have been applied in Sections 3.4 and 3.5, Chapter 3, to show the existence of resonance of a ground.

Theorem 1. Consider a double integral $I = \int_{-\infty}^{\infty}\int_{-\infty}^{\infty}(dxdy / D(x, y))$, where $D(x, y)$ is an analytical function and $(1/ D(x, y))$ is integrable to infinity. The integral I diverges if there exists only one real isolated root (x_0, y_0) of equation $D(x, y) = 0$ such that $\frac{\partial D}{\partial x} = \frac{\partial D}{\partial y} = 0$. (An isolated root (x_0, y_0) of equation $D(x, y) = 0$ means that within a small enough neighbourhood of (x_0, y_0) there is no root of $D(x, y) = 0$ except for (x_0, y_0)).

Proof. The integral can be represented as

$$I = \int_{-\infty}^{\infty}\int_{-\infty}^{\infty}(dxdy / D(x, y)) = \iint_{S}\frac{dxdy}{D(x, y)} + \iint_{S_0}\frac{dxdy}{D(x, y)}$$

where

$$S = \{(x, y):(x - x_0)^2 + (y - y_0)^2 > \rho_0^2\},\ S_0 = \{(x, y):(x - x_0)^2 + (y - y_0)^2 \le \rho_0^2\}$$

ρ_0 is a positive real number.

The integral $\iint_{S}\frac{dxdy}{D(x, y)}$ converges since the integrand has no singular points at which $\frac{\partial D}{\partial x} = \frac{\partial D}{\partial y} = 0$ (see below) in the area S and $1/D(x, y)$ is integrable to infinity. Therefore, convergence of I depends on the integral $\iint_{S_0}\frac{dxdy}{D(x, y)}$. In the classical sense this integral is equal to

$$\iint_{S_0} \frac{dxdy}{D(x,y)} = \lim_{\varepsilon \to 0} \iint_{\varepsilon^2 \le (x-x_0)^2+(y-y_0)^2 \le \rho_0^2} \frac{dxdy}{D(x,y)} \tag{A2.1}$$

As ρ_0 is an arbitrary constant, it can be considered as so small that $D(x, y)$ may be expanded as a Taylor series around the point (x_0, y_0):

$$D(x,y) = D(x_0,y_0) + \sum_{n=1}^{\infty} \frac{1}{n!} d^n D(x_0,y_0) \tag{A2.2}$$

where $d^n D(x_0, y_0)$ is the differential of $D(x, y)$ of order n at (x_0, y_0).

In accordance with the theorem conditions, $D(x_0, y_0) = dD(x_0, y_0) = 0$. Moreover, since (x_0, y_0) is the real isolated root of $D(x, y) = 0$, there exists an even integer $m\,(m \ge 2)$, such that $d^m D(x_0, y_0) \ne 0$ and $d^i D(x_0, y_0) = 0$ for $1 \le i < m$. Therefore, by introducing the polar system of co-ordinates, $x - x_0 = \rho\cos\varphi$, $y - y_0 = \rho\sin\varphi$, $D(x, y)$ can be rewritten as

$$D(\rho,\varphi) = \frac{1}{m!}\rho^m f(\varphi) + o(\rho^m) \tag{A2.3}$$

where $f(\varphi) \ne 0$, since (x_0, y_0) is the isolated zero. For φ varying from 0 to 2π, $f(\varphi)$ does not change its sign otherwise there would be a value of φ such that $f(\varphi) = 0$.

Substituting equation (A2.3) into equation (A2.1) and taking into account the Jacobian ρ, yields

$$\iint_{S_0} \frac{dxdy}{D(x,y)} = \lim_{\varepsilon \to 0} \int_{\varepsilon}^{\rho_0} \int_0^{2\pi} \frac{m!\rho}{f(\varphi)\rho^m} d\rho d\varphi \tag{A2.4}$$

The number $o(\rho^m)$ in equation (A2.3) is dropped, as ρ_0 is an arbitrarily small value. The integral with respect to φ in equation (A2.4) will result in a finite non-zero constant A since $f(\varphi) \ne 0$ and m is a finite number. Then

$$\iint_{S_0} \frac{dxdy}{D(x,y)} = \lim_{\varepsilon \to 0} A\int_{\varepsilon}^{\rho_0} \frac{d\rho}{\rho^{m-1}} = A\lim_{\varepsilon \to 0}\begin{cases} \ln\rho_0 - \ln\varepsilon, & (m=2) \\ \dfrac{1}{2-m}\left(\dfrac{1}{\rho_0^{m-2}} - \dfrac{1}{\varepsilon^{m-2}}\right), & (m>2) \end{cases} = \infty \tag{A2.5}$$

Thus, the integral I diverges.

If the isolated root (x_0, y_0) is not such that $\frac{\partial D}{\partial x} = \frac{\partial D}{\partial y} = 0$, then $m = 1$. From equation (A2.5), the integral $\iint_{S_0} \frac{dxdy}{D(x, y)}$ converges to a finite value $A\rho_0$.

Theorem 2. Consider a single integral $I = \int_0^\infty D_1(x)dx / D(x)$, where $D_1(x)$, $D(x)$ are real or complex functions and $(D_1(x)/ D(x))$ is integrable to infinity. The integral I diverges if there exists a real isolated root x_0 of equation $D(x) = 0$ such that

$$D_1(x_0) \neq 0, \frac{\partial D(x_0^-)}{\partial x} \neq \frac{\partial D(x_0^+)}{\partial x}$$

Proof. The integral can be represented as

$$I = \int_0^\infty \frac{D_1(x)dx}{D(x)} = \int_0^{x_0-\rho_0} \frac{D_1(x)dx}{D(x)} + \int_{x_0-\rho_0}^{x_0+\rho_0} \frac{D_1(x)dx}{D(x)} + \int_{x_0+\rho_0}^\infty \frac{D_1(x)dx}{D(x)}$$

where ρ_0 is a small positive number. The first and the third integrals converge since the integrands have no singular points and $D_1(x)/ D(x)$ is integrable to infinite. Therefore, convergence of I is determined by the second integral. In the classical sense, this integral is equal to

$$\int_{x_0-\rho_0}^{x_0+\rho_0} \frac{D_1(x)dx}{D(x)} = \lim_{\varepsilon \to 0} \left(\int_{x_0-\rho_0}^{x_0-\varepsilon} \frac{D_1(x)dx}{D(x)} + \int_{x_0+\varepsilon}^{x_0+\rho_0} \frac{D_1(x)dx}{D(x)} \right) \tag{A2.6}$$

where $\varepsilon < \rho_0$ is a small positive real number. Expanding $D(x)$ as a Taylor series around the point x_0 yields

$$D(x) = D(x_0) + \sum_{n=1}^\infty \frac{1}{n!} \frac{d^n D(x_0^-)}{dx^n} (x - x_0)^n \quad (x < x_0) \tag{A2.7}$$

$$D(x) = D(x_0) + \sum_{n=1}^\infty \frac{1}{n!} \frac{d^n D(x_0^+)}{dx^n} (x - x_0)^n \quad (x > x_0) \tag{A2.8}$$

In accordance with the theorem conditions, there exist constants $A \neq 0, B \neq 0$, and integers $m, n \geq 1$ such that $D(x)$ can be rewritten as

$$D(x) = A(x - x_0)^m + o((x - x_0)^m) \quad (x < x_0) \tag{A2.9}$$

$$D(x) = B(x-x_0)^n + o((x-x_0)^n) \qquad (x > x_0) \tag{A2.10}$$

where $A = \frac{1}{m!}\frac{d^m D(x_0^-)}{dx^m}, B = \frac{1}{n!}\frac{d^n D(x_0^+)}{dx^n}$, and $A \neq B$ if $m = n$.

Substituting equations (A2.9) and (A2.10) into equation (A2.6) and dropping the number $o((x-x_0)^m)$ in equation (A2.9) and $o((x-x_0)^n)$ in equation (A2.10) as ρ_0 is an arbitrarily small value, gives:

If $m = n = 1$,

$$\begin{aligned} I &= \int_{x_0-\rho_0}^{x_0+\rho_0} \frac{D_1(x)dx}{D(x)} = D_1(x_0)\lim_{\varepsilon\to 0}\left(\int_{x_0-\rho_0}^{x_0-\varepsilon} \frac{dx}{A(x-x_0)} + \int_{x_0+\varepsilon}^{x_0+\rho_0} \frac{dx}{B(x-x_0)}\right) \\ &= D_1(x_0)\{\lim_{\varepsilon\to 0}[\frac{1}{A}\ln(x_0-x)\Big|_{x_0-\rho_0}^{x_0-\varepsilon} + \frac{1}{B}\ln(x-x_0)\Big|_{x_0+\varepsilon}^{x_0+\rho_0}]\} \\ &= D_1(x_0)[(\frac{1}{B}-\frac{1}{A})\ln\rho_0 + \lim_{\varepsilon\to 0}(\frac{1}{A}-\frac{1}{B})\ln\varepsilon] \end{aligned}$$

thus, if $A \neq B, I \to \infty$.

If $m, n > 1$,

$$\begin{aligned} I &= \int_{x_0-\rho_0}^{x_0+\rho_0} \frac{D_1(x)dx}{D(x)} = D_1(x_0)\lim_{\varepsilon\to 0}\left(\int_{x_0-\rho_0}^{x_0-\varepsilon} \frac{dx}{A(x-x_0)^m} + \int_{x_0+\varepsilon}^{x_0+\rho_0} \frac{dx}{B(x-x_0)^n}\right) \\ &= D_1(x_0)\{\lim_{\varepsilon\to 0}[\frac{1}{A(1-m)}(x-x_0)^{1-m}\Big|_{x_0-\rho_0}^{x_0-\varepsilon} + \frac{1}{B(1-n)}(x-x_0)^{1-n}\Big|_{x_0+\varepsilon}^{x_0+\rho_0}]\} \\ &= D_1(x_0)[-\frac{1}{A(1-m)(-\rho_0)^{m-1}} + \frac{1}{B(1-n)\rho_0^{n-1}} + \lim_{\varepsilon\to 0}(\frac{1}{A(1-m)(-\varepsilon)^{m-1}} - \frac{1}{B(1-n)\varepsilon^{n-1}})] \end{aligned}$$

thus, if $m \neq n$, or $m = n$ but $A \neq B$, then $I \to \infty$.

If $m = 1, n > 1$,

$$I = D_1(x_0)[-\frac{1}{A}\ln\rho_0 + \frac{1}{B(1-n)\rho_0^{n-1}} + \lim_{\varepsilon\to 0}(\frac{1}{A}\ln\varepsilon + \frac{1}{B(n-1)\varepsilon^{n-1}})] = \infty$$

From the discussion above, when $m = n =$ an odd number, and $A = B \neq 0$, the integral I converges.

Appendix 3

SOME NOTES ON THE FAST FOURIER TRANSFORM

As has been shown in the preceding chapters, the Fourier transformed displacements of a track and a ground, denoted by $\tilde{w}(\beta)$ for the track and $\tilde{w}(\beta,\gamma)$ for the ground, can be obtained in the frequency-wavenumber domain analytically, where β,γ are wavenumbers in the x- and y-directions respectively. The actual displacements, denoted by $w(x)$ or $w(x, y)$, may then be obtained by performing inverse Fourier transforms on $\tilde{w}(\beta)$ or on $\tilde{w}(\beta,\gamma)$, i.e.,

$$w(x)=\frac{1}{2\pi}\int_{-\infty}^{\infty}\tilde{w}(\beta)e^{i\beta x}d\beta \tag{A3.1}$$

or,

$$w(x,y)=\frac{1}{4\pi^2}\int_{-\infty}^{\infty}\int_{-\infty}^{\infty}\tilde{w}(\beta,\gamma)e^{i(\beta x+\gamma y)}d\beta d\gamma \tag{A3.2}$$

To evaluate the integrals (A3.1) and (A3.2) the FFT technique is used. To do this, the function $\tilde{w}(\beta,\gamma)$ is first sampled at the following points

$$\beta_k=(k-N)\Delta\beta-\frac{\Delta\beta}{2},\gamma_l=(l-N)\Delta\gamma-\frac{\Delta\gamma}{2} \tag{A3.3}$$

where, $k,l=1,2,\cdots,2N$, and $2N$ is an integer equal to an integer power of 2. $\Delta\beta,\Delta\gamma$ are the intervals of β and γ. Then equations (A3.1) and (A3.2) are approximated by

$$w(x)=\frac{1}{2\pi}\sum_{k=1}^{2N}\tilde{w}(\beta_k)e^{i\beta_k x}\Delta\beta \tag{A3.4}$$

$$w(x,y)=\frac{1}{4\pi^2}\sum_{k=1}^{2N}\sum_{l=1}^{2N}\tilde{w}(\beta_k,\gamma_l)e^{i\beta_k x+i\gamma_l y}\Delta\beta\Delta\gamma \tag{A3.5}$$

Let

$$x_m=(m-N)\Delta x,y_n=(n-N)\Delta y,(m,n=1,2,\cdots,2N) \tag{A3.6}$$

where,

$$\Delta x = \frac{2\pi}{2N\Delta\beta},\ \Delta y = \frac{2\pi}{2N\Delta\gamma} \tag{A3.7}$$

then equations (A3.4) and (A3.5) become

$$w(x_m) = \frac{\Delta\beta}{2\pi} e^{-i(N-1/2)(m-N)\pi/N} \sum_{k=1}^{2N} \tilde{w}(\beta_k) e^{i(k-1)(m-N)\pi/N} \tag{A3.8}$$

$$w(x_m, y_n) = \frac{\Delta\beta\Delta\gamma}{4\pi^2} e^{-i(N-1/2)(m+n-2N)\pi/N} \sum_{k=1}^{2N}\sum_{l=1}^{2N} \tilde{w}(\beta_k, \gamma_l) e^{i(k-1)(m-N)\pi/N + i(l-1)(n-N)\pi/N} \tag{A3.9}$$

The so-called FFT algorithm is an efficient technique to calculate

$$\sum_{k=1}^{2N} \tilde{w}(\beta_k) e^{i(k-1)(m-N)\pi/N} \quad \text{and} \quad \sum_{k=1}^{2N}\sum_{l=1}^{2N} \tilde{w}(\beta_k, \gamma_l) e^{i(k-1)(m-N)\pi/N + i(l-1)(n-N)\pi/N}$$

for $m, n = 1,2,\cdots,2N$. A variety of standard subroutines may be found to carry out the calculations. A subroutine has been designed to calculate equations (A3.8) and (A3.9) (notes: not including the factor $\frac{\Delta\beta}{2\pi}$ in equation (A3.8) and $\frac{\Delta\beta\Delta\gamma}{4\pi^2}$ in equation (A3.9)) based on an FFT algorithm presented in reference [Press et al 1992]. This subroutine, called *fftn*(*data, nn, ndim, isign*), requires as input: (i) a scalar, *ndim*, giving the number of dimensions, e.g., 2; (ii) a vector, *nn*, giving the length of the array in each dimension, e.g., (32, 64). Note that these lengths must all be powers of 2 and are the numbers of complex values in each direction; (iii) a scalar, *isign*, equal to ± 1 indicating whether the Fourier transform or its inverse is specified; and finally (iv) the array of data, *data*. The program accesses the data array as a one-dimensional array of real numbers, of length equal to twice the product of the lengths of all dimensions. Each complex value occupies two sequential locations, real part followed by imaginary. Thus, for $2N \times 2N$ complex values of $\tilde{w}(\beta_k, \gamma_l)$, where, $k, l = 1,2,\cdots,2N$, the array *data* contains:

$$data(1) = \mathrm{Re}(\tilde{w}_{11}), data(2) = \mathrm{Im}(\tilde{w}_{11}), data(3) = \mathrm{Re}(\tilde{w}_{12}), data(4) = \mathrm{Im}(\tilde{w}_{12}), \cdots,$$
$$data(4N-1) = \mathrm{Re}(\tilde{w}_{1,2N}), data(4N) = \mathrm{Im}(\tilde{w}_{1,2N})$$
$$data(4N+1) = \mathrm{Re}(\tilde{w}_{21}), data(4N+2) = \mathrm{Im}(\tilde{w}_{21}), \cdots, data(8N) = \mathrm{Im}(\tilde{w}_{2,2N}), \cdots,$$
$$data(8N^2-1) = \mathrm{Re}(\tilde{w}_{2N,2N}), data(8N^2) = \mathrm{Im}(\tilde{w}_{2N,2N})$$

where $\tilde{w}_{kl} = \tilde{w}(\beta_k, \gamma_l)$

When the subroutine is executed, the data in the array *data* are replaced by the outputs in this way:

$$data(1) = \mathrm{Re}(w_{11}), data(2) = \mathrm{Im}(w_{11}), data(3) = \mathrm{Re}(w_{12}), data(4) = \mathrm{Im}(w_{12}), \cdots,$$
$$data(4N-1) = \mathrm{Re}(w_{1,2N}), data(4N) = \mathrm{Im}(w_{1,2N})$$
$$data(4N+1) = \mathrm{Re}(w_{21}), data(4N+2) = \mathrm{Im}(w_{21}), \cdots, data(8N) = \mathrm{Im}(w_{2,2N}), \cdots,$$
$$data(8N^2-1) = \mathrm{Re}(w_{2N,2N}), data(8N^2) = \mathrm{Im}(w_{2N,2N})$$

where $w_{mn} = w(x_m, y_n)$.

It can be seen from equation (A3.3) that the sample points on, e.g., the β-axis, are symmetric about the origin.

REFERENCES

Adolfsson, K., Andreasson, B., Bengtsson, P. E. and Zackrisson, P. 1999 *Proc. 12th Eur. Conf. Soil Mech. and Geotechn. Eng.*, **3**, 1713-1718. High speed train X2000 on soft organic clay--measurements in Sweden.

Ahmad, S. and Al-Hussaini, T. M. 1991 *Journal of Geotechnical Engineering* **117** (1), 67-88. Simplified design for vibration screening by open and in-filled trenches.

Aki, K. and Richards, P. G. 1980 *Quantitative Seismology Theory and Methods, Volume 1 & 2*, W. H. Freeman and Company, San Francisco.

Alabi, B. 1992 *Journal of Sound and Vibration* **153**(1), 77-87. A parametric study on some aspects of ground borne vibrations due to rail traffic.

Apsel, R. and Luco, J. 1983 *Bulletin of the Seismological Society of America* **73**, 931-951. Part II, On the Green's functions for a layered half-space.

Aubry, D., Clouteau, D. and Bonnet, G. 1994 *Wave Propagation and Reduction of Vibrations*, Chouw and Schmid editors, Berg-Verlag, Bochum, 109-121. Modelling of wave propagation due to fixed or mobile dynamic sources.

Auersch, L. 1994 *Journal of Sound and Vibration* **173**(2), 233-264. Wave propagation in layered soils: Theoretical solution in wave number domain and experimental results of hammer and railway traffic excitation.

Balendra, T., Chua, K. H., Lo, K. W. and Lee, S. L. 1989 *Journal of Engineering Mechanics, ASCE*, **115**(1), 145-162. Steady-state vibration of subway-soil-building system.

Balendra, T., Koh, C. G. and Ho, Y. C. 1991 *Earthquake Engineering and Structural Dynamics* **20**, 275-291. Dynamic response of buildings due to trains in underground tunnels.

BANVERKET BVPO 724.001 *Buller Och Vibrationer Från Spårburen Linjetrafik.*

BANVERKET Report 1998 *High-Speed Line on Soft Ground* (in Swedish).

BANVERKET Seminar on High-Speed Line on Soft Ground, Dynamic Soil-Track Interaction and Ground Vibration, 16-17 March, 2000, Gothenburg.

Belotserkovskiy, P. M. 1996 *Journal of Sound and Vibration* **193**(1), 705-712. On the oscillations of infinite periodic beams subjected to a moving concentrated force.

Bencat, J. 1999 *Structural Dynamics-EURODYN'99*, Balkema, Rotterdam, 969-972. Assessment of ground vibration from passing train.

Bert, C. W. 1973 *Journal of Sound and Vibration* **29**(2), 129-153. Material damping: an introductory review of mathematical model, measured and experimental techniques.

Caviglia, G. and Morror, A. 1999 *Journal of the Acoustical Society of America* **106**(4), 1666-1672. A new approach to reflection-transmission between viscoelastic half-space.

Chouw and Schmid editors 2000 *Proceedings of Wave 2000.* Balkema, Rotterdam.

Chua, K. H., Balendra, T. and Lo, K. W. 1992 *Earthquake Engineering and Structural Dynamics* **21**, 445-460. Groundborne vibrations due to trains in tunnels.

Crandall, S. H. 1970 *Journal of Sound and Vibration* **11**(1), 3-18. The role of damping in vibration theory.

De Barros, F. C. P. and Luco, J. E. 1995 *Applied Mathematics and Computation* **67**, 103-134. Stress and displacement in a layered half-space for a moving point load.

De Barros, F. C. P. and Luo, J. E. 1994 *Wave Motion* **19**, 189-210. Response of a layered viscoelastic half-space to a moving point load.

Degrande, G. and Lombaert, G. 2000 *Proceedings of the International Workshop Wave* 2000, 29-42. High-speed train induced free field vibrations: in situ measurements and numerical modelling.

Degrande, G. and Schillemans, L. 1998 *Proc. ISMA 23*, **3**, 1563-1570. Free field vibrations during the passage of HST.

Dieterman, H. A. and Metrikine, A. V. 1997 (a) *European Journal of Mechanics A-solids* **16**(2), 295-306. Steady state displacements of a beam on an elastic half-space due to a uniformly moving constant load.

Dieterman, H. A. and Metrikine, A. V. 1997 (b) *Journal of applied mechanics* **64**, 596-600. Critical velocities of a harmonic load moving uniformly along an elastic layer.

Dieterman, H. A. and Metrikine, A. V. 1997 (c) *European Journal of Mechanics A-solids* **16**(3), 515-527. The equivalent vertical stiffness of an elastic half-space interacting with a beam, including the shear stresses at the beam-halfspace interface.

Dieterman, H. A. and Metrikine, A. V. 1996 *European Journal of Mechanics A-solids* **15**(1), 67-90. Equivalent vertical stiffness of an elastic half-space interacting with a beam, Critical velocities of a moving load along the beam.

Dieterman, H. A. 1999 *Wave Motion* **29**(2), 119-135. The travelling point load revisited.

Dings, P. C. and Dittrich, M. G. 1996 *Journal of Sound and Vibration* **193**(1), 103-112. Roughness on Dutch railway wheels and rails.

Dominguez, J. 1993 *Boundary Elements in Dynamics*. Elsevier Applied Science.

Dowing, C. H. 2000 *Proceedings of the International Workshop Wave* 2000, 269-288. Effects of ground motions from high-speed trains on structures, instruments and humans.

Eason, G., Fulton, J. and Sneddon, I. N. 1955/1956 *Phil. Trans. Roy. Soc. London* **248** (A955), 575-607. The generation of waves in an infinite elastic solid by variable body forces.

Esveld, C. 1989 *Modern Railway Track*. MRT-Productions.

Fenander, Å 1997 *Proceeding of Institute of Mechanical Engineers* **211** Part F, 51-62. Frequency dependent stiffness and damping of railpads.

Forchap, E. A. and Schmid, G. 1999 *Structural Dynamics-EURODYN'99*, Balkema, Rotterdam, 983-988. Determination of sub-soil properties using a frequency-wavenumber analysis of Rayleigh surface waves.

Ford, R. A. J. 1987 *Journal of Sound and Vibration* **116**(3), 585-589. The prediction of ground vibration by railway trains.

Forrest, J. A. and Hunt, H. E. M. 2000 *Proceedings of the Sixth International Congress on Sound and Vibration*, 1483-1490. Ground vibration due to trains in underground railway tunnels.

Forrest, J. A. 1999 *PhD Dissertation in Cambridge University*. Modelling of ground vibration from underground railways.

Fu, C. Y. 1950 *Journal of the Chinese Geophysical Society* **2**(1), 40-59. Some problems of the propagation of elastic waves in a horizontally stratified medium.

Fujikake, J. 1989 *Journal of Sound and Vibration* **128**(3), 524-527. A prediction method for the propagation of ground vibration from railway trains on level track with welded rails.

Fujikake, T. 1996 *Inter-Noise'96*, Liverpool, 1677-1680. Estimation of exposure of dwellers to train induced ground vibration.

Fujikake, T. 1986 *Journal of Sound and Vibration* **111**(2), 375-360. A prediction method for the propagation of ground vibration from railway trains.

Fujikake, T. 1988 *Journal of Sound and Vibration* **121**(1), 182-184. A phase characteristic of ground vibration model for vibration prediction of ground.

Gavrilov, S. 1999 *Journal of sound and vibration* **222** (3), 345-361. Non-stationary problems in dynamics of a string on elastic foundation subjected to a moving load.

Grassie, S. L. and Kalousek, J. 1993 *Proceedings of Institute of Mechanical Engineers, Part F, Journal of Rail and Rapid Transit* **207**, 57-68. Rail corrugation: characteristics, causes and treatments.

Grassie, S. L., Gregory, R. W., Harrison, D. and Johnson, K. L. 1982 *Journal of Mechanical Engineering Science* **24** (2) , 77-90. The dynamic response of railway track to high frequency vertical excitation.

Grassie, S. L., Gregory, R. W. and Johnson, K. L. 1982 *Journal of Mechanical Engineering Science* **24** (2) , 91-95. The dynamic response of railway track to high frequency lateral excitation.

Grassie, S. L., Gregory, R. W. and Johnson, K. L. 1982 *Journal of Mechanical Engineering Science* **24** (2) , 96-102. The dynamic response of railway track to high frequency longitudinal excitation.

Grassie, S. L., Gregory, R. W. and Johnson, K. L. 1982 *Journal of Mechanical Engineering Science* **24** (2) , 103-111. The behaviour of railway wheelsets and track at high frequency of excitation.

Grootenhuis, P. 1977 *Journal of Sound and Vibration* **51**(3), 443-448. Floating track slab isolation for railway.

Grundmann, H., Lieb, M. and Trommer, E. 1999 *Archive of Applied Mechanics* **69**(1), 55-67. The response of a layered half-space to traffic loads moving along its surface.

Grundmann, H. 1999 *EURODYN'99*, 31-41. The Dynamic interaction of structures with subsoil.

Gry, L. 1996 *Journal of Sound and Vibration* **195**(3), 477-505. Dynamic modelling of railway track based on wave propagation.

Gry, L. and Gontier, C. 1997 *Journal of Sound and Vibration* **199**(4), 531-558. Dynamic modelling of railway track: a periodic model based on generalised beam formulation.

Hall, L. 1997 *International Conference on Soil Mechanics & Foundation Engineering*, Hamburg. Frequency characteristic in railway traffic induced ground vibration.

Hao, H. and Ang, T. C. 1998 *Journal of Engineering Mechanics, ASCE*, **124**(8), 921-928. Analytical modelling of traffic-induced ground vibrations.

Haskell, N., 1953 *Bulletin of the Seismological Society of America* **73**, 17-43. The dispersion of surface waves on multilayered medium.

Heelis, M. E., Collop, A. C., Dawson, A. R., Chapman, D. N. and Krylov, V. V. 1999 *Proc. 12th Eur. Conf. Soil Mech. and Geotechn. Eng.*, **3**, 1809-1814. Transient effects of high-speed trains crossing soft soil.

Hunt, H. E. M. 1996 *Journal of Sound and Vibration* **193** (1), 185-194. Modelling of rail vehicle and track for calculation of ground vibration transmission into buildings.

ISO 2631-1: 1997. Mechanical vibration and shock—Evaluation of human exposure to whole-body vibration.

Jenkins, H. H., Stephenson, J. E., Clayton, G. A., Morland, G. W. and Lyon, D. 1974 *Railway Engineering Journal* **3**(1), 2-16. The effect of track and vehicle parameters on wheel/rail vertical dynamic forces.

Jones, C. J. C. 1994 *Proceedings of the Institute of Civil Engineers, Transportation* **105**, 43-51. Use of numerical models to determine the effectiveness of anti-vibration systems in railway.

Jones, C. J. C. 1996 *Better journey time--better business--selected papers presented at "S-tech'96", IMechE, London*, 87-97. Reduction of noise and vibration from freight trains.

Jones, C. J. C. and Block, J. R. 1996 *Journal of Sound and Vibration* **193** (1), 205-213. Prediction of ground vibration from fright trains.

Jones, C. J. C., Sheng, X. and Petyt, M. 2000 *Journal of Sound and Vibration* **231**(3), 739-751. Simulations of ground vibration from a moving harmonic load on a railway track.

Jones, C. J. C., Thompson, D. J. and Petyt, M. 1999 *ISVR Technical Memorandum No. 844, University of Southampton.* Ground-borne vibration and noise from trains: Elastodynamic analysis using the combined boundary element and finite element methods.

Jones, C. J. C., Thompson, D. J. and Petyt, M. 2000 *Proceedings of Seventh International Congress on Sound and Vibration*, Garmisch-Partenkirchen, Germany, 2703-2710. Studies using combined finite element and boundary element model for vibration propagation from railway tunnels.

Jones, C. J. C., Wang, A. and Dawn, T. M. 1995 *Computational Acoustics and its Environmental Applications, Computational Mechanics Publications, Southampton*, 285-292. Modelling the propagation of vibration from railway tunnels.

Jones, D. V. 1987 *PhD Dissertation in the University of Southampton.* The surface propagation of ground vibration.

Jones, D. V. and Petyt, M. 1991 *Journal of Sound and Vibration* **147**(1), 155-166. Ground vibration in the vicinity of a strip load: a two-dimensional half-space model.

Jones, D. V. and Petyt, M. 1993 (a) *Journal of Sound and Vibration* **161**(1), 1-18. Ground vibration in the vicinity of a strip load: an elastic layer on half-space.

Jones, D. V. and Petyt, M. 1993 (b) *Journal of Sound and Vibration* **166**(1), 141-159. Ground vibration in the vicinity of a rectangular load on a half-space.

Jones, D. V. and Petyt, M. 1997 *Journal of Sound and Vibration* **203**(2), 307-319. Ground vibration in the vicinity of a rectangular load acting on a viscoelastic layer over a rigid foundation.

Jones, D. V. and Petyt, M. 1998 *Journal of Sound and Vibration* **212**(1), 61-74. Ground vibration due to a rectangular harmonic load.

Jones, D. V., Le Houedec, D. and Petyt, M. 1998 *European Journal of Mechanics A-Solids* **17**, 153-166. Ground vibration in the vicinity of a moving harmonic rectangular load on a half-space.

Jonsson, J. 2000 *Journal of Sound and Vibration* **236**(2), 359-366. Comments to 'Ground vibration generated by a load moving along a railway track'.

Kausel, E. 1974 *Research Report R74-11, Dept. Civ. Engrg., Massachusetts Inst. of Tech., Cambridge, Mass.* Forced vibration of circular foundation on layered media.

Kausel, E. and Peek, R. 1982 *Bulletin of the Seismological Society of America* **72**(5), 1469-1481. Dynamic loads in the interior of a layered stratum: an explicit solution.

Kausel, E. and Roesset, J. 1981 *Bulletin of the Seismological Society of America* **71**(6), 1743-1761. Stiffness matrices for layered soils.

Kausel, E. 1986 *International Journal for Numerical Method in Engineering* **23**, 1567-1578. Wave propagation in anisotropic layered media.

Kenney, J. T. et el 1954 *Journal of Applied Mechanics* (Dec. 1954), 359-364. Steady-state vibration of beam on elastic foundation for moving load.

Kim, D. S. and Lee, J. S. 2000 *Soil Dynamics and Earthquake Engineering Engineering* **19**(2), 115-126. Propagation and attenuation characteristics of various ground vibrations.

Knothe, K. and Grassie, S. L. 1993 *Vehicle System Dynamics* **22**, 209-262. Modelling of railway track and vehicle/track interaction at high frequencies.

Knothe, K. and Grassie, S. L. 1999 *Journal of Sound and Vibration* **227**(5), 859-897. Workshop on rail corrugations and out-of round wheels.

Knothe, K. and Wu, Y. 1999 *Structural Dynamics-EURODYN'99*, Balkema, Rotterdam, 849-853. Vertical substructural dynamics of vehicle-track-subgrade model.

Knothe, K., Strzyzakowski, Z. and Willner, K. 1994 *Journal of Sound and Vibration* **169**(1), 111-123. Railway vibration in the high-frequency range.

Kononov, A. V. and Dieterman, H. A. 1998 *Journal of Sound and Vibration* **214** (4), 725-746. The elastic field generated by two loads moving along two strings on an elastically supported membrane.

Kononov, A.V. and Dieterman, H. A. 1999 *European Journal of Mechanics A-Solids* **18**(4), 731-743. A uniformly moving constant along a Winkler supported strip.

Krenk, S. and Kellezi, L. 1999 *Structural Dynamics-EURODYN'99*, Balkema, Rotterdam, 447-452. Finite element and transmitting boundary conditions for moving loads.

Krylov, V. V., Dawson, A. R., Heelis, M. E. and Collop, A. C. 2000 *Proceedings of the Institute of Mechanical Engineers, Part F-Journal of Rail and Rapid Transit* **214**(2), 107-116. Rail movement and ground waves caused by high-speed trains approaching track-soil critical velocities

Krylov, V. V. 1999 *Journal of Low frequency Noise, Vibration and Active Control* **18**(4), 207-218. Ground vibration boom from high-speed trains.

Krylov, V. V. 1998 *Acustica-acta acustica* **84**(1), 78-90. Effect of track properties on ground vibrations generated by high-speed trains.

Krylov, V. V. 1997 *Journal of Low Frequency Noise and Vibration* **16**(4), 257-270. Spectra of low-frequency ground vibrations generated by high-speed trains on layered ground.

Krylov, V. V. 1996 *Journal of the Acoustical Society of America* **100**(5), 3121-3134. Vibrational impact of high-speed trains. I. Effect of the track dynamics.

Krylov, V. V. 1995 *Applied Acoustics* **44**, 149-164. Generation of ground vibrations by superfast trains.

Krylov, V. V. 1994 *Applied Acoustics* **42**, 199-213. Calculation of low frequency vibrations from railway trains.

Kurzwell, L. G. 1979 *Journal of Sound and Vibration* **66**(3), 363-370. Ground-borne noise and vibration from underground rail systems.

Lee, G. S. and Ma, C. C. 2000(a) *Proceedings of the Royal Society of London, Series A* **456**(1998), 1355-1374. Transient elastic waves propagating in a multi-layered medium subjected to in-plane dynamic loadings. I. Theory.

Lee, G. S. and Ma, C. C. 2000(b) *Proceedings of the Royal Society of London, Series A* **456**(1998), 1375-1396. Transient elastic waves propagating in a multi-layered medium subjected to in-plane dynamic loadings. II. Numerical calculation and experimental measurement.

Lefeuve-Mesgouez, G., Le Houédec, D. and Peplow, A. T. 2000 *Journal of Sound and Vibration* **231**(5), 1289-1309. Ground vibration in the vicinity of a high-speed moving harmonic strip load.

Luco, J. and Apsel, R. 1983 *Bulletin of the Seismological Society of America* **4**, 909-929. Part I, On the Green's functions for a layered half-space.

Luco, J. E., de Barros, F. C. P. 1993 *Soil Dynamics and Earthquake Engineering* **12**, 565-580. On the three-dimensional seismic response of a class of cylindrical inclusions embedded in layered media.

Lysmer, J. and Waas, G. 1972 *Journal of the Engineering Mechanics Division, Proceedings of the ASCE* **98** (EM1), 85-105. Shear waves in plane infinite structure.

Madshus, C. 1995 *15th International Congress on Acoustics*, 195-198. Prediction model for railway induced low frequency vibrations on soft ground.

Madshus, C. and Kaynia, A. 1998(a) *NGI Report 515177-1.* High speed railway lines on soft ground: dynamic response of rail-embankment-soil system.

Madshus, C. and Kaynia, A. 2000 *Journal of Sound and Vibration* 231(3), 689-701. High speed railway lines on soft ground: dynamic behaviour at critical train speed.

Madshus, C., Bessason, B. and Harvik, L. 1996 *Journal of Sound and Vibration* **193**(1), 195-203. Prediction model for low frequency vibration from high speed railways on soft ground.

Man, A. P and Kok, A. W. M. 2000 *Proceedings of the International Workshop Wave* 2000, 209-218. Recording, estimating and managing the dynamic behaviour of railway tracks.

Mathews, P. M., 1958 *ZAMM* **38** (3/4), 105-115. Vibration of a beam on elastic foundation.

Mathews, P. M., 1959 *ZAMM* **39** (1/2), 13-19. Vibration of a beam on elastic foundation.

Mead, D. J., 1986 *Journal of Sound and Vibration* **104**(1), 9-27. A new method of analysing wave propagation in periodic structures; application to periodic Timoshenko beams and stiffened plates.

Mead, D. J. 1996 *Journal of Sound and Vibration* **190**(3), 495-524. Wave propagation in continuous periodic structures: Research contributions from Southampton.

Mead, D. J. and Yaman, Y. 1991 *Journal of Sound and Vibration* **144**(3), 507-530. The response of infinite periodic beams to point harmonic forces: a flexural wave analysis.

Melke, J. 1988 *Journal of Sound and Vibration* **120**(2), 391-406. Noise and vibration from underground railway lines: Proposals for a prediction procedure.

Metrikine, A. V. and Dieterman, H. A. 1999 *European Journal of Mechanics A-Solids* **18**(1), 147-158. Lateral vibration of an axially compressed beam on an elastic half-space due to a moving lateral load.

Metrikine, A. V. and Popp, K. 1999 *European Journal of Mechanics A-Solids* **18**(4), 679-701. Vibration of a periodically supported beam on an elastic half-space.

Metrikine, A. V. and Vrouwenvelder, A. C. W. M. 2000 *Journal of Sound and Vibration* **234**(1), Surface ground vibration due to a moving train in a tunnel: Two-dimensional model.

Mohammadi, M. and Karabalis, D. L. 1995 *Earthquake Engineering and Structural Dynamics* **24**, 1177-1193. Dynamics 3-D soil-railway interaction by BEM-FEM.

Nawawi Chouw et al 1999 *Structural Dynamics-EURODYN'99*, Balkema, Rotterdam, 977-982. Numerical and experimental investigation on wave impediment in soil.

Newland, D. E. and Hunt, H. E. M. 1991 *Proc. Instn. Mech. Engrs.* **205**, 39-52. Isolation of buildings from ground vibration.

Newlands, M. 1952 *Phil. Trans. A.* **245**, 896. The disturbance due to a line source in a semi-infinite elastic medium with a single surface layer.

Nielsen, J. C. O. and Abrahamsson, T. J. S. 1992 *International Journal for Numerical Methods in Engineering* **33**, 1843-1859. Coupling of physical and modal components for analysis of moving non-linear dynamic systems on general structures.

ORE C116, 1971 *C116/RP1*. Power spectral density of track irregularities. Part 1: definitions, conventions and available data.

Peplow, A. T., Jones, C. J. C. and Petyt, M. 1999. *Applied Acoustics*. **56**(4), 283-296. Surface vibration propagation over a layered elastic half-space with an inclusion.

Petyt, M. and Jones, C. J. C. 1999 1999 *Structural Dynamics-EURODYN'99*, Balkema, Rotterdam, 79-87. Modelling of ground-borne vibration from railway.

Prange, B. 1978 *Dynamic Methods in Soil and Rock Mechanics*, 61-78.

Qiu, W. Y. and Wong, R. 2000 *Prceedings of the Royal Society of Lodon, Series A* **456**(1994), 407-431. Uniform asymptotic expansion of a double integral: coalescence of two stationary points.

Qu Weide 1992 *A Handbook on Mechanical Vibrations*, Mechanical Industry Press of China, Beijing. (In Chinese)

Shamsher Prakash 1981 *Soil Dynamics*, McGraw-Hill Book Company.

Sharif, A. K. 1997 *Civil Engineering Dynamics Ltd, Technical Report for RENVIB II, PHASE 1-State of the Art Review*: Empirical Prediction Methods.

Sheng, X., Jones, C. J. C. and Petyt, M. 1999 (a) *Journal of Sound and Vibration* **225**(1), 3-28. Ground vibration generated by a harmonic load acting on a railway track.

Sheng, X., Jones, C. J. C. and Petyt, M. 1999 (b) *Journal of Sound and Vibration* **228**(1),129-156. Ground vibration generated by a load moving along a railway track.

Sheng, X., Jones, C. J. C. and Petyt, M. 1999 (c) *University of Southampton, Institute of Sound and Vibration Research, Technical Memorandum* 837. The Fourier transformed stationary and moving flexibility matrices of a layered ground.

Sheng, X., Jones, C. J. C., Petyt, M. and Thompson, D. J. 2000 *Journal of Sound and Vibration* **236**(2), 362-366. Authors' reply to the comments to "Ground Vibration Generated by a Load Moving along a Railway track".

Shioda, M. 1996 *Inter-Noise'96*, Liverpool, 1649-1654. The current state and future tasks of prediction technique of environmental ground vibration caused by many kinds of vibration sources.

Stump, B. 1984 *Journal of Sound and Vibration* **92**(2), 181-202. Stress wave in an elastic half-space: single and multiple surface sources.

Suiker, A., Chang, C. et al. 1999 (a) *European Journal of Mechanics A-Solids* **18** (5), 749-768. Surface waves in a stratified half-space with enhanced continuum properties: Part I: Formulation of the boundary value problem.

Suiker, A., Chang, C. et al. 1999 (b) *European Journal of Mechanics A-Solids* **18** (5), 769-784. Surface waves in a stratified half-space with enhanced continuum properties: Part II: Analysis of the wave characteristic in regard to high speed railway tracks

Tadeu, A. J. B. and Kausel, E. 2000 *Journal of Engineering Mechanics* **126**(10), 1093-1097. Green's functions for two-and-a-half-dimensional elastodynamic problems.

Takemiya, H. and Fujiwara, A. 1994 *Soil Dynamics and Earthquake Engineering* **13**, 49-61. Wave propagation/impediment in a stratum and wave impeding block (WIB) measured for SSI response reduction.

Takemiya, H., Shiotsu, Y. and Yuasa, S. 2000 *Proceedings of Japan Society of Civil Engineers*, **661**/I-53, 33-42. Features of ground vibration induced by high-speed trains and the counter vibration measure X-WIB.

Takemiya, H. and Yuasa, S. 1999 1999 *Structural Dynamics-EURODYN'99*, Balkema, Rotterdam, 821-826. Lineside ground vibration induced by high-speed train and mitigation measure WIB.

Tassoulas, J. and Kausel, E. 1983 *International Journal for Numerical Methods in Engineering* **19**(7), 1005-1032. Elements for the numerical analysis of wave motion in layered strata.

Thompson, D. J. 1993 *Journal of Sound and Vibration* **161**, 421-446. Wheel-rail noise generation, Part III: rail vibration.

Thompson, D. J. 1997 *Journal of Sound and Vibration* **203**(5), 867-888. Experimental analysis of wave propagation in railway tracks.

Thomson, W., 1950 *Journal of Applied Physics* **21**, 89-93. Transmission of elastic waves though a stratified solid medium,

Trochides, A. 1991 *Applied Acoustics* **32**, 289-296. Groundborne vibration in buildings near subways.

Van den Broeck, P. and De Roeck, G. 1999 1999 *Structural Dynamics-EURODYN'99*, Balkema, Rotterdam, 837-842. The vertical receptance of track including soil-structure interaction.

Villot, M. and Chanut, J. 1997 *Proceedings of Internoise'97*, Budapest. A layered soils model to study the vibrational behaviour of embedded plates.

Villot, M., Jean, P. and Chanut, J. 1997 Railway Vibration Project RENVIB II, Phase 1: State of the Art Review, Task 3: Mathematical modelling of railway vibration.

Waas, G. 1972 *PhD Dissertation in the University of California.* Linear two-dimensional analysis of soil dynamic problems in semi-infinite layer medium,

Wang, C. and Lai, J. C. S. 2000 *Journal of Sound and Vibration* **229**(3), 453-466. Modelling the vibration behaviour of infinite structure by FEM

Wang, S. M., Shnoi, R. A. and Zhao, L. B. 1998 *Proc Instn. Mech. Engrs.* **212**, 567-575. A new time integration method in structural dynamics using the Taylor series.

Wei, J. and Petyt, M. 1987 *ISVR Technical Memorandum No. 628, University of Southampton.* Application of finite elements techniques to ground vibration transmission using a semi-infinite element model.

Press, William H. et al 1992 *Numerical Recipes in FORTRAN, the Art of Scientific Computing (second edition)*, Cambridge University Press.

Wittrick, W. H. and Williams, F. W. 1971 *Quarterly Journal of Mechanics & Applied Mathematics* **24** (3). A general algorithm for computing natural frequencies of elastic structures.

Woldringh, R. F. and New, B. M. 1999 *Proc. 12th Eur. Conf. Soil Mech. and Geotechn. Eng.*, **3**, 1703-1712. Embankment design for high-speed train on soft soils.

Wolf, J. 1985 *Dynamics Soil-Structure Interaction*, Prentice-Hall, Englewood Gliffs, New Jersey.

Wolfert, A. R. M. and Dieterman, H. A. 1997 *Journal of Sound and Vibration* **203**(4), 597-606. Passing through the "elastic wave barrier" by a load moving along a waveguide.

Wu, T. X. and Thompson, D. J. 1999(a) *Journal of the Acoustical Society of America* **106** (3), 1369-1376. Analysis of lateral vibration behaviour of railway track at high frequency using a continuously supported multiple beam model.

Wu, T. X. and Thompson, D. J. 1999(b) *Journal of Sound and Vibration* **219**(5), 881-904. The effects of local preload on the foundation stiffness and vertical vibration of railway track.

Wu, T. X. and Thompson, D. J. 1999(c) *Journal of Sound and Vibration* 224(2), 329-348. A double Timoshenko beam model for vertical vibration analysis of railway track at high frequencies.

Xu, P. and Mal, A. K. 1985 *Wave Motion* **7**, 235-243. An adaptive integration scheme for irregularly oscillation functions.

Yang, B., Tan, C. A. and Bergman, L. A. 2000 *Journal of Engineering Mechanics*, **126**(5), 462-469. Direct numerical procedure for solution of moving oscillator problems

Yang, J. and Sato, T. 1998 *Journal of Sound and Vibration* **213** (3), 561-568. On the vibration of saturated layered half-space due to low frequency excitation.

Yang, Y. B. and Hung, H. H. A. 1997 *International Journal for Numerical Methods in Engineering* **40**, 3729-3747. Parametric study of wave barriers for reduction of train-induced vibrations.

Zai, W. 1997 *Dynamics of Coupled Vehicle-Track Sytems*. China Railway Press, Beijing. (In Chinese)

Zhang, C. Chen, X. and Wang, G. 1999 *Earthquake Engineering and Structural Dynamics* **28**, 421-441. A coupling model of FE-BE-IBE for non-linear layered soil-structure interaction.

Zhang, R. 2000 *Journal of Sound and Vibration* **229**(5), 1193-1212. Some observations of modelling of wave motion in layered based elastic media.

Zhang, R., Zhang, L. and Shinozuka, M. 1997 *Journal of Applied Mechanics* **64**, 50-65. Seismic waves in laterally inhomogeneous layered medium.

Zhang, X., Wegner, J. L. and Haddow, J. B. 1999 *Earthquake Engineering and Structural Dynamics* **28**, 1501-1524. Three-dimensional dynamic soil-structure interaction analysis in the time domain.